



HAL
open science

Development of SERS nanosensor for detection of water pollution

Inga Tijunelyte

► **To cite this version:**

Inga Tijunelyte. Development of SERS nanosensor for detection of water pollution. Physics [physics]. Université Sorbonne Paris Cité, 2016. English. NNT : 2016USPCD007 . tel-01691637

HAL Id: tel-01691637

<https://theses.hal.science/tel-01691637>

Submitted on 24 Jan 2018

HAL is a multi-disciplinary open access archive for the deposit and dissemination of scientific research documents, whether they are published or not. The documents may come from teaching and research institutions in France or abroad, or from public or private research centers.

L'archive ouverte pluridisciplinaire **HAL**, est destinée au dépôt et à la diffusion de documents scientifiques de niveau recherche, publiés ou non, émanant des établissements d'enseignement et de recherche français ou étrangers, des laboratoires publics ou privés.

Université Paris 13-UFR SMBH

N° attribué par la bibliothèque

--	--	--	--	--	--	--	--	--	--

T H E S E

Pour obtenir le grade de
DOCTEUR DE L'UNIVERSITE PARIS 13

Discipline: Physique et Science des Matériaux

Ecole doctorale Galilée

Présentée et soutenue publiquement par

Inga TIJUNELYTE

Le 26 Janvier 2016

Development of SERS Nanosensor for Detection of Water Pollution

Directeur de thèse: Prof. Marc Lamy de la Chapelle

JURY

Prof. Bernard Humbert	Unniversité de Nantes	Rapporteur
Prof. Nordin Felidj	Université Paris 7	Rapporteur
Dr. Virginie Nazabal	CNRS	Examineur
Dr. Emmanuel Rinnert	IFREMER	Examineur
Dr. Timothée Toury	Université de Technologie de Troyes	Examineur
Dr. Nathalie Lidgi-Guigui	Université Paris 13	Encadrante
Dr. Erwann Guenin	Université Paris 13	Encadrant
Prof. Marc Lamy de la Chapelle	Université Paris 13	Directeur de thèse

This PhD was performed in close collaboration with:

L'Institut Français de Recherche pour
l'Exploitation de la Mer (Ifremer)



Bureau de Recherches Géologiques et Minières
(BRGM)



Centre de documentation, de recherche et
d'expérimentations
sur les pollutions accidentelles des eaux
(CEDRE)



Université de Technologie de Troyes (UTT)



Horiba Scientific



Acknowledgment

This dissertation is a compilation of the studies performed with the help and the support of many people. Thus, I would like to take the opportunity to express my greatest appreciation.

First of all, I would like to thank the members of the evaluation committee for their kind agreement to revise this work. Hence, I would like to acknowledge professor Bernard Humbert and professor Nordin Felidj for accepting to be reporters. Thank you for your time spent to evaluate my thesis. Equally, I would like to express my gratitude to doctor Virginie Nazabal, doctor Timothée Toury and doctor Emmanuel Rinnert for their acceptance to be examiners.

My PhD studies were performed in the CSPBAT laboratory and I would like to thank to professor Véronique Migonney for welcoming me here.

Particularly, I would like to acknowledge the director of my thesis professor Marc Lamy de la Chapelle for always having time to answer all my questions, for providing endless guidance toward the success and giving me constant motivation. Thank you for your encouragement to face my fear of public speaking; by attending national and international conferences I gained a lot of experience and knowledge. Nonetheless, I would like to express my appreciation to my supervisors doctor Nathalie Lidgi-Guigui and doctor Erwann Guenin. You were always available to help me and offer advices on all matters. Thank you for your support which made my three years easier.

Also I would like to acknowledge ANR REMANTAS project for funding my thesis and all partners included in the project. I thank to doctor Emmanuel Rinnert for welcoming me in Ifremer for experimental exchange. He together with Florent Colas and doctor Jonathan Moreau always provided me help. I would like to express my great thanks to doctor Joyce Ibrahim and doctor Timothée Toury from UTT for providing us the substrates which are essential component in SERS based nanosensors. Equally, I want to express my thanks to members of Horiba, Cedre and BRGM that I had chance to meet and discuss. Thank you for advising me and sharing your knowledge. Particularly, I am grateful to doctor Stephanie Betelu, for very close collaboration lasting for all these three years.

Many thanks to past and present PhD students in SBMB group. For the great discussions, about the science and more often about the life, I want especially thank to Sadequa Sultana, Maximilien Cottat, Raymond Gillibert, Nene Thioune and Nicolas Guillot. Additional thanks to the master students that were present in our team during my thesis.

I would like to express great gratitude towards all members of LBPS and SBMB groups for their help and support.

Also I am very grateful to professor Benjamin Carbonnier and doctor Julien Babinot for accepting me in their laboratory and providing help in chemical synthesis. I thank to doctor Leïla Boubekeur-Lecaque and doctor Nathalie Dupont for performed DFT calculations.

Last but not least I thank you all my friends and family for understanding my long absence, for their support and encouragement. Finally, I thank Julien, for his love and care during these years. Thank you!

Abbreviations

ADD(s) - Aryl-Diazonium Derivative(s)	MIP - Molecularly Imprinted Polymers
Anti-BAP13 - clone name for anti-body against benzo[a]pyrene	MOH - 6-Mercapto-1-hexanol
ATR - Attenuated Total Reflectance	MS - Mass Spectrometry
BaP - Benzo[a]pyrene	MUA - Mercaptoundecanoic Acide
BSA - Bovine Serum Albumin	NAP - Naphthalene
BTEX - Benzene, Toluene, Ethylbenzene, Xylenes	NHS - N-hydroxysuccinimide
CD(s) - Cyclodextrin(s)	NMR - Nuclear Magnetic Resonance
CTAB - Cetrimonium bromide	PAH(s) - Polycyclic Aromatic Hydrocarbon(s)
DFT - Density Functional Theory	Phe - Phenylalanine
DNA - Deoxyribonucleic Acid	PM-IRRAS - Polarization Modulation Reflection Absorption Infrared Spectroscopy
DS - Benzenediazoniumtetrafluoroborate	QCM - Crystal Microbalance
DS-(CH₂)₂NH₂ - 4-(aminoethyl) benzenediazoniumtetrafluoroborate	RNA - Ribonucleic Acid
DS-C₁₀H₂₁ - 4-decyl benzenediazoniumtetrafluoroborate	RNase-A - Ribonuclease A
DS-COOH - 4-carboxybenzene diazoniumtetrafluoroborate	SAM(s) - Self Assembled Monolayer(s)
E.U. WFD - European Union Water Framework Directive	SAW - Surface Acoustic Wave
EBL - Electron Beam nano-Lithography	SBSE - Stir Bar Sorptive Extraction
EDC - 1-ethyl-3-(3-dimethylamino-propyl)carbodiimide hydrochloride	SERRS - Surface Enhanced Raman Resonance Scattering
F(ab')₂ - Fragments of Antigen Binding	SERS - Surface Enhanced Raman Scattering
FID - Flame Ionization Detection	SPE - Solid Phase Extraction
FL - Fluoranthene	SPME - Solid Phase Microextraction
FLD - Fluorometric Detection	SPR - Surface Plasmon Resonance
GC - Gas Chromatography	TGA - Thermogravimetric analysis
GNCs - Gold Nanocylinder(s)	TOL - Toluene
GNPs - Gold Nanoparticles(s)	TOM - Orthomonooxygenase
HPLC - High Pressure Liquid Chromatography	Trp - Tryptophan
ISO - International Organization for Standardization	Tyr - Tyrosine
K_{ow} - Octanol/water Partition Coefficient	U.S. EPA - United States Environment Protection Agency
LLE - Liquid-Liquid Extraction	UVD - Ultraviolet Detection
LODs - Limit(s) of Detection	VOCs - Volatile Organic Compound(s)
LOQs - Limit(s) of Quantization	XPS - X-Ray Photoelectron Spectroscopy
LSPR - localized Surface Plasmon Resonance	

TABLE OF CONTENTS

GENERAL INTRODUCTION	1
1 ENVIRONMENTAL WATER POLLUTION BY AROMATIC HYDROCARBONS	3
1.1 INTRODUCTION	3
1.2 AROMATIC HYDROCARBONS	4
1.3 SOURCE OF AROMATIC HYDROCARBONS	6
1.4 TOXICITY CAUSED BY AROMATIC HYDROCARBONS	7
1.5 COMMON POLLUTION MONITORING TECHNIQUES	10
1.6 SENSORS AS AROMATIC COMPOUND MONITORING PLATFORMS	12
1.7 REFERENCES	17
2 SURFACE ENHANCED RAMAN SPECTROSCOPY AND ITS APPLICATION TO SENSING PLATFORMS	23
2.1 INTRODUCTION	23
2.2 PRINCIPLE	23
2.3 SENSING PLATFORMS FOR SERS	36
2.4 CONCLUSION	60
3 FUNCTIONALISATION OF THE NANOSENSOR WITH ANTI-BODIES FOR BENZO[A]PYRENE DETECTION	61
3.1 INTRODUCTION	61
3.2 ANTI-BODY IMMOBILISATION ON THE SENSOR SURFACE	61
3.3 STRATEGIES OF DESIGN OF F(AB') ₂ BASED NANOSENSORS FOR BENZO[A]PYRENE DETECTION	71
3.4 CONCLUSION	81
3.5 REFERENCES	81
4 CYCLODEXTRINS FUNCTIONALISATION FOR SIZE SELECTIVE POLLUTANT DETECTION	84
4.1 INTRODUCTION	84
4.2 INVESTIGATION OF AROMATIC HYDROCARBON INCLUSION INTO CYCLODEXTRINS BY RAMAN SPECTROSCOPY AND THERMAL ANALYSIS	84
4.3 APPLICATION OF THIOLATED CD AS RECEPTOR OF SERS ACTIVE SENSORS	98
4.4 CONCLUSION	113
5 EXPLOITATION OF DIAZONIUM SALTS FOR NANOSENSORS FUNCTIONALISATION FOR POLLUTANT DETECTION	114
5.1 INTRODUCTION	114
5.2 RAMAN CHARACTERIZATION OF PHENYL-DERIVATIVES: FROM PRIMARY AMINE TO DIAZONIUM SALTS	115
5.3 DIAZONIUM SALT-BASED SERS SUBSTRATES: AT THE ROOT OF THE DEVELOPMENT OF INNOVATIVE “LONG LIFE” ROBUST SERS SENSORS	133

5.4 DIAZONIUM SALT-BASED SERS ACTIVE SENSOR: TOWARDS DETECTION AND QUANTITATION OF THE AROMATIC HYDROCARBONS IN WATER SAMPLES	150
5.5 CONCLUSION	170
6 NANOPLASMONICS EXPLOITATION FOR SELECTIVE NANOSURFACE FUNCTIONALISATION	171
6.1 INTRODUCTION	171
6.2 NANOPLASMONICS TUNED “CLICK CHEMISTRY”	172
6.3 CONCLUSION	188
GENERAL CONCLUSION AND PERSPECTIVES	189
ANNEX 1: EXPERIMENTAL SERS SET-UPS	193
ANNEX 2: ELECTRONIC SUPPLEMENTARY MATERIAL FOR INVESTIGATION OF AROMATIC HYDROCARBONS INCLUSION INTO CYCLODEXTRINS BY RAMAN SPECTROSCOPY AND THERMAL ANALYSIS	196
ANNEX 3: CHEMICAL SHIFT OBTAINED BY NMR OF CD AND CD-SH	201
ANNEX 4: ELECTRONIC SUPPLEMENTARY INFORMATION ON RAMAN CHARACTERIZATION OF PHENYL DERIVATIVES: FROM PRIMARY AMINE TO DIAZONIUM SALTS	202
ANNEX 5: SUPPORTING INFORMATION FOR DIAZONIUM SALT-BASED SERS SUBSTRATES: AT THE ROOT OF THE DEVELOPMENT OF INNOVATIVE “LONG LIFE” ROBUST SERS SENSORS	208
ANNEX 6: SUPPLEMENTARY INFORMATION FOR DIAZONIUM SALT-BASED SERS ACTIVE SENSOR: TOWARDS DETECTION AND QUANTITATION OF THE AROMATIC HYDROCARBONS IN WATER SAMPLES	210
ANNEX 7: SUPPLEMENTARY INFORMATION FOR NANOPLASMONICS TUNED “CLICK CHEMISTRY”	213

GENERAL INTRODUCTION

The environmental water pollution by aromatic compounds is an ongoing worldwide issue demanding for an improvement of the environmental quality monitoring. The objectives of the REMANTAS project (approved by the National Research Agency under the ECOTECH 2011 program) were to address such issues. Initiated in 2012, it aimed in developing an original analytical tool allowing on-site measurements of organic contaminants in aquatic environments (seawater and freshwater) and offering a better estimation of the spatial and temporal variability of water contamination. The molecules targeted within the REMANTAS project and during my PhD are summarised in the table 1. The innovation proposed within this project is related with the exploitation of the Surface Enhanced Raman Scattering (SERS) method. It has been selected for its qualitative and quantitative analytical performances. However, to be able to provide a specific detection, it has to be combined with a (bio)chemical receptor that enable the pre-concentration of the analytes present in water media at the sensor surface.

Table 1 The targeted substances chosen in the frames of the Remantas project, regarding their presence on the list of priority substances under the Water Framework Directive 2000/60/EC and/or on the list of the 100 chemicals most transported by sea.

PAHs	LOD (ppb)	Clorinated solvents	LOD (ppb)	BTEX	LOD (ppb)
Naphthalene	2.4	Chloroethylene	10	Benzene	10
Fluoranthene	0.1	1,1-dichloroethane	10	Toluene	74
Benzo[a]pyrene	0.05	Trichloromethane	2.5	Ethylbenzene	65
				Xylenes	1

In the framework of the REMANTAS project, this manuscript will be dedicated to the presentation of the experiments performed in order to design robust, sensitive, selective and reproducible SERS nanosensors for the detection of the selected pollutants.

First of all, the Chapter 1 will give a review of the environmental water pollution and of the main issues related to this topic. The Chapter 2 will be devoted to the description of the general principle of SERS including the explanation of various phenomena contributing to the enhancement effect. In the same chapter we will also review the techniques for SERS substrates fabrication and the strategies for surface functionalisation proposed in the literature.

Chapters 3 to 5 will be dedicated to the presentation of the results obtained for the sensor surface functionalisation in order to design a robust molecular layer capable to selectively interact with the targeted molecules.

In Chapter 3 I will overview the works done for the design of a highly specific nanosensors based on the use of antibodies as bioreceptor. In the first part, experiments on the whole antibody immobilisation will be described, whereas the second part will be devoted to the exploration of the benefits offered by the use of the fragment antigen-binding (Fab).

Chapter 4 will be focused on the cyclodextrins (CDs). Such molecules have been exploited to pre-concentrate the targeted pollutants thanks to host-guest interaction between the CDs cavity and the guest molecules. First, the complexes formation achieved by mixing molecules in bulk solution and allowing them to interact will be presented. The results of the formed complexes analysis by Raman spectroscopy and thermogravimetric analysis (TGA) will be summarized. Finally, in a second part, I will present the results of the CDs application as surface receptor for the nanosensor design.

Chapter 5 will summarise the efforts made towards the diazonium salts (DSs). These latter ones have been chosen to pre-concentrate apolar pollutants by π - π stacking and hydrophobic interactions. The first part of this chapter will describe the synthesis of the DSs followed by their characterisation by Raman spectroscopy. The second part will be devoted to the surface functionalisation of the sensor by DS. Based on the results achieved by SERS and DFT calculations, we will propose the characteristics of the DS based layers on gold nanostructures. Finally, the last part of this chapter I will focus on polycyclic aromatic hydrocarbons (PAHs) detection using DS-based SERS nanosensors.

Chapter 6 will be dedicated to an innovative approach of surface functionalisation and modification. Herein, the specific molecular immobilisation thanks to radical mediated thiol-ene reaction on plasmonic nanostructures will be described. As it will be demonstrated, this strategy stands as a first test in the synthesis of multi-targeted sensing platforms.

Finally, a general conclusion will give a summary of all the works developed during this PhD and will open to new research perspectives.

1 Environmental water pollution by aromatic hydrocarbons

1.1 Introduction

Water is crucial for the existence of all organisms, including humans. Our planet stocks a huge amount of water and this amount will not diminish on shorter than geological time scale [1]. However, only about 3 % of environmental waters are considered as fresh water (Figure 1.1) whereby the biggest part is stored as glaciers or deeply underground [2] [3]. Thus, since part of consumable water is very little, ensuring clean water supplies is of first importance.

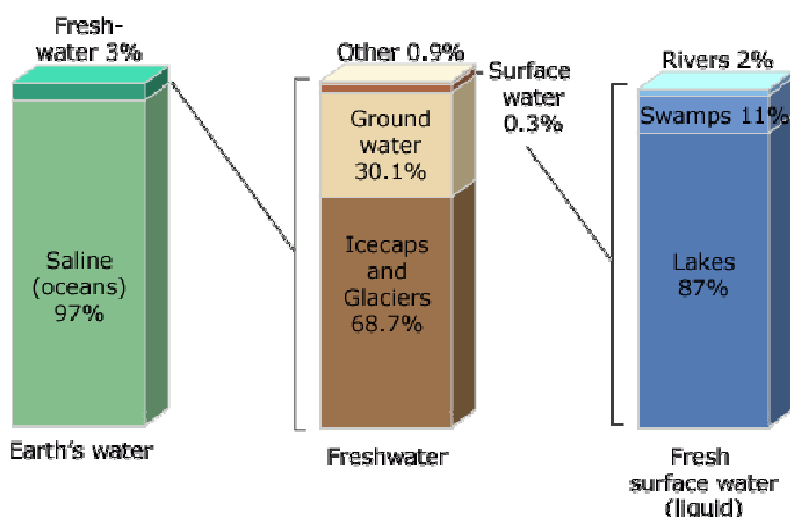


Figure 1.1 Distribution of water in Earth.

On the other hand, marine and coastal waters serve as highways for the shipping industry or provide extractable sand and gravel areas for agriculture production. At the same time it is a source of wild fishes for human consumption and important recreational opportunities [4]. In order to maintain these functions it is essential that environmental quality is ensured.

However, the increasing chemical industry such as pharmaceuticals, petrochemicals, agrochemicals, industrial and consumer chemicals have raised the public awareness and concern about the presence of these chemicals in the environment. Today, chemical pollution is one of the main pressures affecting environmental water. The global production of chemicals is increasing worldwide (Figure 1.2). Up to now about 100 000 chemicals are available in market of European Union (EU) and very likely some of these substances are being released in aquatic system [4].

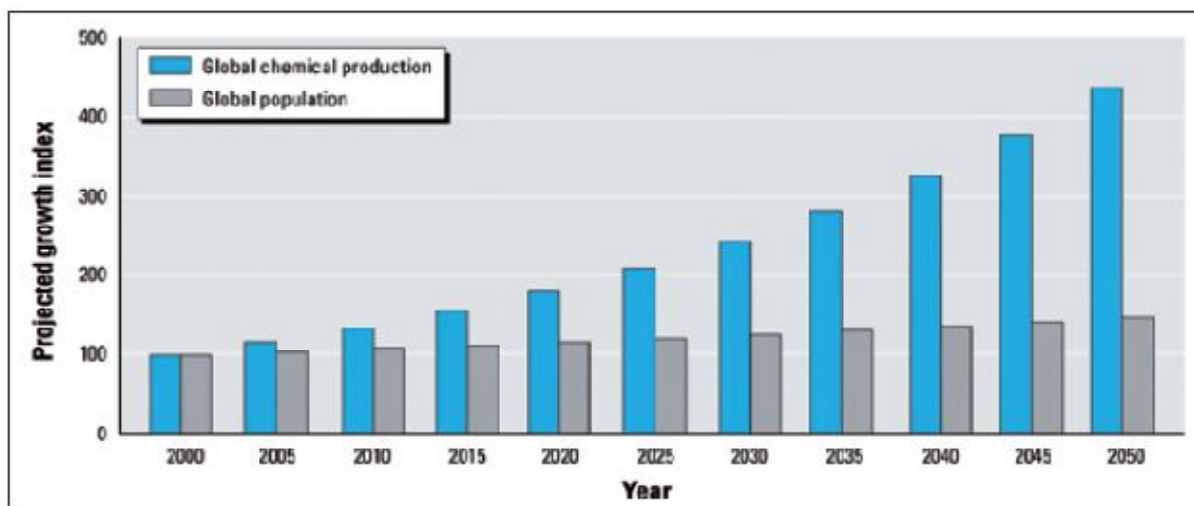


Figure 1.2 Global population grow rate in comparison with the global chemical production grow [5].

The environmental pollution is defined as the presence of chemicals, which induce harm to the environment or living organisms and as a consequence, any pollutant causing one or more effects if presented in water at high enough concentrations. However, certain chemicals have been identified by international agreements or regulations as being “priority chemicals for control”. The criteria on which these chemicals have been selected are as follows [6]:

- The chemicals are frequently found by monitoring programs
- They are toxic at low concentrations
- They bioaccumulate
- They are persistent
- They are carcinogens

Mononuclear aromatic hydrocarbons often referred as BTEX (benzene, toluene, ethylbenzene and xylenes) as well as polycyclic aromatic hydrocarbons (PAHs) are consistent with all these criteria. This chapter will be especially devoted to the aromatic hydrocarbons: their appearance in environmental waters, their induced toxicity and the proposed ways of monitoring them in environmental waters.

1.2 Aromatic hydrocarbons

Aromatic molecules (or aromatic groups within a larger molecule) are characterized by a fully conjugated cyclic structure having notable stability with respect to ring opening, notable lack of reactivity with respect to substitution or addition and notable diamagnetic ring current effects in nuclear magnetic resonance. In the simplest terms, a monocyclic molecule (or part of a molecule) may be identified as aromatic according to whether or not it satisfies the so-called Hückel rule, which requires that it have $4n + 2$ electrons within its conjugated π system. [7].

Mono-aromatic hydrocarbons are often referred as BTEX which is standing for Benzene, Toluene, Ethylbenzene and three isomers of Xylenes (Figure 1.3). Due to high volatility, these organic solvents are included in the group of volatile organic compounds (VOCs). Benzene as priority substance is included in the list of the European Union Water Framework Directive (E.U. WFD) [8] whereas toluene, ethylbenzene and xylenes take a part of the selected substances of the French circular of the 7 may 2007.

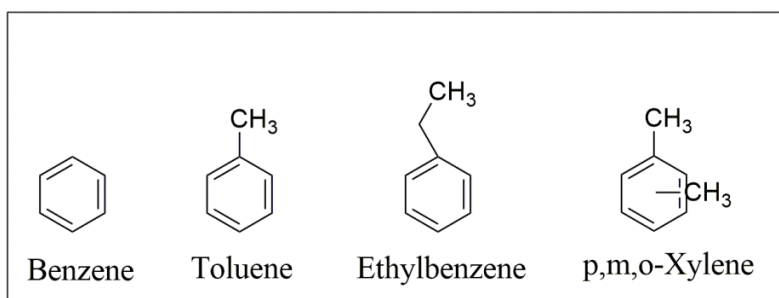


Figure 1.3 Molecular structure of BTEX.

Polycyclic aromatic hydrocarbons (PAHs) are conjugated systems built on benzene rings. They are considered as a fused aromatic ring systems where a pair of carbon atoms is shared and all atoms within molecule lie in one plane [9]. These organic molecules vary from two fused aromatic rings (C₁₀H₈) called naphthalene till eight conjugated rings (C₂₄H₁₁) called coronene (few examples of PAHs structures are illustrated in Figure 1.4). The number of aromatic rings and molecular structure define their physical and chemical properties [9]. In this range there are large number of molecules differing in the position and the number of aromatic rings. The solubility of PAHs in aqueous environment is very low due to their hydrophobic nature (the octanol/water partition coefficient $\log K_{ow} = 3 - 8$) and decreasing with increasing molecular weight [10]. Some of the PAHs can be classified as semi-VOCs, whereas all of them are included in the persistent organic compounds group. Due to their toxicity and potential carcinogenicity PAHs are listed as the priority substances to be detected in the environment by the E.U. WFD [8] and by the United States Environment Protection Agency (U.S. EPA) [11].

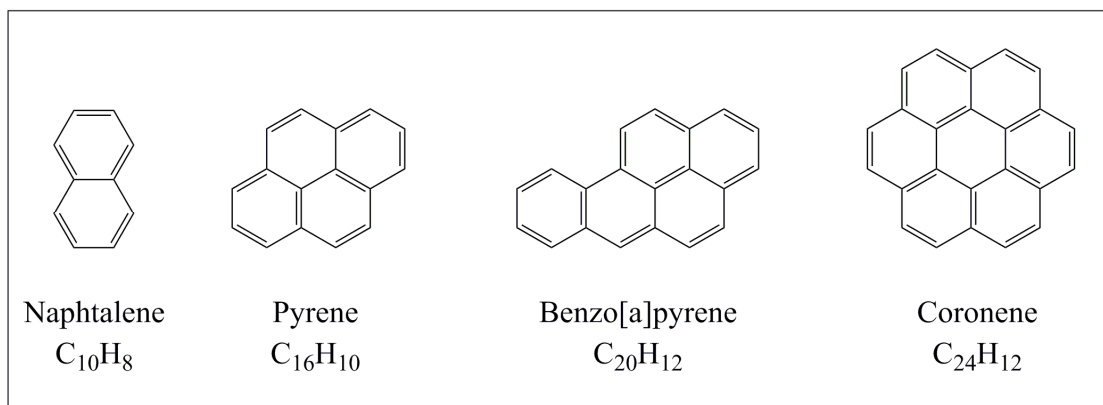


Figure 1.4 Few examples of PAHs molecular structure.

1.3 Source of aromatic hydrocarbons

The aromatic hydrocarbons are emitted into environment via natural and anthropogenic combustion processes. The major natural sources of aromatics are volcanic eruptions, forest and prairie fires. The most important anthropogenic sources of PAHs consist of combustion of fossil fuels, waste burning, petroleum coke and asphalt production and many other industrial activities. The environmental pollution originating from industrial activities is very complex since the chemicals can be released to the environment at many stages of their life cycle, from development and testing, through manufacture, cargo space and circulation through to use and finally dumping.

Due to the water exchange cycle, the major part of aromatic organic pollutants, loading to aquatic systems have a component which is atmospheric in origin [10]. Atmospheric deposition ways has been estimated to cause 10 to 80% of total input of organic pollutants into surface waters [9]. For instance, the atmospheric input of PAHs to the Mediterranean Sea have been assessed to be 47.5 tons per year, while the contribution of the rivers to the pollution was found to be around 5.3 and 1.3 tons per year from Rhone and Ebro rivers, respectively [12].

As a result surface and marine waters are then loaded by aromatic compounds via atmospheric fallout, urban runoff, municipal influents and industrial influents [10]. In most of the case, these events are classified as nonpoint source pollution.

On the contrary, point source pollution is a single event issued from an identified source. The examples of point source pollution could be the oil spillage and leakage or discharge of produced water. Further elaboration on these pollution sources will be provided in order to emphasize its huge impact on the marine health.

1.3.1 Oil as a source of PAHs to the environmental waters

PAHs in the composition of the crude oil are introduced in environmental waters through the leaking from oil natural reservoirs. This process of oil seeps are registered all over the world with higher concentrations in certain regions [13]. Measured worldwide rates of the oil seeps vary between 0.02 and 2.0×10^6 tons per year with the most realistic estimate being 0.2×10^6 tons per year. Additionally to the natural oil seeping, PAHs are introduced into marine waters via accidental oil spills. For instance, recently the “Deepwater Horizon” accident in the Mexican Gulf (in 2010) resulted in a release of 779×10^6 liters of crude oil [14]. Another significant example is the accident of the “Exxon Valdez” in Prince William Sound, Alaska, USA (in 1989) which spilt 42×10^6 liters of crude oil [15]. Important incidents were registered in European waters as well. For instance, the “Erika” accident (in 1999) released 18 000 tons of crude oil into French coastal waters and in Spain, the “Prestige” (in 2002) spilted 60 000 tons of heavy fuel oil into the waters outside of Galicia [16]. These are just few examples of accidental release of large quantities of oil to the aquatic environment.

1.3.2 Produced water as a source of PAHs to the environmental waters

So called produced water is the one involved in the oil production offshore and onshore processes. The most often, it consists of a mixture of the water contained naturally in the reservoir and of injected water used for the recovery of oil combined with the treatment chemicals added during production process [17]. Records published from offshore oil production platforms in the North Sea demonstrated that produced water mainly consist of BTEX (97%). Remaining 3% is mixture between naphthalene, phenanthrene and dibenzothiophene where naphthalene represents the largest fraction (92%). The residues of the larger PAHs (<0.2%) can also be found in produced waters with the decreasing concentrations of one order of magnitude for the compounds bearing additional rings [17] [18]. Produced water is defined as a chronic source of PAH to the marine environment, with a possible long term impact on the environment [19].

1.4 Toxicity caused by aromatic hydrocarbons

The pollution by aromatic hydrocarbons is an ongoing worldwide concern due to their high potential carcinogenic and mutagenic activities. The potential PAHs carcinogenic effect was first time recognized in 1775 by Pott who observed the relationship between soot and cancer. In the 1930,

pioneering studies by Kennaway and Hieger (1930) and Cook et al. (1933) described, that PAHs were carcinogenic components. Later investigations showed that many PAHs act as potent carcinogens or mutagens via deoxyribonucleic acid (DNA) adduct formation [20].

1.4.1 DNA adducts from PAHs

Aquatic vertebrates such as fishes are capable of metabolizing PAHs, producing reactive intermediates species and occasionally resulting in formation of hydrophobic DNA adducts. It is worth to note that metabolic activation of PAHs to reactive radicals constitutes their major toxic effect. Two main metabolic pathways that yield the intermediates which covalently binding to DNA were described by Xue and Warshawsky [21]. The interaction between reactive PAHs intermediates and DNA sites depends on the reactive species, the nucleophilicity of the DNA site and some steric factors [20]. Formed DNA and PAH metabolites complexes are known to be the crucial factors in cancer development together with low efficiency of repair systems and long term exposure [22]. DNA adducts with benzo[*a*]pyrene (model compound for the PAHs) were the most studied [23] [24]. However, similar effect, induced by lower molecular weight PAHs were also reported [25]. The schematic illustration of the adduct formation process is given in Figure 1.5.

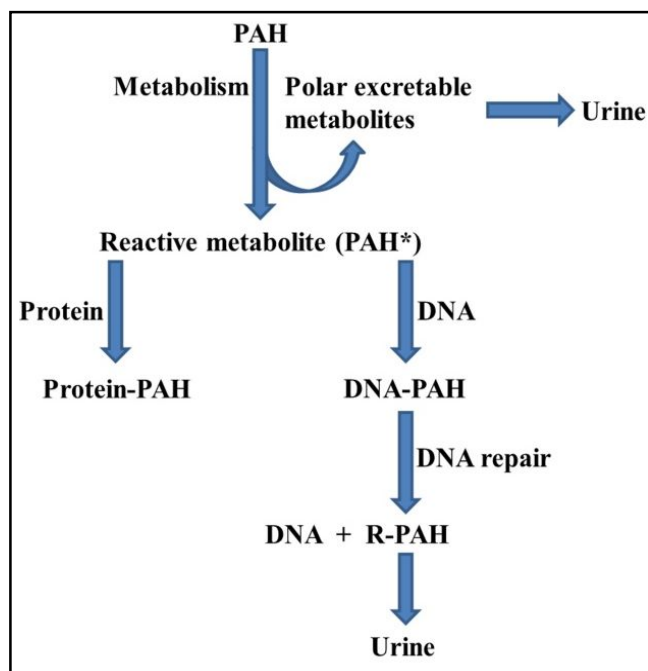


Figure 1.5 Schematic pathway of PAH metabolism leading to a formation of protein and DNA adducts [26].

DNA adducts have been used as a biomarker of exposure to PAHs since the 1990. For instance, monitoring of DNA adducts has been performed in order to assess the impact of the “Erika” oil spill along the coasts of French Brittany. In this study, human hepatocyte (HePG2 cells) were introduced to an “Erika” fuel extract which lead to the formation of DNA adducts similar to the ones observed in the study using fish (*Solea solea*). These data indicates that human hepatocytes biotransform “Erika” fuel into genotoxic metabolites similarly to hepatic cells of fishes [27].

1.4.2 Proteins adducts from polycyclic aromatic hydrocarbons

Along with the high affinity to a DNA, PAH metabolites form adducts with the proteins as well (Figure 1.6). Adducts formation has been demonstrated between human serum albumin and diol epoxides of fluoranthene and benzo[*a*]pyrene [28]. It is highly likely that the same type of mechanism is operating in animals and fishes [20].

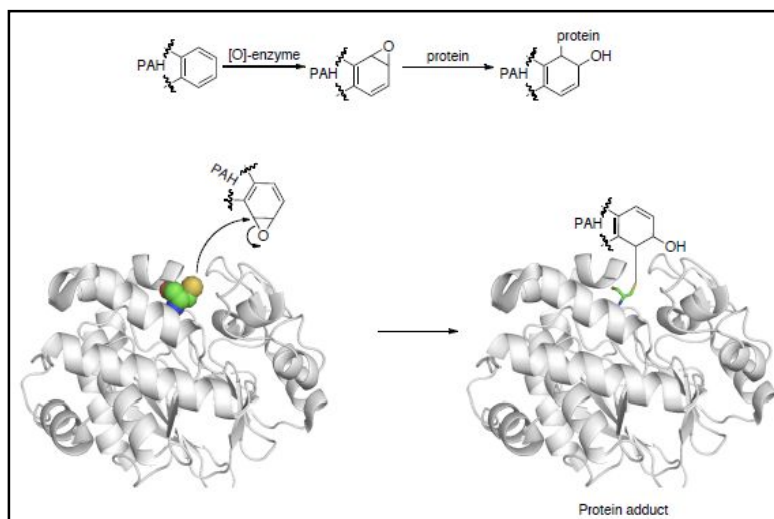


Figure 1.6 Schematic illustration of the mechanism of PAH protein adduct formation.

Adduct formation between PAH metabolites and human proteins, particularly human hemoglobin and serum albumin have been widely studied and well documented [29] [30] [31]. In most of the case the PAHs adductation affects the proteins activity and as a consequence the adduct formation will have specific effect depending on the protein structure [20].

Due to their environmental concern, aromatic compounds as mentioned before are included in both US EPA and the U. E. WFD priority lists of dangerous compounds. It is then of first importance to detect such compounds in fresh or sea waters as fast as possible and to be able to monitor them at

lower concentrations than the harmful ones. This latter concern depends not only on the different regulations of the states but also on the analysis techniques available for their detection as will be explained in the following.

1.5 Common pollution monitoring techniques

A number of analytical methods for the determination of aromatic hydrocarbons in complex environmental samples have been developed [10]. Some of them are reported in Table . The first official method published in 1985 and named EPA-610 [32] has offered analysis of 16 PAHs in water samples at the ppb and sub-ppb concentration range. This method was provided for high pressure liquid chromatography (HPLC) and gas chromatography (GC) approaches. However, procedure proposed in EPA-610 was found limited in the successful separation and resolution of the compounds reporting the sum of an unresolved molecular pairs. In 2007 a published improved procedure EPA-8270D was devoted to the analysis of 16 PAHs and various semi-VOCs by employing gas chromatography coupled with mass spectrometry (GC-MS) [33]. Later, in 2002, standard protocol for PAHs determination in environmental waters was released by the International Organization for Standardization (ISO), ISO 17993:2002 [34]. In this case, the PAH analysis is based on liquid-liquid extraction (LLE) and final determination by HPLC combined with fluorescence detector [35].

Table 1 Standard procedures for determining of PAHs in aqueous samples (modified from [36]).

Method	Application	Sample preparation	Determination technique
EPA-610	PAHs in municipal and industrial wastewaters	About 1L of water samples is extracted with dichloromethane, the extract is then dried and concentrated to a final volume of less than 10 mL.	GC with A flame ionization detector or HPLC with UV and fluorescence detectors (with a packed column)
EPA-8270D	Aqueous samples	EPA 3500 series methods (version 3, 2000)	GC-MS with use of high resolution capillary columns and deuterated internal standard
ISO 17993:2002	Water quality (determination of 15 PAHs)	Water samples collected in brown glass bottles are stabilized by adding sodium thiosulfate. 1 L of sample is extracted using hexane. The extract is dried with sodium sulfate and then enriched by removal of hexane by rotary evaporation	HPLC and fluorescence detector

These environmental analysis procedures are essentially based on sampling techniques which are problematic since they bring uncertainty on the analysis due to spatial and temporal variability of

pollutants in the environment [37]. In order to obtain meaningful analytical results, a large number of samples is required. The sampling strategy is highly influenced by the nature of waters and the amount of solid content in the water matrix [10].

For PAHs recovery from water samples LLE and solid phase extraction (SPE) were widely investigated and used as conventional techniques. LLE is based on the common Soxhlet extraction and benefits in equipment cost. However, the main disadvantage is related to the need of large volumes of toxic and flammable solvents (*n*-hexane, benzene, toluene, dichloromethane, ect.) [38]. In this context LLE does not need to requirements of green analytical chemistry [39]. SPE, on the other hand, offers wide variety of extraction conditions [40] which does not demand outsized quantities of organic solvents. SPE separates different compounds by using principle of liquid chromatography, where employed cartridges are usually packed with polymer or silica based sorbents. However, SPE demands of multi-step time-consuming operations (washing, conditioning and eluting steps) which promote the loss of analytes if not fully automated and it still uses the toxic solvents [41]. It is worth to note that breakthrough volumes and the capacities of cartridge used in SPE method are often too low to reach good detection limits [42]. Another disadvantage of SPE is the limitation to semi-VOCs compounds since the boiling points of the components should be significantly higher than the solvents.

An improved SPE procedure so called solid-phase micro-extraction (SPME) was then introduced to pre-concentrate VOCs (including BTEX) in aqueous samples [43], [44], [45]. SPME combined with GC-FID (flame ionization detection) led the analysis of BTEX with the limits of detection (LODs) ranged from 0.07 to 0.24 µg/L. This system ensured single polymer-coated fused silica fiber (used to adsorb and pre-concentrate analytes) repeatability of 7%, but fiber-to-fiber reproducibility was amounted up to 22% [45].

In order to improve analysis of VOCs and semi-VOCs, and to reach sub-trace detection limits other solid adsorbents strategies were investigated. For instance, the analysis of aromatic compounds in aqueous environment using stir bar sorptive extraction (SBSE) is gaining increasing interest [46]. The SBSE is defined as a robust, sufficient and convenient technology which requires minimal sample volumes, performs the recovery rate of 90% for most non-polar compounds and 100% of the sorbed molecules are analyzed [47]. SBSE is an equilibrium technique [46] based on the partitioning of analytes between a polymer phase (polydimethylsiloxane (PDMS)) and the aqueous media. SBSE method under optimized procedure allows achieving extremely low detection limits. For example, the detection of PAHs in seawater down to sub-ppt level has been demonstrated by Roy et al. [42].

After analytes recovery and pre-concentration procedures (LLE, SPE, SPME or SBSE), the determination of solutes are most widely performed using GC [48] [49] combined with either FID or

MS detection or HPLC [50] equipped with fluorometric detection (FLD) or ultraviolet detection (UVD) [51].

It is necessary to point out that the research on the analytical methods for the determination of aromatic compounds in complex environmental waters is ongoing. Depending on the selected method numerous problems still have to be faced. In the conventional procedures main issues are approaching the sample collection, transportation, storage and its preparation for final determination [52]. Both SBSE and SPME techniques require the co-injection of organic solvents and high temperature in order to desorb pre-concentrated analytes [42] [46]. Finally, despite the benefits in sensitivity and reliability these techniques are undergoing problems of miniaturization and are not applicable for real-time monitoring of the chemical pollution. As a consequence, there is a great interest in developing alternative analytical methods such as chemical and biochemical sensors, noting that later approach of sensing tools could be applied for on-site and *in-situ* monitoring of environmental quality.

1.6 Sensors as aromatic compound monitoring platforms

A (bio) chemical sensor is a tool that transforms the chemical information related to a composition and/or concentration of a specific analyte into an analytically valuable signal [53]. The chemical information here might come from the chemical reaction of the analyte or from a physical processes occurring in the investigated system. Generally, (bio) chemical sensors are containing two functional units: a receptor and a transducer (Figure 1.7).

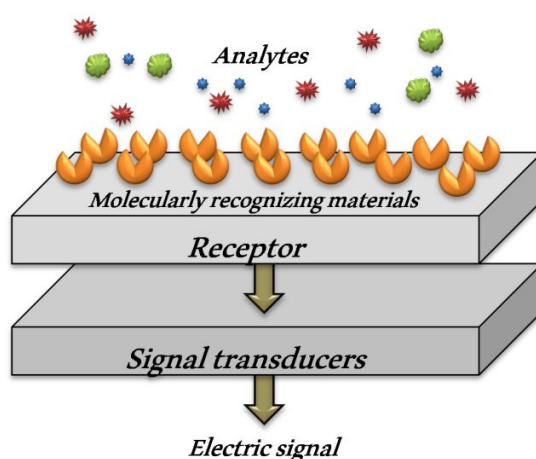


Figure 1.7 Schematic illustration of the components of chemical (bio) sensors.

The receptor unit is responsible for a chemical information transformation to a certain form of energy which can then be recognized by a transducer. The transducer is the device capable of transforming later energy into measurable analytical signal.

1.6.1 Biochemical sensors for monitoring of aromatic compound

Selected pollutants monitoring in environmental waters is a challenging task due to the great variety of the compounds present in the studied media. For this purpose the designed sensors have to be selective towards targeted molecules. Among the proposed sensors with a specific receptor, biosensors remain an important tool [54]. Biosensors are measurement devices combined with the bio-recognition element ensuring high affinity and specificity to the targeted molecule. The most popular biomolecules used for biosensors design are antibodies, oligonucleotides, enzymes and cells (Figure 1.8).

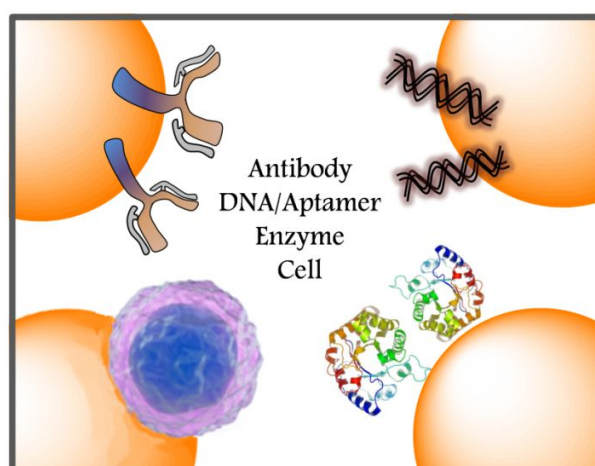


Figure 1.8 Most used biological objects used as bioreceptor in biosensors.

For instance, Eltzov *et al.* reported fiber-optic biosensor for monitoring chlorinated pollutants in air by exploiting immobilized bioluminescent bacteria. They have demonstrated that the bioluminescence was suppressed when designed biosensor was introduced in the environment with the toxic compounds. Using this method, LOD for chloroform in air was estimated to 6.6 ppb [55]. Later the same group has developed a flow-through fiber-optic sensing system employing other two bacterial strains for the monitoring of toxic chlorinated compounds in water [56].

Other class of molecules showing great potential in building biosensors is enzymes. Enzymes are used because of their catalytic activity towards analyte. For example, Zhong *et al.*, have described the construction of biosensor for toluene detection in water based on orthomonooxygenase (TOM) catalytic activity. In their study, optical fiber was coated by an oxygen-sensitive phosphorescent dye

which intensity was monitored. In this system toluene was detected thanks to the enzymatic reaction catalyzed by TOM, resulting in the consumption of oxygen and consequentially the change in the phosphorescence expression [57]. The restrictions concerning enzymes applications are mostly related with the limited number of biological substrates designed with the specific enzymes [58].

Aptamers are often single-stranded oligonucleotides, ribonucleic acid (RNA) or deoxyribonucleic acid (DNA) molecules that have high affinity and specificity to their target molecules [59]. They possess a three-dimensional structure and folding pattern, commonly undergoing changes in structure, upon binding to the target molecule. In addition, the synthesis of aptamers is rather easy, and the procedure does not demand purification. Moreover, they show high stability and resistivity to a denaturation and degradation [60]. These characteristics make aptamers to be excellent candidates for developing robust surface enhanced Raman scattering (SERS) based biosensors for an on-site sensing of pollutants. However, up to now only aptamers to polychlorinated biphenyls [61] [60] and organophosphorus compounds [62] have been produced and reported. Further efforts have to be made in the synthesis of aptamers to aromatic hydrocarbons.

The last class of biomolecules proposed as a good prospect for biosensor design is antibodies. Similarly to the aptamers, antibodies possess highly specific and affinitive interaction format, enabling targeted environmental contaminant recognition that can further be monitored by electronic or optical transducers [63]. Antibodies against small organic pollutants, such as pesticides, persistent organic pollutants, and endocrine disrupting chemicals, are prepared by immunizing the complex of target molecule bind to a carrier protein into animals [54]. In this way the prepared and now commercially available antibodies against PAH were already investigated to design biosensors [64] [65;66]. Boujday *et al.*, have proposed immunosensor with immobilized antibodies through their affinity to protein G which was covalently attached to an aldehyde layer [65]. Benzo[a]pyrene (BaP) was then monitored by polarization modulation reflection absorption infrared spectroscopy (PM-IRRAS) by following the intensity of the band presented at 3039 cm^{-1} corresponding to an aromatic C-H stretching mode. Designed biosensor led to the detection of BaP at $5\text{ }\mu\text{M}$ concentration.

In addition to biochemical sensors, efforts have been devoted to the design of chemical sensors capable of pre-concentrations and detection of aromatic hydrocarbons.

1.6.2 Chemical sensors for monitoring of aromatic compound

Any material that interacts with the aromatic hydrocarbons via its adsorption or absorption processes can be considered as potential receptor for a chemical sensor [67]. Table and Table summarize the

most common materials in order to build the receptors of mass/piezoelectric and optical transducers, respectively. Among them, polymeric materials are the most popular.

The capability of various polymers in aromatic pollutants sensing was evaluated mainly in the gas phase. However, some studies have been made towards the pollutants detection in water samples [68] [69;70] by quartz crystal microbalance (QCM) and surface acoustic wave (SAW). It appears that polymers display promising capability in molecular pre-concentration. However, it is obvious that many of them are lacking of desired selectivity. Due to this reason, particular interest has been devoted to molecularly imprinted polymers (MIP) as a method enabling the creation of host-guest materials. Dickert *et al.* have demonstrated the application of various polymers for the design of MIP-based QCM sensors for benzene, toluene and xylene (BTX) as well as few PAHs discrimination in mixed samples [71].

However, polymer-based mass sensors were found to have some drawbacks related to an inadequate change in frequency due to the different processes induced in polymer coating. Thus, the response mechanisms of later sensors were identified as complex and demanding of good understanding before application to environmental samples. In addition, the inconvenience of mass based sensors was found also due to poor discrimination of compounds in mixed media.

Table 2 Aromatic hydrocarbon detection using mass/piezoelectric sensors.

Receptor	Transducer	Analyte	LOD	Selectivity	Ref.
Various polymers	QCM	BTX and PAH	NA	Good	[71]
Anthracene-Polymer	QCM	PAH	2ppb	Poor	[72]
Silicone	QCM	gasoline, fuel oil, diesel oil	NA	Poor	[68]
	QCM	Gasoline, aromatic aliphatic hydrocarbons	20-900ppb	Poor	[73]
Polymer (various)	SAW	Aromatic hydrocarbons	~ppb	Poor	[69] [70]
Polymer calixarene -	QCM	various aromatic compounds	~ppm	Good	[74] [75]
Calixarene-	QCM	various aromatic compounds	~mM	Good	[76] [77]

In other words, mass response using later transducers could be generated from anything that has mass. Thus, the non-specific interaction between the pollutants and sensor surface has to be minimized.

Problems related to the molecular identification issues were solved by introducing optical transducers. These sensors exploit the electromagnetic waves in order to gain important information concerning the molecular structure and thus their identification. As it seen in Table the applications of various polymeric matrixes dominate in order to build receptor system for aromatic hydrocarbons

pre-concentration. In order to address the issue of water facilitating polymer degradation resulting in modifying response characteristics, it was proposed to use a Teflon membrane over the receptor coating [78]. This latter improvement led to the detection of VOCs down to 250 ng/mL concentration.

Table 3 Aromatic hydrocarbon detection using optical sensors.

Receptor	Transducer	Analyte	LOD	Selectivity	Ref.
Resin support	luminescence spectrometer	Benzo[a]pyrene	3ng/L	Good	[79]
Polymer (various) coated ATR crystal	ATR-FTIR spectroscopy	Aromatic compounds, chloroform	9mg/L	Good	[80]
Polymer (ethylene/propylene) coated ATR fiber optic	MIR spectroscopy	Halogenated aromatic hydrocarbons	20-100ppb	Good	[81] [82] [83]
Ethylene/propylene copolymer -coated ATR crystal	MIR spectroscopy	BTX	~ppm	Good	[83]
Polymer (polyacrylonitrile-cobutadiene) coated ATR fiber optic	MIR spectrometry	Toluene	~1ppm	Good	[84]
poly(dimethylsiloxane) rod optical fiber	NIR spectrometry	Halogenated, aliphatic aromatic hydrocarbons	~3-8mg/L 0.1-2mg/L	Good	[85] [86]
Polyisobutylene-coated ATR crystal	IR spectroscopy	VOCs	~250 ng/mL	Good	[78]
Teflon membrane					
Polymer (polyvinylmercaptopylsiloxane)	reflectometric interference spectrometry	VOCs	3.3 mg/L (toluene)	Good	[87]
Fluoro polymer membrane	fiber optic IR reflectometer	Gasoline, diesel insulating oil	NA	NA	[88]
poly(dimethylsiloxane)-coated fiber optic	optical time domain reflectometry	Halogenated, aliphatic aromatic hydrocarbons	9-123 mg/L	Good	[89]

As a transducer in optical sensor, infrared spectroscopy (IR) is the most common method applied for aromatic compounds detection, although it has been reported that fluorescence-based sensors are more sensitive [79]. In order to improve the sensitivity of the IR spectroscopy based sensors different strategies were investigated. For instance, attenuated total reflectance (ATR) is one of the approaches that helped to improve a molecular detection. ATR is a surface sensitive technique which is able to discriminate any molecule adsorbed or absorbed onto polymeric layer coated over the ATR crystal [80]. Further improvement in sensitivity was ensured by employing optical fibers, which results in signal amplification of several orders of magnitude over ATR systems due to internal reflections [81] [82] [83].

Other types of transducers are based on reflectometric spectrometry responding to a refractive index change of a coated polymer due to interactions with the analytes [87] [88] [89]. Combined with the optical fiber this later technique was identified as highly suitable for on-site measurements.

To conclude, the receptor and transducer units have to be optimized in order to satisfy the (bio) chemical sensor requirements: sensitivity, selectivity and robustness. Receptors including biomolecules and MIPs are showing great selectivity towards single analyte. Combined with mass based transducers, targeted analytes can be monitored in trace (less than 100 ppm) concentrations. Despite of their great sensitivity, their response are too complex and in some cases it can be hard to interpret. These uncertainties can arise from non specific adsorption or even from some modifications in the physical properties of the sensing film. On the other hand, optical transducers provide more information on the processes occurring in the receptor. Due to possibility of molecular identification these sensors overcome issues related with selectivity. In this case the receptors can be then chosen regarding their degree of binding with different analytes. The improvements performed on optical sensor makes them a suitable tool for a real time monitoring on-site.

1.7 References

- 1 Oki, T. and Kanae, S. (2006). Global hydrological cycles and world water resources, *Science*, 313, pp. 1068-1072.
- 2 Gleick, P. H. (1996). Water resources, *Encyclopedia of climate and weather*, 2, pp. 817-823.
- 3 Oki, T. and Kanae, S. (2006). Global hydrological cycles and world water resources, *Science* (New York, N.Y.), 313, pp. 1068-1072.
- 4 Roose, P., Albaigés, J., Bebianno, M. J., Camphuysen, C., Cronin, M., de Leeuw, J., Gabrielsen, G., Hutchinson, T., Hylland, K., Jansson, B., Jenssen, B. M., Schulz-Bull, D., Szefer, P., Webster, L., Bakke, T. and Janssen, C. (2011). Monitoring Chemical Pollution in Europe's Seas: Programmes, Practices and Priorities for Research, *Marine Board-ESF*, pp.
- 5 Wilson, M. P. and Schwarzman, M. R. (2009). Toward a New U.S. Chemicals Policy: Rebuilding the Foundation to Advance New Science, Green Chemistry, and Environmental Health, *Environmental health perspectives*, 117, pp. 1202-1209.
- 6 Harrison, R. M. (2001). *Pollution: Causes, Effects and Control*: Royal Society of Chemistry.
- 7 Jenkins, S. J. (2009). Aromatic adsorption on metals via first-principles density functional theory, *Proceedings of the Royal Society of London A: Mathematical, Physical and Engineering Sciences*, 465, pp. 2949-2976.
- 8 Directive 2008/105/EC of the European Parliament and of the Council of 16 December 2008 on environmental quality standards in the field of water policy, amending and subsequently repealing Council Directives 82/176/EEC, 83/513/EEC, 84/156/EEC, 84/491/EEC, 86/280/EEC and amending Directive 2000/60/EC of the European Parliament and of the Council pp.
- 9 Moore, J. W. and Ramamoorthy, S. (1984). *Organic Chemicals in Natural Waters. Applied Monitoring and Impact Assessment*: Springer New York.
- 10 Manoli, E. and Samara, C. (1999). Polycyclic aromatic hydrocarbons in natural waters: sources, occurrence and analysis, *TrAC Trends in Analytical Chemistry*, 18, pp. 417-428.

- 11 Office of the Federal Registration (OFR) Appendix A: priority pollutants. Fed Reg. 1982;47:52309. pp.
- 12 Lipiatou, E., Tolosa, I., Simó, R., Bouloubassi, I., Dachs, J., Marti, S., Sicre, M. A., Bayona, J. M., Grimalt, J. O., Saliott, A. and Albaiges, J. (1997). Mass budget and dynamics of polycyclic aromatic hydrocarbons in the Mediterranean Sea, Deep Sea Research Part II: Topical Studies in Oceanography, 44, pp. 881-905.
- 13 Tedesco, S. A. (2012). Surface Geochemistry in Petroleum Exploration: Springer US.
- 14 Crone, T. J. and Tolstoy, M. (2010). Magnitude of the 2010 Gulf of Mexico oil leak, Science, 330, pp. 634.
- 15 Mascarelli, A. (2010). After the oil., Nature, 467, pp. 22-24.
- 16 Redondo, J. M. and Platonov, A. K. (2009). Self-similar distribution of oil spills in European coastal waters, Environmental Research Letters, 4, pp. 014008.
- 17 Utvik, T. I. R. (1999). Chemical characterisation of produced water from four offshore oil production platforms in the North Sea, Chemosphere, 39, pp. 2593-2606.
- 18 Durell, G., Utvik, T. R., Johnsen, S., Frost, T. and Neff, J. (2006). Oil well produced water discharges to the North Sea. Part I: Comparison of deployed mussels (*Mytilus edulis*), semi-permeable membrane devices, and the DREAM model predictions to estimate the dispersion of polycyclic aromatic hydrocarbons, Marine Environmental Research, 62, pp. 194-223.
- 19 Neff, J. M., Johnsen, S., Frost, T. K., Utvik, T. I. R. and Durell, G. S. (2006). Oil well produced water discharges to the North Sea. Part II: Comparison of deployed mussels (*Mytilus edulis*) and the DREAM model to predict ecological risk, Marine Environmental Research, 62, pp. 224-246.
- 20 Pampanin, D. M. and Sydnes, M. O. (2013). Polycyclic Aromatic Hydrocarbons a Constituent of Petroleum: Presence and Influence in the Aquatic Environment.
- 21 Xue, W. and Warshawsky, D. (2005). Metabolic activation of polycyclic and heterocyclic aromatic hydrocarbons and DNA damage: a review, Toxicology and applied pharmacology, 206, pp. 73-93.
- 22 French, B. L., Reichert, W. L., Hom, T., Nishimoto, M., Sanborn, H. R. and Stein, J. E. (1996). Accumulation and dose-response of hepatic DNA adducts in English sole (*Pleuronectes vetulus*) exposed to a gradient of contaminated sediments, Aquatic Toxicology, 36, pp. 1-16.
- 23 Hsu, G. W., Huang, X., Luneva, N. P., Geacintov, N. E. and Beese, L. S. (2005). Structure of a high fidelity DNA polymerase bound to a benzo [a] pyrene adduct that blocks replication, Journal of Biological Chemistry, 280, pp. 3764-3770.
- 24 Christian, T. D. and Romano, L. J. (2009). Monitoring the conformation of benzo [a] pyrene adducts in the polymerase active site using fluorescence resonance energy transfer, Biochemistry, 48, pp. 5382-5388.
- 25 Noaksson, E., Tjämlund, U., Ericson, G. and Balk, L. (1998). Biological effects on viviparous blenny exposed to chrysene and held in synthetic as well as in natural brackish water, Marine Environmental Research, 46, pp. 81-85.
- 26 Skipper, P. L. and Tannenbaum, S. R. (1990). Protein adducts in the molecular dosimetry of chemical carcinogens, Carcinogenesis, 11, pp. 507-518.
- 27 Amat, A., Burgeot, T., Castegnaro, M. and Pfohl-Leszkowicz, A. (2006). DNA adducts in fish following an oil spill exposure, Environmental Chemistry Letters, 4, pp. 93-99.
- 28 Brunmark, P., Harriman, S., Skipper, P. L., Wishnok, J. S., Amin, S. and Tannenbaum, S. R. (1997). Identification of subdomain IB in human serum albumin as a major binding site for polycyclic aromatic hydrocarbon epoxides, Chemical research in toxicology, 10, pp. 880-886.
- 29 Day, B. W., Skipper, P. L., Zaia, J., Singh, K. and Tannenbaum, S. R. (1994). Enantiospecificity of covalent adduct formation by benzo [a] pyrene anti-diol epoxide with human serum albumin, Chemical research in toxicology, 7, pp. 829-835.
- 30 Meyer, M. J. and Bechtold, W. E. (1996). Protein adduct biomarkers: state of the art, Environmental health perspectives, 104, pp. 879.

- 31 Kafferlein, H. U., Marczynski, B., Mensing, T. and Bruning, T. (2010). Albumin and hemoglobin adducts of benzo [a] pyrene in humans—analytical methods, exposure assessment, and recommendations for future directions, *Critical reviews in toxicology*, 40, pp. 126-150.
- 32 US Environmental Protection Agency (2005) Method 610-polynuclear aromatic hydrocarbons, PART 136 guidelines establishing test procedures for the analysis of pollutants; appendix A: methods for organic chemical analysis of municipal and industrial wastewater, 40CFR136.1, US Environmental Protection Agency, Washington D.C.
<http://www.epa.gov/waterscience/methods/guide/610.pdf>
- 33 US Environmental Protection Agency (1980) Test methods for evaluating solid waste, physical/chemical methods, SW-846, US Environmental Protection Agency, Washington D.C.
<http://www3.epa.gov/epawaste/hazard/testmethods/sw846/pdfs/8270d.pdf>
- 34 ISO 17993:2002, Water quality -- Determination of 15 polycyclic aromatic hydrocarbons (PAH) in water by HPLC with fluorescence detection after liquid-liquid extraction.
- 35 ISO Procedure 1799. Water quality-determination of 15 PAHs in water by HPLC with fluorescence detection. (2002).
- 36 Wolska, L. (2008). Determination (monitoring) of PAHs in surface waters: why an operationally defined procedure is needed, *Analytical and Bioanalytical Chemistry*., 391, pp. 2647-2652.
- 37 Ballesteros-Gomez, A. and Rubio, S. (2011). Recent Advances in Environmental Analysis, *Analytical Chemistry*, 83, pp. 4579-4613.
- 38 Reupert, R. and Brausen, G. (1994). Bestimmung von polycyclischen aromatischen Kohlenwasserstoffen in Wasser, Sediment, Schlamm und Boden mittels Hochleistungs-Flussigkeitschromatographie Determination of Polycyclic Aromatic Hydrocarbons in Water, Sludges, Sediments, and Soils by High Performance Liquid Chromatography, *Acta hydrochimica et hydrobiologica*, 22, pp. 202-215.
- 39 Demeestere, K., Dewulf, J., De Witte, B. and Van Langenhove, H. (2007). Review: Sample preparation for the analysis of volatile organic compounds in air and water matrices, *Journal of Chromatography A*, 1153, pp. 130–144.
- 40 Brouwer, E. R., Hermans, A. N. J., Lingeman, H. and Brinkman, U. A. T. (1994). Determination of polycyclic aromatic hydrocarbons in surface water by column liquid chromatography with fluorescence detection, using on-line micelle-mediated sample preparation, *Journal of Chromatography A*, 669, pp. 45-57.
- 41 Grosjean, E. and Logan, G. A. (2007). Incorporation of organic contaminants into geochemical samples and an assessment of potential sources: Examples from Geoscience Australia marine survey S282, *Organic Geochemistry*, 38, pp. 853-869.
- 42 Roy, G., Vuillemin, R. and Guyomarch, J. (2005). On-site determination of polynuclear aromatic hydrocarbons in seawater by stir bar sorptive extraction (SBSE) and thermal desorption GC–MS, *Talanta*, 66, pp. 540-546.
- 43 Vas, G. and Vekey, K. (2004). Solid-phase microextraction: a powerful sample preparation tool prior to mass spectrometric analysis, *Journal of Mass Spectrometry*, 39, pp. 233-254.
- 44 Zwank, L., Berg, M., Schmidt, T. C. and Haderlein, S. B. (2003). Compound-specific carbon isotope analysis of volatile organic compounds in the low-microgram per liter range, *Analytical Chemistry*, 75, pp. 5575-5583.
- 45 Panavaite, D., Padarauskas, A. and Vickackaite, V. (2006). Silicone glue coated stainless steel wire for solid phase microextraction, *Analytica Chimica Acta*, 571, pp. 45-50.
- 46 David, F. and Sandra, P. (2007). Stir bar sorptive extraction for trace analysis, *Journal of Chromatography A*, 1152, pp. 54-69.
- 47 Konn, C., Charlou, J. L., Donval, J. P. and Holm, N. G. (2012). Characterisation of dissolved organic compounds in hydrothermal fluids by stir bar sorptive extraction - gas chromatography - mass spectrometry. Case study: the Rainbow field (36 degrees N, Mid-Atlantic Ridge), *Geochemical Transactions*, 13, pp. 8.

- 48 Arthur, C. L., Killiam, L. M., Motlagh, S., Lim, M., Potter, D. W. and Pawliszyn, J. (1992). Analysis of substituted benzene compounds in groundwater using solid-phase microextraction, *Environmental Sciences & Technology*, 26, pp. 979-983.
- 49 Buchholz, K. D. and Pawliszyn, J. (1993). Determination of phenols by solid-phase microextraction and gas chromatographic analysis. , *Environmental Sciences & Technology*, 27, pp. 2844-2848.
- 50 Arthur, C. L. and Pawliszyn, J. (1990). Solid phase microextraction with thermal desorption using fused silica optical fibers, *Analytical chemistry*, 62, pp. 2145–2148.
- 51 Zhang, Z. and Pawliszyn, J. (1995). Quantitative Extraction Using an Internally Cooled Solid Phase Microextraction Device, *Analytica Chemistry*, 67 pp. 34-43.
- 52 Konieczka, P., Wolska, L. and Namieśnik, J. (2010). Quality problems in determination of organic compounds in environmental samples, such as PAHs and PCBs, *TrAC Trends in Analytical Chemistry*, 29, pp. 706-717.
- 53 Hulanicki, A., Glab, S. and Ingman, F. (1991). Chemical sensors: definitions and classification, *Pure and Applied Chemistry*, 63, pp. 1247-1250.
- 54 Long, F., Zhu, A. and Shi, H. (2013). Recent advances in optical biosensors for environmental monitoring and early warning, *Sensors (Basel, Switzerland)*, 13, pp. 13928-13948.
- 55 Eltzov, E., Pavluchkov, V., Burstin, M. and Marks, R. S. (2011). Creation of a fiber optic based biosensor for air toxicity monitoring, *Sensors and Actuators B: Chemical*, 155, pp. 859-867.
- 56 Eltzov, E., Marks, R. S., Voost, S., Wullings, B. A. and Heringa, M. B. (2009). Flow-through real time bacterial biosensor for toxic compounds in water, *Sensors and Actuators B: Chemical*, 142, pp. 11-18.
- 57 Zhong, Z., Fritzsche, M., Pieper, S. B., Wood, T. K., Lear, K. L., Dandy, D. S. and Reardon, K. F. (2011). Fiber optic monooxygenase biosensor for toluene concentration measurement in aqueous samples, *Biosensors and Bioelectronics*, 26, pp. 2407-2412.
- 58 Long, F., Zhu, A., Gu, C. and Shi, H. (2013). Recent Progress in Optical Biosensors for Environmental Applications.
- 59 Arugula, M. A. and Simonian, A. (2014). Novel trends in affinity biosensors: current challenges and perspectives, *Measurement Science and Technology*, 25, pp. 032001.
- 60 Mehta, J., Rouah-Martin, E., Van Dorst, B., Maes, B., Herrebout, W., Scippo, M.-L., Dardenne, F., Blust, R. and Robbens, J. (2012). Selection and Characterization of PCB-Binding DNA Aptamers, *Analytical Chemistry*, 84, pp. 1669-1676.
- 61 Xu, S., Yuan, H., Chen, S., Xu, A., Wang, J. and Wu, L. (2012). Selection of DNA aptamers against polychlorinated biphenyls as potential biorecognition elements for environmental analysis, *Analytical Biochemistry*, 423, pp. 195-201.
- 62 Wang, L., Liu, X., Zhang, Q., Zhang, C., Liu, Y., Tu, K. and Tu, J. (2012). Selection of DNA aptamers that bind to four organophosphorus pesticides, *Biotechnol Lett*, 34, pp. 869-874.
- 63 Rogers, K. R. (2006). Recent advances in biosensor techniques for environmental monitoring, *Analytica Chimica Acta*, 568, pp. 222-231.
- 64 Wei, M. Y., Wen, S. D., Yang, X. Q. and Guo, L. H. (2009). Development of redox-labeled electrochemical immunoassay for polycyclic aromatic hydrocarbons with controlled surface modification and catalytic voltammetric detection, *Biosensors & bioelectronics*, 24, pp. 2909-2914.
- 65 Boujday, S., Gu, C., Girardot, M., Salmain, M. and Pradier, C. M. (2009). Surface IR applied to rapid and direct immunosensing of environmental pollutants, *Talanta*, 78, pp. 165-170.
- 66 Boujday, S., Nasri, S., Salmain, M. and Pradier, C. M. (2010). Surface IR immunosensors for label-free detection of benzo[a]pyrene, *Biosensors & bioelectronics*, 26, pp. 1750-1754.
- 67 Pejcic, B., Eadington, P. and Ross, A. (2007). Environmental Monitoring of Hydrocarbons: A Chemical Sensor Perspective, *Environmental Science & Technology*, 41, pp. 6333-6342.
- 68 Ueyama, S., Hijikata, K. and Hirotsuji, J. (2002). Water monitoring system for oil contamination using polymer-coated quartz crystal microbalance chemical sensor, *Water science and technology : a journal of the International Association on Water Pollution Research*, 45, pp. 175-180.

- 69 Jones, Y. K., Zhonghui, L., Johnson, M. M., Josse, F. and Hossenlopp, J. M. (2005). ATR-FTIR spectroscopic analysis of sorption of aqueous analytes into polymer coatings used with guided SH-SAW sensors, *Sensors Journal, IEEE*, 5, pp. 1175-1184.
- 70 Li, Z., Jones, Y., Hossenlopp, J., Cernosek, R. and Josse, F. (2005). Analysis of Liquid-Phase Chemical Detection Using Guided Shear Horizontal-Surface Acoustic Wave Sensors, *Analytical Chemistry*, 77, pp. 4595-4603.
- 71 Dickert, F. L., Lieberzeit, P., Gazda-Miarecka, S., Halikias, K. and Mann, K.-J. (2004). Modifying polymers by self-organisation for the mass-sensitive detection of environmental and biogenic analytes, *Sensors and Actuators B: Chemical*, 100, pp. 112-116.
- 72 Stanley, S., Percival, C. J., Auer, M., Braithwaite, A., Newton, M. I., McHale, G. and Hayes, W. (2003). Detection of polycyclic aromatic hydrocarbons using quartz crystal microbalances, *Analytical Chemistry*, 75, pp. 1573-1577.
- 73 Applebee, M. S., Geissler, J. D., Schellinger, A. P., Jaeger, R. J. and Pierce, D. T. (2004). Field screening of waterborne petroleum hydrocarbons by thickness shear-mode resonator measurements, *Environmental Science & Technology*, 38, pp. 234-239.
- 74 Lucklum, R., Rösler, S., Hartmann, J. and Hauptmann, P. (1996). On-line detection of organic pollutants in water by thickness shear mode resonators, *Sensors and Actuators B*, 35-36, pp. 103-111.
- 75 Hartmann, J., Auge, J., Lucklum, R., Rosler, S., Hauptmann, P., Adler, B. and Dalcanale, E. (1995, 25-29 June 1995). Supramolecular Interactions On Mass Sensitive Sensors In Gas Phases And Liquids. Paper presented at the Solid-State Sensors and Actuators, 1995 and Eurosensors IX.. Transducers '95. The 8th International Conference.
- 76 Rösler, S., Lucklum, R., Borngräber, R., Hartmann, J. and Hauptmann, P. (1998). Sensor system for the detection of organic pollutants in water by thickness shear mode resonators, *Sensors and Actuators B*, 48, pp. 415-424.
- 77 Cygan, M. T., Collins, G. E., Dunbar, T. D., Allara, D. L., Gibbs, C. G. and Gutsche, C. D. (1999). Calixarene monolayers as quartz crystal microbalance sensing elements in aqueous solution, *Analytica Chimica Acta*, 71, pp. 142-148.
- 78 Yang, J. and Ramesh, A. (2005). Membrane-introduced infrared spectroscopic chemical sensing method for the detection of volatile organic compounds in aqueous solutions, *Analyst*, 130, pp. 397-403.
- 79 Fernandez-Sanchez, J. F., Carretero, A. S., Cruces-Blanco, C. and Fernandez-Gutierrez, A. (2004). Highly sensitive and selective fluorescence optosensor to detect and quantify benzo a pyrene in water samples, *Analytica Chimica Acta*, 506, pp. 1-7.
- 80 Flavin, K., Hughes, H., Dobbyn, V., Kirwan, P., Murphy, K., Steiner, H., Mizaikoff, B. and Mcloughlin, P. (2006). A comparison of polymeric materials as pre-concentrating media for use with ATR/FTIR sensing, *International Journal of Environmental Analytical Chemistry*, 86, pp. 401-415.
- 81 Mizaikoff, B. (1999). Mid-infrared evanescent wave sensors-a novel approach for subsea monitoring, *Measurement Science and Technology*, 10, pp. 1185.
- 82 Kraft, M., Jakusch, M., Karlowatz, M., Katzir, A. and Mizaikoff, B. (2003). New frontiers for mid-infrared sensors: Towards deep sea monitoring with a submarine FT-IR sensor system, *Applied Spectroscopy*, 57, pp. 591-599.
- 83 Karlowatz, M., Kraft, M. and Mizaikoff, B. (2004). Simultaneous quantitative determination of benzene, toluene, and xylenes in water using mid-infrared evanescent field spectroscopy, *Analytical Chemistry*, 76, pp. 2643-2648.
- 84 Hahn, P., Tacke, M., Jakusch, M., Mizaikoff, B., Spector, O. and Katzir, A. (2001). Detection of hydrocarbons in water by MIR evanescent-wave spectroscopy with flattened silver halide fibers, *Applied Spectroscopy*, 55, pp. 39-43.
- 85 Albuquerque, J. S., Pimentel, M. F., Silva, V. L., Raimundo, I. M., Rohwedder, J. J. and Pasquini, C. (2005). Silicone sensing phase for detection of aromatic hydrocarbons in water employing near-infrared spectroscopy, *Analytical Chemistry*, 77, pp. 72-77.

- 86 Bürck, J., Mensch, M. and Krämer, K. (1998). Field experiments with a portable fiber-Optic sensor system for monitoring hydrocarbons in water, *Field Analytical Chemistry & Technology*, 2, pp. 205-219.
- 87 Yan, H., Kraus, G. and Gauglitz, G. (1995). Detection of mixtures of organic pollutants in water by polymer film receptors in fibre-optical sensors based on reflectometric interference spectrometry, *Analytica Chimica Acta*, 312, pp. 1-8.
- 88 Ritchie, L. J., Ferguson, C. P., Bessant, C. and Saini, S. (2000). A ten channel fibre-optic device for distributed sensing of underground hydrocarbon leakage, *Journal of Environmental Monitoring*, 2, pp. 670-673.
- 89 Buerck, J., Roth, S., Kraemer, K. and Mathieu, H. (2003). OTDR fiber-optical chemical sensor system for detection and location of hydrocarbon leakage, *Journal of Hazardous Materials*, 102, pp. 13-28.

2 Surface Enhanced Raman Spectroscopy and its application to sensing platforms

2.1 Introduction

In the previous section some (bio)chemical sensors based on piezoelectric or optical transducers were described and compared. This chapter will be devoted essentially to Surface Enhanced Raman Scattering (SERS) based molecular sensing. Recently, SERS has been extensively exploited and applied as a signal transduction mechanism for numerous sensing applications [1;2]. Lead by a great sensing improvement, SERS is currently identified as a simple, rapid, low-cost, reliable, and robust method for simultaneous detection of single or multiple compounds [3-5].

As indicated in its acronym, the SERS effect is based on three main components [6]:

- Raman. Raman spectroscopy is a powerful tool allowing molecular identification.
- Enhanced. The signal enhancement in SERS is due to the exploitation of the optical properties of metal nanoparticles (NPs) under specific conditions. Thus, it is necessary to optimize the SERS substrates and more especially the geometrical parameters of the NPs for gaining the maximum signal enhancement.
- Surface. SERS is a surface spectroscopy technique. Thus, in order to perform sensitive molecular detection the analytes has to be in close contact with the NPs surface. If targeted analyte does not possess particular affinity to a surface, receptors have to be used for molecular pre-concentration.

Brief overview of all these components will be provided in this chapter. First of all, the principle of Raman spectroscopy will be introduced. A second part will be devoted to explain the light interaction with metallic NPs as it is an essential component in the SERS signal. The chapter will conclude by a review of SERS substrates and of the proposed strategies of surface functionalisations.

2.2 Principle

2.2.1 Raman Spectroscopy

In 1921 C. V. Raman observed a light scattering with shifted wavelengths and named this effect a new type of secondary radiation [7]. In 1930 he was awarded Nobel Prize in physics for this discovery. Since then this effect was referred to Raman scattering or Raman effect, and the measurement and the analysis of the signal arising from Raman effect is called Raman spectroscopy.

In fact, the Raman spectroscopy is a vibrational spectroscopy which provides a fingerprint of a biological or chemical compound. More precisely, it probes the different vibrations occurring in the excited molecule. These vibrations are highly related with the molecular structure and the frequencies of vibration depend on the mass of the atoms, on the nature and the strength of the chemical bonds

and on the global structural conformation of the molecule. Thus, Raman spectroscopy can be used for the molecule identification and as well as for characterization purposes.

The Raman spectroscopy is based on inelastic scattering processes induced by indirect transition between two vibrational levels.

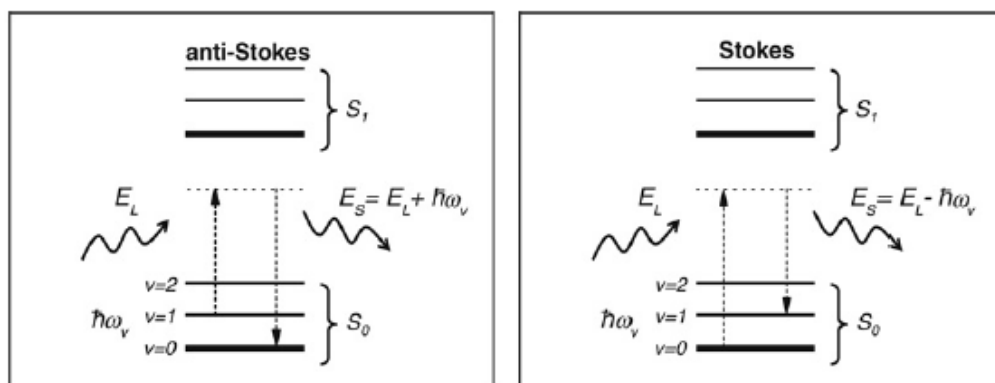


Figure 2.1 Simplified Jablonski diagrams illustration of inelastic scattering (left: anti-Stokes; right: Stokes) processes [6].

In the Figure 2.1 the scattering process is represented as a two steps process starting by the absorption of an incident photon and followed by the spontaneous emission of a scattered photon. After the photon absorption, the molecule is excited to a higher-energy level represented as an intermediate virtual state. If the energy of the intermediate virtual state matches with one of the electronic levels, then a resonant scattering process is induced. The scattered photon may have either higher or lower energy in comparison to the incident photon. In case of Stokes process the scattered photon has less energy than the incident one ($E_S < E_L$) (Figure 2.1) and it corresponds to the excitation of the molecule from its ground state $v = 0$ to the first excited state $v = 1$ of a vibrational mode with energy $\hbar\omega_v = E_L - E_S$. In case of anti-Stokes process, the scattered photon is more energetic than the incident one ($E_S > E_L$) and it corresponds to a transition from an excited vibrational state $v = 1$ to its ground state $v = 0$. The energy of the vibration is then equal to $\hbar\omega_v = E_S - E_L$. The dipolar moment of the scattering processes is written as:

$$\mathbf{P} = \alpha \cdot \mathbf{E} \quad (1)$$

where \mathbf{E} is the excitation electric field, and α is the polarizability of the vibrational mode.

An important benefit of Raman spectroscopy is that no sample preparation is needed. Unfortunately, due to low scattering efficiency the sensitivity of Raman spectroscopy is rather poor. The discovery of tremendous Raman signal enhancement when molecule is adsorbed on rough metal surface has allowed the investigation of very low concentrations of analytes.

2.2.2 Surface Plasmon

The enhancement of Raman scattering can be achieved due to a local enhancement of the electric field resulting from the interaction between an electromagnetic wave and a nanostructured metal surface. In this section, the light and matter interaction will be detailed in order to show how the electric field is enhanced. One of the characteristics of metals is the presence of a free electron gas, which can oscillate under the application of an electromagnetic wave. These oscillations occur at a given frequency and are named plasma oscillations. To highlight how an electromagnetic wave produces this plasma oscillation, it is important to understand how this wave interacts with matter and particularly with the electrons inside.

2.2.2.1 Light - matter interaction and dielectric constant

The interaction between an electromagnetic wave and the atoms at the microscopic level is explained by the Drude-Lorentz model which describes the material response to an incident electromagnetic field. In Drude-Lorentz model the electron-nuclear system is assumed as a harmonic oscillator where electron will oscillate at a specific frequency when it meets the electromagnetic wave. To resolve the problem, we should first identify the forces acting on the electron. These ones are:

- An elastic force F_e . As for a spring, this force opposes to the motion of the electron induced by Coulomb force by moving it back to its equilibrium position. F_e is written as:

$$F_e = -\alpha x \quad (2)$$

where α is the spring constant and x is the electron displacement from its equilibrium position.

- A damping force F_d which models the interaction of the electron with the neighbor nucleus:

$$F_d = -\gamma \dot{x} \quad (3)$$

Where γ is the viscosity constant and \dot{x} is the electron velocity.

Since the electrons are excited by an electromagnetic wave a third force, known as Coulomb force is involved in the electron motion:

$$F_c = -|e|E_0 e^{-i\omega t} = -|e|E \quad (4)$$

where E_0 is the amplitude vector of the electric field E , $-|e|$ is the charge of the electron and ω is the frequency of the electromagnetic wave.

The motion of an electron with a mass m and a charge $-|e|$ and located at a mean distance x_0 from the nucleus can be then deduced from the second Newton's law, which gives the acceleration \ddot{x} of this electron as:

$$ma = F_e + F_d + F_c \quad (5)$$

$$m\ddot{x} = -\alpha x - \gamma\dot{x} - |e|E_0 e^{-i\omega t} \quad (6)$$

The resolution of this equation gives time dependent $x(t)$ electron oscillation around its mean position $x_0(\omega)$ influenced by the angular frequency ω of the excitation:

$$x(t) = x_0(\omega)e^{-i\omega t} \quad (7)$$

where

$$x_0(\omega) = |e|E_0 \frac{|e|E_0}{m(\omega^2 + i\omega\gamma_m - \omega_0^2)} \quad (8)$$

with

$\omega_0^2 = \frac{\alpha}{m}$, the resonant frequency of the damped system;

$\gamma_m = \frac{\gamma}{m}$, the reduced constant linked to a viscous friction with the other charges in the material.

This shows that under the effect of an electric field, the electrons move relatively to their equilibrium position as a function of time. This displacement creates a space free of charge that can be linked to a positive charge. The electrons oscillation induces a dipole in the direction of the electric field \mathbf{E} described as a dipolar moment \mathbf{p} such as:

$$\mathbf{p} = -|e|x\mathbf{u} = \frac{-|e|^2}{m(\omega^2 + i\omega\gamma_m - \omega_0^2)} \mathbf{E} \quad (9)$$

with \mathbf{u} , a unitary vector in the motion direction.

The polarizability α of the considered dipole can then be defined from equations (1) and (8), and can be expressed as:

$$\alpha = \frac{-|e|^2}{m\varepsilon_0(\omega^2 + i\omega\gamma_m - \omega_0^2)} \quad (10)$$

where ε_0 is corresponding to dielectric constant of vacuum.

Entering from atomic scale to a macroscale the total number of electrons, N , has to be considered. The total polarization \mathbf{P} , of a solid material composed then can be described as a sum of all dipole moments:

$$\mathbf{P} = N\mathbf{p} = N\alpha\varepsilon_0\mathbf{E} \quad (11)$$

Assuming that the polarization is proportional to the incident field, \mathbf{P} can also be expressed as follows:

$$\mathbf{P} = \chi \varepsilon_0 \mathbf{E} \quad (12)$$

with χ , the electric susceptibility of the material.

The entire response of the material is in fact represented by the electrical excitation \mathbf{D} which is the sum of the polarization and of the incident electric field as:

$$\mathbf{D} = \varepsilon_0 \mathbf{E} + \mathbf{P} = \varepsilon_0 (1 + \chi) \mathbf{E} = \varepsilon_0 \varepsilon_M \mathbf{E} \quad (13)$$

with ε_M , the dielectric constant of the material. Its frequency dependence is expressed by:

$$\varepsilon_M = 1 + \frac{N|e|^2}{m\varepsilon_0(\omega_0^2 - \omega^2 - i\omega\gamma_m)} \quad (14)$$

Equation (13) allows the determination of the plasma frequency ω_p , which corresponds to the oscillation frequency of the electrons such as:

$$\varepsilon_M = 1 + \frac{\omega_p^2}{(\omega_0^2 - \omega^2 - i\omega\gamma_m)} \quad (15)$$

with $\omega_p = \sqrt{\frac{Ne^2}{m\varepsilon_0}}$

It is worth to remark, that ε_M is complex and its real and imaginary parts ($\varepsilon_M = \Re(\varepsilon_M) + i\Im(\varepsilon_M)$) can be written as follows:

$$\Re(\varepsilon_M) = 1 - \omega_p^2 \frac{\omega^2 - \omega_0^2}{(\omega^2 - \omega_0^2)^2 + (\omega\gamma_m)^2} \quad (16)$$

$$\Im(\varepsilon_M) = \omega_p^2 \frac{\omega\gamma_m}{(\omega^2 - \omega_0^2)^2 + (\omega\gamma_m)^2} \quad (17)$$

The real part describes the conductive nature of the considered material while the imaginary part describes the material ability to absorb light.

2.2.2.2 Delocalised surface plasmon

In the case of a flat metal surface, the interaction of the light with the metal at the metal/dielectric interface will create the surface plasmons (Figure 2.2).

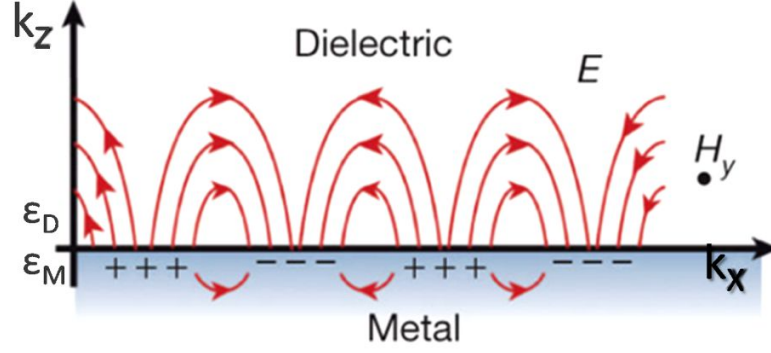


Figure 2.2 Schematic illustration of the electric field related with the surface plasmons at a metal–dielectric interface (the permittivity of metallic and dielectric medium are given as ϵ_M and ϵ_D , respectively). The electromagnetic field is presented with electric field, E , plotted in the z - x plane and magnetic field, H_y , drawn in the y direction. The schema was adopted from [8] and presented with slight modifications.

The electric field at the interface is then expressed taking into account the dielectric constants of the metal ϵ_M and of the dielectric medium ϵ_D :

$$\mathbf{E}_D = (\mathbf{E}_{xD}, 0, \mathbf{E}_{zD})e^{i(k_{xD}.x+k_{zD}.z-\omega t)} \text{ (in the dielectric medium)} \quad (18)$$

$$\mathbf{E}_M = (\mathbf{E}_{xM}, 0, \mathbf{E}_{zM})e^{i(k_{xM}.x+k_{zM}.z-\omega t)} \text{ (in the metal medium)} \quad (19)$$

with x in the interface direction and z perpendicular to the surface.

Then the resolution of the Maxwell equations at the interface gives:

$$k_{xD} = k_{xM} = k_x \quad (20)$$

$$\frac{k_{zD}}{\epsilon_D} \frac{k_{zM}}{\epsilon_M} = 0 \quad (21)$$

$$k_x^2 k_{zD}^2 = \epsilon_D \left(\frac{\omega}{c}\right)^2 \quad (22)$$

$$k_x^2 k_{zM}^2 = \epsilon_M \left(\frac{\omega}{c}\right)^2 \quad (23)$$

It is then possible to determine the relation of dispersion of a surface wave along the interface:

$$\omega = c \left(\frac{\epsilon_M + \epsilon_D}{\epsilon_M \cdot \epsilon_D}\right)^{\frac{1}{2}} k_x \quad (24)$$

This surface wave is called surface plasmon and can propagate along the metal interface based on longitudinal electronic oscillations parallel to the metal surface.

2.2.2.3 Localised surface plasmon

In the case of metallic NPs, due to their small size all electrons are involved in the collective oscillation in presence of light. This electron cloud oscillation is called localized surface plasmon (LSP) since it is confined within the nanoparticle. When the frequency of the excitation light is equal to the proper frequency of the electron oscillation, the resonance condition is reached and the light will highly interact with the NPs. Such condition is known as LSP resonance (LSPR) (Figure 2.3). For gold and silver NPs, the resonance conditions can be achieved in the visible region of the electromagnetic spectrum.

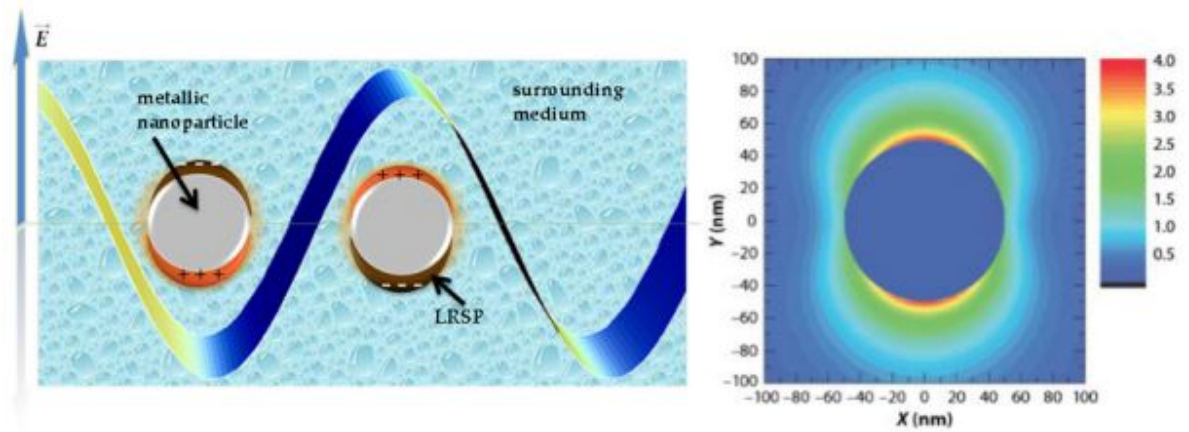


Figure 2.3 Left: schematic illustration of the electron charge displacement in a metallic NP interacting with an incident plane wave [9]. Right: The corresponding electric field strength for a 100 nm silver sphere, irradiated with a 514 nm wavelength [10].

The LSPR of NPs depends on its chemical nature, its size and its shape as well as on its surrounding media. The resonance can be experimentally measured by extinction spectroscopy. Extinction spectrum represents the efficiency of the interaction of the light with the NPs depending on the wavelength. The maximum of the spectrum corresponds to the LSPR.

It is worth to precise, that the extinction process consists in two processes: the light absorption and the light scattering.

The optical extinction of spherical NPs can be precisely calculated using the Mie theory. However, due to the complexity of the resolution of the Mie equation, it is possible to simplify the problem using the quasi-static approximation. In this case, the diameter of NPs is assumed to be largely smaller than the excitation wavelength ($2r \ll \lambda$) and as a consequence, the electric field amplitude is supposed to be constant throughout the NPs. Then, the cross sections of the absorption and of the scattering processes (σ_{abs} and σ_{sca} , respectively) can be calculated as:

$$\sigma_{abs}(\lambda) = 6\pi \frac{V}{\lambda} \Im m \left(\frac{\epsilon_M - \epsilon_D}{\epsilon_M + 2\epsilon_D} \right) \quad (25)$$

$$\sigma_{sca}(\lambda) = 24\pi^3 \frac{V^2}{\lambda^4} \left| \frac{\varepsilon_M - \varepsilon_D}{\varepsilon_M + 2\varepsilon_D} \right|^2 \quad (26)$$

$$\sigma_{ext}(\lambda) = \sigma_{abs}(\lambda) + \sigma_{sca}(\lambda) \approx \sigma_{abs}(\lambda) \quad (27)$$

With the V , the volume of the particle ($V=4/3\pi r^3$ for spherical NPs).

Thus, the resonance can be deduced from the equations (24) and (25) as $\Re(\varepsilon_M) = -2\varepsilon_D$. This condition only depends on the dielectric constants of the metal and of the surrounding medium. Concerning NPs with larger diameters ($2r > \lambda/10$), quasi-static approximation can no more be applied and correction factors have to be considered, such as:

- The radiation damping, expressed as: $-\frac{16\pi^3}{3} \left(\frac{r}{\lambda}\right)^3 i$, $-\frac{16\pi^3}{3} \left(\frac{r}{\lambda}\right)^3 i$, explains the energy losses due to the radiation induced by the scattering field. It decreases the polarization and sequentially, the extinction efficiency. As a consequence, the damping induces the broadening of the plasmon resonance.
- The dynamic depolarization written as: $-4\pi^2 \left(\frac{r}{\lambda}\right)^2$, $-4\pi^2 \left(\frac{r}{\lambda}\right)^2$, which describes the induced de-phasing of electron cloud oscillation inside the NPs volume. As a consequence, induced depolarization of electron cloud in the whole volume decreases the energy of the plasmon (observed as a red-shift of LSPR).

Taking into account these two factors, the expressions of the cross sections can be modified as:

$$\sigma_{abs}(\lambda) = 6\pi \frac{V}{\lambda} \Im m \left(\frac{\beta}{1 - 4\beta\pi^2 \left(\frac{r}{\lambda}\right)^2 - i\beta \frac{16\pi^3}{3} \left(\frac{r}{\lambda}\right)^3} \right) \quad (28)$$

$$\sigma_{sca}(\lambda) = 24\pi^3 \frac{V^2}{\lambda^4} \left| \frac{\beta}{1 - 4\beta\pi^2 \left(\frac{r}{\lambda}\right)^2 - i\beta \frac{16\pi^3}{3} \left(\frac{r}{\lambda}\right)^3} \right|^2 \quad (29)$$

Where $\beta = \frac{\varepsilon_M - \varepsilon_D}{\varepsilon_M + 2\varepsilon_D}$

Then the maximum of extinction cross section is reached for:

$$\Re(\varepsilon_M) = - \left(\frac{2 + 4\pi^2 \left(\frac{r}{\lambda}\right)^2}{1 - 4\pi^2 \left(\frac{r}{\lambda}\right)^2} \right) \varepsilon_D \quad (30)$$

In this case, the LSP resonance depends on the size of NPs and on the dielectric constant of the surrounding environment. It also worth to note that the shape of metallic NPs plays an important role in the absorption and scattering cross sections and influences the LSPR position. As an example, an ellipsoid NP is defined by its three axis and exhibits three distinct plasmon resonances in each direction.

The excitation of LSP induces the local enhancement of the electric field, $M(\lambda)$, around the NPs:

$$M(\lambda) = \left| \frac{\|E_{loc}(d)\|}{\|E_{inc}\|} \right| \quad (31)$$

where, E_{inc} is the amplitude of the incident field and $E_{loc}(d)$ is the amplitude of the local electric field induced at the distance d from the NP surface. The enhancement factor can be estimated employing the factor β used for spherical NPs:

$$M(\lambda) = \frac{V}{2\pi(r+d)^3} |\beta| \quad (32)$$

In this case, it is evident that the enhancement factor is maximum at the close surface of NPs (d close to 0) and when β is maximum (corresponding to the LSPR conditions). The enhancement factor decreases rapidly when the distance from the surface increases.

To summarize, the LSPR position strongly depends on the size and the shape of the NPs as well as on the surrounding environment. Thus, in the case of molecular adsorption to a NPs surface LSPR position would shift due to the change in the refractive index. Hence, extinction spectroscopy might be applied for direct molecular sensing [11] or as a tool to monitor surface functionalisation [12].

2.2.3 Surface enhanced Raman Spectroscopy

Surface Enhanced Raman Spectroscopy (SERS) is a technique that overcomes the limitations related with the sensitivity observed in conventional Raman spectroscopy. More precisely, SERS enables the increase of the Raman signal of a targeted molecule by several orders of magnitude when it is at the vicinity of a nano-scaled metallic surface (metallic NPs of any shape and with size varying from few tens to few hundreds of nanometers) [13]. Silver and gold are among the most often used metals for SERS substrates fabrication since their plasmon resonance conditions can be achieved in the visible and in the near-infrared frequency range. It is worth to note that silver NPs ensure higher SERS response with an enhancement factor 10-100 fold greater than the one reached with gold NPs. However, for many SERS applications especially related to sensing purposes in complex environmental medium substrates fabricated or protected (shell layer) using gold are preferred due to its resistance to corrosion and oxidation [14].

SERS has been observed for the first time in 1974 by Fleischmann *et al.*, who evidenced a strong increase of the Raman signal of pyridine adsorbed on electro-chemical roughened silver electrode [15]. Few years later an electromagnetic explanation of the observation has been proposed [16] [17]. Since then, continuous research is ongoing in order to explain the mechanisms involved in SERS. Up

to now, two processes contributing to the SERS have been identified: the chemical effect and the electromagnetic effect.

2.2.3.1 The chemical effect

The contribution of the chemical effect to SERS enhancement is not completely solved. The chemical effect results from the interaction between the molecules and the metallic surface. This interaction produces modifications in the electronic structure of the molecule due to molecule-metal complex formation or the charge transfer between the molecule and the metal [18] [19] [20]. In both cases, the increase of the molecule polarizability can be induced. This effect was notably found to be amplified on defected surface (adatoms model) [21]. The input of the chemical effect to the enhancement is fewer than a factor 100 [19].

It is worth to note that, the contributions of the chemical effect to the SERS enhancement are complex and difficult to estimate experimentally. Thus, for better understanding, the suitable electronic structure calculation methods have to be employed, such as density functional theory (DFT) and molecular dynamics [22].

2.2.3.2 The electromagnetic effect

The electromagnetic effect is contributing to the SERS through the field enhancement at the vicinity of plasmonic NP surface [18]. As it was already discussed, this field enhancement strongly depends on the properties of the metallic NPs as well as the position of the excitation wavelength in comparison to the position of plasmon resonance. Thus, it is necessary to optimize the system in order to achieve higher enhancement factor.

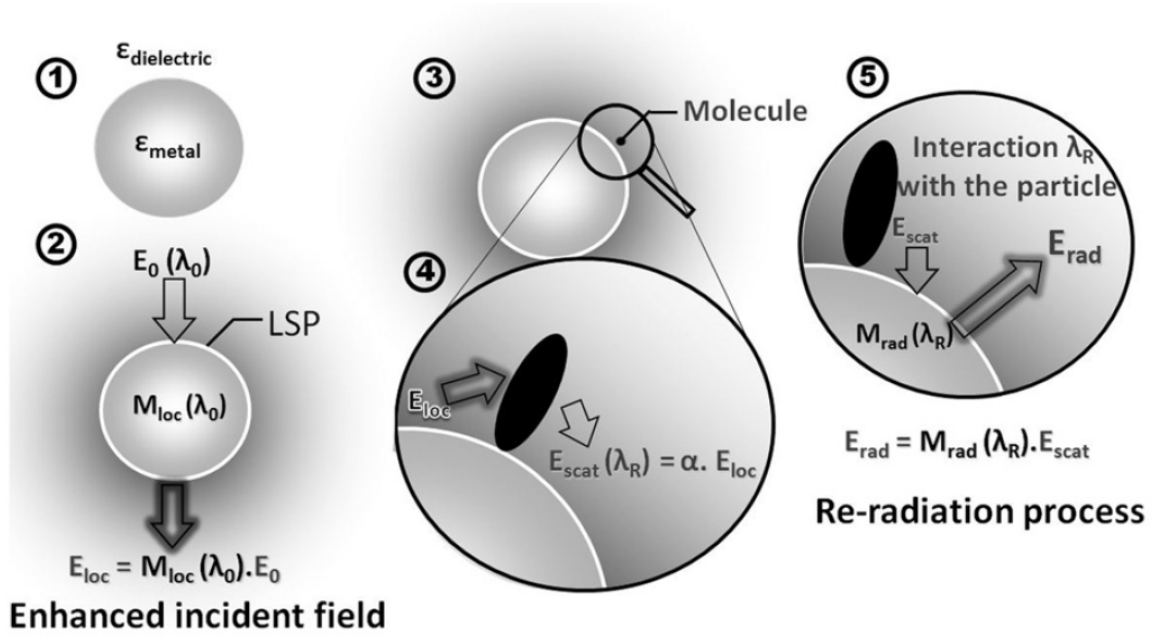


Figure 2.4 Schematic illustration of electromagnetic effect in SERS. Figure reproduced from Guillot et al. [13].

According to Wokaun [18] the electromagnetic interaction between a molecule and metallic NP involves two distinct processes (summarized in Figure 2.4). If the molecule adsorbed on the metallic NP surface is considered as two bodies system, the incoming light will interact with them both distinctly. Firstly, the excitation field \mathbf{E}_0 (at the wavelength λ_0) interacts with the metal NP, resulting in the induction of the local field \mathbf{E}_{loc} (proportional to \mathbf{E}_0 and to the enhancement factor $M_{loc}(\lambda_0)$). The molecule at the NP surface will then be excited by this enhanced field and will scatter a Raman signal (at a red-shifted wavelength λ_R). Since the dipole moment of the vibrational mode is proportional to the field (equation (1)) the scattered field \mathbf{E}_{sca} will be enhanced by the same factor as the local field. A second process then occurs. The scattered field by the molecule can interact with the NP and its plasmon creating a re-radiated field \mathbf{E}_{rad} (proportional to the scattered field and to the enhancement factor $M_{rad}(\lambda_R)$). This process induces a second enhancement of the Raman signal at the Raman wavelength λ_R . In the end, the intensity of enhanced Raman signal I_{SERS} scattered by the adsorbed molecule is written as follows:

$$I_{SERS} = \alpha^2 M_{loc}^2(\lambda_0) M_{rad}^2(\lambda_R) E^2 = G I_0 \quad (33)$$

with $G = M_{loc}^2(\lambda_0) M_{rad}^2(\lambda_R)$ corresponding to the total electromagnetic enhancement factor and I_0 , the intensity of the scattered Raman signal with the absence of NPs. If one supposes that the excitation and the Raman wavelengths are close, these two enhancement factors can be assumed as $M_{loc}^2 \approx M_{rad}^2$ and thus $G = M_{loc}^4$. This explains why it is commonly assumed that SERS enhancement is at the fourth power of the local electromagnetic field enhancement induced by a NP.

In conclusion, SERS is a spectroscopic technique which exploits optical properties of metallic NPs. The performance of this technique is thus highly dependent on the size, shape and the nature of metallic NPs. Furthermore, since SERS effect takes place in the local fields of NP, it results in strongly increased Raman signals of the molecules which are attached or presented at the vicinity of the metallic surface. The following sections of this chapter will address the aspects related with the design of good SERS nanosensors, such as the selection of the SERS substrates and the strategies of the surface functionalisation in order to pre-concentrate analytes to the nanosensor surface.

2.2.4 References

- 1 Qian, X. M. and Nie, S. M. (2008). Single-molecule and single-nanoparticle SERS: from fundamental mechanisms to biomedical applications, *Chemical Society Reviews*, 37, pp. 912-920.
- 2 Schlücker, S. (2014). Surface-Enhanced Raman Spectroscopy: Concepts and Chemical Applications, *Angewandte Chemie International Edition*, 53, pp. 4756-4795.
- 3 Hering, K., Cialla, D., Ackermann, K., Dörfer, T., Möller, R., Schneidewind, H., Mattheis, R., Fritzsche, W., Rösch, P. and Popp, J. (2008). SERS: a versatile tool in chemical and biochemical diagnostics, *Analytical and Bioanalytical Chemistry*, 390, pp. 113-124.
- 4 Golightly, R. S., Doering, W. E. and Natan, M. J. (2009). Surface-enhanced Raman spectroscopy and homeland security: a perfect match?, *ACS Nano*, 3, pp. 2859-2869.
- 5 Xuaná Quang, L., HunáSeong, G. and JunáDo, K. (2008). A portable surface-enhanced Raman scattering sensor integrated with a lab-on-a-chip for field analysis, *Lab on a Chip*, 8, pp. 2214-2219.
- 6 Ru, E. L. and Etchegoin, P. (2008). *Principles of Surface-Enhanced Raman Spectroscopy: and related plasmonic effects*: Elsevier Science.
- 7 Raman, C. V. and Krishnan, K. S. (1928). A new type of secondary radiation, *Nature*, 121, pp. 501-502.
- 8 Guillot, N. and De La Chapelle, M. L. (2001) *Wiley Encyclopedia of Electrical and Electronics Engineering*, chapter "Nanoantenna," (John Wiley & Sons, Inc.).
- 9 Rivera, V. A. G., Ferri, F. A. and Jr., E. M. (2012). Localized Surface Plasmon Resonances: Noble Metal Nanoparticle Interaction with Rare-Earth Ions.
- 10 Lu, X., Rycenga, M., Skrabalak, S. E., Wiley, B. and Xia, Y. (2009). Chemical Synthesis of Novel Plasmonic Nanoparticles, *Annual review of physical chemistry*, 60, pp. 167-192.
- 11 Chen, Y.-Q. and Lu, C.-J. (2009). Surface modification on silver nanoparticles for enhancing vapor selectivity of localized surface plasmon resonance sensors, *Sensors and Actuators B: Chemical*, 135, pp. 492-498.
- 12 Fujiwara, K., Watarai, H., Itoh, H., Nakahama, E. and Ogawa, N. (2006). Measurement of antibody binding to protein immobilized on gold nanoparticles by localized surface plasmon spectroscopy, *Analytical and Bioanalytical Chemistry*, 386, pp. 639-644.
- 13 Guillot, N. and de la Chapelle, M. L. (2012). The electromagnetic effect in surface enhanced Raman scattering: Enhancement optimization using precisely controlled nanostructures, *Journal of Quantitative Spectroscopy and Radiative Transfer*, 113, pp. 2321-2333.
- 14 Gong, J. and Mullins, C. B. (2009). Surface Science Investigations of Oxidative Chemistry on Gold, *Accounts of Chemical Research*, 42, pp. 1063-1073.
- 15 Fleischmann, M., Hendra, P. J. and McQuillan, A. J. (1974). Raman spectra of pyridine adsorbed at a silver electrode, *Chemical Physics Letters*, 26, pp. 163-166.
- 16 Jeanmaire, D. L. and Van Duyne, R. P. (1977). Surface raman spectroelectrochemistry: Part I. Heterocyclic, aromatic, and aliphatic amines adsorbed on the anodized silver electrode, *Journal of Electroanalytical Chemistry and Interfacial Electrochemistry*, 84, pp. 1-20.
- 17 Albrecht, M. G. and Creighton, J. A. (1977). Intense Raman spectra of pyridine at a silver electrode, *Journal of the American Chemical Society* 99, pp. 5215-5217.

- 18 Wokaun, A. (1984). Surface-Enhanced Electromagnetic Processes, *Solid State Physics*, 38, pp. 223-294.
- 19 Champion, A. and Kambhampati, P. (1998). Surface-enhanced Raman scattering, *Chemical Society Reviews*, 27, pp. 241-250.
- 20 Otto, A. (1984) *Light Scattering in Solids IV*, chapter 6 "Surface-enhanced Raman scattering: "Classical" and "Chemical" origins," (Springer Berlin Heidelberg) pp. 289-418.
- 21 Otto, A., Billmann, J., Eickmans, J., Ertürk, U. and Pettenkofer, C. (1984). The "adatom model" of SERS (Surface Enhanced Raman Scattering): The present status, *Surface Science*, 138, pp. 319-338.
- 22 Wu, D.-Y., Duan, S., Ren, B. and Tian, Z.-Q. (2005). Density functional theory study of surface-enhanced Raman scattering spectra of pyridine adsorbed on noble and transition metal surfaces, *Journal of Raman Spectroscopy*, 36, pp. 533-540.

2.3 Sensing platforms for SERS

As resumed in previous section, the key point of successful SERS application in molecular sensing is the properties of designed nanosensor which essentially depends on both: SERS-active substrate and the molecular recognition elements capable of analytes pre-concentration.

This section will be composed by the part titled “Application of SERS to chemical sensing”, where we will overview the methodologies of substrates fabrication processes and the surface functionalisation strategies proposed in the literature for chemical pollutants sensing. This part has been published as a chapter in the book “Handbook of Enhanced Spectroscopy” (edited by Lamy de la Chapelle, M.; Gucciardi, P.; Lidgi-Guigui, N), which was recently published by Pan Stanford.

Chapter 10

Application of SERS to Chemicals Sensing

Inga Tijunelyte,^a Nathalie Lidgi-Guigui,^a
and Emmanuel Rinnert^b

^a*CSPBAT, Sorbonne Paris Cité, Bobigny, France*

^b*Laboratoire Détection, Capteurs et Mesures, Ifremer, Brest, France*
nathalie.lidgi-guigui@univ-paris13.fr

10.1 Introduction

During the last years, surface-enhanced Raman spectroscopy (SERS) has appeared as a relevant analytical technique. Thanks to its many advantages such as selectivity, sensitivity, and ease of operation; it is a promising analytical tool and is concerned with many fields of application, such as environmental sciences, clinical or food applications, etc.

The necessity of diagnosis tools in these domains and the progress in science—photonics, plasmonics, nanotechnologies, and molecular chemistry—ensure nowadays a research structuring around SERS technique for analysis and sensor applications for tomorrow.

The aim of this chapter is to present some recent investigations on the elaboration of SERS substrates in order to detect specific molecules in different field. Some studies are presented in detail

Handbook of Enhanced Spectroscopy

Edited by Marc Lamy de la Chapelle, Pietro Giuseppe Gucciardi, and Nathalie Lidgi-Guigui

Copyright © 2015 Pan Stanford Publishing Pte. Ltd.

ISBN 978-981-4613-32-3 (Hardcover), 978-981-4613-33-0 (eBook)

www.panstanford.com

to focus on the need of complementarities for the elaboration of SERS-active substrates. An exhaustive study is difficult to achieve in such a progressive scientific environment. We will first consider the nanostructures' production possibilities. Then a review of the strategies for specific detection will be given. Eventually, an overview of some SERS commercial solutions will also be described in order to confirm the potential market of the technique.

10.2 Nanostructures for SERS Detection

A good SERS substrate has to be sensitive, stable, easy to handle, and give reproducible results. Another very important point in the purpose of making commercial SERS surfaces is their price. As we will see in the following this is the determining parameter to choose the mean of fabrication.

Metallic nanoparticles chemically synthesized are possibly one of the simplest ways to produce SERS substrates. They are very easily synthesized; their production is well documented; and the literature is overflowing with strategies to control their shape, size, and surface chemistry. In the framework of SERS sensors, colloids can be used in several manners. An option is to form a single layer of nanoparticles on top of a functionalized glass substrates [1]. Another possibility is to take advantage of a fluidic system in order to aggregate the nanoparticles into a multitude of hot spots [2]. Eventually, fiber optic SERS sensors are using colloids to functionalize standard fiber optics (see Chapter 8 of this book). While being cheap and easily handled, the use of colloids rarely make reproducible substrates. The reason for this is that the size and positions of the colloids cannot be finely controlled. The colloids assemblies often present defects such as a missing nanoparticle or a random number of aggregates forming hot spots. As it is not possible to control the number of defects, some substrates will exhibit extraordinary enhancement factors due to a high number of hot spots while other substrates will be less performant.

Gold and silver colloids are commercially available (see Section 10.5 below) for SERS, these two metals give the highest enhancement factors. Silver is known to give the best enhancement factor,

whereas gold is highly stable, biocompatible, and its chemistry is well-known. However, a lot of work is in progress concerning metamaterials, which could concurrence the sensitivity of gold at lower cost.

The shape and organization of the nanostructures also contribute to the sensitivity of the SERS sensor. Tips and near-field coupling can lead to extraordinary enhancement factors. This is what is happening when colloids aggregates. But as these aggregates are difficult to control and thus reproduce, it can be a better option to choose lithography techniques to fabricate the nanoparticles. The resolution needed to get nanoparticles with tips (nanoantennas, triangles, stars, etc.) and spaced out of a few nanometers requires the use of e-beam lithography (EBL). In this technique an electron-sensitive resist is exposed to the electron beam of a scanning electron microscope (SEM) (see Fig. 10.1a).

At the same time, large nanostructured surfaces (at least 1 mm^2) have to be produced in order to be easily handled by a potential end-user. For example, in the case of *in situ* SERS experiments, it is not always possible to adjust the sample position. Fabrication of a $1 \times 1 \text{ mm}$ network of nanocylinders can take up to 72 hours with standards EBL. Such a long time for the production of a single substrate is in contradiction with any commercial view.

In order to overcome this issue other nanofabrication techniques can be used. Nanosphere lithography (NSL) and its derivatives can be cited [3] (Fig. 10.1c) as well as innovative techniques such as nanoimprint lithography (NIL) [4] (see Fig. 10.1b). NSL is well known to produce an assembly of nanotriangles. It is possible to tune the size and shape of the nanostructures by varying the way of stacking the nanospheres. Yet, it is not trivial to do so in a reproducible way. In the latter, a mother mold is made by EBL that is used to produce a stamp which in turn is used to pattern a substrate. Since the mother mold is made with EBL the nanoparticle assembly can be shaped for a specific requirement and then duplicated as many times as required.

As a conclusion, many different nanoparticles are available for SERS purposes, but they are more or less difficult to produce. Before choosing a substrate one has to finely define his need in term of price, reproducibility, and sensitivity. It is important to highlight

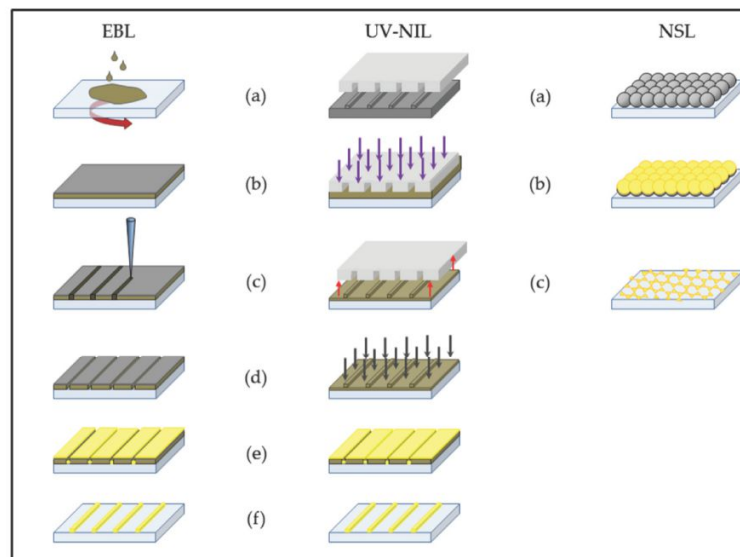


Figure 10.1 EBL: (a) spin coating, (b) metallization, (c) exposure to electron beam, (d) development, (e) gold evaporation, (f) lift-off. UV-NIL: (a) stamp fabrication from master mold, (b) the stamp is pressed against a resist and the system is exposed to UV, (c) separation, (d) etching, (e) gold evaporation, (f) lift off. NSL: (a) Nanospheres self-assembly, (b) gold deposition, this substrate can be used like this for SERS, it is then called film over nanospheres (FON), (c) nanospheres removal.

that the notion of sensitivity depends on the chemical aimed to be detected. For example, the European commission has fixed the maximum amount of naphthalene in sea water to $2.4 \mu\text{g/L}$ but only to $0.05 \mu\text{g/L}$ for benzo[a]pyrene.^a The SERS industry is still in its young years and for the moment users still have to make their own test in order to validate a SERS substrate for a specific application.

10.3 Sensing Molecules Using SERS-Active Substrates

SERS is a powerful tool for toxic and hazard chemical compounds detection, identification, and quantification. For a molecular de-

^aEuropean Parliament Directive 2008/105/EC, published 24 December 2008

tection approach by SERS, optimization of the size and shape of plasmonic nanostructure is a very important parameter. However, in the matter of sensing, it is of prime importance to consider the issue of affinity between the analyte and the SERS surface. Some molecules, especially those containing oxygen, nitrogen, or sulfur atoms can be directly pre-concentrated near the surface due to strong interactions. These interactions are induced by charge-transfer complex formation, where molecule acts as electron donor and the metal surface as an acceptor [5]. In the literature, many examples have been reported on such molecules' detection and identification by SERS method. For instance *trans*-1,2-bis(4-pyridyl)ethylene (BPE) adsorbed on gold nanoparticles [6]. Other reported example is adsorption of azodicarbonamide (ADC) on as prepared gold nanoparticles of 50 nm in diameter, which have been monitored in low concentrations [7].

However, nonmodified metallic surface shows several disadvantages for a chemical sensing application. Interaction of some molecules with a surface is so strong that chemical change can be induced: molecular decomposition or polymerization has been observed [8–12]. Moreover, chemical sensor application for complex environment gives a crucial issue of nonselectivity against target compound. Metal surface functionalization is important to ensure affinity to a molecular group or even to a single molecule.

Another important disadvantage is related with detection of nonpolar substances such as polycyclic aromatic hydrocarbons (PAHs) and volatile toxic atmospheric pollutants that consist of fused aromatic rings and do not show affinity to metallic surfaces due to the absence of functional groups [13].

Finally, functionalization ensures metallic surface protection against environmental degradation especially by working with the silver-based substrates [14].

10.4 Surface Functionalization Strategies

10.4.1 *Self-Assembled Monolayers*

Self-assembly in general is the ability of organic molecules to construct different structures by noncovalent interactions [15].

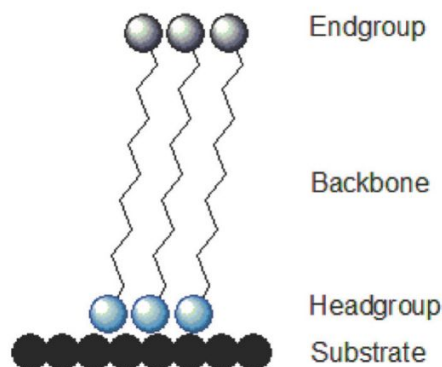


Figure 10.2 Graphical model for self-assembled monolayer of alkanethiols on metal surface.

Many types of compounds, mostly amphiphilic molecules can be involved in self-assembly processes. However, considering functionalization of solid surfaces for a steady and robust nanosensor design, molecules that strongly interact with metal are mostly appropriated.

Self-assembled monolayers (SAMs) on solid surfaces have structural similarities (Fig. 10.2). These molecules consist of three main parts, including head group, backbone or spacer unit, and a terminal or functional group [16]. The head group ensures strong interaction with the surfaces. Usually silane heads groups are devoted to oxide surfaces, whereas thiols or amine are more adapted to noble metals. In the framework of SERS it is thus no surprise that most of the functionalization procedures involve an -SH group. Considering noble metals (gold, silver, or platinum) surface functionalization, molecules bearing thiol groups are mostly used [17], because of the very strong bonding between metal and sulfur atoms (the true nature of the bond is still under debate, but most claims that it is irreversible).

The backbone of SAMs is used as a spacer between the head and the end group. It controls the orientated formation of homogeneous monolayer due to weak Van der Waals forces between the molecules forming the SAM.

In addition to easy functionalization procedure, a reason why SAMs are extremely attractive is the large range of possibilities offered by SAMs terminal groups. Depending on the purpose of the

SAMs, a vast range of end groups are available (commercially or *via* synthesis) and it can subsequently be used in various chemical reactions [18]. In this manner, hydrophobic decorated surface can be turned to hydrophilic [19], thanks to end groups modifications.

Nature of SAM-forming molecules is very important for a chemical nanosensor design. Considering small molecules detection, the hydrophobic nature of octadecylthiol, which was used to coat roughened silver surface, was found to preconcentrate nonpolar aromatic pollutants following the Langmuir isotherm [20]. The selectivity of this sensor was successfully tested with three isomers of xylene. The sensor sensitivity was measured by detecting benzene at 7.5 ppm and naphthalene at 2.3 ppm.

The length of carbon chain (spacer) in alkanethiol plays a crucial role in the formation of a well-packed monolayer [21]. However, nanosensor decorated by short alkanethiols, such as 1-propanethiol, have shown ability to preconcentrate small molecules at the similar concentration level via hydrophobic interactions [22]. Gold nanoparticles grafted to solid substrates were employed for more efficient detection of nonpolar molecules. Nanosensors were designed on quartz substrates, functionalized by SAMs of (3-mercaptopropyl)trimethoxysilane (MPTMS) or (3-aminopropyl)trimethoxysilane (APTMS), and gold nanoparticles were then grafted via S–Au or N–Au interactions [1]. With such SERS-active substrate, detection limit in artificial sea water was found to be 10 ppb for naphthalene and pyrene.

In addition to SAMs ability to preconcentrate chemicals by hydrophobic interactions they can also be applied for polar molecules detection via electrostatic interactions. Thus, for pentachlorophenol (PCP) sensing, cysteamine-decorated silver nanoparticle aggregates have been used by Jiang et al. [23]. Cysteamine SAM formed in this model has provided both rapid target molecule adsorption and internal reference of a quantitative sensing. In this manner, PCP has been monitored in a range from 0.5 to 100 μ M.

10.4.2 Polymers

Polymer-based sensors are used for a wide range of chemical detection, a good review can be found in Ref. [24]. However, for a

long time, polymer-decorated nanosensors were not applicable as a matrix for SERS detection due to the great thickness of the deposited layer. To overcome this disadvantage, sol-gel derived layers with encapsulated metal nanoparticles have been proposed. For instance, Murphy et al. [25] have reported a study, where SERS-active substrates were produced by using gold and silver nanoparticles along with tetraethoxysilane (TEOS) and methyltriethoxysilane (MTEOS) precursors. MTEOS with incorporated silver nanoparticles has shown greater detection limits than TEOS for chlorobenzene and phenylacetylene (100 and 10 ppb, respectively) [25]. In addition to the sensitivity, sol-gel-derived xerogels with encapsulated metallic nanoparticles are excellent SERS-based sensors for the *in situ* environmental conditions. The lifetime of at least 5 weeks in sea water has been estimated by Lucht et al. [26]. Moreover, the detection of nonpolar molecules has been improved by applying ethyltriethoxysilane (ETEOS) in the mixture with MTEOS. This has led to increased sensor hydrophobicity and reached detection limit as low as 9 ppb for phenylacetylene and 135 ppb for biphenyl [25].

Other strategies of nanostructures functionalized with polymers for the detection of organic molecules have been proposed. For instance, polystyrene (PS) beads coated with gold nanoparticles have been suggested as SERS-active substrate, by Peron et al. [27]. Prepared core-shell nanocomposites were immobilized on silanized quartz surface. The successful preconcentration of naphthalene via hydrophobic interactions has been achieved in the range of 1 to 20 ppm (7.8–160 μM) in aqueous media. For the quantification, Raman signal of the PS has been used as an internal spectral reference. Another group proposed the synthesis of core-shell nanoparticles for melamine detection in the 100 nM range [28]. Therein *in situ* chemically reduced silver nanoparticles were immobilized on poly(styrene-co-acrylic acid) (PSA) nanospheres.

Recently, great improvement in sensor selectivity has been proposed by constructing a synthetic receptor for specific molecule detection employing molecularly imprinted polymers (MIPs). MIPs are made by imprinting molecules of interest into the polymeric matrix followed by washing out the template molecules to ensure permanent grooves [29] (Fig. 10.3). This technique led to create MIP-based system that is complementary to the molecule of interest in

shape, size, and molecular interactions. Thus, MIPs can be applied for a complex environment condition for its excellent recognition of template as well as mechanical and chemical stability [30]. Coupling SERS with molecular imprinting technique has been applied to provide not only selectivity but also sensitivity to the nanosensor. In 2009, Kantarovich et al. have proposed a method to print a MIP on Klarite[®] substrate (see Section 10.5) for a direct monitoring of beta-blocking drug S-propranolol uptake and release [31]. MIP droplets were deposited on a surface using a pipette or a nanofountain pen. SERS signal of S-propranolol has been observed even if the MIP layer deposited on the surface was not homogeneous and thick. By minimizing distance between template molecules and metallic moieties, great enrichment of chemical detection has been achieved. The controlled thickness of MIP layer was applied by Bompert et al. choosing propranolol as a template molecule [32]. In this article, core-shell composite particles of submicrometer size were designed. For SERS signal amplification, gold nanoparticles were incorporated as interlayer between polymeric core and MIP shell. Detection limit of 100 nM for a template molecule has been reached on single MIP composite by a core-shell-based nanosensor [32]. Recently, similar system was applied for a spectroscopic monitoring of bisphenol A, known as endocrine disruptor [33]. In this work, gold nanoparticles were decorated with molecularly imprinted shell via sol-gel process. The imprinted polymeric layer of 2 nm has been achieved ensuring an effective recognition sites by complete removal of template molecules. This improvement of nanosensor has led to rapid binding kinetics and a great detection limit of 0.12 mg·l⁻¹. MIPs concept has also been exploited for sensing explosive agent 2,4,6-trinitrotoluene (TNT). Detection of TNT at 3 μM has been reached, thanks to sol-gel-derived xerogels, adsorbed on an SERS-active surface [34]. Yang et al. have demonstrated a nanosensor capable of monitoring TNT molecules in ultratrace concentration as low as 10⁻¹² M [35]. Silver molybdate nanowires, decorated by crosslinked silver nanoparticles, have been used as a chemical sensor. Chang et al. have reached a particularly high detection limit of 10⁻¹⁵ M for a 4-mercaptobenzoic acid (4-MBA) by employing core-shell Ag-MIP hybrid as SERS-active substrate [36]. In this case, the MIP had a thickness of 40 nm, which is 2.7 times larger than

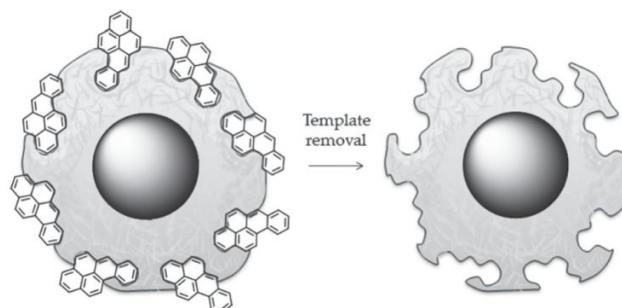


Figure 10.3 Graphical model of MIP preparation.

the maximum reported SERS distance [37]. A possible mechanism, dealing with a “gate effect” model [38] has been proposed to explain this great SERS enhancement.

10.4.3 Host Materials

Molecular host-guest systems have been studied for many years because of their great number of applications in different fields. Herein will be described some of the molecules which were applied for the design of nanosensor intended to detect trace concentrations of organic molecules such as PAHs, pesticides, or explosive agents by SERS. Nature of chemical interactions between host and guest molecules is noncovalent and provides the possibility of reusable sensor approach. Furthermore, organic molecule inside host material is protected from degradation by light or temperature, which can be induced by an electromagnetic field.

10.4.3.1 Cyclodextrins

Cyclodextrins (CDs) are cup-like molecules widely studied since the middle of 20th century. The enthusiasm was born after the demonstration of their ability to form host-guest complexes with hydrophobic molecules [39]. The most common CD forms are: α -CD, β -CD, and γ -CD. The difference between them is the number of glucopyranoside units (six for α -, seven for β -, and eight for γ)-attached by α -1,4-linkages [40]. CDs form specific 3D structure of

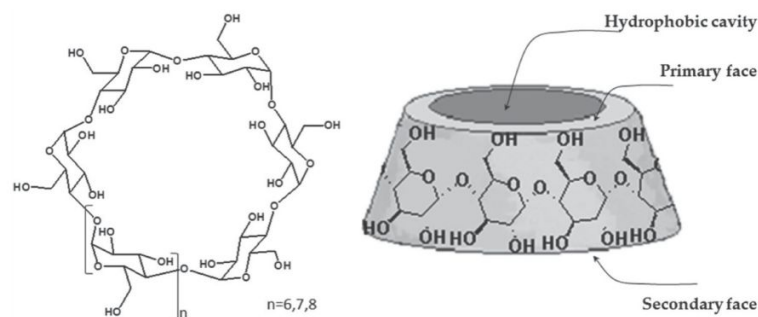


Figure 10.4 Chemical and 3D structure of cyclodextrins (CDs).

molecule, having inner hydrophobic cavity with a large entrance (Fig. 10.4). Cavity diameter depends on the number of glucosyl units. For this reason the smallest α -CD with the cavity size of 4.7 to 5.2 nm is known to form complexes with benzene, β -CD can capture molecules not bigger than 6.4 nm, and γ -CD having the cavity of 7.5 to 8.3 nm able to include two aromatic guest [40]. Since a wide variety of guest compounds can form complexes with CDs (aliphatic chains, aldehydes, ketones, alcohols, organic and fatty acids, PAHs, gases, and volatile compounds [41]), they can be applied for the design of nanosensor for pollutants detection based on SERS.

CDs have a number of primary hydroxyl groups on one edge called primary face as well as secondary hydroxyl groups on the other edge called secondary face. Those groups are orientated toward the outside of a cup-like structure, making the molecule soluble in water. Hydroxyl group's availability and reactivity are very important for CDs chemical modification in order to functionalize metallic surface. Many methods for the synthesis of controlled and selective CD derivatives have been studied and described [42, 43]. However, among all of them thiolated CDs remain the most used for surface decoration. Thiolated CDs can form packed monolayers as alkanethiols, but the chemisorption's kinetics strongly depends on the length between the SH function and the CD [44]. However, for an SERS-active surface functionalization, thiolated CDs without alkyl chain are preferred in order to increase the nanosensor sensitivity by preconcentrating chemicals closer to the metal surface.

Per-6-thio- β -cyclodextrins have been applied for decoration of rough silver surface to detect gaseous aromatic substances such as benzene, toluene, *m*-xylene, chlorobenzene, and *m*-dichlorobenzene, with the detection limits of 10000, 400, 1400, 250, and 15 ppm, respectively [45]. Detection limits have been greatly improved by applying metallic nanoparticles as SERS-active substrate. Xie et al. have described qualitative and quantitative detection of anthracene, pyrene, chrysene, and triphenylene with a per-6-deoxy-(6-thio)- β -cyclodextrin-modified gold and silver nanoparticles [46, 47]. The limit of detection was found to be 100, 10, 100, and 1000 nM for anthracene, pyrene, chrysene, and triphenylene, respectively. Triangular gold nanoprisms functionalized by mono-6-thio-beta-cyclodextrin have been applied for SERS detection of explosive agent 2,4-dinitrotoluene (DNT) at the concentration of 10 pM [48]. Methyl parathion insecticide (1 pM) was detected by investigating gold nanorods, decorated with mono-6-thio-beta-cyclodextrin [49].

10.4.3.2 Calixarenes

Calixarenes (CXs) are compounds, belonging to cavitands class as CDs. They are described as synthetic cyclo-oligomers whose structure forms cup-like shape (Fig. 10.5), which make them serve as host for various molecules [50]. Specific CXs structure ensures specificity in recognizing small species such as ions, anions, or neutral molecules [51]. Chemical modification of upper or lower rims ensures the molecular selectivity regarding functional affinity

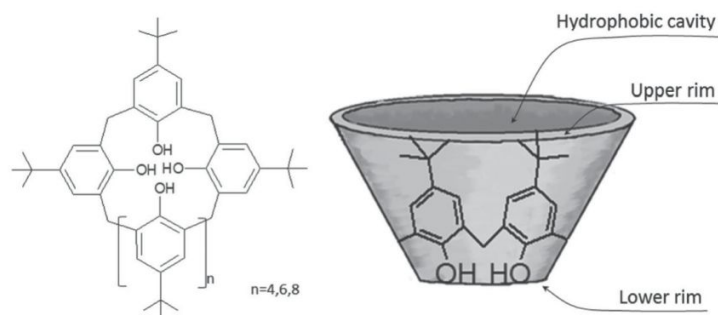


Figure 10.5 Chemical and 3D structure of calixarenes (CXs).

with the targeted chemicals. Because of the following reason this group of molecules is well applicable for SERS sensor design. As for the CD case, CXs offer different size of cavity depending on number of phenolic units (4, 6, 8) linked by methylene bridges. For the interest to detect pollutants, CXs propose hydrophobic cavity and π - π stacking between its structural unit of *p-tert*-butyl phenol and benzene ring-bearing compounds. Based on this interaction aromatic pollutants have been monitored by the mean of SERS. For instance, silver nanoparticles, covered by calix[4]arene and its derivatives having dicarboethoxy and dicyano substitutes in the lower rim have been studied by Leyton et al. [52, 53]. They have discovered that CXs show analytical selectivity to the guest systems bearing four benzene rings, mainly pyrene. Later, successful improvement of metallic surface functionalization have been proposed by Guerrini et al., using dithiocarbamate-modified calix[4]arenes [54]. In the mean of this substrate, PAHs such as benzo[*c*]phenanthrene, triphenylene, and coronene were monitored in the concentration interval between 10 and 100 ppb [55]. Ability of CXs-based nanosensor performance in seawater has also been demonstrated. Therein, SERS-active sensor was constructed by encapsulating Ag nanoparticles, previously decorated with 25,27-dimercaptoacetic acid-26,28-dihydroxy-4-*tert*-butylcalix[4]arene (DMCX) into sol-gel matrix [56]. A calibration procedure has approved sensitivity and stability in artificial sea water. The potential detection limits of 0.3 nM for pyrene and 13 nM for naphthalene have been calculated.

10.4.4 Carbon Derivatives

The interaction of chemical molecules with a single-walled carbon nanotube (SWNT) and two multiwalled carbon nanotubes (MWNTs) have been studied by Star et al. [57] and the adsorption affinity have been determined. Higher affinity has been found with nonpolar aromatics in comparison with nonpolar aliphatic molecules. This advantage took place in PAHs' preconcentration and detection by SERS. Experimental procedure to detect pyrene at the concentration as low 1 nM has been proposed by Leyton et al. Therein single-walled carbon nanotubes were deposited on colloidal silver nanoparticles,

evaporated on glass slide. Pyrene then was preconcentrated near surface by a π - π electronic stacking with the nanotube [58].

10.4.5 Biomolecules

Aptamer are nucleic acid sequence [59], which can be generated against various molecules [60, 61]. Application of aptamers in nanosensor design deals with their high affinity and specificity toward the target molecule. A selective detection of ochratoxin-A (OTA) has been suggested by Galarreta et al. [62]. In this work two-dimensional gold nanostructures prepared by EBL were decorated with adsorbed oligonucleotides. The sensing ability of this system comes from the difference of the aptamer spectrum before and after it has been in contact with OTA. This suggests efficient aptamer-ochratoxin complex formation. Other model for indirect sensing of a melanine molecule has been proposed by Wen et al. [63], where silver nanoparticles of 10 nm, modified by oligonucleotide were used as SERS substrates. They have demonstrated that interaction of target molecules with aptamers induce nanoparticles release, which are then subsequently aggregating. This process has been monitored by SERS in the low frequency range. With this system melamine concentrations ranging from 6.3 to 403.6 $\mu\text{g/L}$ have been analyzed.

10.5 Commercial Solutions for SERS Substrates

Concerning SERS commercial solutions, many providers appeared in the last ten years. Different kinds of companies share out the market: start-up, spin-out, multinational, etc. The commercialized solutions are various from colloids by chemical reduction to physical deposition of metals. Gold and silver are used as nanoparticles to enhance the Raman signal. The variety of substrates includes usually a chemical functionalization as described previously.

As far as we know, Mesophotonics was the first company to provide a SERS solution. Mesophotonics is a spin-out from the University of Southampton. Their Klarite[®] substrates are made of gold deposited on nanostructured silicon through chemical etching. The sensitive pattern is a square of 4×4 mm available free

or on a microscope slide. The sub-micron patterning allows an enhancement able to detect signal on concentrations as low as ppb. The manufacturing of these substrates ensures a standard deviation below 10% with both laser excitation of 633 and 785 nm. Klarite[®] substrates are now available at Renishaw since their investment in D3 Technologies Ltd., which holds different SERS patents. The application domains are various: analytical chemistry, pharmaceutical drug development, forensics, etc.

A new company based in Vilius, Lithuania, and specialized in laser manufacturing supplies an SERS solution based on silver nanostructures named Randa. The possible range of excitation is foreshadowed from blue to near infrared. Standard areas are squares of 4×4 mm, but larger substrates of 10×10 mm are also available. The concept of manufacturing is 100% monolithic in order to avoid various risks during the elaboration or during the transportation. The samples are very reactive but consequently unstable so that they have to be stored under vacuum and are usable during 2 months after the manufacturing date. Integrated Optics is the only producer to mention an uncertainty principle: one has to choose either very high enhancement ratio or good repeatability of measurements. Randa samples are developed for trace detection but not for concentration determination.

Diagnostic anSERS Inc. sells original affordable substrates based on a production by ink-jet method. The patent-pending ink-jet printing process allows the company to produce the P-SERS[™] substrates at very low cost without sacrificing sensitivity. Moreover, the substrates are very easy to use since only a pipette is needed to drop off the sample. Diagnostic anSERS Inc. also provides SERS solutions through their SERS-active gold or silver nanoparticles available in colloidal forms.

SILicon MEtal COating or Silmeco is a nanotechnology company specialized in SERS substrates. Designed for a wide range of applications and R&D-purposes, Silmeco provides very large area substrates on silicon wafers. The SERS signal is uniform on the covered surface that can reach up to 10 cm in diameter. Based on patented nanofabrication technologies without any lithography process, the fabrication method involves only two steps. Consequently, high-volume manufacturing processes and specific

nanostructure patterns made of gold or silver are the know-how of Silmeco.

Nanova Inc., which is a high-tech company using cutting-edge technology provides also SERS solutions in their field of expertise in nanotechnology, sensors, medical science, and food safety. Thanks to its proprietary technology, the Q-SERS™ substrate is capable of detecting chemical and biochemical compounds at trace concentrations. It consists of nanoparticles from 15 to 60 nm of a metal (not defined) randomly organized on a silicon support glued on a microscope slide. The substrate is able to provide high enhancement factors, with reliable and reproducible results. The fields of application are analytical chemistry, food and water safety, pharmaceutical, medical, and forensic science.

In contrast to the the previous companies Enhanced Spectrometry, Inc. or EnSpectr develops SERS substrates in the framework of the promotion of the portable Raman spectrometry as a solution for advanced substances control, quality inspection, real-time testing, and innovative brand protection. This solution is based on a proprietary technology designed for substances detection and coding of information. EnSpectr SERS Substrates are able to identify various compounds at trace concentrations for chemical analysis or fundamental scientific research. The targeted applications are prohibited substances, cells and tissues, bioscience and pharmaceutical research, and authentication of products with spectral markers technology. Supplied substrates are unmounted squared chips of 5 × 5 mm. They are stored in an inert atmosphere until their utilization. The suggested wavelength is in the 450 to 550 nm range.

With the same market objectives, real-time analyzers provides SERS substrates with the analytical tools such as a portable Raman analyzer and with their process environment. On the opposite of all previous solutions, real-time analyzers has chosen to include silver nanoparticles in an organic sol-gel matrix. This choice allows to provide different substrates such as SERS Vials, SERS Microplates, or SERS Capillaries. These different presentations enlarge the field of application of liquid analyses. Furthermore, the presence of an organic matrix can exhibit a best sensitivity, thanks to the

preconcentration effect for organic compounds. Coupled with the SERS Raman Analyzer, SERS substrates are applied to explosives, chemical weapons, narcotics, and hazardous materials.

The worldwide leader in Raman spectrometry Horiba JobinYvon proposes SERS substrates from ST Japan. This kind of substrates offers excellent reproducibility and significant enhancement. The substrates are available in different sizes, coated with pure gold or gold–silver alloy. Furthermore, the company has recently communicated about SERS through a study of nanoparticles themselves. It is well-known that metallic Au or Ag nanostructures provide ideal substrates for SERS measurements. Surface plasmon resonance (SPR) (see Chapter 2 of this book for details about SPR measurements) is used in order to optimize the SERS substrates. The use of SERS and SPR concomitantly promises great enthusiasm.

10.6 Conclusion

SERS has entered a few years ago in a new era. Several companies are selling SERS sensors. This evolution has been made possible, thanks to the evolution of the nanostructuring techniques (lithography, etching, metal deposition, etc.). However, surface chemistry has been another key factor to the selling of SERS sensors. As it was shown in the second part of this chapter, surface chemistry is essential to conceive a specific SERS sensor.

Numerous companies provide SERS solutions. Most of them use gold or silver nanoparticles made by the routes developed for the semiconductor or the nanotechnology industry. Chemical-based colloids are also used alone or coupled to organic matrix. A very high enhancement factor is always described. The reproducibility is often presented as good, with a standard deviation around 10%. But, in all likelihood, a lack of standards conducts to an impossibility to compare the SERS products: sensitivity, selectivity, and reproducibility are only mentioned but not really quantified.

Moreover, as other optical methods, SERS is suitable for miniaturization. Concomitantly to the advances in photonics and nanotechnologies, SERS will certainly be available in the future as on field sensors for many applications.

Acknowledgment

The authors want to acknowledge the ANR REMANTAS project (ANR-11-ECOT-0010) for financial support.

References

1. Péron, O., Rinnert, E., Lehaitre, M., Crassous, P. and Compère, C. (2009). Detection of polycyclic aromatic hydrocarbon (PAH) compounds in artificial sea-water using surface-enhanced Raman scattering (SERS), *Talanta*, **79**, pp. 199–204.
2. Delhaye, C., Bruneel, J.-L., Talaga, D., Guirardel, M., Lecomte, S. and Servant, L. (2012). Tailoring surface-enhanced Raman scattering effect using microfluidics, *J. Phys. Chem. C*, **116**, pp. 5327–5332.
3. Haynes, C. L. and Van Duyne, R. P. (2001). Nanosphere lithography: a versatile nanofabrication tool for studies of size-dependent nanoparticle optics, *J. Phys. Chem. B*, **105**, pp. 5599–5611.
4. Guo, L. J. (2007). Nanoimprint lithography: methods and material requirements, *Adv. Mater.*, **19**, pp. 495–513.
5. Guerrini, L., Jurasekova, Z., Domingo, C., Pérez-Méndez, M., Leyton, P., Campos-Vallette, M., Garcia-Ramos, J. V. and Sanchez-Cortes, S. (2007). Importance of metal–adsorbate interactions for the surface-enhanced Raman scattering of molecules adsorbed on plasmonic nanoparticles, *Plasmonics*, **2**, pp. 147–156.
6. Péron, O., Rinnert, E., Colas, F., Lehaitre, M. and Compère, C. (2010). First steps of in situ surface-enhanced Raman scattering during shipboard experiments, *Appl. Spectrosc.*, **64**, pp. 1086–1093.
7. Xie, Y., Li, P., Zhang, J., Wang, H., Qian, H. and Yao, W. (2013). Comparative studies by IR, Raman, and surface-enhanced Raman spectroscopy of azodicarbonamide, biurea and semicarbazide hydrochloride, *Spectrochim. Acta A*, **114**, pp. 80–84.
8. Alvarez-Ros, M. C., Sanchez-Cortes, S., Francioso, O. and Garcia-Ramos, J. V. (2001). Catalytic modification of gallic acid on a silver surface studied by surface-enhanced Raman spectroscopy, *J. Raman Spectrosc.*, **32**, pp. 143–145.
9. Lin, X. M., Cui, Y., Xu, Y. H., Ren, B. and Tian, Z. Q. (2009). Surface-enhanced Raman spectroscopy: substrate-related issues, *Anal. Bioanal. Chem.*, **394**, pp. 1729–1745.

10. Sanchez-Cortes, S., Francioso, O., Garcia-Ramos, J. V., Ciavatta, C. and Gessa, C. (2001). Catechol polymerization in the presence of silver surface, *Colloids Surf. A*, **176**, pp. 177–184.
11. Sanchez-Cortes, S. and Garcia-Ramos, J. V. (2000). FT surface-enhanced Raman evidence of the oxidative condensation reactions of caffeic acid in solution and on silver surface, *Appl. Spectrosc.*, **54**, pp. 230–238.
12. Sanchez-Cortes, S. and Garcia-Ramos, J. V. (2000). Adsorption and chemical modification of phenols on a silver surface, *J. Colloid Interface Sci.*, **231**, pp. 98–106.
13. Alvarez-Puebla, R. A. and Liz-Marzan, L. M. (2012). Traps and cages for universal SERS detection, *Chem. Soc. Rev.*, **41**, pp. 43–51.
14. Águas, H., Silva, R. J. C., Viegas, M., Pereira, L., Fortunato, E. and Martins, R. (2008). Study of environmental degradation of silver surface, *Phys. Stat. Sol. c*, **5**, pp. 1215–1218.
15. Discher, D. E. and Eisenberg, A. (2002). Polymer vesicles, *Science*, **297**, pp. 967–973.
16. Schreiber, F. (2000). Structure and growth of self-assembling monolayers, *Prog. Surf. Sci.*, **65**, pp. 151–256.
17. Smith, R. K., Lewis, P. A. and Weiss, P. S. (2004). Patterning self-assembled monolayers, *Prog. Surf. Sci.*, **75**, pp. 1–68.
18. Shon, Y. S. and Choo, H. (2003). Organic reactions of monolayer-protected metal nanoparticles, *C. R. Chim.*, **6**, pp. 1009–1018.
19. Schreiber, F. (2000). Structure and growth of self-assembling monolayers, *Prog. Surf. Sci.*, **65**, pp. 151–257.
20. Carron, K., Peitersen, L. and Lewis, M. (1992). Octadecylthiol-modified surface-enhanced Raman-spectroscopy substrates: a new method for the detection of aromatic-compounds, *Environ. Sci. Technol.*, **26**, pp. 1950–1954.
21. Love, J. C., Estroff, L. A., Kriebel, J. K., Nuzzo, R. G. and Whitesides, G. M. (2005). Self-assembled monolayers of thiolates on metals as a form of nanotechnology, *Chem. Rev.*, **105**, pp. 1103–1170.
22. Costa, J. C. S., Sant'Ana, A. C., Corio, P. and Temperini, M. L. A. (2006). Chemical analysis of polycyclic aromatic hydrocarbons by surface-enhanced Raman spectroscopy, *Talanta*, **70**, pp. 1011–1016.
23. Jiang, X., Yang, M., Meng, Y., Jiang, W. and Zhan, J. (2013). Cysteamine-modified silver nanoparticle aggregates for quantitative SERS sensing of pentachlorophenol with a portable Raman spectrometer, *ACS Appl. Mater. Interfaces*, **5**, pp. 6902–6908.

24. Hierlemann, A., Weimar, U., Kraus, G., Schweizer-Berberich, M. and Göpel, W. (1995). Polymer-based sensor arrays and multicomponent analysis for the detection of hazardous organic vapours in the environment, *Sens. Actuators, B*, **26**, pp. 126–134.
25. Murphy, T., Schmidt, H. and Kronfeldt, H. D. (1999). Use of sol-gel techniques in the development of surface-enhanced Raman scattering (SERS) substrates suitable for in situ detection of chemicals in seawater, *Appl. Phys. B*, **69**, pp. 147–150.
26. Lucht, S., Murphy, T., Schmidt, H. and Kronfeldt, H. D. (2000). Optimized recipe for sol-gel-based SERS substrates, *J. Raman Spectrosc.*, **31**, pp. 1017–1022.
27. Peron, O., Rinnert, E., Toury, T., Lamy de la Chapelle, M. and Compere, C. (2011). Quantitative SERS sensors for environmental analysis of naphthalene, *Analyst*, **136**, pp. 1018–1022.
28. Li, J.-M., Ma, W.-F., Wei, C., You, L.-J., Guo, J., Hu, J. and Wang, C.-C. (2011). Detecting trace melamine in solution by SERS using Ag nanoparticle coated poly(styrene-co-acrylic acid) nanospheres as novel active substrates, *Langmuir*, **27**, pp. 14539–14544.
29. Cheong, W. J., Yang, S. H. and Ali, F. (2013). Molecular imprinted polymers for separation science: a review of reviews, *J. Sep. Sci.*, **36**, pp. 609–628.
30. Jung, B. M., Kim, M. S., Kim, W. J. and Chang, J. Y. (2010). Molecularly imprinted mesoporous silica particles showing a rapid kinetic binding, *Chem. Commun.*, **46**, pp. 3699–3701.
31. Kantarovich, K., Tsarfati, I., Gheber, L. A., Haupt, K. and Bar, I. (2009). Writing droplets of molecularly imprinted polymers by nano fountain pen and detecting their molecular interactions by surface-enhanced Raman scattering, *Anal. Chem.*, **81**, pp. 5686–5690.
32. Bompert, M., De Wilde, Y. and Haupt, K. (2010). Chemical nanosensors based on composite molecularly imprinted polymer particles and surface-enhanced Raman scattering, *Adv. Mater.*, **22**, pp. 2343–2348.
33. Xue, J.-Q., Li, D.-W., Qu, L.-L. and Long, Y.-T. (2013). Surface-imprinted core-shell Au nanoparticles for selective detection of bisphenol A based on surface-enhanced Raman scattering, *Anal. Chim. Acta*, **777**, pp. 57–62.
34. Holthoff, E. L., Stratis-Cullum, D. N. and Hankus, M. E. (2011). A nanosensor for TNT detection based on molecularly imprinted polymers and surface enhanced Raman scattering, *Sensors*, **11**, pp. 2700–2714.

35. Yang, L., Ma, L., Chen, G., Liu, J. and Tian, Z.-Q. (2010). Ultrasensitive SERS detection of TNT by imprinting molecular recognition using a new type of stable substrate, *Chem.-Eur. J.*, **16**, pp. 12683–12693.
36. Chang, L. M., Ding, Y. and Li, X. (2013). Surface molecular imprinting onto silver microspheres for surface enhanced Raman scattering applications, *Biosens. Bioelectron.*, **50**, pp. 106–110.
37. Singh, A. K., Khan, S. A., Fan, Z., Demeritte, T., Senapati, D., Kanchanapally, R. and Ray, P. C. (2012). Development of a long-range surface-enhanced Raman spectroscopy ruler, *J. Am. Chem. Soc.*, **134**, pp. 8662–8669.
38. Piletsky, S. A., Panasyuk, T. L., Piletskaya, E. V., Nicholls, I. A. and Ulbricht, M. (1999). Receptor and transport properties of imprinted polymer membranes—a review, *J. Membr. Sci.*, **157**, pp. 263–278.
39. Del Valle, E. M. M. (2004). Cyclodextrins and their uses: a review, *Process Biochem.*, **39**, pp. 1033–1046.
40. Ogoshi, T. and Harada, A. (2008). Chemical sensors based on cyclodextrin derivatives, *Sensors*, **8**, pp. 4961–4982.
41. Schmid, G. (1989). Cyclodextrin glycosyltransferase production—yield enhancement by overexpression of cloned genes, *Trends Biotechnol.*, **7**, pp. 244–248.
42. Boger, J., Corcoran, R. J. and Lehn, J.-M. (1978). Cyclodextrin chemistry. Selective modification of all primary hydroxyl groups of α - and β -cyclodextrins, *Helv. Chim. Acta*, **61**, pp. 2190–2218.
43. Khan, A. R., Forgo, P., Stine, K. J. and D'Souza, V. T. (1998). Methods for selective modifications of cyclodextrins, *Chem. Rev.*, **98**, pp. 1977–1996.
44. Weisser, M., Nelles, G., Wohlfart, P., Wenz, G. and Mittler-Neher, S. (1996). Immobilization kinetics of cyclodextrins at gold surfaces, *J. Phys. Chem.*, **100**, pp. 17893–17900.
45. Hill, W., Fallourd, V. and Klockow, D. (1999). Investigation of the adsorption of gaseous aromatic compounds at surfaces coated with heptakis(6-thio-6-deoxy)- β -cyclodextrin by surface-enhanced Raman scattering, *J. Phys. Chem. B*, **103**, pp. 4707–4713.
46. Xie, Y., Wang, X., Han, X., Song, W., Ruan, W., Liu, J., Zhao, B. and Ozaki, Y. (2011). Selective SERS detection of each polycyclic aromatic hydrocarbon (PAH) in a mixture of five kinds of PAHs, *J. Raman Spectrosc.*, **42**, pp. 945–950.
47. Xie, Y., Wang, X., Han, X., Xue, X., Ji, W., Qi, Z., Liu, J., Zhao, B. and Ozaki, Y. (2010). Sensing of polycyclic aromatic hydrocarbons with cyclodextrin inclusion complexes on silver nanoparticles by surface-enhanced Raman scattering, *Analyst*, **135**, pp. 1389–1394.

48. Xu, J. Y., Wang, J., Kong, L. T., Zheng, G. C., Guo, Z. and Liu, J. H. (2011). SERS detection of explosive agent by macrocyclic compound functionalized triangular gold nanoprisms, *J. Raman Spectrosc.*, **42**, pp. 1728–1735.
49. Wang, J., Kong, L. T., Guo, Z., Xu, J. Y. and Liu, J. H. (2010). Synthesis of novel decorated one-dimensional gold nanoparticle and its application in ultrasensitive detection of insecticide, *J. Mater. Chem.*, **20**, pp. 5271–5279.
50. Gutsche, C. D. (1984) *Structural chemistry*, Chapter 1 “The calixarenes” (Springer, Berlin, Heidelberg), pp. 1–47.
51. Deligöz, H., Karakuş, Ö. Ö. and Çilgi, G. K. (2012). A brief review on the thermal behaviors of calixarene-azocalixarene derivatives and their complexes, *J. Macromol. Sci., Part A: Pure Appl. Chem.*, **49**, pp. 259–274.
52. Leyton, P., Sanchez-Cortes, S., Garcia-Ramos, J. V., Domingo, C., Campos-Vallette, M., Saitz, C. and Clavijo, R. E. (2004). Selective molecular recognition of polycyclic aromatic hydrocarbons (PAHs) on calix[4]arene-functionalized Ag nanoparticles by surface-enhanced Raman scattering, *J. Phys. Chem. B*, **108**, pp. 17484–17490.
53. Leyton, P., Domingo, C., Sanchez-Cortes, S., Campos-Vallette, M. and Garcia-Ramos, J. V. (2005). Surface enhanced vibrational (IR and Raman) spectroscopy in the design of chemosensors based on ester functionalized p-tert-butylcalix[4]arene hosts, *Langmuir*, **21**, pp. 11814–11820.
54. Guerrini, L., Garcia-Ramos, J. V., Domingo, C. and Sanchez-Cortes, S. (2006). Functionalization of Ag nanoparticles with dithiocarbamate calix[4]arene as an effective supramolecular host for the surface-enhanced Raman scattering detection of polycyclic aromatic hydrocarbons, *Langmuir*, **22**, pp. 10924–10926.
55. Guerrini, L., Garcia-Ramos, J. V., Domingo, C. and Sanchez-Cortes, S. (2009). Sensing polycyclic aromatic hydrocarbons with dithiocarbamate-functionalized Ag nanoparticles by surface-enhanced Raman scattering, *Anal. Chem.*, **81**, pp. 953–960.
56. Kwon, Y. H., Sowoidnich, K., Schmidt, H. and Kronfeldt, H. D. (2012). Application of calixarene to high active surface-enhanced Raman scattering (SERS) substrates suitable for in situ detection of polycyclic aromatic hydrocarbons (PAHs) in seawater, *J. Raman Spectrosc.*, **43**, pp. 1003–1009.
57. Star, A., Han, T.-R., Gabriel, J.-C. P., Bradley, K. and Grüner, G. (2003). Interaction of aromatic compounds with carbon nanotubes: correlation

- to the Hammett parameter of the substituent and measured carbon nanotube FET response, *Nano Lett.*, **3**, pp. 1421–1423.
58. Leyton, P., Gómez-Jeria, J. S., Sanchez-Cortes, S., Domingo, C. and Campos-Vallette, M. (2006). Carbon nanotube bundles as molecular assemblies for the detection of polycyclic aromatic hydrocarbons: surface-enhanced resonance Raman spectroscopy and theoretical studies, *J. Phys. Chem. B*, **110**, pp. 6470–6474.
59. Sassolas, A., Blum, L. J. and Leca-Bouvier, B. D. (2011). Optical detection systems using immobilized aptamers, *Biosens. Bioelectron.*, **26**, pp. 3725–3736.
60. Osawa, Y., Takase, M., Sode, K. and Ikebukuro, K. (2009). DNA aptamers that bind to PQQGDH as an electrochemical labeling tool, *Electroanalysis*, **21**, pp. 1303–1308.
61. Subramanian, P., Lesniewski, A., Kaminska, I., Vlandas, A., Vasilescu, A., Niedziolka-Jonsson, J., Pichonat, E., Happy, H., Boukherroub, R. and Szunerits, S. (2013). Lysozyme detection on aptamer functionalized graphene-coated SPR interfaces, *Biosens. Bioelectron.*, **50**, pp. 239–243.
62. Galarreta, B. C., Tabatabaei, M., Guieu, V., Peyrin, E. and Lagugne-Labarthe, F. (2013). Microfluidic channel with embedded SERS 2D platform for the aptamer detection of ochratoxin A, *Anal. Bioanal. Chem.*, **405**, pp. 1613–1621.
63. Wen, G., Zhou, L., Li, T., Liang, A. and Jiang, Z. (2012). A sensitive surface-enhanced Raman scattering method for determination of melamine with aptamer-modified nanosilver probe, *Chin. J. Chem.*, **30**, pp. 869–874.

2.4 Conclusion

Raman based sensors function thanks to the scattered waves produced by molecules attached to the sensor surface. Since these scattered waves are too weak to accomplish detection in low concentrations, the incident field has to be enhanced by the process called SERS. In Chapter 2 the theoretical explanation of two main effects involved in SERS mechanism, electromagnetic and chemical, has been provided. While the chemical effect, related with charge transfer between surface and attached molecule, gives an enhancement of less than 10^2 , the electromagnetic one has been shown to be the main contributing effect to the signal amplification in SERS, providing enhancement factor up to 10^8 . Latter effect comes from the electromagnetic local field enhancement through the LSPR created by the interaction between light and metallic nanoparticle. In this regard, it was concluded that in order to develop good SERS based nanosensor, an essential attention has to be paid to the selection and the optimization of metallic NPs, and to ensure the targeted molecules presence as close as possible to the sensor surface.

In the second part of the chapter, we presented the most popular SERS substrates fabrication methodologies and overviewed the surface functionalisation strategies used for pre-concentration and sensing of chemical molecules.

In the following chapters of this manuscript we will demonstrate the results obtained by exploiting different approaches of surface functionalisation in order to pre-concentrate and detect aromatic hydrocarbons. As a SERS active substrate for these studies we chose gold nanocylinder (GNCs) arrays fabricated by electron beam nanolithography (EBL) which give a good sensitivity, extremely reliable reproducibility and freedom towards SERS substrate customization. In addition, for some studies we also applied colloidal NPs or NPs based solid SERS substrates.

The instrumental SERS set-up as well as indications on measuring conditions used for investigations related to a SERS based nanosensor design and further targeted pollutants detection are summarized in ANNEX 1.

3 Functionalisation of the nanosensor with anti-bodies for benzo[a]pyrene detection

3.1 Introduction

The detection of the targeted pollutants in the environmental waters is a challenging task due to the great variety of compounds that are present. For this purpose, the designed sensors have to permit certain selectivity towards the targeted molecules. As it was already described in the Chapter 1, the best candidate in selective molecular detection is biosensor. Anti-body against benzo[a]pyrene (BaP) is developed and commercially available, but SERS based study of its application is not provided in the literature. For this reason, in this chapter, we will focus on the approaches related with the immobilisation of anti-bodies at the sensor surface.

The sensitivity and stability of biosensors depend directly on the number of immobilised biomolecules, on their preserved activity and on their controlled orientation. In this regard, two strategies of functionalisation will be exploited: (i) random antibody immobilization by carbodiimide coupling reaction and (ii) random physical adsorption of synthesized fragments of antigen binding ($F(ab')_2$). The performance of developed biosensors will be tested by sensing BaP in 500 ppb concentration.

3.2 Anti-body immobilisation on the sensor surface

3.2.1 Introduction

The immobilisation of biomolecules on the nanostructured metallic surface paves the way to the selective molecular detection by SERS. Such strategy is all the most relevant since antibodies against BaP are commercially available.

As mentioned before in Chapter 1 the characteristics of a good sensing tool is the sensitivity, the stability and the robustness. However, the design of a biosensor based on these characteristics can only be achieved by a great control of the surface chemistry. Indeed, the performance of the biosensor would be essentially dependant on the amount of grafted anti-bodies on the surface and the preservation of their conformation, leading to no loss of their initial activity. Thus, the surface chemistry for biosensor design has to be seriously considered.

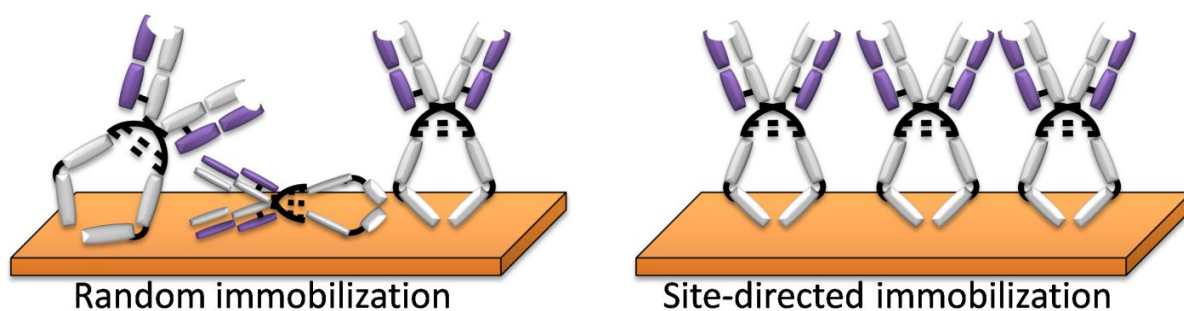


Figure 3.1 Schematic illustration of random and site-directed anti-bodies immobilization approaches.

Generally, two main strategies, random and site-directed immobilization, can be used for anti-bodies based biosensors [1]. Site-directed grafting approach is preferred, since the anti-bodies are asymmetric molecules and their orientation after immobilization is very important. The most often used method in order to control anti-bodies orientation on the surface is the application of proteins A and G, due to their specific interaction to the Fc region of the anti-body [2]. The performance of this kind of biosensors has been widely tested. For instance, concerning the detection of pollutants, protein G has been exploited by Boujday *et al.*, in order to immobilize anti-body against benzo[a]pyrene (anti-BAP13) [3]. Direct detection of BaP was then performed using mid-IR transduction. The detection limit reached by this system was 5 μM . Despite the convenience of the latter functionalisation method it can be seen as a major drawback for SERS applications the thickness of the coating layer (Protein G with the molecular mass of 22 kDa has a radius of around 3.5 nm [4]). Thus, for SERS biosensor, the random anti-bodies immobilisation could be more advantageous. With such strategy, we have a higher probability that some antigen binding sites will be close to the sensor surface, enabling then the analytes detection by SERS.

Two methods for random anti-bodies immobilisation can be used: the physical adsorption and the grafting through the carbodiimide coupling approach. While physical adsorption method leads to biomolecule denaturation and loss in stability [5] [6], carbodiimide coupling chemistry was shown to be a rather simple method ensuring biosensor robustness. It is based on the formation of covalent bonds between the biomolecules and a surface coating such as SAMs, dextran or polymers [7] [8].

As a consequence, during this study, the latter antibodies immobilisation approach was exploited in order to design a SERS biosensor. First, the surface functionalisation and further biomolecular grafting was tested using antibodies for bovine serum albumine (BSA) and for ribonuclease A (RNase-A) as cheaper equivalent to anti-BAP13. The performances of the biosensors were examined for the BSA and RNase-A proteins detections, respectively. The developed surface functionalisation protocol was then applied for anti-BAP13 immobilization and SERS based BaP sensing.

3.2.2 Experimental

3.2.2.1 Materials and reagents

4-carboxybenzene diazoniumtetrafluoroborate (DS-COOH) was chemically synthesized (method described in chapter 5), mercaptoundecanoic acid (MUA) (95%), 6-Mercapto-1-hexanol (MOH) (97%), 1-ethyl-3-(3-dimethylamino-propyl)carbodiimide hydrochloride (EDC), N-hydroxysuccinimide (NHS), Ribonuclease A (RNase-A) from bovine pancreas (salt-free, lyophilized powder), Bovine Serum Albumin (BSA) (lyophilized powder, $\geq 96\%$), anti-BSA (fractionated antiserum, lyophilized powder) and benzo[a]pyrene ($\geq 96\%$ HPLC), were purchased from Sigma Aldrich. Phosphate buffer saline (PBS), 10 \times solution. pH=7.4 \pm 0.1 was provided by Fischer BioReagent. Ethanol (96%, technisolv) was purchased from VWR; Methanol (100%, Reg.Ph.Eur) from Prolabo. Anti-benzo[a]pyrene (monoclonal antibody purified, clone B[a]P 13) was provided by Abcam. Monoclonal Anti-RNase-A was provided by Thermo scientific.

MilliQ water (18 M Ω , Millipore, France) was used for the preparation of the solutions and for all rinses.

3.2.2.2 Substrates

For SPR measurements plane gold sensor chips (GE healthcare) were used. These substrates were used as received for the experiments.

For SERS experiments gold nanocylinders (GNCs) with variable diameters from 50nm up to 200 nm were fabricated by electron beam lithography (EBL). In both cases GNCs were designed on glass substrate, and the gap between individual GNCs is fixed to 200 nm in both directions.

3.2.2.3 Antibodies immobilisation on flat gold surfaces

Prior experiments on GNCs based SERS substrates protocol on biomolecular immobilization was tested on plane gold surface using SPR system. Herein, the gold chip was first incubated in ethanolic solution of mercaptoundecanoic acid (MUA, $100 \times 10^{-3} \text{ mol L}^{-1}$) for 12 hours. After SAM formation substrate was rinsed with ethanol three times and dried. Sample was then placed in SPR system and following procedures were performed by measuring kinetics in real time.

The coupling of the antibodies with such surface was based on the reaction between COOH carried functions and 1-ethyl-3-(3-dimethylaminopropyl) carbodiimide hydrochloride (EDC). The addition of N-hydroxysuccinimide (NHS) was used to obtain a semi-stable ester that could react with the amine function of the antibody to obtain a stable amide. For this purpose, carboxyl groups presented on sensor surface were activated by EDC/NHS. Solution was prepared by mixing 76.68 mg of EDC

($400 \times 10^{-3} \text{ mol L}^{-1}$) with 11.5 mg of NHS ($100 \times 10^{-3} \text{ mol L}^{-1}$) in ethanol (10 mL) and circulated in SPR system for 60 min. After activation step, anti-BSA solution ($10^{-6} \text{ mol L}^{-1}$) in PBS was injected 5 times for 20 min each followed by rinsing with PBS buffer. After antibody immobilization step remaining active succinimide groups were blocked with ethanolamine (1 mol L^{-1}). In order to test prepared sensor capability in analyte sensing, BSA solution in PBS buffer was then injected at different concentrations.

3.2.2.4 Antibodies immobilisation on GNCs

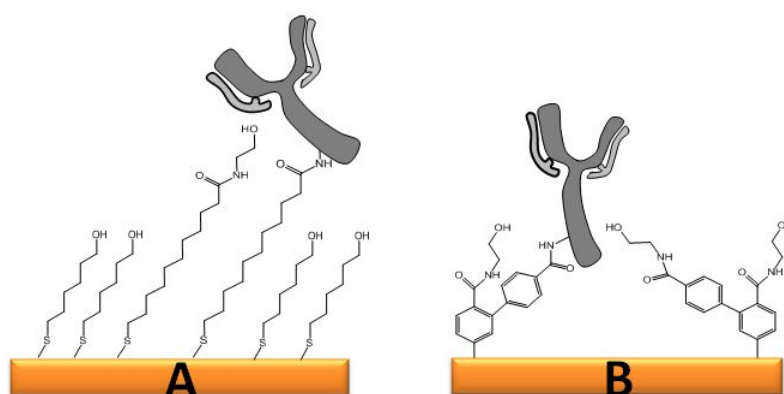


Figure 3.2 General illustration of anti-bodies immobilised on MUA/MOH SAMs (substrate A) and DS-COOH layers (substrate B).

Before any experiment GNCs were cleaned using UV-Ozone cleaner. This procedure was performed during 20 min, followed by two times substrates rinsing in ethanol and water. The washing procedure was controlled by extinction and SERS measurements. Two main surface functionalisation approaches has been developed as illustrated in Figure 3.2.

For sample A, the substrate was first covered by self assembled monolayer (SAM) containing mercaptoundecanoic acide (MUA) and mercaptohexanol (MOH). Solution was prepared by mixing 5.45 mg of MUA ($2.5 \times 10^{-3} \text{ mol L}^{-1}$) and 10.22 μL of MOH ($7.5 \times 10^{-3} \text{ mol L}^{-1}$) in 10 mL of ethanol. SERS substrates were then incubated in this solution for 12 hours in order to create a mix SAM layer. Physically adsorbed overlayers were removed by washing substrate 3 times in ethanol.

In the case of sample B, GNCs were immersed in 10 mL of the DS-COOH ($10^{-3} \text{ mol L}^{-1}$) in H_2SO_4 (0.1 mol L^{-1}) solution during 15 hours at $+4^\circ\text{C}$. Substrates were then rinsed 3 times by immersion into milliQ water 10mL over 10 minutes and mildly dried by using nitrogen flux. The description of DS-COOH chemical synthesis can be found in chapter 5.

Carboxyl groups presented on GNCs functionalised by MUA/MOH or DS-COOH (sample A and sample B respectively) were activated by EDC/NHS as previously described. After activation step, substrates were incubated in a solution of $70 \mu\text{g} \cdot \text{mL}^{-1}$ of anti-Rnase in PBS buffer for 90 min at 4°C .

Removed samples were rinsed several times by PBS. Remaining active succinimide groups were blocked with ethanolamine by incubating substrates in 1 mol.L⁻¹ ethanolamine solution for 20 min. Prepared SERS active substrates were then tested for biomolecular sensing by immersing them in a solution of RNase (10⁻³ mol L⁻¹) in PBS buffer. Incubation time was set to 90 min at 4°C. Each step of surface functionalisation was monitored by extinction spectroscopy and SERS.

3.2.2.5 Optical measurements

SPR response of anti-BSA immobilization on plane gold surface and further BSA detection was monitored using a BIAcore 1990 GE Healthcare system (Pewaukee, WI, USA). SERS substrates were investigated with an Xplora ONE micro-spectrometer (HORIBA Scientific). For extinction measurements transmitted white light was collected with a x20 objective (N.A.=0.4). Measured spectral range was from 450 nm to 900 nm with spectral resolution of 0.5 nm. For SERS measurements laser excitation wavelengths of 660 nm were used with applied power of 0.32 mW. The signal was collected using a x100 objective (N.A. = 0.9) when measurements were proceeded in air conditions and a x60 objective (N.A. = 0.7) when it was measured in liquid. Achieved spectral resolution was less than 3 cm⁻¹. Acquisition time for each measure was set to 60s with two repetitions (will be indicated in the text if differ).

3.2.3 Results and discussion

3.2.3.1 Antibodies immobilization on gold surfaces

Carbodiimide coupling procedure via reactive esters created by EDC/NHS mechanism is already well studied and documented [9]. However, the antibodies immobilization was first tested on plane gold surface using SPR system. Figure 3.3 shows the achieved results on the anti-BSA immobilization (sensogram in graph A) and the related BSA detection (graph B).

After carboxyl groups activation by circulating EDC/NHS mixture the anti-BSA solution was injected 5 times that leads to the surface saturation after 100 minutes. Immobilization of the antibodies on the surface gave an increase of the SPR response of about 1000 RU. In the following step ethanolamine was circulated in the system for 10 min to block any remaining succinimide ester groups.

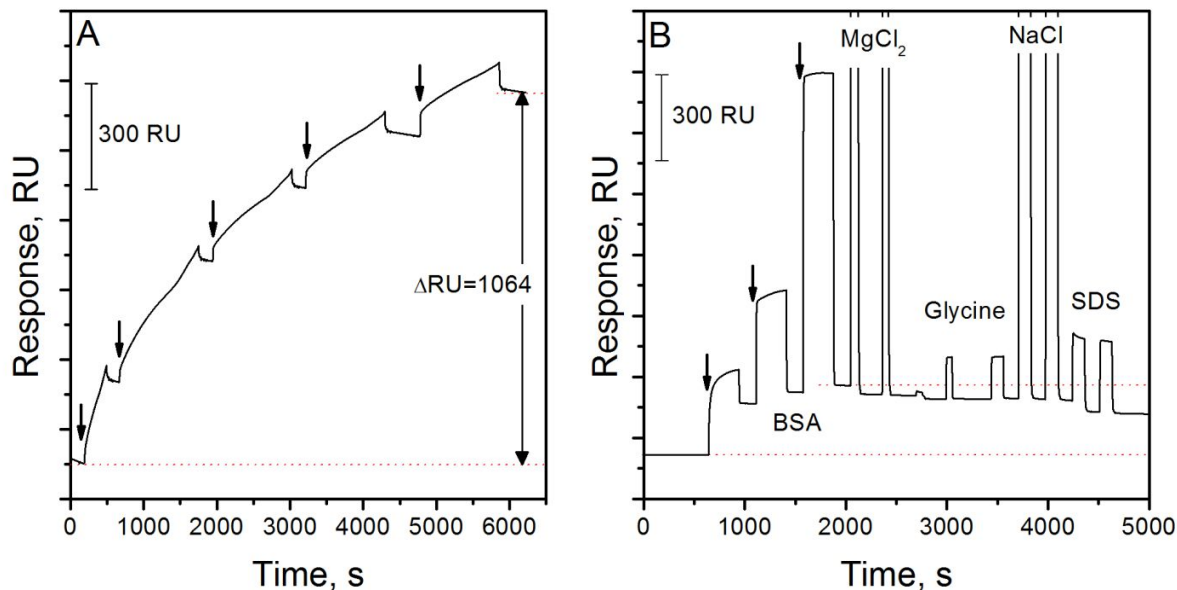


Figure 3.3 SPR sensorgram, presenting kinetics of the anti-BSA immobilization (A) and the BSA detection (B) followed by several washing steps. Arrows indicates the injections of 1 μM concentration anti-BSA solution (A) and the injections of BSA solutions at 111 μM, 333 μM and 1 mM concentrations.

In order to test the biosensor performance, BSA solutions at three different concentrations (111 μM, 333 μM and 1 mM) in PBS buffer were injected in the system. The sensorgram in figure 3.3B exhibits an increase of the SPR response induced by the interaction between the anti-BSA and the BSA. 74 % of saturation was registered after injecting the lowest BSA concentration. Total increase in response at the end of kinetics was 227 RU. Further steps seen in sensorgram B correspond to several surface washing procedures in order to remove non-specifically adsorbed BSA molecules. First, nanosensor was rinsed with MgCl₂ solution of 4 M 2 times for 1 min each. After this step a decrease in response of around 30 RU was registered. The use of glycine solution of 10 mM and NaCl solution of 5 M again washed surface but not as significantly (the decrease of 10 and 5 RU was measured after glycine and NaCl injection, respectively). The most important decrease in the intensity of almost 45 RU was observed after injecting SDS 1% solution. In the end of washing procedure, the remaining BSA signal was 135 RU and could then be assigned to specifically bonded molecules.

The results obtained by experiments performed in BIAcore systems confirmed the success in antibody immobilization and encouraged to apply this protocol for the SERS nanosensors.

3.2.3.2 Antibodies immobilisation on GNCs

Herein, the developed protocol of an antibody immobilization was applied on nanostructured surfaces for the detection of RNase by LSPR and SERS. Nanocylinders were cleaned by UV-ozone and ethanol prior experiments and surface functionalisation steps were then performed as previously

described (experimental section). However, few improvements were considered. Regarding the literature, the immobilization of proteins onto carboxylate-terminated SAMs utilizing EDC and NHS are much more efficient when the SAM layer is created by mixing two different length thiols [10]. The improved reactivity of this system is due to the disorder achieved by co-adsorption of the mixed thiols. The carboxylic groups are then more accessible for the activation and as a consequence for the biomolecular immobilisation.

Thus, in this study two approaches of surface coatings were tested. First approach was related with the application of a mixed SAM (Sample A in Figure 3.4). In this case the SERS substrate was incubated in the ethanolic solution of MUA/MOH (1:3 molar ratio) for 12 hours. The second approach was related with the employment of diazonium salts bearing a carboxylic group (DS-COOH) (Sample B in Figure 3.4). The surface functionalisation based on diazonium salts approach is more detailed in chapter 5. The application of diazonium salt for this study is suitable since it forms non-homogeneous thickness surface coating. In order to obtain DS-COOH surface functionalisation, SERS substrate was incubated in the solution for 12 hour at +4°C.

The carboxylic groups activation (EDC/NHS protocol) and antibodies immobilisation were then proceeded on both substrates similarly. All steps of surface modification and final analyte detection were monitored by extinction spectroscopy and SERS.

Figure 3.4A and 3.4B present the LSPR position shifts achieved after each step of functionalisation with regards to the LSPR position of non-functionalised GNCs. Comparing the two figures, it can be noticed that initial surface coverage by mixed SAM and the formation of NHS esters led to a positive LSPR shift of 8 nm whereas, the same procedure repeated using DS-COOH induced negative LSPR shift of -5 nm. This first result could be related with imperfect surface cleaning prior to experiment. It is worth noting that the presence of carbonaceous contamination on common SERS surfaces has been shown as a great limitation to the analytical utility of SERS [11]. UV-Ozone cleaning procedure is an efficient tool helping to remove large part of this carbonaceous contamination. However, in this case strong reactivity of DS-COOH toward the gold surface acted as additional surface cleaning procedure. Such a cleaning behavior has already been observed by using SAMs [12] [13] [11].

Measured extinction spectra after anti-Rnase immobilization step revealed LSPR position shift towards higher wavelength of 8 nm for both systems. Noteworthy, comparable LSPR red-shift was observed by others [14]. However, after the non-reacted NHS esters blocking procedure by ethanolamine, blue-shifts of 1 nm and 4 nm were recorded for mixed SAM and DS-COOH substrates, respectively. Generally, this shift might be explained by removal of physically adsorbed anti-RNase

antibodies, which would lead to the conclusion that there was less anti-Rnase covalently immobilized onto DS-COOH coating.

At the last stage the biosensors were applied for the detection of Rnase at high concentration (10^{-3} mol.L⁻¹) in order to confirm the performance of the systems. After an incubation of 30 min in RNase solution and washing in PBS, the LSPR were red-shifted of 19 nm and 7 nm for mixed SAM and DS-COOH substrates, respectively. Such a great shift suggests that RNase protein was not only successfully captured by immobilized antibody but also aggregated on the surface by non-specific interactions.

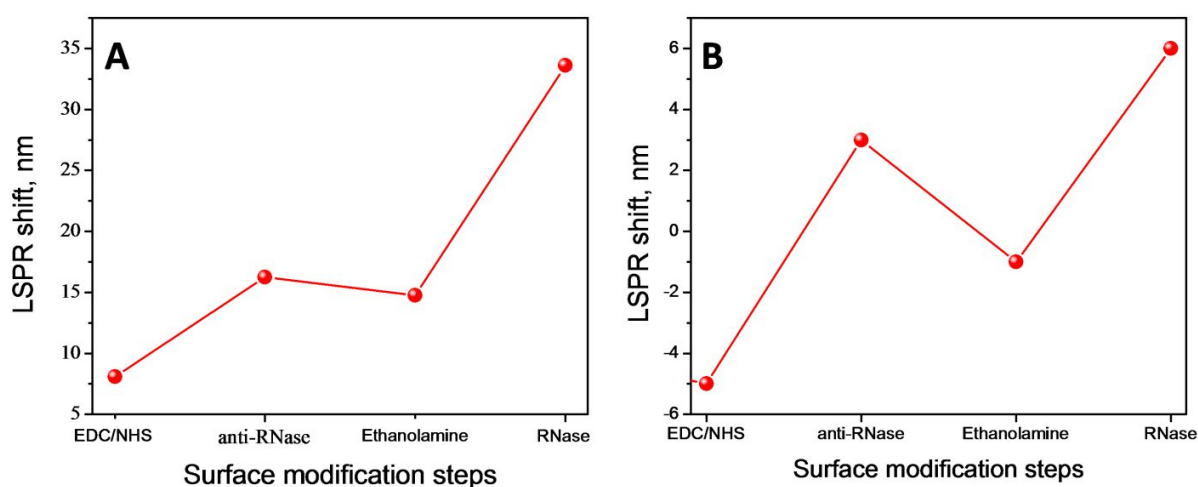


Figure 3.4 LSPR shift obtained during anti-Rnase immobilization and Rnase detection procedures on MUA/MOH substrate (A) and DS-COOH substrate (B). LSPR shifts are compared starting from carboxylic groups activation step.

Complementary, SERS measurements were conducted for each step of the functionalisation procedure and after the antigen/antibody-interaction. Figure 3.5A and 3.5B present the SERS spectra recorded after each step for the mixed SAMs and DS-COOH functionalised GNCs, respectively. The SERS spectra were obtained using 660 nm laser wavelength with a power of 320 μ W. For this laser wavelength, the 160 nm diameter GNCs were used to ensure maximal enhancement. Accumulation time for one spectrum was 30 seconds and the spectra were averaged from three measurements.

In the first step of surface functionalisation using mixed SAMs SERS spectrum revealed two strong bands at the range of 1400-1600 cm^{-1} (Figure 3.5A black spectra) that can be assigned to C-H in-plane bending and O-C-O stretching modes [15]. SERS signature of mixed SAM was changed after surface modification steps due to formation of succinimide ester. New bands were observed after antibody grafting at 829 cm^{-1} , 1002 cm^{-1} , 1149 cm^{-1} , 1265 cm^{-1} , 1415 cm^{-1} , 1515 cm^{-1} (Figure 3.5 A green spectrum). These bands in much lower intensity were still presented in spectrum after blocking

step using ethanolamine. Thus, results obtained by SERS confirmed the removal of non-specifically adsorbed antibodies by ethanolamine.

On the other substrate, functionalised by DS-COOH (Figure 3.5 B black spectrum) two strong contributions at 1073 cm^{-1} and 1582 cm^{-1} were registered and assigned to C-H in plane bending for para- and monosubstituted benzenes [16;17] combined with C-N stretching [18] and C=C stretching [19], respectively. These vibrations were constantly observed in SERS spectra obtained after each surface modification step, providing proofs of the primer functionalisation stability.

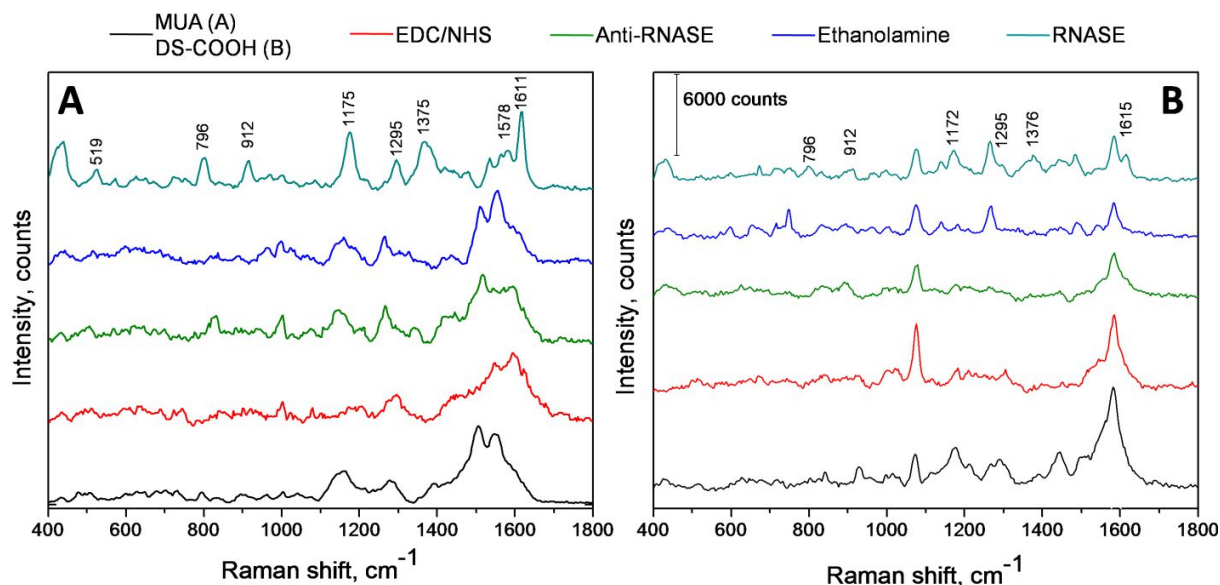


Figure 3.5 SERS spectra for each step of surface modification for (A) the mixed SAMs and graph for (B) the DS-COOH functionalised GNCs surface. Spectra are baseline-corrected and scaled for better observation.

As mentioned before, describing the results obtained by the extinction spectroscopy EDC/NHS procedure is showing ability in the removal of non-grafted over-layers. Thus, in the SERS spectrum three broad peaks at 1178 , 1289 and 1445 cm^{-1} were removed during this step (Figure 3.5 B red spectrum). Surprisingly, no new peaks were found in the SERS spectrum obtained after the anti-Rnase coupling with the DS-COOH despite that the redshift of the LSPR confirms its grafting.

The last spectra in the Figure 3.5 (light blue in both figures) represent the detection of RNase. The positions of the new features observed in both SERS spectra are very comparable (summarized in table 1) to the ones already observed for the SERS detection of Rnase by C. David *et al.*, [20]. This is a clear proof of the detection of the Rnase with both functionalised surfaces. First of all, it is important to note that in both systems SERS spectra lack in the amide I band which is normally observed at 1672 cm^{-1} for Rnase [20]. Even if all the Raman modes of the proteins can be strongly enhanced in SERS, not all these modes are observable in SERS, due to the fast decay length of the enhanced field [21]. Furthermore, the SERS signal of proteins are also dominated by the bands

related with the aromatic side chain vibrations of amino acids such as tyrosine (Tyr), tryptophan (Trp) and phenylalanine (Phe). Such bands assigned to amino acids were observed at 796 cm^{-1} , around 1175 cm^{-1} , 1578 cm^{-1} (for the mix SAM based substrate) and around 1615 cm^{-1} (for DS-COOH functionalised substrate).

Table 1. Summary of important peaks observed in SERS spectra of Rnase-A for both nanosensors.

Mixed SAM based GNCs	DS-COOH based GNCs	Assignment [20] [22]
519		S-S st
796	796	Tyr
912	912	C-C st
1175	1172	Phe, Tyr
1295	1295	Amide III
1375	1376	C-H
1578		Trp
1611	1615	Trp, Phe, Tyr (ring st)

In the literature it has been shown that the vibrational modes of the aromatic amino acids are sensitive to the microenvironment upon protein folding/unfolding process [23] [24] [25] [20]. Thus, the presence in the SERS spectrum of strongly enhanced bands related to aromatic amino acids vibrations can indicate the induced conformational change in the structure of RNase.

3.2.3.3 Anti-BAP13 immobilization on GNCs

Developed protocol of anti-body immobilization via amine coupling approach was then tested with the anti-BAP13 for both SAM and DS-COOH functionalisation layer. Unfortunately, in these cases we did not reach success. Similarly to the results obtained with anti-RNase-A, after anti-body graphing procedure, no spectral changes corresponding to the anti-body were observed. Moreover, BaP detection was not reached even after one night incubation time in 500 ppb concentration pollutant solution.

3.2.4 Conclusion

With this study we were intended to demonstrate the feasibility of the grafting an anti-body at the sensor surface for selective detection of an analyte. However, results, achieved during investigation of anti-RNase and RNase as a model system, were contradictory. First conducted extinction measurements confirmed that little amount of anti-bodies has been grafted to the GNCs surface, but SERS spectra of anti-bodies were not obtained. On the other hand, after substrates incubation in 1mM Rnase-A solutions, the molecular detection was evidenced by SERS. We have registered signature of Rnase-A on both tested nanosensors. Moreover, by comparing obtained SERS spectra of detected

protein with the ones provided in literature we found that Rnase-A overcomes the structural conformation changes induced by its adsorption onto nanosensor surface.

All obtained results can not be easily explained due to the lack of literature. However, there is high possibility that monitoring anti-bodies immobilized onto the GNCs is prohibited due to its great size and thus, the detected Rnase-A molecules were not pre-concentrated by affinity interaction with its anti-body. These results suggest that signals were recorded on Rnase-A physically adsorbed to the surface coatings with mixed SAMs or DS-COOH.

Assuming that the proposed hypothesis is correct, the evidenced failure of the BaP detection can be explained by a non-adsorption of the BaP due to the hydrophilic nature of the coating layers.

3.3 Strategies of design of F(ab')₂ based nanosensors for benzo[a]pyrene detection

3.3.1 Introduction

Ultrasensitive molecular sensing by SERS can be achieved when the molecule is close to the nanoparticle surface, since the sensitivity decreases exponentially with increasing distance. Molecules located in approximately 10 nm distance are no more detectable. Thus the SERS nanobiosensor based on immobilized anti-bodies, as demonstrated in previous section, is not particularly meaningful, due to the great size of the anti-bodies.

It is worth to remind, that anti-bodies are a class of large proteins having around 150 kDa molar mass. They are composed of two identical heavy chains (about 50 kDa) and two identical light chains (25 kDa) [26]. Each anti-body molecule has two independent antigen binding sites that can bind a single antigen molecule (Figure 3.6). The overall size of antibody can be reduced through enzymatic degradation procedure resulting in one Fc fragment and one F(ab')₂ fragment with two antigen binding sites connected by disulfide bonds (Figure 3.6).

In this study we will exploit these disulfide bridges located in the hinge region which maintains the structure of the antibody. The literature demonstrates that these bridges can be reduced and half-antibody molecules can be immobilized onto the gold surface via free sulfhydryl groups [27].

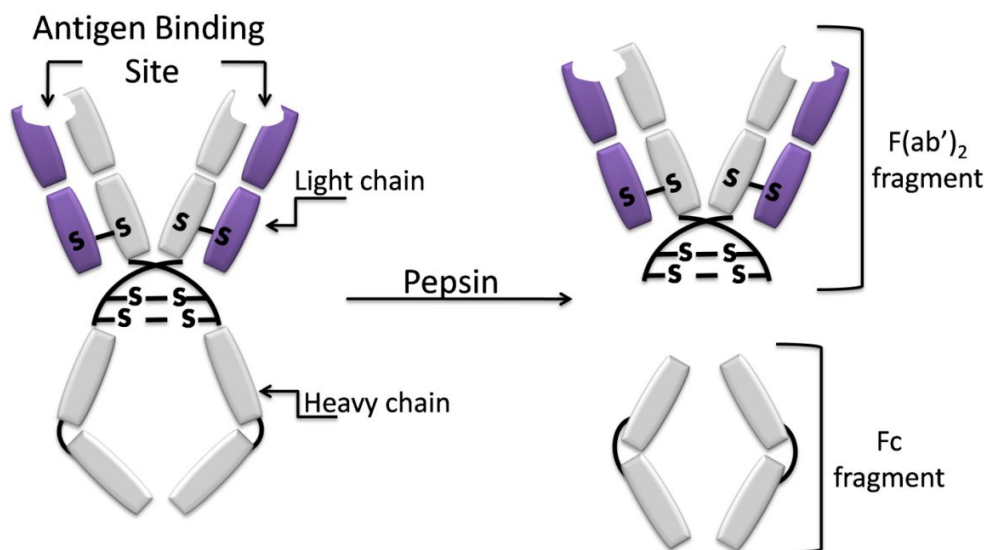


Figure 3.6 Schematic representation of antibody molecule (left), indicating heavy and light chains as well as antigen binding sites) and of the $F(ab)_2$ fragment (right) achieved after enzymatic digestion reaction.

In order to prepare $F(ab')_2$ fragments we tested the most widely used method, related with the digestion of anti-body by pepsin [28] [29]. Pepsin is an acidic endopeptidase that performs the degradation of proteins into small peptides. Its activity is highly dependent on the pH (it is mostly active at pH 1-2 and it is irreversibly denatured above pH 6). The digestion procedure using pepsin is variable for individual antibody, consequently many differing protocols are reported in the literature [30].

Herein, we exploited one of the procedures proposed for anti-body digestion by pepsin. As a first test, we used the obtained $F(ab')_2$ fragments without reducing their disulfide bridges. The surface functionalisation with $F(ab')_2$ was tested on GNCs produced by EBL and substrates with attached GNPs. Finally, sensors were tested for the detection of BaP.

3.3.2 Materials and methods

Sodium tricitrate, gold(III)chloride trihydrate ($\text{HAuCl}_4 \cdot \text{H}_2\text{O}$; $\geq 99.9\%$), (3-aminopropyl)triethoxysilane (APTES; 99%), sulfuric acid, (96%), hydrogen peroxide, 30%, benzo[a]pyrene (96%), acetic acid (ACS reagent, $\geq 99.7\%$), ethanol and methanol were purchased from Sigma Aldrich. Mouse monoclonal [BAP-13] was provided by Abcam. MilliQ water (18 M Ω , Millipore, France) was used for the preparation of the solutions.

3.3.2.1 SERS Substrates

Gold nanocylinders (GNCs) substrates produced by Electron-Beam Lithography (EBL) were provided by University of technology of Troyes. Details of the EBL procedure are described by Grand et al. [31]. This technique ensures the fabrication of nanostructures with the expected shape, size and arrangement. The substrates contain several patterns ($50\mu\text{m} \times 50\mu\text{m}$) of 2D arrays of GNCs with variable diameters (from 100nm in diameter up to 200 nm). The height of GNCs was set to 60 nm and the gap between 2 GNCs was kept constant to 200 nm (from edge to edge) in both directions. The SERS substrates were cleaned prior any experiment using UV-Ozone cleaner (PSD Standard instrument, Novascan) for 20 min.

3.3.2.2 Gold Nanoparticles synthesis

The colloidal spherical gold nanoparticles (GNPs) for this study were prepared following a method introduced by Turkevich *et. al.* [32]. A volume of 30 mL of a chlorauric acid (HAuCl_4) solution at the concentration of 0.3 mM was refluxed. When solution reached a boiling point sodium citrate solution (0.3 mL of 1%) was added. The reduction of the gold ions by the citrate ions was complete within 1 min while the solution was left further to boil for 10 min and was then cooled to room temperature. The result of later synthesis protocol is spherical GNPs with an average diameter of about 40 nm.

3.3.2.3 GNPs SERS substrate production

First, borosilicate glass substrates were carefully washed in ethanol in an ultrasonic bath for 20 min. Substrates were, then, immersed in piranha solution ($\text{H}_2\text{SO}_4:\text{H}_2\text{O}_2=3:1$) at room temperature for 30 min in order to remove organic contamination and to create Si-OH groups. After the incubation chips were extensively washed in milli Q water and dried under nitrogen gas. To further improve the quality of the glass slides UV ozone treatment for 30 min. was subsequently applied. Prepared substrates were then immersed in the ethanolic solution of the amine-terminated silane (APTES) with 0.5 mM concentration. After incubation time of 1 hour the substrates were extensively washed twice by sonification in ethanol for 10 min, dried under nitrogen flow and placed onto heating at $120\text{ }^\circ\text{C}$ for 1 hour. After silanized substrates were immersed in freshly prepared citrate-stabilized GNPs solution for 1 hour. Substrates were then washed twice in water and dried under nitrogen.

3.3.2.4 Enzymatic digestion of anti-BAP and protocol for surface functionalisation

The protocol of enzymatic digestion of anti-bodies was adapted from the literature [33]. However, brief description of the used procedure is given. In the first stage 1 mg of pepsin was dissolved in 1 ml of acetic buffer (pH=4.5) containing 0.7 M of sodium acetate and 1.5 M of acetic acid. 50 μL of prepared pepsin solution was introduced into 100 μL of as received anti-BAP13 solution. Mixture

was placed in thermostat an oven pre-heated at 38 °C and left to incubate for 4 hours. In order to stop the digestion reaction the pH of the reaction mixture was adjusted to 7.4 by adding 50 μL 3 M Tris buffer. In order to purify the produced F(ab')_2 fragments thiophilic adsorption kit (Thermo Fisher Scientific) was used. During elution step, absorbance of each fraction has been monitored, following the band at 280 nm (Figure 3.7) in order to select the fractions containing purified F(ab')_2 fragments. Collected fractions were then stored at -20°C till its usage.

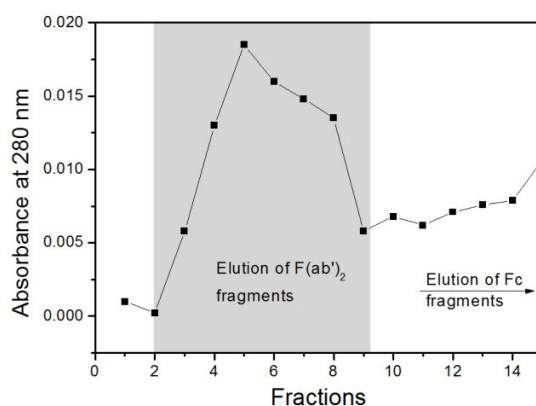


Figure 3.7 Absorbance intensity of the band at 280 nm obtained for each fraction during elution step.

In order to functionalise the surface a drop of 100 μL solution containing F(ab')_2 fragments was deposited on both substrates (GNCs and GNPs). After 12 hour incubation at $+4^\circ\text{C}$ substrates were washed with acetic buffer and then water.

3.3.2.5 Characterization

GNPs were characterized by extinction spectroscopy with a Kontron Uvikon 941 spectrophotometer (spectral range of 400 to 800 nm with 1 nm spectral resolution). Surface functionalisation was monitored by extinction spectroscopy and SERS using Xplora ONE micro-spectrometer (HORIBA Scientific). For extinction measurements transmitted white light was collected by a x20 objective (N.A.=0.4). Measured spectral range was from 450 nm to 900 nm with resolution of 0.5 nm. For SERS measurements laser excitation wavelength of 660 nm was used, applied power was around 0.2 mW. The signal was collected with x60 (with collar slide) objective (N.A.=0.75). Achieved spectral resolution was less than 3 cm^{-1} . Measurements were performed in liquid to avoid the biomolecules denaturation. Acquisition time for each measurement was set to 60s with two repetitions.

3.3.3 Results and discussion

The antibodies digestion and F(ab')_2 fragments purification procedures were performed adopting the protocols proposed in literature. Worth to note, that it has been demonstrated that pepsin based

antibodies digestion results in $F(ab')_2$ fragments of 118 kDa where the heavy chains of initially 50 kDa are reduced into 28 kDa fragments, and the light chains of 31 kDa are remaining intact [34] [35].

3.3.3.1 GNCs functionalisation by $F(ab')_2$ fragments

Prepared $F(ab')_2$ fragments were used for direct surface functionalisation of the GNCs. It is worth to note, that no free surface blocking procedure was performed because BaP has low affinity to gold surface [36]. After surface functionalisation, the LSPR was redshifted of 4 nm. One can notice that it is nearly the half of the LSPR shift observed for the whole anti-body. This confirms the effective cut the anti-body in Fab and that the coverage rate should be similar to the one reached with the anti-body. Moreover, SERS measurements showed spectral signature that can be assigned to proteins. On the Figure 3.8 SERS spectra obtained on 140 nm and 160 nm GNCs are presented as red and black spectrum, respectively. These are the averaged spectra of 8 individual measurements on the GNCs arrays. The spectral range ($200\text{-}1600\text{ cm}^{-1}$) is known to be the most relevant for the vibrational modes of the proteins and gives important information on their structure.

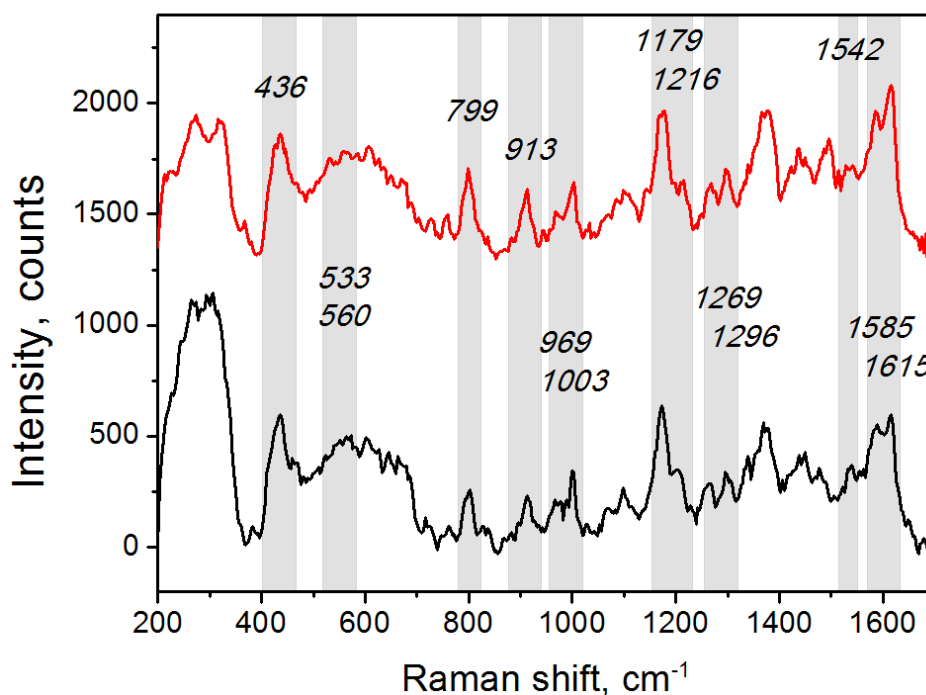


Figure 3.8 Averaged SERS spectra obtained on 140 nm GNCs (red spectrum) and on 160 nm GNCs (black spectrum). Spectra are baseline-corrected and red spectrum is shifted in Y axis for better observation.

It is clearly visible that the spectra are very reproducible. In both of them the presence of amide II bond at 1542 cm^{-1} and amide III bonds at 1296 cm^{-1} (for α -helix) and at 1269 cm^{-1} (for β -sheet) can be seen [37]. Amide I bond is absent in these spectra. Other characteristic bands can be assigned to several amino acids, having aromatic moieties, such as tryptophan (Trp), Tyrosine (Tyr) and

Phenylalanine (Phe). For instance, Trp bands can be observed at 759 cm^{-1} , 883 cm^{-1} , 969 cm^{-1} , and 1585 cm^{-1} . Bands assigned to the vibrations of Phe are detectable at 606 cm^{-1} , 1003 cm^{-1} , 1179 cm^{-1} (combined with Tyr) and 1216 cm^{-1} (combined with Tyr). The ones belonging to Tyr are seenable at 436 cm^{-1} , 626 cm^{-1} , 799 cm^{-1} and 1615 cm^{-1} (combined with Trp and Phe). Since anti-BAP13 was never been studied by Raman or SERS and its spectra cannot be found in the literature, we have assigned the bands by comparing spectra with the ones documented for other proteins [37] [20] [22].

The observation of the SERS signature of $F(ab')_2$ fragments grafted on the surface makes this biosensor a promising tool for the detection of analytes. However, after the incubation in the solutions of different concentrations of BaP (maximum 500 ppb), no spectral differences were evidenced. Before making a conclusion we decided to test the same surface functionalisation approach on GNPs SERS substrates, expecting to achieve higher sensitivity.

3.3.3.2 GNPs functionalisation by $F(ab')_2$ fragments

The extinction spectrum of GNPs exhibit a plasmon band centered around 522 nm (Figure 3.9 A). The Figure 3.9 B shows the extinction spectrum after the GNPs grafting into silanised substrates. The LSPR around 522 nm was still observed. However, a second broad plasmon band can be seen centered around 650 nm. The presence of this latter broad band can be the result of GNPs self-organization and the interaction between themselves [38]. Such substrate is rather convenient for SERS measurement since the position of the latter LSPR band matches well with the selected laser wavelength (660 nm).

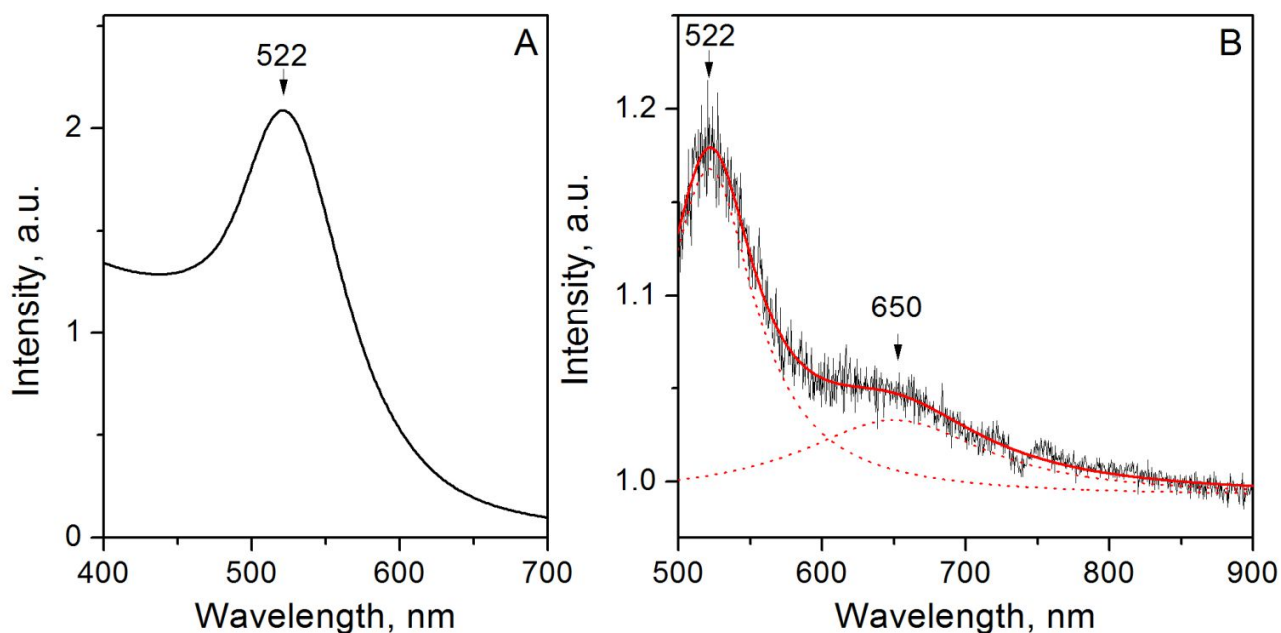


Figure 3.9 Extinction spectra of GNPs in solution (A) and GNPs SERS substrates (B). The latter one is the average of 6 measurements obtained in different places.

The SERS substrates were then functionalised with the $F(ab')_2$ in the a same manner as it was done for GNCs. SERS spectra were recorded after each step, starting from the surface cleaning and finishing with the BaP detection at 500 ppb concentration. Additionally, as negative controls, BaP detection at same concentration was performed on as-prepared GNPs SERS substrates as well as on the substrate functionalised with physically adsorbed anti-BAP13 (complete anti-body). All spectra are presented in the Figure 3.10 and Figure 3.11. In both figures spectra are plotted similarly. The Raman reference spectrum of BaP is given at the bottom (green spectrum). Red spectra correspond to the SERS signature of GNPs SERS substrates. SERS spectra recorded after $F(ab')_2$ or anti-BAP13 grafting is given as black spectra. For better observation of spectral changed we have substrated the red spectra to the black one. The result is plotted as violet spectra. Finally, the detection of BaP is presented as dark blue spectra. A subtraction step was also performed between the dark blue and the black spectra (blue spectra) that could be directly compared to the BAP reference spectrum (green one).

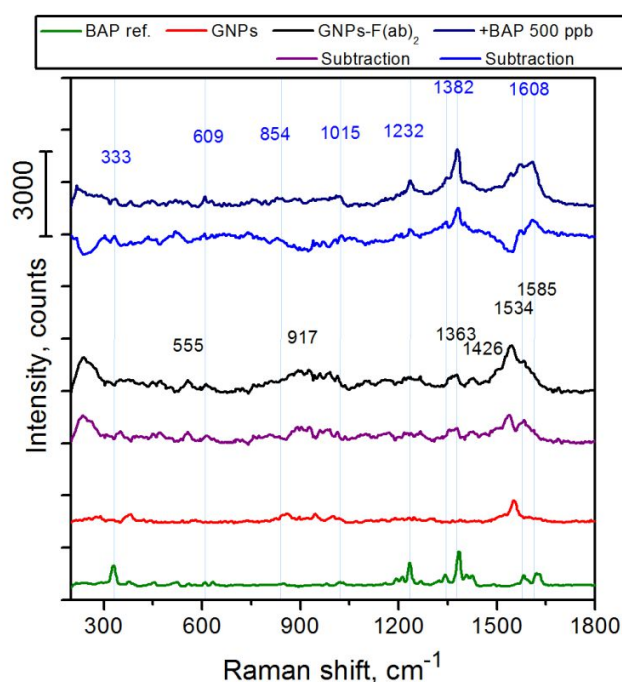


Figure 3.10 SERS spectra recorded after GNPs SERS substrate cleaning (red spectrum), after $F(ab')_2$ fragments grafting (black spectrum) and after incubation in 500 ppb BaP solution (water/methanol 9/1 v/v) (dark blue spectrum). For better observation the subtracted spectra are also given: between the red and the black ones for $F(ab')_2$ (violet spectrum) and between the black and the dark blue ones for BaP detection (blue spectrum). All spectra are average for 6 individual measurements. Green spectrum at the bottom is the Raman reference of the BaP.

First of all it is worth to compare the SERS spectra of the GNPs substrate. Even if all substrates used for this study were synthesized and cleaned in same manner, they are dissimilar in resulting SERS signature, and in the performance of molecular signal enhancement. The observed SERS signal is

coming from remaining citrate molecules and silanization layer used for GNPs attachment. These spectral differences were already reported for similarly prepared SERS active substrates [36].

After surface functionalisation by $F(ab')_2$ (Figure 3.10) and anti-BAP13 (Figure 3.11 B) several new peaks were observed. SERS spectra of grafted $F(ab')_2$ fragments is highly comparable with the ones recorded on GNPs concerning the bands position. However, the relative intensities for vibrational modes were found to strongly differ. Concerning the spectrum of adsorbed anti-BAP13 (Figure 3.11 B, black spectrum), clear evidence of biomolecules presence can be seen. Emerged bands at 752 cm^{-1} , 1002 cm^{-1} , 1372 cm^{-1} , 1601 cm^{-1} can essentially be assigned to the aromatic amino acids, whereas the bands at 1542 cm^{-1} and 1252 cm^{-1} might correspond to amide II and amide III, respectively.

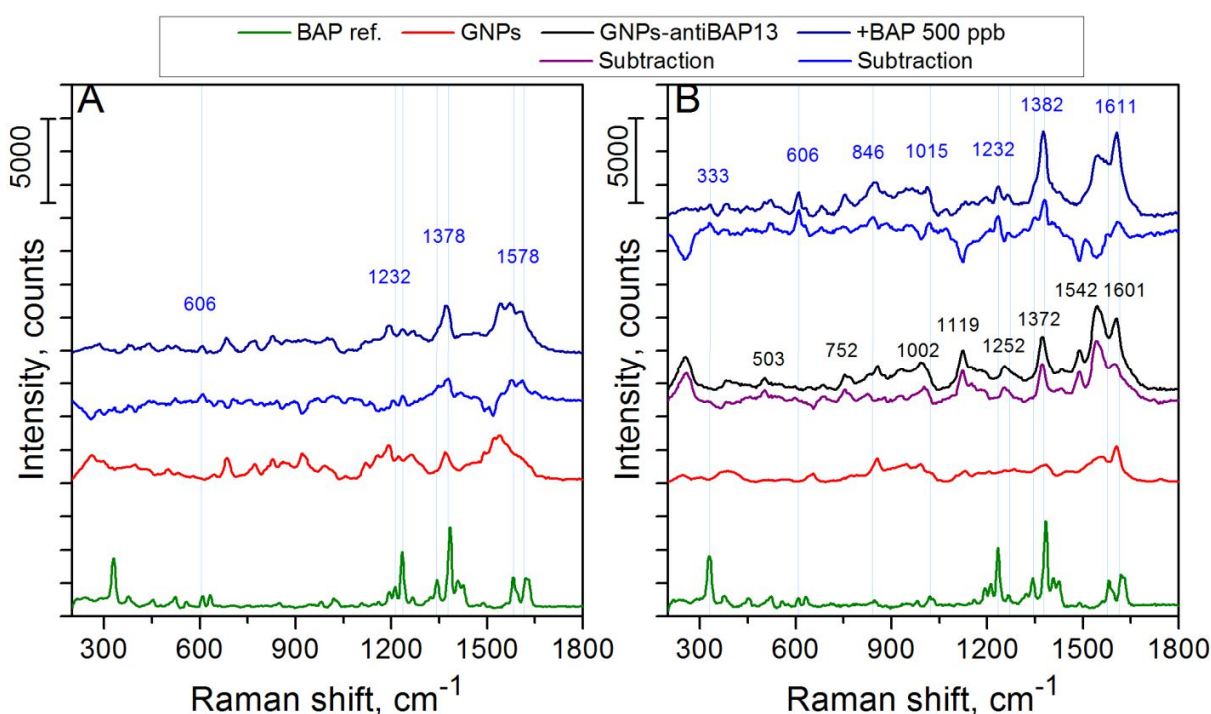


Figure 3.11 Detection of BaP(A) by the as-prepared GNPs SERS substrate and (B) by SERS substrate with physically adsorbed anti-BAP13. In both figures green spectra represent the Raman reference of BaP. Red spectra show the signal of GNPs SERS substrates. Black spectrum (in graph B) corresponds to the signal obtained after anti-BAP13 adsorption. Dark blue spectra were recorded after incubation in 500 ppb BaP solution (water/methanol 9/1 v/v). For better observation the subtracted spectra are also given: (A) between the red and the dark blue ones for (blue spectrum) and (B) between the red and the black ones (violet spectrum) and between the black and the dark blue ones (blue spectrum). All spectra are average for 6 individual measurements.

Having proofs of successful surface functionalisation by the selected biomolecules we were then focusing on the biosensors capability to detect the targeted analyte. One can notice that BaP detection was achieved for all tested systems. The observed peaks of BaP are summarized in table 2.

Table 2. Comparison of BaP peaks positions (in cm^{-1}) obtained by SERS on three tested sensors.

Raman of BaP	GNPs	GNPs-ati-BAP13	GNPs-F(ab') ₂
333	-	333	333
559	-	-	559
608	606	606	609
633	-	-	629
847	-	846	854
1020	-	1015	1015
1159	-	-	1162
1235	1232	1232	1232
1342	1347	1347	1344
1383	1378	1382	1382
1582	1578	1577	1570
1619	1616	1611	1608

The comparison of the BaP peaks observed on the three nanosensors with the ones found on the Raman spectrum of BaP (measured in solid) provided some evidences of the analyte interaction with the nanosensor surface. First of all, observed BaP signal on the as-prepared SERS substrate indicated that analyte is attracted by the APTMS molecules that were used for glass surface silanisation and GNPs attachment. This observation is not surprising because CH_2 groups in APTMS molecule provides rather hydrophobic environment which can promote apolar molecules pre-concentration. Similar SERS substrates based on sol-gel process with NPs trapped with a methyl/ethyl-tetraethoxysilane (MTEOS/ETEOS) precursor was already applied for SERS PAHs detection [39]. Using later substrate, authors demonstrated detection of naphthalene with LOD of 430 ppb.

Nevertheless, slight shifts of peaks positions of BaP as well as of the biomolecules, indicate that the BaP interacts also with the biomolecules and are pre-concentrated through the Fab or anti-body functionalisation layer. For this reason, more vibrational modes assigned to BaP were found with these latter substrates. Moreover, substrate functionalised by F(ab')_2 fragments possess greater shifts in the pollutant peaks, that could be induced by affinitive interaction with the antigen binding sites. In order to compare the two latter sensors the spectra recorded for BaP detection were normalized regarding to the bands in the range of $1500\text{-}1700\text{ cm}^{-1}$, assigned to the aromatic amino acids vibrational modes (see Figure 3.12). Intensity of the BaP peak at 1382 cm^{-1} shows that the signal of the pollutant molecules is higher with the F(ab')_2 sensor. This could be due to (i) a higher number of BaP at the GNPs surface through better interaction with the Fab or (ii) to higher enhancement of the BaP signal since the Fab is shorter than the whole anti-body and as a consequence the BaP are closer to the GNPs surface. Furthermore, the BaP peaks observed with the Fab layer are narrower, indicating that molecules interacting with the nanosensor surface are organized in similar orientation.

This might be an indication of affinitive detection of analyte favored by $F(ab')_2$ fragments grafted to the substrate.

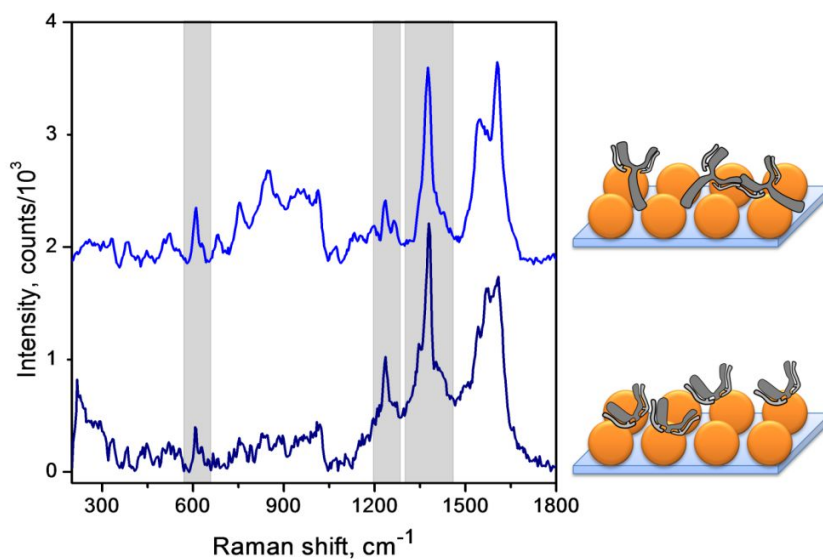


Figure 3.12 BaP detection achieved on anti-BAP13 functionalised substrate (light blue spectrum) and on $F(ab')_2$ functionalised substrate (dark blue spectrum). Both spectra were normalized regarding the intensity of the bands at 1500-1700 cm^{-1} .

3.3.4 Conclusion

Herein, we performed the anti-body digestion procedure employing enzymatic activity of pepsin. Produced $F(ab')_2$ fragments were applied for direct SERS substrates functionalisation. Successful surface functionalisation was achieved on GNCs and GNPs substrates. While good SERS signal of grafted $F(ab')_2$ was recorded on GNCs, affinitive pre-concentration of BaP was not successful. On the other hand, GNPs sensor provided good detection of analyte.

However, obtained results on the BaP detection did not provide conclusive information. In order to qualitatively compare the signal achieved by the sensors and thus, to find how much each process: (i) physical pollutant adsorption into silanisation layer, (ii) physical adsorption onto biomolecules or (iii) affinitive interaction with antigen binding sites, is contributing to the overall molecular pre-concentration, it is necessary to reproduce these experiments on SERS substrates which offers better reproducibility.

3.4 Conclusion

To conclude this chapter, two surface functionalisation approaches were tested in order to immobilise anti-bodies for specific analyte detection. In the first part of this study, SPR and LSPR detection of biomolecular immobilisation via amide coupling reaction are provided. However, results, achieved during SERS investigation of model biomolecules were found contradictory, since signal of grafted antibodies was absent, while SERS spectra of detected antigen was achieved. For this reason, we assumed that investigated analytes were not pre-concentrated due to affinitive interaction but physically adsorbed on the sensor surface. Moreover, we concluded that antibody is a too big molecule to be monitored by SERS.

With regards to the later conclusion, the second section of this chapter was devoted to the F(ab')₂ fragments synthesis and application. Using an approach of direct F(ab')₂ based surface functionalisation, we have demonstrated the SERS based evidences of biomolecule presence on the surface of GNCs. After employing GNPs SERS active substrates for their better sensitivity we have demonstrated BaP detection. However, substrates served as negative controls showed the similar performance in BaP sensing.

The approach of F(ab')₂ fragments application was found to be promising strategy that has to be further exploited and developed.

3.5 References

- 1 Makaraviciute, A. and Ramanaviciene, A. (2013). Site-directed antibody immobilization techniques for immunosensors, *Biosensors and Bioelectronics*, **50**, pp. 460-471.
- 2 Sauer-Eriksson, A. E., Kleywegt, G. J., Uhlen, M. and Jones, T. A. (1995). Crystal structure of the C2 fragment of streptococcal protein G in complex with the Fc domain of human IgG, *Structure (London, England : 1993)*, **3**, pp. 265-278.
- 3 Boujday, S., Gu, C., Girardot, M., Salmain, M. and Pradier, C. M. (2009). Surface IR applied to rapid and direct immunosensing of environmental pollutants, *Talanta*, **78**, pp. 165-170.
- 4 Suri, C. R. and Mishra, G. C. (1996). Activating piezoelectric crystal surface by silanization for microgravimetric immunobiosensor application, *Biosensors and Bioelectronics*, **11**, pp. 1199-1205.
- 5 Buijs, J., Norde, W. and Lichtenbelt, J. W. T. (1996). Changes in the Secondary Structure of Adsorbed IgG and F(ab')₂ Studied by FTIR Spectroscopy, *Langmuir*, **12**, pp. 1605-1613.
- 6 Wiseman, M. E. and Frank, C. W. (2012). Antibody Adsorption and Orientation on Hydrophobic Surfaces, *Langmuir*, **28**, pp. 1765-1774.
- 7 Zhou, C., De Keersmaecker, K., Braeken, D., Reekmans, G., Bartic, C., De Smedt, H., Engelborghs, Y. and Borghs, G. (2005). Construction of High-performance Biosensor Interface through Solvent Controlled Self-assembly of PEG grafted Polymer.
- 8 Kyprianou, D., Chianella, I., Guerreiro, A., Piletska, E. V. and Piletsky, S. A. (2013). Development of optical immunosensors for detection of proteins in serum, *Talanta*, **103**, pp. 260-266.
- 9 Fischer, M. J. (2010). Amine coupling through EDC/NHS: a practical approach, *Methods in molecular biology (Clifton, N.J.)*, **627**, pp. 55-73.

- 10 Patel, N., Davies, M. C., Hartshorne, M., Heaton, R. J., Roberts, C. J., Tendler, S. J. B. and Williams, P. M. (1997). Immobilization of Protein Molecules onto Homogeneous and Mixed Carboxylate-Terminated Self-Assembled Monolayers, *Langmuir*, **13**, pp. 6485-6490.
- 11 Karen, N. L. and Kathy, R. L. (1998). Removal of Carbonaceous Contamination from SERS-Active Silver by Self-Assembly *Journal of Raman Spectroscopy*, **29**, pp. 739-742.
- 12 Bain, D. B., Troughton, E. B., Tao, Y. T., Evall, J., Whitesides, G. M. and Nuzzo, R. G. (1989). Formation of monolayer films by the spontaneous assembly of organic thiols from solution onto gold, *Journal of American Society*, **111**, pp. 321-335.
- 13 Tarlov, M. J. (1992). Silver metalization of octadecanethiol monolayers self-assembled on gold, *Langmuir*, **8**, pp. 80-89.
- 14 Li, W., Jiang, X., Xue, J., Zhou, Z. and Zhou, J. (2015). Antibody modified gold nano-mushroom arrays for rapid detection of alpha-fetoprotein, *Biosensors and Bioelectronics*, **68**, pp. 468-474.
- 15 Castro, J. L., López-Ramírez, M. R., Centeno, S. P. and Otero, J. C. (2004). Adsorption of mercaptoacetic acid on a colloidal silver surface as investigated by Raman spectroscopy, *Biopolymers*, **74**, pp. 141-145.
- 16 Laurentius, L., Stoyanov, S. R., Gusarov, S., Kovalenko, A., Du, R., Lopinski, G. P. and McDermott, M. T. (2011). Diazonium-Derived Aryl Films on Gold Nanoparticles: Evidence for a Carbon–Gold Covalent Bond, *ACS Nano*, **5**, pp. 4219-4227
- 17 Socrates, G. (2001). *Infrared and Raman Characteristic Group Frequencies: Tables and Charts (3ed)* (Chichester (U.K.) ed.): Wiley.
- 18 Ahmad, R., Boubekeur-Lecaque, L., Nguyen, M., Lau-Truong, S., Lamouri, A., Decorse, P., Galtayries, A., Pinson, J., Felidj, N. and Mangeney, C. (2014). Tailoring the Surface Chemistry of Gold Nanorods through Au–C/Ag–C Covalent Bonds Using Aryl Diazonium Salts, *The Journal of Physical Chemistry C*, **118**, pp. 19098-19105.
- 19 Badawi, H. M., Förner, W. and Ali, S. (2013). A comparative study of the infrared and Raman spectra of aniline and o-, m-, p-phenylenediamine isomers, *Spectrochimica Acta A.*, **112**, pp. 388-396.
- 20 David, C., Guillot, N., Shen, H., Toury, T. and Lamy de la Chapelle, M. (2010). SERS detection of biomolecules using lithographed nanoparticles towards a reproducible SERS biosensor, *Nanotechnology*, **21**, pp. 475-501.
- 21 Siddhanta, S. and Narayana, C. (2012). Surface enhanced Raman spectroscopy of proteins. Implications in drug designing, *Nanomaterials. nanotechnology*, **2**, pp. 1-13.
- 22 Das, G., Mecarini, F., Gentile, F., De Angelis, F., Mohan Kumar, H. G., Candeloro, P., Liberale, C., Cuda, G. and Di Fabrizio, E. (2009). Nano-patterned SERS substrate: Application for protein analysis vs. temperature, *Biosensors and Bioelectronics*, **24**, pp. 1693-1699.
- 23 Siamwiza, M. N., Lord, R. C., Chen, M. C., Takamatsu, T., Harad, I., Matsuura, H. and Shimanouchi, T. (1975). Interpretation of the doublet at 850 and 830 cm⁻¹ in the Raman spectra of tyrosyl residues in proteins and certain model compounds, *Biochemistry*, **14**, pp. 4870-4876.
- 24 Van Dael, H., Lafaut, J. P. and Van Cauwelaert, F. (1987). Tyrosine group behaviour in bovine α -lactalbumin as revealed by its Raman effect *European Biophysics Journal*, **14**, pp. 409-414.
- 25 Jenkins, A. L., Larsen, R. A. and Williams, T. B. (2005). Characterization of amino acids using Raman spectroscopy, *Spectrochimica Acta Part A*, **61**, pp. 1585-1594.
- 26 Mian, I. S., Bradwell, A. R. and Olson, A. J. (1991). Structure, function and properties of antibody binding sites, *Journal of Molecular Biology*, **217**, pp. 133-151.
- 27 Brogan, K. L. and Schoenfisch, M. H. (2005). Influence of Antibody Immobilization Strategy on Molecular Recognition Force Microscopy Measurements, *Langmuir*, **21**, pp. 3054-3060.
- 28 Waller, M., Curry, N. and Mallory, J. (1968). Immunochemical and serological studies of enzymatically fractionated human IgG globulins—I: Hydrolysis with pepsin, papain, ficin and bromelin, *Immunochemistry*, **5**, pp. 577-583.
- 29 Mariant, M., Camagna, M., Tarditi, L. and Seccamani, E. (1991). A new enzymatic method to obtain high-yield F(ab)₂ suitable for clinical use from mouse IgG1, *Molecular Immunology*, **28**, pp. 69-77.

- 30 Rousseaux, J., Rousseaux-Prevost, R. and Bazin, H. (1986) *Methods in Enzymology*, chapter "[63] Optimal conditions for the preparation of proteolytic fragments from monoclonal IgG of different rat IgG subclasses," (Academic Press) pp. 663-669.
- 31 Grand, J., Kostcheev, S., Bijeon, J. L., de la Chapelle, M. L., Adam, P. M., Rumyantseva, A., Lérondel, G. and Royer, P. (2003). Optimization of SERS-active substrates for near-field Raman spectroscopy, *Synthetic Metals*, **139**, pp. 621-624.
- 32 Turkevich, J., Stevenson, P. C. and Hillier, J. (1951). A study of the nucleation and growth processes in the synthesis of colloidal gold, *Discussions of the Faraday Society*, **11**, pp. 55-75.
- 33 Liddell, J. E. and Cryer, A. (1991). *A Practical Guide to Monoclonal Antibodies*: Wiley.
- 34 Turner, M. W., Bennich, H. H. and Natvig, J. B. (1970). Pepsin digestion of human G-myeloma proteins of different subclasses. II. Immunochemical investigations of the products of peptic digestion, *Clinical and experimental immunology*, **7**, pp. 627-640.
- 35 Inouye, K. and Morimoto, K. (1993). Single-step purification of F(ab')₂μ fragments of mouse monoclonal antibodies (immunoglobulins M) by hydrophobic interaction high-performance liquid chromatography using TSKgel Ether-5PW, *Journal of Biochemical and Biophysical Methods*, **26**, pp. 27-39.
- 36 Costa, J. C. S., Sant'Ana, A. C., Corio, P. and Temperini, M. L. A. (2006). Chemical analysis of polycyclic aromatic hydrocarbons by surface-enhanced Raman spectroscopy, *Talanta*, **70**, pp. 1011–1016.
- 37 Jones, D. D. (1975). Amino acid properties and side-chain orientation in proteins: A cross correlation approach, *Journal of Theoretical Biology*, **50**, pp. 167-183.
- 38 Peron, O., Rinnert, E., Lehaitre, M., Crassous, P. and Compere, C. (2009). Detection of polycyclic aromatic hydrocarbon (PAH) compounds in artificial sea-water using surface-enhanced Raman scattering (SERS), *Talanta* **79**, pp. 199-204.
- 39 Lucht, S., Murphy, T., Schmidt, H. and Kronfeldt, H. D. (2000). Optimized recipe for sol–gel-based SERS substrates, *Journal of Raman Spectroscopy*, **31**, pp. 1017-1022.

4 Cyclodextrins functionalisation for size selective pollutant detection

4.1 Introduction

SERS as a vibrational spectroscopy tool provides an opportunity to work in complex environments with the possibility to discriminate targeted molecule signal from the whole spectrum. Therefore, the requirement for sensor to be highly selective in this case can be overlooked. In fact, development of sensors with partial selectivity would even improve the SERS based molecular sensing since it would allow number of different molecules with comparable properties to be pre-concentrated and detected.

Among various chemical molecules allowing analyte pre-concentration due to physical interactions, cavitands are well known systems permitting size selective molecular encapsulation. One of them, so called cyclodextrin (CD), is a natural cyclic oligosaccharide which possesses doughnut like structure with a relatively hydrophobic internal cavity. The outside of the rim being hydrophilic, CDs are soluble in water and capable to form host-guest complexes with hydrophobic molecules presented in aquatic media.

This chapter will be devoted to the exploitation of the CDs capability to interact with non-polar targeted substances. First, thermogravimetric analysis and Raman spectroscopy will be employed in order to investigate the complexes formed between CDs and analytes. This study has been published as article in journal of Environmental Science and Pollution Research.

In a second part, strategies of CDs based surface functionalisation will be discussed, including applications of thiolated-CDs and CD-based polymer. The ability of CDs based nanosensors in molecular pre-concentration will be tested using toluene (TOL), naphthalene (NAP) and fluoranthene (FL).

4.2 Investigation of aromatic hydrocarbon inclusion into cyclodextrins by Raman spectroscopy and thermal analysis

-supplementary information for this paper can be found in ANNEX 2

Investigation of aromatic hydrocarbon inclusion into cyclodextrins by Raman spectroscopy and thermal analysis

Inga Tijunelyte¹ · Nathalie Dupont¹ · Irena Milosevic¹ · Carole Barbey¹ · Emmanuel Rinnert² · Nathalie Lidgi-Guigui¹ · Erwann Guenin¹ · Marc Lamy de la Chapelle¹

Received: 14 October 2014 / Accepted: 11 March 2015
© Springer-Verlag Berlin Heidelberg 2015

Abstract Among various cavitand molecules, cyclodextrins are extensively studied due to their ability to form host-guest complexes with small hydrophobic molecules. Aiming to explore cyclodextrin implementation on the scopes related to the environmental pollution monitoring or remediation, extensive studies for understanding the cyclodextrin-based host-guest complex formation with selected targeted substances are conducted. In this context, two polycyclic aromatic hydrocarbons, naphthalene and fluoranthene as well as toluene as a member of volatile organic compounds, were studied regarding their ability to encapsulate into cyclodextrin cavities. Synthesised complexes were examined by thermogravimetric analysis combined with Raman spectroscopy. The obtained results demonstrated that the size between targeted molecules and the cyclodextrin cavities strongly correlates with its ability to engage in complexation. Thus, this latter parameter plays an important role in the inclusion complex formation as well as in the strength of the interaction between the molecules.

Keywords Raman spectroscopy · Thermogravimetric analysis · Cyclodextrin · Polyaromatic hydrocarbons · PAH · Host-guest complex

Introduction

Environmental water pollution by organic compounds is a worldwide concern due to its continuous emission in both natural (Kvenvolden and Cooper 2003) and anthropogenic (Readman et al. 1992) ways. The contaminants, consisting of two or more fused aromatic rings known as polycyclic aromatic hydrocarbons (PAHs), are a group of pollutants which have received considerable attention because of their documented significant toxicity and carcinogenicity (Diggs et al. 2011; Harris et al. 2013; Lienig 1980; Varanasi et al. 1987). Therefore, constant monitoring of these water contaminants at the trace level is of first importance regarding the latest European Water Framework Directives (2000/60/EC, 2006/118/EC and 2006/11/EC).

Within this scope, many efforts have been devoted for the development of an analytical tool capable of sensitive and rapid detection of chemical water bodies with minimal sample handling (Pejcic et al. 2007). In the course of the last decades, surface-enhanced Raman spectroscopy (SERS)-based pollutant detection has attracted more and more interest (Bantz and Haynes 2009; Carron et al. 1992; Costa et al. 2006; Guerrini et al. 2009; Halvorson and Vikesland 2010). SERS is based on the exploitation of the optical properties of metallic nanostructures and especially on their ability to provide a tremendous enhancement of the electromagnetic field at the nanostructure vicinity. Any molecules close to the nanostructure surface can benefit from this enhancement and scatter a Raman signal magnified by a factor up to 10^{10} . This highly sensitive method allows observing chemical compounds at the trace level as

Responsible editor: Philippe Garrigues

Electronic supplementary material The online version of this article (doi:10.1007/s11356-015-4361-6) contains supplementary material, which is available to authorized users.

✉ Marc Lamy de la Chapelle
marc.lamydelachapelle@univ-paris13.fr

¹ Laboratoire CSPBAT UMR CNRS 7244, UFR Santé Médecine Biologie Humaine, Université Paris 13, 74 rue Marcel Cachin, 93017 Bobigny, France

² IFREMER, Laboratoire Détection, Capteurs et Mesures, Unité Recherches et Développement Technologiques, CS10070, 29280 Plouzané, France

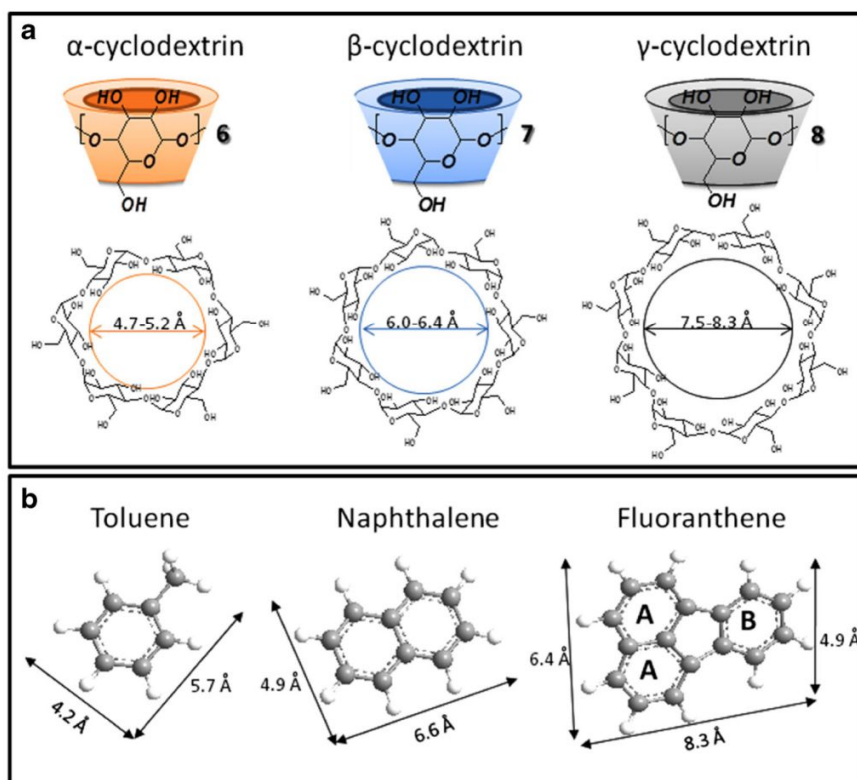
low as the single molecule sensitivity (Chang et al. 2013; Yang et al. 2010) and can provide quantitative and qualitative multi-analysis in complex environment (Pfannkuche et al. 2012). However, in SERS configuration, the molecules that are close to the nanostructure surface will experience the high field enhancement and the Raman spectrum will be then composed of all the spectroscopic features of these molecules including the non-targeted ones. To have a specific detection, it is then necessary to pre-concentrate the targeted molecules at the nanostructure surface. For this, a specific molecular layer that exhibits higher affinity to the targeted molecules has to be used. Among different strategies to design a SERS-based nanosensor able to pre-concentrate aromatic compounds, supramolecular cage systems as cyclodextrins or calixarenes appear to be particularly promising (Guerrini et al. 2006; Hill et al. 1999; Shi et al. 2013; Xie et al. 2010, 2011).

Cyclodextrins (CDs) are natural cyclic oligosaccharides. The three commercially available CDs— α CD, β CD and γ CD—are consisting of six, seven, or eight α -D-glucose units, respectively, linked through α -1,4 glycosidic bonds (Fig. 1a). Torus-shaped structure of CDs possesses a relatively hydrophobic internal cavity which is known to provide binding sites for wide variety of molecules (Del Valle 2004). Mainly for this reason, CDs are applied in food (Astray et al. 2009), pharmaceuticals (Loftsson and Brewster 1996),

cosmetics (Buschmann and Schollmeyer 2002), bioconversion (Dufosse et al. 1999) and textile industries (Cireli and Yurdakul 2006) as well as in environmental research (Viglianti et al. 2006).

Host-guest complex formation between CDs and organic molecules have been widely studied by different techniques, such as thermoanalytical methods, microscopy, chromatography and spectroscopy (Singh et al. 2010). For solid state analysis, Raman (Amado et al. 1994; Amado and Ribeiro-Claro 2000) and infrared (García-Zubiri et al. 2004; Nagao et al. 2009) spectroscopies are the most used techniques to collect important evidences on the complex formation, thanks to changes in the molecular vibrational modes (frequency and relative intensity) due to the molecular interaction between the host and the guest molecules. However, literature reveals that complexes formed between CDs and non-polar aromatic compounds are still undergoing difficulties in spectroscopic based analysis (García-Zubiri et al. 2004) due to very weak molecular interactions. In the present work, three forms of CDs were employed in host-guest complex formation with toluene (TOL), naphthalene (NAP), and fluoranthene (FL). Complexes in solid state were synthesised and studied by Raman spectroscopy and thermogravimetric (TG) analysis. We investigated the molecular affinity comparing the size of the guest with the diameter of the host cavity. We also studied

Fig. 1 Illustrated scheme of a molecular and 3D structures of three forms of CDs, with indications of diameters of the cavities; **b** molecular structure of the three selected pollutants with their sizes



the changing in vibrational modes of the complexes in order to subsequently use enhanced spectroscopy techniques for the detection of those compounds in the wild aquatic environments.

Experimental

Materials

Pharmaceutical grade CDs (α , β and γ CD) were purchased from Wacker Chemie (Germany) and used without further purification. Aromatic compounds, TOL, NAP and FL, and ethanol were obtained from Sigma-Aldrich (France) at high purity grade and were used as received.

Inclusion complex preparation

Following the procedure described in literature (Sardo et al. 2009), based on co-precipitation method, saturated aqueous solutions of α CD, β CD and γ CD were mixed with aromatic compounds (TOL, NAP and FL) dissolved in ethanol at the concentration of 50 mM. The addition of the pollutant solutions into CDs was made dropwise using strong agitation at ambient temperature. This process led to immediate formation of white precipitants. Mixed solutions were then kept in shaker for 2 h and precipitants were collected using centrifuge. To make sure that there were no non-included aromatic compounds, precipitants were briefly washed with ethanol/water solution 50:50 (v/v) and dried for 2 days at room temperature.

To obtain additional information on complex formation, extensive study was performed on β CD:NAP complexes. For this, NAP dissolved in ethanol was mixed with saturated β CD solution at different molar ratios (2 β CD:1NAP, 1 β CD:1NAP and 1 β CD:2NAP). Further steps of sample collection, washing and drying were performed as previously described.

For analysis of CD-based selectivity towards the pollutant molecules, the complexes were prepared as follows: TOL, NAP and FL were dissolved together in ethanol at 50 mM concentration and added in saturated aqueous solutions of each— β CD and γ CD. Ethanol solution containing both TOL and NAP at 50 mM concentration was added into α CD solution. Further steps of sample collection, washing and drying were performed as previously described.

Thermogravimetric analysis

For TG analysis, LabSys evo instrument (SETARAM) was used. Each sample (8–12 mg) was kept for 1 h at 30 °C in alumina pan before heating over the temperature range from 30 to 600 °C under argon atmosphere with the flow rate of

20 mL/min. The empty sealed alumina pan was used as reference. For data processing, Calisto software was used.

Raman spectroscopy measurements

Raman spectra of α , β and γ CD, and TOL, NAP and FL as well as of their inclusion complexes in solid powder were recorded using Xplora ONE (Horiba scientific) microspectrometer. Laser excitation wavelength of 785 nm with a power of 8 mW was focused on the sample with $\times 100$ objective (N.A. 0.9). Integration time for signal collection was set to 60 s for CDs and their complexes and to 5 s for aromatic compounds. Each spectrum is the average of two repetitive measurements. Applied grating of 1200 grooves/mm has ensured spectral resolution of less than 1 cm^{-1} . It is important to note that the studied aromatic molecules adsorb in the UV range (Koban et al. 2004; Maeda et al. 2012; Saranya et al. 2011). Thus, the energy of the near-infrared laser could not match with any electronic transitions of these compounds, and as a consequence, the measured Raman scattering is not in resonant condition.

Computational

All calculations were carried out using the Gaussian09 suite of programs (Frisch et al. 2009). Following full geometry optimisation of FL with C_{2v} symmetry using the density functional three-parameter hybrid model B3LYP (Becke 1996; Lee et al. 1988) with the 6-311G (d,p) basis set, vibrational frequencies and Raman activities were calculated. The B3LYP method with the 6-311G (d,p) basis set is frequently used in predicting vibrational spectra of polyaromatic molecules. Raman intensities were computed from activities with GaussSum 3.0 (O'Boyle et al. 2008) using an excitation wavelength of 785 nm. The calculated harmonic frequencies of C–H stretching vibrations were scaled by a factor of 0.96 and all the other frequencies by 0.98 to allow a good agreement with observed ones for FL alone within almost 10 cm^{-1} on the whole spectra. Gaussview 5 (Dennington et al. 2009) was used to visualise the participation and direction of atoms in vibrational normal modes in order to make band assignments easier.

Results and discussion

Study of complexes formed between β -CD and variable concentration of NAP

Aiming to determine the relevant parameters that describe the host-guest interaction, we first studied the ratio between the host and the guest in the complex β CD:NAP. For this purpose different molar ratios (2 β CD:1NAP, 1 β CD:1NAP and

1 β CD:2NAP) between the host and the guest were used to form the complexes. Two techniques, TG analysis and Raman spectroscopy, were then employed to analyse the complexes in solid state.

Thermogravimetric analysis

Thermal analysis is a powerful tool to study the complex formation between guest molecules and CD and to evaluate the inclusion compound stoichiometry (Giordano et al. 2001). Among the various thermoanalytical techniques, TG analysis is frequently used to determine whether the guest exhibits some changes in its phase transition temperatures indicating inclusion complex formation.

The thermograms and the derivatives of the three prepared stoichiometries regarding molar ratio (2 β CD:1NAP, 1 β CD:1NAP and 1 β CD:2NAP), as well as the thermograms of pure compounds, are presented in Fig. 2.

Isolated CD thermal degradation profile consists of three parts. In the first stage, a gradual loss of hydrated water from ambient to 120 °C corresponding to the dehydration process can be recorded. During the second stage, in a temperature

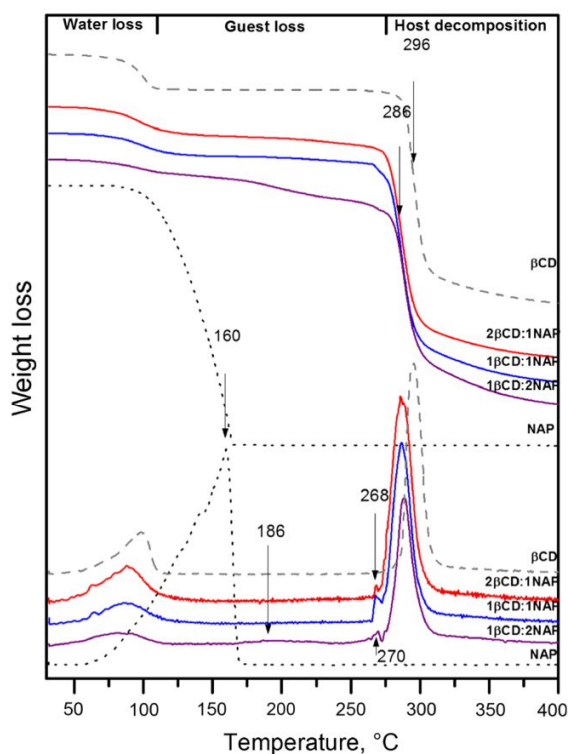


Fig. 2 Top: thermograms of the reference molecules—NAP and β CD presented as dot and dash lines, respectively, and of the inclusion complexes formed mixing different molar ratios (2 β CD:1NAP (red curve), 1 β CD:1NAP (blue curve) and 1 β CD:2NAP (violet curve). Bottom: derivatives of the TG curves

range between 270 and 350 °C, single-step weight loss is observed, corresponding to the thermal breaking of CD ring and further glucosidic ring decomposition (Russell and McNamara 1989). The remaining 30–40 % of residue is then showing loss in mass at a temperature range upon 350 °C and is assigned to a slow degradation of char (Trotta et al. 2000). On the other hand, pure aromatic compounds decompose at much lower temperature. In the case of NAP, the thermal decomposition occurs in one step between 80 and 160 °C temperature range.

The TG curves of the complexes are quite different from those of pure components. Worth to remind is that complexes were prepared in aqueous solution and should be considered as ternary water-guest-CD systems. In thermograms, the initial weight loss observed until 120 °C is attributed to the release of water molecules. However, it is noticeable that the number of water molecules is continuously decreasing within the complexes with growing number of the guest (Table 1). This change in number of water can be contemplated as a first proof of the complex formation since the inclusion process is considered as the replacement of the internal water molecules by a guest. Additionally, a peak around 62 °C can be observed on the derivatives of TG analysis curves for some complexes. This peak might be assigned to the ethanol molecules remaining after complexes formation. However, since the evaporating temperature is close to boiling point of the ethanol, we assume that the ethanol does not form complexes with the CD molecule. Further analysis of the thermograms revealed no peak corresponding to free NAP molecule decomposition after the complex formation. Instead, a small endothermic peak centred at around 268 °C appears for 2 β CD:1NAP and 1 β CD:1NAP complex systems. Considering comparable mass loss in the complexes (Table 1), the peak around 268 °C could be assigned to a thermal decomposition of NAP placed inside the CD cavity. Indeed, since this temperature is intermediate between the ones observed for individual CD and for individual NAP, we assume that it should be assigned to third process corresponding to the decomposition of NAP included inside the CD. A similar shift in guest decomposition temperature has been already observed by other groups (Nolasco et al. 2009; Sardo et al. 2009). The shift in decomposition temperature between free NAP and the one embedded into host indicates that the host-guest interaction protects the pollutant molecules from early volatilisation. For the system with higher concentration of NAP (1 β CD:2NAP), the latter peak is found slightly shifted to 270 °C. Moreover, a new peak at lower temperature, centred at around 186 °C, can be observed and assigned to the NAP molecules placed outside the cavities. However, the higher decomposition temperature of those NAP molecules in comparison with free NAP signifies that they are in interaction with the complex.

Table 1 TG analysis based calculation on stoichiometry for inclusion complexes

System	Theoretical stoichiometry	% (wt) (Guest)	% (wt) (H ₂ O)	Calculated stoichiometry	Water per CD
2 β CD:1NAP	2:1	9.2	4.1	2:1	10
1 β CD:1NAP	1:1	5.1	7.2	1:1	7
1 β CD:2NAP	1:2	10.6	4.6	2:3	5

CD cyclodextrin, NAP naphthalene

Finally, the weight loss in temperature range from 270 to 350 °C was observed and assigned to the CD decomposition. A slight shift of 10 °C to lower degradation temperature can be noticed when comparing with the free CD decomposition. This slight shift could be induced by the engaged guest which disorders the hydrogen bonded supramolecular structure of CD (Trotta et al. 2000).

The quantification of the mass losses upon temperature increase provides the information on the molar ratio between CD, NAP and H₂O in the systems. Calculated stoichiometries of the complexes are summarised in Table 1.

As explained previously, the studied complexes are actually ternary β CD-NAP-H₂O systems. Nevertheless, an increase of the initial guest concentration leads to an increase of the NAP molecules included into CD cavities. On the contrary, the number of water molecules per CD decreases in agreement with the increasing number of engaged NAP molecules, as already mentioned proving the successful replacement of the water molecules.

The cavity of β CD is generally considered large enough to accommodate aromatic guest molecule (Köhler and Grzelschak-Mick 2013). The 1 β CD:1NAP stoichiometry was observed to be in good agreement with the predicted one, as well as in case of 2 β CD:1NAP formed inclusion complex where 1 molecule of NAP is between 2 β CD molecules. Unusual host-to-guest stoichiometry was calculated for the last complex with the highest NAP concentration. Calculated stoichiometry of 3 NAP molecules per 2 β CD was found. Similar stoichiometry has been already observed and documented for a complex formed between β CD and 1,10-phenanthroline (Liu et al. 2004). With the help of X-ray diffraction, authors have observed that two 1,10-phenanthroline molecules were individually included into two β CD cavities and stabilised by the third guest molecule located in the interstitial space between two head-to-head CD molecules. The observed stoichiometry of 2 β CD:3NAP should have similar structure. In the complex, two NAP molecules which were found to decompose at 270 °C are included into 2 β CD individually. These 1 β CD:1NAP complexes are then stabilised by a third NAP molecule placed outside the CD. NAP molecules located in the interstitial space between two complexes decompose at around 186 °C as observed in TG analysis.

Raman spectroscopy based analysis

The complexes synthesised mixing different molar ratios between β CD and NAP were then studied by Raman spectroscopy. Figure 3 presents the Raman spectra of the native β CD, of the NAP and of the three inclusion complexes: 2 β CD:1NAP, 1 β CD:1NAP and 1 β CD:2NAP.

Peaks corresponding to naphthalene were observed in the spectra of all the complexes. Moreover, the proof of molecular inclusion and interaction with the CD cavities was clearly noticeable by comparing the relative intensities of isolated NAP peaks with the ones of NAP included in the complexes. Significant differences in intensities can be observed for several peaks (Fig. 4).

First, the one located at 761 cm⁻¹, corresponding to ring breathing mode and C–C central stretch, appears as the most intensive peak in the NAP spectrum whereas it is remarkably diminished in the spectra of complexes. On the contrary, the peak at 1379 cm⁻¹, assigned to a C–C stretching and ring deformation, is becoming the most intense mode when the NAP is embedded into the cavity of the CD. Other modes which are varying after the complex formation are less obvious in the presented graph; thus, their relative intensities and positions are summarised in Table 2. The peak located at

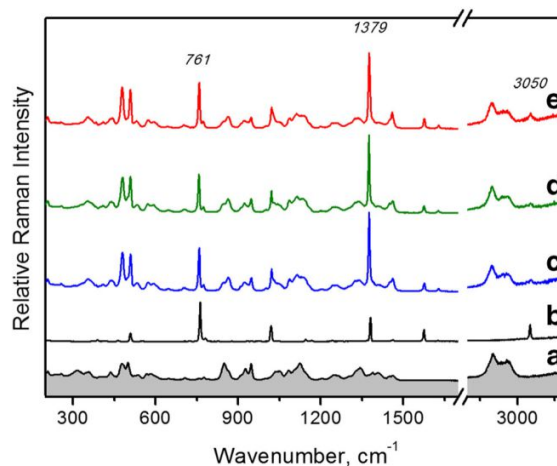
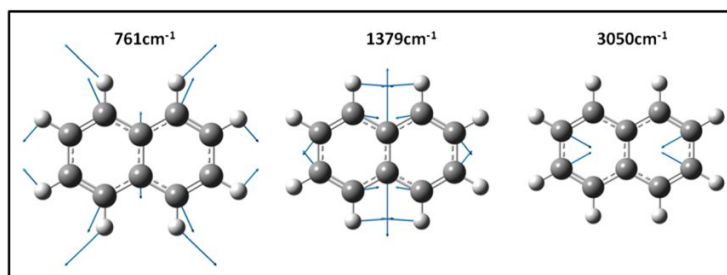


Fig. 3 Raman spectra of the β CD (a), of the NAP (b) and of the inclusion complexes (c–e) obtained after mixing β CD with NAP in molar equivalents of 2:1, 1:1 and 1:2 respectively

Fig. 4 Three vibrational modes of NAP which are the most impacted by the interaction with β CD.



1379 cm^{-1} was used as reference for the relative intensity calculation given in Table 2. An increase of the relative intensity is clearly observed for the C–C–C bending at 508 cm^{-1} . On the contrary, the C–H out of plane stretching mode at 3050 cm^{-1} as well as in plane C=C stretching at 1575 cm^{-1} was less visible when NAP is included into CD. The observed change indicates that the stretching modes inducing a potential interaction of H atoms with the CD as well as the radial mode or the C–H stretching exhibit a lower intensity compared to the other modes, which is an evidence of the inclusion of the NAP in the β CD cavity.

Some changes were also examined on CD vibrational modes after inclusion complex formation. For example, a change in the relative intensities of the doublet at 927–943 cm^{-1} was observed as well as for the bands located between 1050 and 1200 cm^{-1} . To have a better insight on such changes, Fig. 5 shows the subtractions of the isolated CD spectrum from normalised 2 β CD:1NAP, 1 β CD:1NAP and 1 β CD:2NAP complex spectra. The observation of several positive and negative peaks superimposed with the NAP modes indicates that a large number of the CD vibrational modes are strongly modified by the interaction with the NAP molecule. The most impacted vibrational modes are related with skeletal vibrations (478, 850 and 927 cm^{-1}) (Egyed 1990), O–H wagging (562 cm^{-1}) (Yao et al. 2014), C–O stretching (943, 1051, 1076 and 1124 cm^{-1}) (Yao et al. 2014) and C–H stretching or wagging (1345, 2914 and 2966 cm^{-1}) (Yao et al. 2014). We observed that the spectral modifications become more visible when the number of

naphthalene molecules increase compared to CD ones, since the intensities of the negative or positive bands increase. Thus, the host/guest complex behaves as a global system that induces large variation on the vibrational modes of both compounds.

Study of complexes between α , β and γ CD with TOL, NAP and FL

Further investigations on CD ability to form the complexes were realised by mixing selected aromatic compounds: TOL, NAP and FL dissolved in ethanol, with the saturated aqueous solutions of each CD (α CD, β CD and γ CD). This study was performed to determine the ability of complex formation between the host and the guest in regards to their sizes.

Thermogravimetric analysis

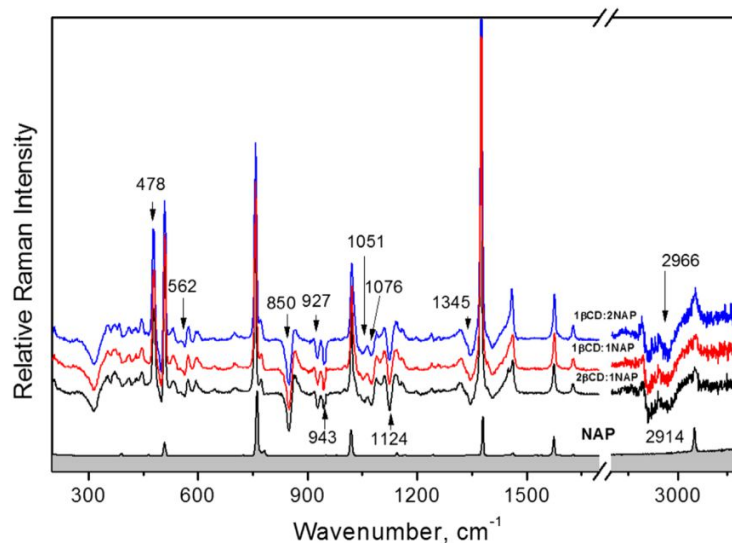
In this part, a study of the inclusion compounds of the three types CD (α CD, β CD and γ CD) is presented using TOL, NAP and FL molecules as guests. Decomposition temperatures were found for each pollutant molecule: Total mass loss of TOL was recorded from ambient to 113 $^{\circ}\text{C}$, NAP (as mentioned in the “Thermogravimetric analysis” section) decomposes from 80 to 160 $^{\circ}\text{C}$, and FL thermal decomposition occurs from 125 to 280 $^{\circ}\text{C}$. For the pure CD, no important dissimilarity in the degradation temperature regarding to the cavity size was found.

Table 2 Positions of the vibrational modes and their calculated relative intensities for free NAP and NAP included in the β CD

NAP		2CD:1NAP		1CD:1NAP		1CD:2NAP		Assignment
Peak	Rel.Int	Peak	Rel.Int	Peak	Rel.Int	Peak	Rel.Int	
508	0.2	508	0.39	508	0.41	508	0.44	CCC bend
762	3	757	0.77	758	0.83	758	0.87	Ring breathing
1379	1	1375	1	1376	1	1376	1	CC str.; ring def.
1575	0.65	1575	0.12	1576	0.13	1576	0.15	C=C str.
1627	0.05	1627	0.04	1628	0.05	1628	0.05	C=C str.
3050	0.82	3055	0.06	3055	0.12	3055	0.18	CH str.

Assignment of isolated NAP vibrational modes found in literature (Srivastava and Singh 2007)
CD cyclodextrin, NAP naphthalene

Fig. 5 Normalised Raman spectra obtained after β CD spectrum subtraction from 2 β CD:1NAP (black spectrum), 1 β CD:1NAP (red spectrum) and 1 β CD:2NAP (blue spectrum) inclusion complex spectra. The bottom Raman spectrum corresponds to the isolated NAP



Generally, an increasing number of guest molecules involved in the complex were expected (with an increasing cavity size (α CD < β CD < γ CD)). The γ CD cavity is wider and may be able to accommodate two guest molecules (Sardo et al. 2009). On the contrary, α CD is the smaller host so its cavity is not large enough to accommodate one aromatic guest. Usually, one guest is stacked between two α CDs (Nolasco et al. 2009).

As shown in the first part, the inclusion of the guest into the cavity of the CD permits the guest to withstand higher temperature comparing to free molecules. For instance, toluene which is known to have a boiling point at 111 °C was found to decompose at more than 270 °C when it is in contact with the α CD.

Table 3 shows the calculated stoichiometries for the host/guest complexes. As expected, in the case of TOL, complexes are composed of one guest molecule between two α CDs (1:2 stoichiometry), whereas one molecule of TOL can be included in one molecule of both: β CD and γ CD (1:1). As a consequence, in the system of 2 α CD:1TOL, a shift towards higher

decomposition temperature was found, showing higher thermal stability.

Concerning NAP, one guest per one host molecule was calculated regardless to the cavity dimension. Unexpectedly, we observed that thermal stability of the NAP molecules is also independent on the size of the host. This behaviour could be related with different orientations of guest molecule inside the cavity of guest.

Finally, FL molecules formed a complex only with γ CD. Indeed, in this case, calculation revealed that two γ CD molecules were engaged with one molecule of FL.

Raman spectroscopy based analysis

Raman spectroscopy measurements were performed on complexes in order to observe spectral evidence of guest-host interactions. It has already been observed that small shifts and variation in intensities for some bands in Raman spectra of the guest molecule appear upon formation of inclusion complexes (Amado et al. 1994; Amado and Ribeiro-Claro 2000). The

Table 3 TG analysis based calculation on stoichiometry for inclusion complexes

System	°C (Guest)	% (wt) (Guest)	% (wt) (H ₂ O)	Calculated stoichiometry	Water per CD
α CD:TOL	273	4	7.3	2:1	6
α CD:NAP	268	9.9	7.5	1:1	6
β CD:TOL	268	3.5	8.8	1:1	9
β CD:NAP	269	5.1	7.2	1:1	7
γ CD:TOL	265	3.5	8.2	1:1	9
γ CD:NAP	270	2.7	7.4	1:1	9
γ CD:FL	272	5.1	8.2	2:1	9

CD cyclodextrin, NAP naphthalene, TOL toluene, FL fluoranthene

moieties of guest molecules that suffer from intermolecular interactions can be identified by assigning the shifted bands using DFT calculation. Starting from the nature of vibrations modified upon complexation, it becomes also possible to discuss about the orientation of the guest molecules in the inclusion complexes.

Quantum chemical computations predicting harmonic frequencies and spectral intensities are essential for interpretation of experimental spectra, particularly for large molecules. Accurate computation of IR and Raman intensities is difficult because of their dependence on dipole moment and polarisability derivatives. For this reason, it is invariably the relative, rather than absolute, band intensities that are used since experimental determination of absolute band intensities, especially for Raman bands, is difficult. Accordingly, the intensity of some bands is enhanced in experimental data in comparison with the calculated ones, especially for the more intensive bands, but the order of magnitude is kept on the whole spectra (Zvereva et al. 2010).

In experimental IR absorption spectra of inclusion complexes, bands due to CD are prominent (Nagao et al. 2009) while it is not so obvious in Raman spectra. Hence, it becomes easier to observe Raman bands attributed to the guest molecules.

Figure 6 shows the Raman spectra of complex formation of CDs with TOL and NAP, respectively. Both graphs A and B are composed of isolated pollutant spectrum (a) and the spectra of guests engaged in complexes with α CD (c), β CD (e) and γ CD (g). The native CD spectra (b), (d) and (f) for α , β and γ CD respectively are also given.

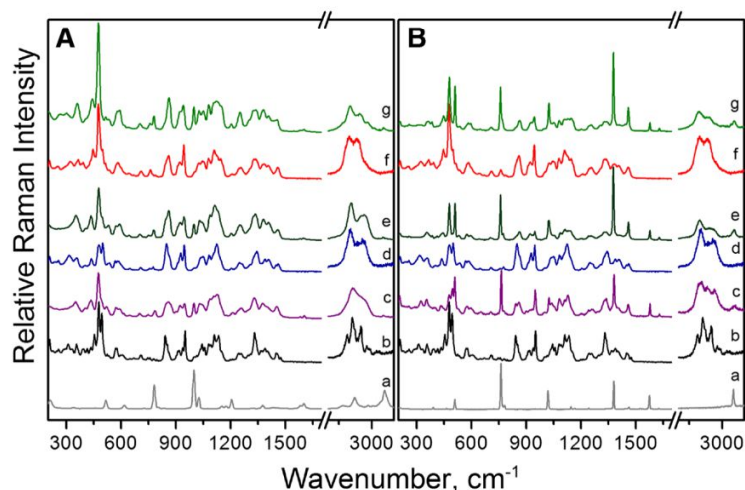
As demonstrated previously by study based on TG analysis, TOL and NAP form complexes with all three kinds of CD. Some weak peaks attributed to TOL vibrations were observed in Raman spectra, confirming the TOL contribution in complex formation. Unexpectedly, TOL vibrational modes are just

weakly impacted by interaction with host molecule. Subtle changes can be noticed in the position of peaks assigned to in-plane C–C stretch and ring deformation at 516 cm^{-1} , methyl group stretch at 781 cm^{-1} and in-plane C=C stretching at 1026 cm^{-1} (vibrational mode assignment was found in literature (Tasumi et al. 1986)). Worth noting is that latter peak was absent in the spectrum of the α CD:TOL complex. The more impacted vibrations related with C–H stretching modes were observed. Unfortunately, analysis of C–H stretching mode belonging to methyl group at 2921 cm^{-1} is rather impossible due to strong signal of CDs in this region. However, another peak representing later mode in the ring presented at 3058 cm^{-1} was found to remarkably decrease after complex formation. The comparison of shift in positions of the peaks belonging to isolated TOL and TOL engaged to the complexes with CDs can be found in Online Resource Table S6.

The interactions with TOL have caused more steric hindrance on α CD molecules than on the ones having larger diameter of cavity. Comparable effect on α CD vibrations was observed in the case of interaction with NAP. In contrary, just small disturbance on γ CD vibrations can be noticed after hosting these two aromatic guests.

The analysis of NAP peaks in inclusion complex spectra revealed similarities with those discussed previously (the “Thermogravimetric analysis” section). The most impacted modes by the complexation are related with the ring breathing, ring deformation, C–C central stretching and C–H in-plane stretching located at 761 , 1379 and 3050 cm^{-1} respectively (Fig. 4). Furthermore, considering relative intensities of these peaks, some differences were observed regarding the diameter of host cavity. The C–H symmetric stretch is supposed to be more constrained if NAP is inserted in horizontal or diagonal orientations into the CD cavity. These orientations can be achieved in $1\beta\text{CD}:1\text{NAP}$ and $1\gamma\text{CD}:1\text{NAP}$ systems. Calculated relative intensities of the peak at 3050 cm^{-1}

Fig. 6 Raman spectra of complexes formed based on CDs with TOL and NAP are presented in graphs (a) and (b) respectively. In each graph (a, b, d, f), spectra are indicating vibrations of isolated pollutant, α CD, β CD and γ CD respectively; Raman spectra of the inclusion complexes between pollutants and α CD, β CD and γ CD are given in (b), (d) and (f) respectively



showed less intensity in latter systems confirming guest diagonal orientation. Contrary, in complex with α CD, decrease in C–H stretching mode intensity is less important, suggesting the vertical guest orientation. Latter NAP orientation can be further confirmed analysing peak at 1379 cm^{-1} . This vibrational mode is less impacted when NAP is included vertically into the smallest CD. Worth noting is that a slight shift of this vibration was observed. However, for the complexes with β CD and γ CD, it shifted to a lower frequency by 3 cm^{-1} , and in the case of complex with α CD, it is moved by 2 cm^{-1} to a higher frequency, again indicating different guest interaction with the host molecule. Furthermore, comparing relative intensities of this peak, we noticed that in NAP interaction with α CD case, it increases two times, and in case of interaction with other two hosts, this vibration is three times more intense. Collation of calculated NAP vibrational modes with the relative intensities as well as of the experimentally achieved isolated NAP and NAP engaged in complexes is presented in Online Resource Table S7. To find relative intensities of NAP peaks, spectra of CDs with included NAP and the spectra of the isolated CDs were normalised regarding the peak at 2879 cm^{-1} (corresponding to the in-plane C–H stretching vibration). Then, the spectra of isolated CDs were subtracted from the complex ones and compared with NAP spectrum regarding the peak at 1025 cm^{-1} (corresponding to symmetric in-plane C–C stretching motion).

In our case, shifts in frequency and intensity of the guest peaks are mostly observed for the complex between γ CD and FL demonstrating that intermolecular interactions involved in its formation are stronger than those involved in the association of TOL and NAP in the hosts. As mentioned before, FL is compatible just with γ CD diameter of cavity for inclusion complex formation. TG analysis study has revealed that FL embedded into CD has a stoichiometry of two FL molecules in complex with one molecule of host. FL structure includes the five-member cycle connecting naphthalene and benzene units (Fig. 1b), and most likely, latter units would be responsible for an interaction with the γ CD cavities. Raman spectroscopy based analysis confirmed this arrangement, since these units have few isolated non-overlapping vibrational modes which can be studied independently. With the help of literature (Manal 2011), we have calculated the FL vibration frequencies and Raman scattering intensities of all the 72 normal modes. We present them in Online Resource Table S8 together with the achieved experimental values of isolated FL and of its complex with γ CD.

Many important spectral changes of FL can be observed in regards to complexation. The spectral comparison can be seen in Fig. 7, where FL spectra (obtained by calculations (a) and experimentally (b)) are plotted together with spectrum of FL embedded between γ CDs (d). The spectrum (c) is corresponding to the isolated γ CD.

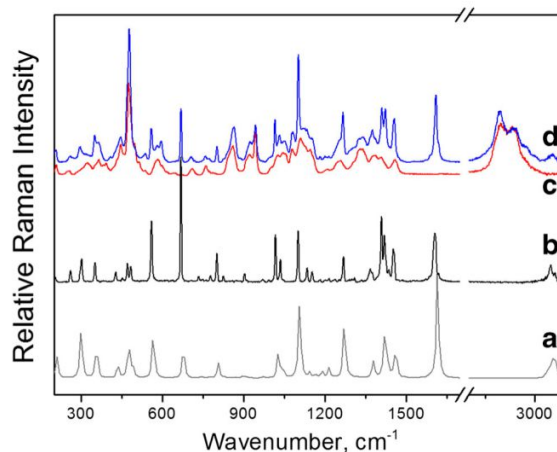


Fig. 7 Raman spectra of FL calculated and experimentally obtained are presented in graphs (a) and (b) respectively. The spectrum (c) corresponding to a free γ CD and spectrum (d) corresponds to the complex formed between FL and γ CD

The most important vibrational modes impacted by a complexation are related with the two moieties A and B that must be both involved in intermolecular interactions (scheme of molecule is presented in Fig. 1b). For instance, intensities of in-plane C–C and C–H bending seen in FL spectrum at 560 cm^{-1} for ring A breathing and at 669 cm^{-1} for ring B decrease significantly upon complexation. Other evidence is related with the three equivalent in-plane C–H rocking and C–C stretching observed in FL spectrum at 1018 cm^{-1} for ring B, 1409 cm^{-1} for both rings and 1608 cm^{-1} for ring A. All of them equally decreased and it can be explained by steric hindrances of FL molecule included into host. The important shifts in frequency, superior to 10 cm^{-1} , are observed for C–H asymmetric stretching upon complexation at 3037 , 3051 and 3059 cm^{-1} . Those three families of modified

Table 4 Comparison of FL peak shifts and relative intensities (free FL and engaged in complexes with γ CD)

FL		Complex		Assignment
Peak	Rel.Int.	Peak	Rel.Int.	
560	1.40	559	0.62	N°14 δ ring (δ CCC) A breathing
669	2.73	669	0.65	N°19 δ ring (δ CCC) B breathing
1018	1.25	1016	0.35	N°37 δ ring B (CH rock. and CC str.)
1101	1.00	1102	1.00	N°40 δ ring (CCH and CCC bending)
1409	1.71	1410	0.67	N°52 δ ring (CH rock. and CC str.)
1608	1.72	1610	1.14	N°60 δ ring A (CH rock. and CC str.)
3022	0.17	3037	0.05	N°63–65 δ CH Asym. Str.
3034	0.09	3051	0.24	N°66 δ CH Asym. Str.(ring B)
3048	0.83	3059	0.05	N°67–69 δ CH Str.

Numbers correspond to assignment in Online Resource Table S8
 γ out plane of the molecule, δ in plane of the molecule

vibrations—two breathing vibrations, three C–H rocking and C–C stretching vibrations and asymmetrical C–H stretching vibrations—can be considered as fingerprint of complexation.

Summarised comparison of the discussed FL vibrational modes with their shifted positions and changed intensities upon complexation is presented in Table 4. To find relative intensities of FL peaks, first, spectra of CD with included FL and γ CD were normalised regarding the peak at 2879 cm^{-1} (corresponding to the in plane C–H stretching vibration). Second, the spectrum of isolated γ CD was subtracted from the complex one and then compared with FL spectrum regarding the peak at 1101 cm^{-1} (corresponding to symmetric in-plane C–C–H and C–C–C bending motions).

Graphical illustration of vibrational modes which were found to be the most affected when FL is engaged in the complexes with γ CD is presented in Fig. 8.

Finally, the changes in γ CD vibrations have appeared due to FL inclusion. Mostly, they are related with C–O stretching modes ($945, 1059, 1069\text{ cm}^{-1}$) (Yao et al. 2014) and C–H stretching or wagging modes ($1341, 2875$ and 2934 cm^{-1}) (Yao et al. 2014).

The CD selectivity for complex formation. Test of specificity

The CD selectivity discussed in previous section was herein tested by mixing each CD with a solution of the three pollutants (TOL, NAP, FL). Experiments were performed by dropwise addition of the ethanol solution containing three pollutants into saturated aqueous solutions of each CD. A different procedure was applied for α CD: In this case, FL was absent in mixture of pollutants. Figure 9 presents achieved spectra of complexes formed between guests and α CD (a), β CD (c) and γ CD (e). They were normalised

Fig. 8 The main normal modes of FL vibrations mostly impacted by the complexation (C–H asymmetrical stretching modes are not represented). Numbers correspond to assignment in Table 4 and Online Resource Table S8

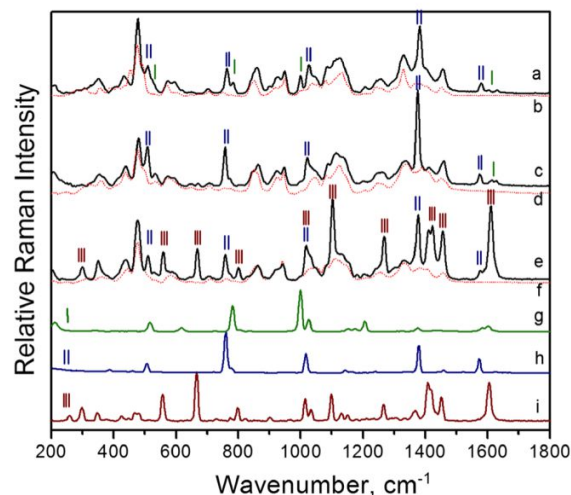
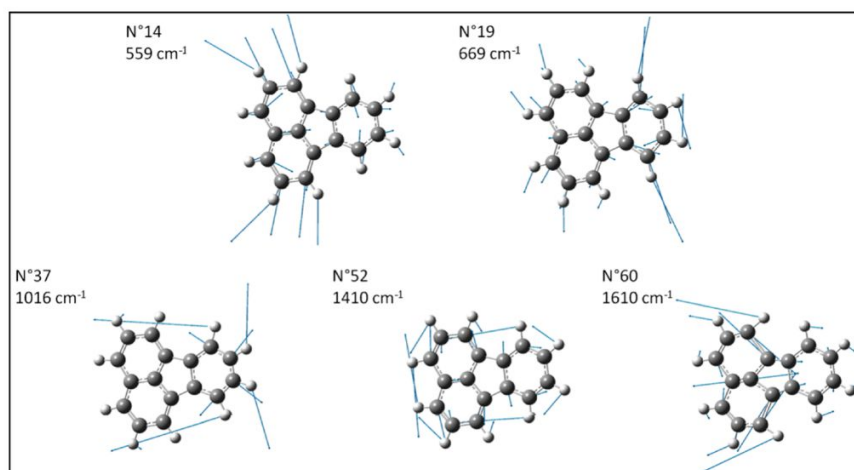


Fig. 9 Raman spectra of complexes formed mixing aromatic molecules and α CD, β CD and γ CD are presented in graphs (a), (c) and (e) respectively. The spectra (b), (d) and (f) correspond to α CD, β CD and γ CD respectively and (g), (h) and (i) correspond to TOL, NAP and FL respectively

regarding the band at 2879 cm^{-1} corresponding to a C–H stretching vibration of CD and compared to CD native forms— α CD (b), β CD (d) and γ CD (f) respectively—as well as the pollutant spectra—TOL (g), NAP (h) and FL (i) respectively.

To determine the selective interaction of the CD with specific pollutants (N_{complex}), we have calculated the ratio between the Raman intensity of the pollutants involved in the CD complex for both experiments: individual pollutant and mixture of pollutants. This ratio has been calculated as follows:

$$N_{\text{complex}}(\%) = \left(\frac{I_{\text{guest peaks}}}{I_{\text{CD,C-H mode}}} \right)_{\text{individual}} * \left(\frac{I_{\text{CD,C-H mode}}}{I_{\text{guest peaks}}} \right)_{\text{mixed}} * 100\%$$

The first term corresponds to the relative intensity of the individual pollutant in the CD complex whereas the second term corresponds to the relative intensity of the pollutant in the CD complex in the case of the mixture. Both relative intensities were normalised by the intensity of the C–H vibration mode of the CD in order to use the CD as a reference. This ratio is then independent on the Raman cross section of the pollutant modes and allows comparing directly the proportion of pollutants forming a complex with the CD.

Raman spectra of precipitants collected after mixing α CD with TOL and NAP show the appearance of peaks belonging to both pollutants (roman numerals I and II indicate peaks from TOL and NAP respectively). Further calculation of the relative intensities belonging to TOL peak located at 999 cm^{-1} and NAP peak at 761 cm^{-1} revealed that $62\pm 7\%$ of complexes in this system are formed between TOL and α CD. This latter result demonstrates higher affinity of the α CD to the TOL and then to the NAP. On the contrary, $92\pm 5\%$ of NAP was found in the complex formed between β CD and mixture of pollutants. Calculation of relative intensities of the peaks belonging to NAP and further comparison with the values presented in Table 1 confirmed 1 β CD:1NAP stoichiometry in the system. Raman spectrum of precipitants collected after mixing γ CD with three pollutants showed peaks coming from NAP and FL (roman numerals II and III indicate peaks from NAP and FL respectively). Calculation of relative intensities of guest vibrational modes (peaks at 761 cm^{-1} for NAP and at 669 cm^{-1} for FL) revealed that FL dominates in this system forming $70\pm 9\%$ of all complexes with γ CD. The explanation of why no inclusion of TOL in β CD and γ CD occurred can be related with the competitive exchange in parallel reactions. Another reason contributing more in γ CD case is that the size of the cavity is not adapted to a small TOL molecule. As a consequence, a molecule smaller than the cavity will have less interactions (hydrophobic, van der Waals, etc.) and thus less affinity with the CD. Since TOL is the smallest molecule in this reaction and γ CD shows better affinity to bigger molecules, it is possible that interaction between TOL and the large cavity of CD is too low and can be easily replaced.

Conclusion

In this study, results of TG analysis, Raman spectroscopy and DFT calculations provide information on the complex formation between organic pollutants (TOL, NAP and FL) and three forms of CDs (α , β , γ CD) in the solid state. In the first part of this study, three stoichiometries of β CD:NAP system have been analysed. The obtained results permit to rationalise the host-guest complex formation in regards to different stoichiometry. The second part of the study was dedicated to description of complexes formed between all selected pollutants with three kinds of CD. Data collected from TG analysis suggested

that mainly stoichiometry of one guest per one host was formed with the exception in α CD:TOL and γ CD:FL systems, where one guest is interacting with two host molecules. It is noteworthy that FL was found to form complex just with γ CD due to its larger size.

Using Raman spectroscopy, the most impacted vibrational modes after complex formation were analysed. In the case of TOL, a strong decrease in relative intensity of ring C–H stretching mode was observed. Other subtle changes were found for the motions related to the ring deformation, C=C stretching and methyl group symmetric deformation. The study of NAP peaks assigned to the ring breathing, ring deformation, C–C central stretching and C–H in-plane stretching gave the possibility to discuss of potential guest orientation inside the host cavity. Due to differences in the relative intensities of these modes, we assumed that vertically orientated NAP is inserted into α CD cavity. With the bigger hosts, NAP is most likely interacting in diagonal or horizontal orientations. The spectroscopic evidence of a guest molecule orientation and intermolecular interaction was found especially obvious in the FL case. Three classes of mostly impacted vibrations were found and proposed as the fingerprint for a FL engaged in complex.

Finally, all achieved spectral evidence opened the way for analysis of more complexed systems. Test of CD specificity regarding the guest size showed considerable affinity in the systems of α CD:TOL, β CD:NAP and γ CD:FL.

All achieved information could be exploited in the CD applications related to the environmental pollution monitoring and remediation.

Acknowledgments The authors would like to acknowledge the Remantas project (ANR-11-ECOT-0010), supported by French National Research Agency (ANR) for a financial support.

Conflict of interest The authors declare no conflict of interest.

References

- Amado AM, da Silva Moreira AM, Ribeiro-Claro PJA, Teixeira-Dias JJC (1994) Meta-substituted styrene molecules included in cyclodextrins: a Raman spectroscopic study. *J Raman Spectrosc* 25:599–605
- Amado AM, Ribeiro-Claro PJA (2000) Selection of substituted benzaldehyde conformers by the cyclodextrin inclusion process: a Raman spectroscopic study. *J Raman Spectrosc* 31:971–978
- Astray G, Gonzalez-Barreiro C, Mejuto JC, Rial-Otero R, Simal-Gándara J (2009) A review on the use of cyclodextrins in foods. *Food Hydrocoll* 23:1631–1640
- Bantz KC, Haynes CL (2009) Surface-enhanced Raman scattering detection and discrimination of polychlorinated biphenyls. *Vib Spectrosc* 50:29–35
- Becke AD (1996) Density-functional thermochemistry. IV. A new dynamical correlation functional and implications for exact-exchange mixing. *J Chem Phys* 104:1040–1046

- Buschmann HJ, Schollmeyer E (2002) Applications of cyclodextrins in cosmetic products: a review. *J Cosmet Sci* 53:185–191
- Carron K, Peitersen L, Lewis M (1992) Octadecylthiol-modified surface-enhanced Raman spectroscopy substrates: a new method for the detection of aromatic compounds. *Environ Sci Technol* 26:1950–1954
- Chang LM, Ding Y, Li X (2013) Surface molecular imprinting onto silver microspheres for surface enhanced Raman scattering applications. *Biosens Bioelectron* 50:106–110
- Cireli A, Yurdakul B (2006) Application of cyclodextrin to the textile dyeing and washing processes. *J Appl Polym Sci* 100:208–218
- Costa JCS, Sant'Ana AC, Corio P, Temperini MLA (2006) Chemical analysis of polycyclic aromatic hydrocarbons by surface-enhanced Raman spectroscopy. *Talanta* 70:1011–1016
- Del Valle EMM (2004) Cyclodextrins and their uses: a review. *Process Biochem* 39:1033–1046
- Dennington R, Keith T, Millam J (2009) GaussView, Version 5. Semichem Inc., Shawnee Mission
- Diggs DL et al (2011) Polycyclic aromatic hydrocarbons and digestive tract cancers. *Perspect J Environ Sci Health Part C* 29:324–357
- Dufosse L, Souchon II, Feron G, Latrasse A, Spinnler HE (1999) In situ detoxification of the fermentation medium during gamma-decalactone production with the yeast *Sporidiobolus salmonicolor*. *Biotechnol Prog* 15:135–139
- Egyed O (1990) Spectroscopic studies on beta-cyclodextrin. *Vib Spectrosc* 1:225–227
- Frisch MJ, Trucks GW, Schlegel HB, Scuseria GE, Robb MA, Cheeseman JR, Scalmani G, Barone V, Mennucci B, Petersson GA, Nakatsuji H, Caricato M, Li X, Hratchian HP, Izmaylov AF, Bloino J, Zheng G, Sonnenberg JL, Hada M, Ehara M, Toyota K, Fukuda R, Hasegawa J, Ishida M, Nakajima T, Honda Y, Kitao O, Nakai H, Vreven T, Montgomery JA Jr., Peralta JE, Ogliaro F, Bearpark M, Heyd JJ, Brothers E, Kudin KN, Staroverov VN, Kobayashi R, Normand J, Raghavachari K, Rendell A, Burant JC, Iyengar SS, Tomasi J, Cossi M, Rega N, Millam JM, Klene M, Knox JE, Cross JB, Bakken V, Adamo C, Jaramillo J, Gomperts R, Stratmann RE, Yazyev O, Austin AJ, Cammi R, Pomelli C, Ochterski JW, Martin RL, Morokum K, Zakrzewski VG, Voth GA, Salvador P, Dannenberg JJ, Dapprich S, Daniels AD, Farkas Ö, Foresman JB, Ortiz JV, Cioslowski J, Fox DJ (2009) Gaussian 09, Revision A.02. Gaussian, Inc, Wallingford
- García-Zubiri Í, González-Gaitano G, Sánchez M, Isasi J, Ramón (2004) Infrared study of solid dispersions of β -cyclodextrin with naphthalene derivatives. *J Incl Phenom* 49:291–302
- Giordano F, Novak C, Moyano JR (2001) Thermal analysis of cyclodextrins and their inclusion compounds. *Thermochim Acta* 380:123–151
- Guerrini L, Garcia-Ramos JV, Domingo C, Sanchez-Cortes S (2006) Functionalization of Ag nanoparticles with dithiocarbamate calix[4]arene as an effective supramolecular host for the surface-enhanced Raman scattering detection of polycyclic aromatic hydrocarbons. *Langmuir* 22:10924–10926
- Guerrini L, Garcia-Ramos JV, Domingo C, Sanchez-Cortes S (2009) Sensing Polycyclic Aromatic Hydrocarbons with Dithiocarbamate-Functionalized Ag Nanoparticles by Surface-Enhanced Raman Scattering. *Anal Chem* 81:953–960
- Halvorson RA, Vikesland PJ (2010) Surface-Enhanced Raman Spectroscopy (SERS) for environmental analyses. *Environ Sci Technol* 44:7749–7755
- Harris KL, Myers JN, Ramesh A (2013) Benzo(a)pyrene modulates fluoranthene-induced cellular responses in HT-29 colon cells in a dual exposure system. *Environ Toxicol Pharmacol* 36:358–367
- Hill W, Fallour V, Klockow D (1999) Investigation of the adsorption of gaseous aromatic compounds at surfaces coated with heptakis(6-thio-6-deoxy)- β -cyclodextrin by surface-enhanced Raman scattering. *J Phys Chem B* 103:4707–4713
- Koban W, Koch JD, Hanson RK, Schulz C (2004) Absorption and fluorescence of toluene vapor at elevated temperatures. *PCCP* 6:2940–2945
- Köhler JEH, Greczschak-Mick N (2013) The β -cyclodextrin/benzene complex and its hydrogen bonds – a theoretical study using molecular dynamics, quantum mechanics and COSMO-RS. *Beilstein J Org Chem* 9:118–134
- Kvenvolden KA, Cooper CK (2003) Natural seepage of crude oil into the marine environment. *Geo-Mar Lett* 23:140–146
- Lee C, Yang W, Parr RG (1988) Development of the Colle-Salvetti correlation-energy formula into a functional of the electron density. *Phys Rev B* 37:785–789
- Lienig D (1980) J. M. Neff: polycyclic aromatic hydrocarbons in the aquatic environment. 30 fig., 89 tab., 262 pp. - London: Applied Science Publishers 1979. *Int Rev Gesamten Hydrobiol Hydrogr* 65: 898
- Liu Y, Chen G-S, Zhang H-Y, Song H-B, Ding F (2004) Interaction between β -cyclodextrin and 1,10-phenanthroline: uncommon 2:3 inclusion complex in the solid state. *Carbohydr Res* 339:1649–1654
- Loftsson T, Brewster ME (1996) Pharmaceutical applications of cyclodextrins. 1. Drug solubilization and stabilization. *J Pharm Sci* 85: 1017–1025
- Maeda H, Maeda T, Mizuno K (2012) Absorption and fluorescence spectroscopic properties of 1- and 1,4-silyl-substituted naphthalene derivatives. *Molecules (Basel, Switzerland)* 17:5108–5125
- Manal OH (2011) Theoretical study of vibration spectroscopy for neutral and charged fluoranthene molecule. *J Baghdad Sci* 8:366–374
- Nagao A, Kan-no A, Takayanagi M (2009) Infrared spectra of monosubstituted toluene derivatives in cyclodextrin: orientation of guest molecules in included complexes. *J Mol Struct* 929:43–47
- Nolasco MM, Amado AM, Ribeiro-Claro PJA (2009) Spectroscopic and thermal studies on the inclusion of trans-cinnamic acid and a number of its hydroxyl-derivatives with α , β and γ -cyclodextrins molecules. *J Raman Spectrosc* 40:687–695
- O'Boyle NM, Tenderholt AL, Langner KM (2008) Cclib: a library for package-independent computational chemistry algorithms. *J Comput Chem* 29:839–845
- Pejic B, Eadington P, Ross A (2007) Environmental monitoring of hydrocarbons: a chemical sensor perspective. *Environ Sci Technol* 41: 6333–6342
- Pfannkuche J, Lubecki L, Schmidt H, Kowalewska G, Kronfeldt HD (2012) The use of surface-enhanced Raman scattering (SERS) for detection of PAHs in the Gulf of Gdansk (Baltic Sea). *Mar Pollut Bull* 64:614–626
- Readman JW, Fowler SW, Villeneuve JP, Cattini C, Oregioni B, Mee LD (1992) Oil and combustion-product contamination of the Gulf marine environment following the war. *Nature* 358:662–665
- Russell N, McNamara M (1989) FT-IR and Raman spectral evidence for metal complex formation with β -cyclodextrin as a first sphere ligand. *J Inclusion Phenom Mol Recognit Chem* 7:455–460
- Saranya G, Kolandaivel P, Senthilkumar K (2011) Optical absorption and emission properties of fluoranthene, benzo[k]fluoranthene, and their derivatives. A DFT study. *J Phys Chem A* 115:14647–14656
- Sardo M, Amado AM, Ribeiro-Claro PJA (2009) Inclusion compounds of phenol derivatives with cyclodextrins: a combined spectroscopic and thermal analysis. *J Raman Spectrosc* 40:1624–1633
- Shi, XF, Kwon, YH, Ma, J, Zheng, RE, Wang, CY, Kronfeldt, HD (2013). Trace analysis of polycyclic aromatic hydrocarbons using calixarene layered gold colloid film as substrates for surface-enhanced Raman scattering. *J Raman Spectrosc* 44:41–46
- Singh R, Bharti N, Madan J, Hiremath S (2010) Characterization of cyclodextrin inclusion complexes—a review. *J Pharm Sci Technol* 2:171–183
- Srivastava A, Singh VB (2007) Theoretical and experimental studies of vibrational spectra of naphthalene and its cation Indian. *J Biochem Biophys* 45:714–720

- Tasumi M, Urano T, Nakata M (1986) Some thoughts on the vibrational modes of toluene as a typical monosubstituted benzene. *J Mol Struct* 146:383–396
- Trotta F, Zanetti M, Camino G (2000) Thermal degradation of cyclodextrins. *Polym Degrad Stab* 69:373–379
- Varanasi U, Stein JE, Nishimoto M, Reichert WL, Collier TK (1987) Chemical carcinogenesis in feral fish: uptake, activation, and detoxication of organic xenobiotics. *Environ Health Perspect* 71:155–170
- Viglianti C, Hanna K, de Brauer C, Germain P (2006) Removal of polycyclic aromatic hydrocarbons from aged-contaminated soil using cyclodextrins: experimental study. *Environ Pollut* 140:427–435
- Xie Y et al (2011) Selective SERS detection of each polycyclic aromatic hydrocarbon (PAH) in a mixture of five kinds of PAHs. *J Raman Spectrosc* 42:945–950
- Xie Y et al (2010) Sensing of polycyclic aromatic hydrocarbons with cyclodextrin inclusion complexes on silver nanoparticles by surface-enhanced Raman scattering. *Analyst* 135:1389–1394
- Yang L, Ma L, Chen G, Liu J, Tian Z-Q (2010) Ultrasensitive SERS detection of TNT by imprinting molecular recognition using a new type of stable substrate. *Chem-Eur J* 16:12683–12693
- Yao Q, You B, Zhou SL, Chen M, Wang YJ, Li W (2014) Inclusion complexes of cypermethrin and permethrin with monochlorotriazinyl-beta-cyclodextrin: a combined spectroscopy, TG/DSC and DFT study. *Spectrochim Acta Part A* 117:576–586
- Zvereva EE, Shagidullin AR, Katsyuba SA (2010) Ab initio and DFT predictions of infrared intensities and raman activities. *J Phys Chem A* 115:63–69

4.3 Application of thiolated CD as receptor of SERS active sensors

4.3.1 Introduction

As demonstrated in the previous publication, Raman spectroscopy based study provided useful knowledge regarding the cyclodextrins host-guest complex formation with selected non-polar targeted substances (toluene, naphthalene and fluoranthene). Looking further, this section is devoted to the exploitation of the cyclodextrins ability for pollutants pre-concentration in a SERS based detection system. For this approach immobilization of the host molecules are required. As mentioned before cyclodextrins have several primer hydroxyl groups on one edge and secondary hydroxyl groups on the other edge. These groups availability and reactivity are very important for cyclodextrins chemical modification in order to functionalise metallic surfaces. Despite the development of many methods to synthesize controlled and selective cyclodextrins derivatives [1-2], thiolated cyclodextrins remains the most used for functionalisation of surfaces. Early investigations on thiolated cyclodextrins have provided significant evidences of their ability to successfully graft gold and silver surfaces ([3-5]. Studies concerning the immobilisation and orientation of cyclodextrin, their surface packing and mobility were provided by Nelles *et al.* [5]. By investigating mono- and per-thiolated cyclodextrins with various spacer lengths, they have found that mono-thiolated cyclodextrins form more packed layers, whereas a longer spacer group provide a higher layer mobility. On the other hand, more blocked surfaces were achieved by employing multi-thiolated cyclodextrins. In this case, due to multiple interactions with metallic surface, all cavities of host molecules were found to be orientated parallel to the surface.

One of the first examples of thiolated cyclodextrin application for metal surface functionalisation and observation of inclusion complexes by SERS has been proposed by Maeda *et al.* [3]. In their study, 6-(2-mercaptoethylamino)-6-deoxy- β -CD was grafted on silver colloids. Successful surface functionalisation was confirmed by SERS and Surface Enhanced Raman Resonance Spectroscopy (SERRS) was then applied to investigate the azo dyes assembly. These results encouraged other scientific groups to examine cyclodextrin-based SERS nanosensors for molecular detection applications [6-9]. It is worth to note that gold or silver colloidal nanoparticles were mainly employed in these studies. Thus, even if reported molecular detection at the trace concentrations can be reached thanks to cyclodextrin decorated colloidal nanoparticles, these systems are strictly limited to laboratory conditions.

In order to design a sensitive and reproducible SERS nanosensor for organic pollutants, we used gold nanocylinders (NCs) arrays produced by Electron-Beam Lithography (EBL). Per-6-thio-cyclodextrins were synthesized and applied to SERS nano-sensor functionalisation. Successful thiolated-

cyclodextrins synthesis was confirmed by Nuclear Magnetic Resonance (NMR) and Raman spectroscopy. Surface functionalisation step was monitored by Localized Surface Plasmon Resonance (LSPR) and UV-Visible spectroscopies. However, tested nanosensors based on grafted cyclodextrins did not exhibit relevant performances for the molecular detection. Some reasons to explain fail in detection are discussed and the chapter is finished by a short overview of the solutions in order to improve this sensing system.

4.3.2 Experimental

4.3.2.1 Materials and methods

Pharmaceutical grade CDs (α , β and γ CD) were purchased from Wacker Chemie (Germany) and used without further purification. Aromatic compounds: toluene (TOL), naphthalene (NAP) and fluoranthene (FL), and ethanol, acetone, DMF, thiourea, iodine and and triphenylphosphine were obtained from Sigma-Aldrich (France) at high purity grade and were used as received.

4.3.2.2 Chemical synthesis of thiolated cyclodextrins

- Synthesis of Per-6-iodo-cyclodextrins

These compounds were prepared according to a slightly modified procedure reported by Gadelle and Defaye [10].

β -cyclodextrin (5 g, 4.4 mmol) was added to a solution of triphenylphosphine (21 g, 80 mmol) and I_2 (20.2 g, 80 mmol) in DMF (80 mL) under argon and the mixture was stirred at 80°C for 15h. The solution was then concentrated under reduced pressure to half its volume and 30 mL of NaOMe solution (3 M) was slowly added with simultaneous cooling. The mixture was stirred 30 min at room temperature and subsequently precipitated in 800 mL of acetone (x3). The product was filtered, washed with 30 mL of ice water, and extensively dried under vacuum at 60°C. $m = 6.5$ g, 77.5%. The same procedure was applied for the synthesis of Per-6-iodo- α -cyclodextrin (6.1 g, 73%) and Per-6-iodo- γ -cyclodextrin (6.6 g, 79%).

- Synthesis of Per-6-thio-cyclodextrins

These compounds were prepared according to a slightly modified procedure reported by Rojas *et al.* [11]

Thiourea (0.718 g, 9.45 mmol) was added to a solution of Per-6-iodo- β -cyclodextrin (2g, 1.05 mmol) in 20 mL of DMF and the mixture was stirred 19h at 70°C under argon atmosphere. DMF was then removed under vacuum and NaOH (0.62 g) in 100 mL of water was added. The solution was refluxed

for 1 hour under argon, and 5 mL of HCl 2 M was added, inducing the precipitation of the product. Per-6-thio- β -cyclodextrin was filtered, washed with water and extensively dried under vacuum at 60°C. $m = 1.144$ g, 87%. The same procedure was applied for the synthesis of Per-6-thio- α -cyclodextrin (1.075 g, 82.5%) and Per-6-thio- γ -cyclodextrin (1.055 g, 84%).

4.3.2.3 Gold Nanoparticles functionalisation by thiolated cyclodextrins

Spherical gold nanoparticles (GNPs) of 80 nm stabilized by CTAB (provided by BBI solutions) were washed and pre-concentrated in solution by centrifugation (3 times at 10 000 rpm), discarding supernatant. The GNPs were then re-dispersed in 1 mL of water/DMF (1/10 v/v) solution. Subsequently, thiolated- α -cyclodextrin (3.2 mg), thiolated- β -cyclodextrin (3.7 mg) or thiolated- γ -cyclodextrin (4.3 mg) were introduced in separated vials containing GNPs. Final concentration of thiolated cyclodextrins in each vial was 3 mmol.L⁻¹. Solutions were then kept to react for 12 hours. The functionalisation procedure was terminated by centrifuging colloidal solutions 2 times at 10 000 rpm for 5 min in DMF and 2 times in water.

4.3.2.4 Gold nano-cylinders functionalisation by thiolated cyclodextrins

Gold nanocylinders (GNCs) were produced by Electron-Beam Lithography (EBL) at the University of technology of Troyes. Details of EBL procedure is described by Grand et al.[12]. This technique ensures the fabrication of nanostructures with desired shape, size and arrangement. The GNCs based substrates contained several patterns (50 μ m \times 50 μ m) with variable diameters of GNCs arrays (from 100nm in diameter up to 200 nm). The height of GNCs was set to 60 nm and the gap was kept constant to 200 nm (from edge to edge). As prepared SERS substrates prior any experiment were cleaned using UV-Ozone plasma cleaner (PSD Standard instrument, Novascan) for 20 min.

For surface functionalisation SERS substrates were immersed in thiolated cyclodextrins solutions of 3 mmol.L⁻¹ in DMF and left to incubate for 12 hours. After incubation GNCs were washed in DMF for 1 hour two times and then 1 hour in water.

4.3.2.5 Characterization

Synthesized thiolated cyclodextrins were characterized with NMR and Raman spectroscopies. All ¹H-NMR spectra were recorded in CD₃SOCD₃ using a Bruker 400 MHz spectrometer. For Raman measurements Xplora ONE micro-spectrometer (HORIBA Scientific) was used. Laser excitation wavelength of 785 nm with a power of 8 mW was focused on the sample with a x100 objective (N.A.=0.9). Integration time for signal collection was set to 60 s for CDs and their thiolated derivatives. Each spectrum was averaged of two repetitive measurements. Applied grating of 600 grooves/mm has ensured spectral resolution of less than 3 cm⁻¹.

Surface functionalisation was monitored by Extinction and SERS spectroscopies. In case of colloidal GNPs, before and after functionalisation, extinction spectra were recorded with Kontron Uvikon 941 spectrophotometer in the spectral range of 400 to 800 nm with 1 nm resolution. SERS substrates based on GNCs were monitored with Xplora ONE micro-spectrometer (HORIBA Scientific). For extinction measurements transmitted white light was collected with a x20 objective (N.A.=0.4). Measured spectral range was from 450 nm to 900 nm with a resolution of 0.5 nm. For SERS measurements laser excitation wavelength of 785 nm for colloidal solutions and 660 nm for GNCs were used. The applied powers were around 5 mW and 0.2 mW, respectively. The signal was collected with a x100 objective (N.A.=0.9) in case of GNCs whereas colloidal solutions were monitored using macroobjective with a focal length of 40 mm (NA = 0.18). Achieved spectral resolution was less than 3 cm^{-1} . Acquisition time for each measurement was set to 60s with two repetitions.

4.3.3 Results and discussion

4.3.3.1 Chemical synthesis of thiolated cyclodextrins

Chemical synthesis of thiolated CDs was monitored at each step using NMR spectroscopy. The chemical shifts are summarized for iodated and thiolated α -, β - and γ -CDs (presented in ANNEX 3).

The Figure 4.1 presents the NMR spectra comparison between native β -CD (up) and β -CD-SH (down). The recorded proton NMR shifts are in good agreement with the ones described in literature [6].

Protons involved in primary and secondary OH groups are well separated in NMR spectrum. It has been already demonstrated that, the secondary hydroxyl groups are involved in hydrogen bondings around the secondary CD rim, giving molecule rigid structure, while, the primary hydroxyl groups are not involved in any intermolecular interactions [13]. Due to hydrogen interactions, chemical shift displacement of about 1 ppm can be found between 2,3-OH and 6-OH. In NMR spectrum of β -CD protons chemical shift of secondary OH groups (2-OH and 3-OH) were observed at 5.7 and 5.6 ppm, respectively. After CD thiolation reaction these protons were slightly up-shifted. On the other hand, protons from primary OH found at 4.4 ppm completely disappeared in NMR spectrum of thiolated β -CD. Instead, a triplet around 2.1 ppm was observed, corresponding to the protons of SH group. Finally, protons from 6-CH were observed downshifted of about 0.5 and 1 ppm, respectively.

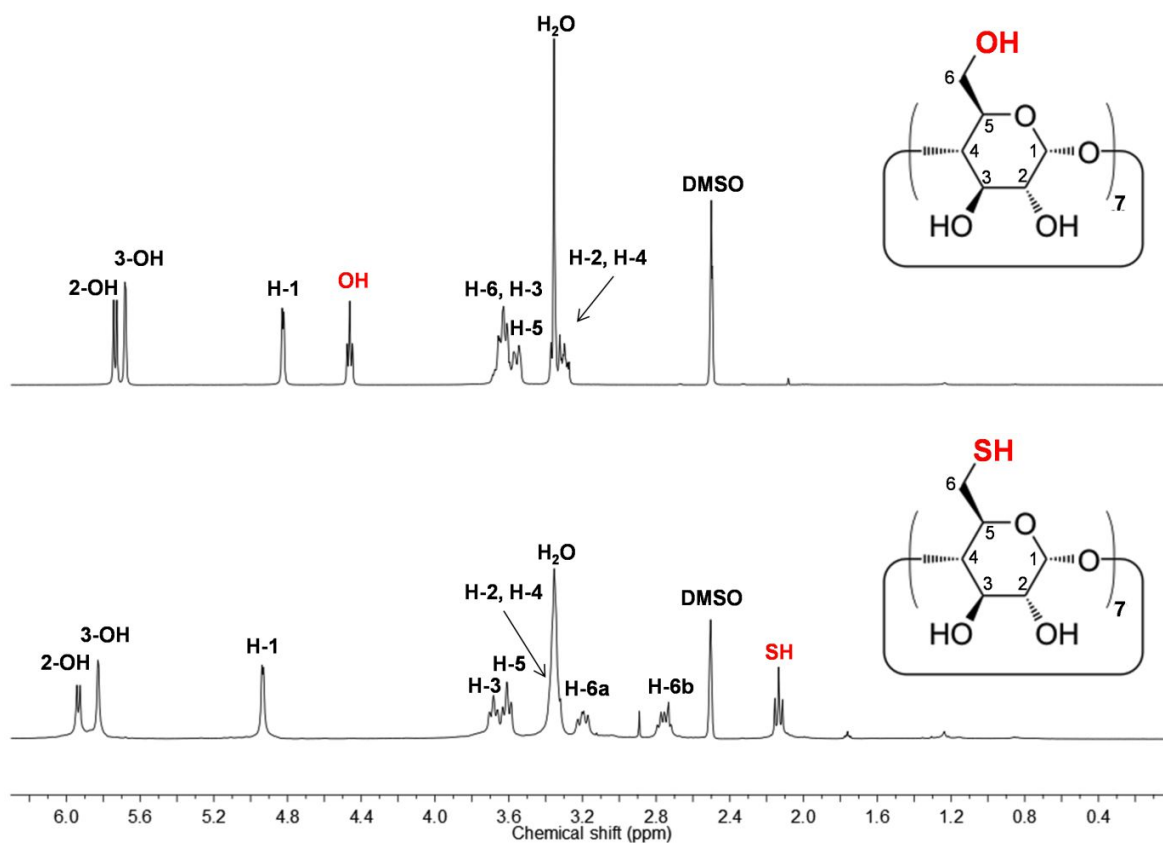


Figure 4.1 NMR spectra of native β -CD (up) and β -CD-SH (down).

The molecular conversion was also investigated by Raman spectroscopy (Figure 4.2). It is worth to note that spectra of three kinds of CDs are very similar. For this reason the peak comparison in Table 2 is presented only for native β -CD and its thiolated derivative. Given vibrational modes for β -CD can be found in spectra of other CDs with slight shift in wavenumbers.

Skeletal vibrations for all modified and native CDs were observed at similar wavenumbers with the exception of the band at 855 cm^{-1} in β -CD spectrum. This band is assigned to the breathing mode of the glucose ring [14] and more precisely related to the vibrations involving anomeric carbon atoms [15]. After chemical CDs modification this later band is not seen in this spectral region, instead new band in thiolated CDs spectra arise at 895 cm^{-1} . This indicates that the substitution of the OH group by the SH one has a direct influence on the vibrations of the glucose ring since the SH has a larger mass than the OH. This is confirmed by the increase of the intensity of the in plane deformation of the glucose ring (707 and 752 cm^{-1}) on the β -CD-SH Raman spectra.

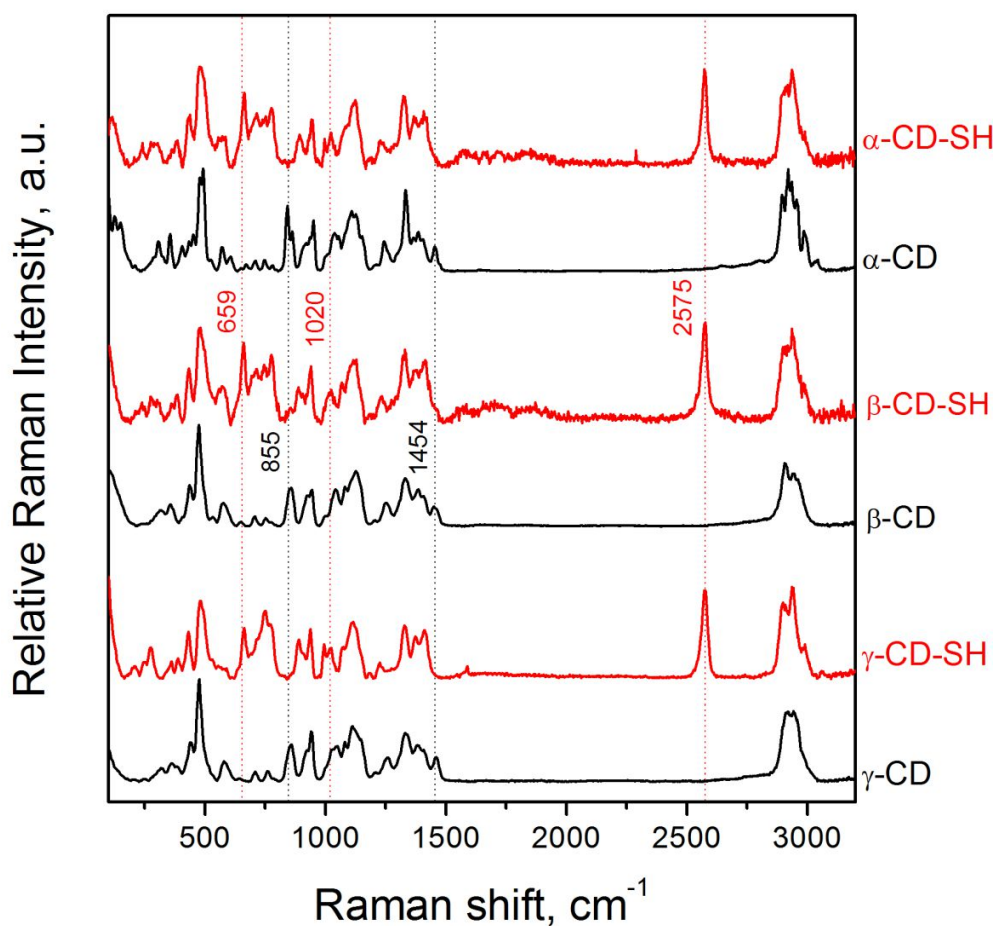


Figure 4.2 Raman spectra of native α -, β -, and γ -CD (black spectra) and their thiolated derivatives (red spectra).

The direct proof of successful primary hydroxyl groups exchange with the thiol groups was the band observed at 2575 cm^{-1} , assigned to the S-H stretching mode [16]. The position of this vibration was found exactly at the same wavenumber for all thiolated CDs.

Comparing spectra, other feature modifications are related with the C-H vibrations. For instance, C-H stretching modes at around 2900 cm^{-1} in native CDs exhibits number of peaks. One can notice, that in case of the smallest CD, the peaks in this area can be well distinguished, whereas with enclosing number of glucopyranose units, the resolution of later stretching modes is decreasing. As a consequence, in case of γ -CD one band can be seen in this spectral region. After CDs chemical modification latter peaks are more comparable between different size thiolated-CDs. Another example is related with CH_2 scissoring mode at 1454 cm^{-1} that was not observable in spectra of thiolated CDs. Moreover, the vibrational modes at 1330 cm^{-1} and 1386 cm^{-1} for β -CD were shifted, respectively, by 5 cm^{-1} and 10 cm^{-1} for thiolated ones. The decrease in wavenumber can be related with the higher molar mass of sulfur atom. The most important shift of 20 cm^{-1} was registered for peak at 1252 cm^{-1} and 1233 cm^{-1} for β -CD and β -CD-SH, respectively and was assigned to $\text{CH}_2\text{-OH/SH}$

complex related vibrations. Continuing on later feature modifications, peak at 1042 cm^{-1} in spectra of CDs were replaced by C-S stretching mode at 1020 cm^{-1} . Two additional SH stretching modes were observed in thiolated CDs spectra at lower frequency, more precisely, at 568 cm^{-1} and 659 cm^{-1} . However, due to complexity of CDs spectra later described assignments are not unambiguous and should be confirmed by molecular modeling tools.

Table 2 Experimentally registered Raman band with the assignment for β -CD and β -CD-SH.

No	β -CD	Assignment [15] [14]	β -CD-SH	No	β -CD	Assignment [15] [14]	β -CD-SH
1	316	δ CCC		13	1042	ν CO	-
2	359	γ OH	360, 383	14	1078	ν CO	1067
3	437	γ OH	432	15	1128	ν CC	1115
4	475	Out-of-pl def of gluc. ring	477	16	-		1233
5	576	γ OH/SH	568	17	1252	δ CH, γ COH	-
6	-	γ SH	659	18	1330	δ CH	1325
7	707	In-pl def of gluc. ring	701	19	1386	δ CH	1375
8	752	In-pl def of gluc. ring	748, 779	20	1406	δ OH	1414
9	855	Breath of gluc. ring		21	1454	δ CH ₂	-
10	-		895	22	-	ν SH [16]	2575
11	922, 943	ν (sym) COC	938	23	2904	ν CH	2902
12	-	ν CS	1020	24	2947	ν (asym) CH	2942

δ - scissoring; ν - stretching; γ - out-of-plane bending; sym - symmetric; asym - asymmetric.

Concerning secondary OH groups, two out-of-plane bending modes registered in low frequency range and another bands (including four peaks) found at higher frequency above 3200 cm^{-1} (not shown in Figure 4.2) for all CDs were assigned to a stretching vibrations of secondary OH groups and were observed with slight shifts after CDs modification.

This spectral analysis by both Raman and NMR techniques gave evidence of successful synthesis of the expected thiolated CDs derivatives.

4.3.3.2 Thiolated CDs application for GNPs functionalisation

Colloidal GNPs of 80 nm diameter were applied here in order to examine thiolated CDs based surface functionalisation. As described in experimental section the GNPs were introduced in a n-CD-SH (3 mmol.L^{-1}) solution. The functionalisation of the colloidal GNPs was monitored by extinction spectroscopy and SERS.

Figure 4.3 represents the comparison of extinction spectra of as prepared spherical GNPs (black spectrum) and the ones measured after functionalisation with the three kinds of thiolated-CDs. Surface plasmon resonance band observed at 549 nm wavelength for non-functionalised GNPs is redshifted by 8 nm, 3 nm and 4 nm for α , β and γ -CDs functionalised GNPs, respectively (Table 3). Worth to note that, after GNPs surface functionalisation procedure relatively more colloidal GNPs were found to be aggregated. The main issue using this kind of nanoparticles can be related with the CTAB layer since it has been already demonstrated that cyclodextrins forms host-guest complexes with CTAB molecules [17]. Thus, from the observed LSPR shift it is difficult to claim that thiolated CDs have been covalently grafted to the gold surface or are just adsorbed on CTAB layer.

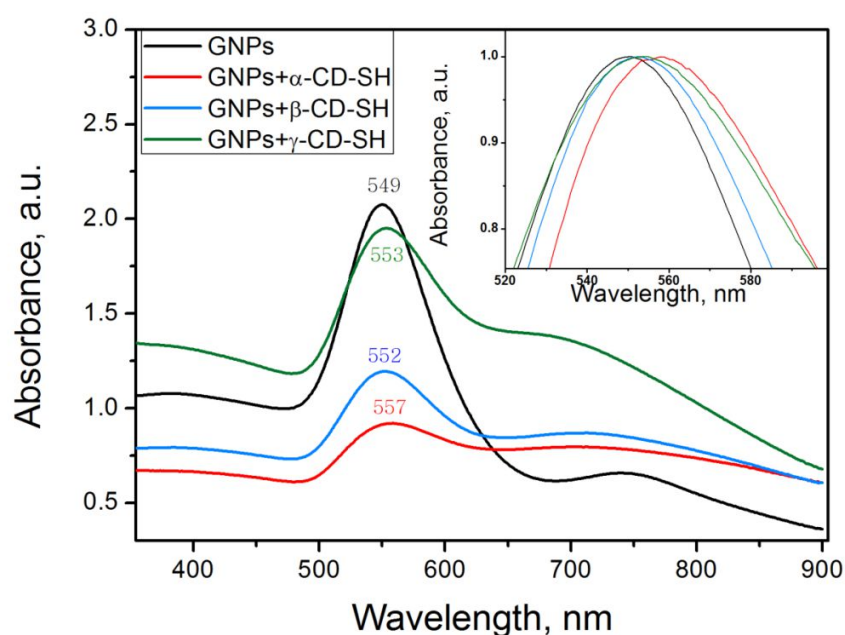


Figure 4.3 Extinction spectra of as prepared GNPs (black) and GNPs functionalised by thiolated α -CD (red), thiolated β -CD (blue) and thiolated γ -CD (green).

SERS based analysis of colloidal GNPs before and after functionalisation are presented in Figure 4.4 (purple spectra corresponding to non-modified GNPs whereas the orange ones show the spectra after the CD functionalisation). The figure contains three graphs dedicated to each CD. The black spectra in each graph represent the Raman signal of thiolated-CDs. The SERS signal of CD based GNPs (orange spectrum) are notably similar with the ones observed in Raman spectra of thiolated-CDs (black spectrum). Several bands are highly comparable between Raman and SERS measurements: the observed ones in the range of 1200 cm^{-1} and 1400 cm^{-1} corresponding to a CH and secondary OH scissoring modes as well as the OH stretching vibrational modes in lower frequency between 400 cm^{-1} and 700 cm^{-1} . These similarities confirm the thiolated CDs derivatives presence at the surface of the GNPs. However, little dissimilarity can be observed. For instance, peak at 1455 cm^{-1} assigned to scissoring of CH_2 group was not visible in spectra after CD thiolation reaction but has arisen in the

spectra of functionalised GNPs spectra at 1450 cm^{-1} . Moreover, two bands in spectra of n-CD-SH at 1065 cm^{-1} and 1115 cm^{-1} that could be related with the stretching modes of CS and CC, respectively are noticeably diminished after interaction with colloidal particles. Same observation can be done for vibrations assigned to glucose ring deformation (seen in thiolated CDs spectra at 748 cm^{-1} and 938 cm^{-1}). These spectral differences between synthesized CDs derivatives and the ones registered after grafting at the GNPs surface indicate that molecules experience some conformational modifications. However, this lead to the conclusion that the thiolated CDs were effectively attached to the NPs surface.

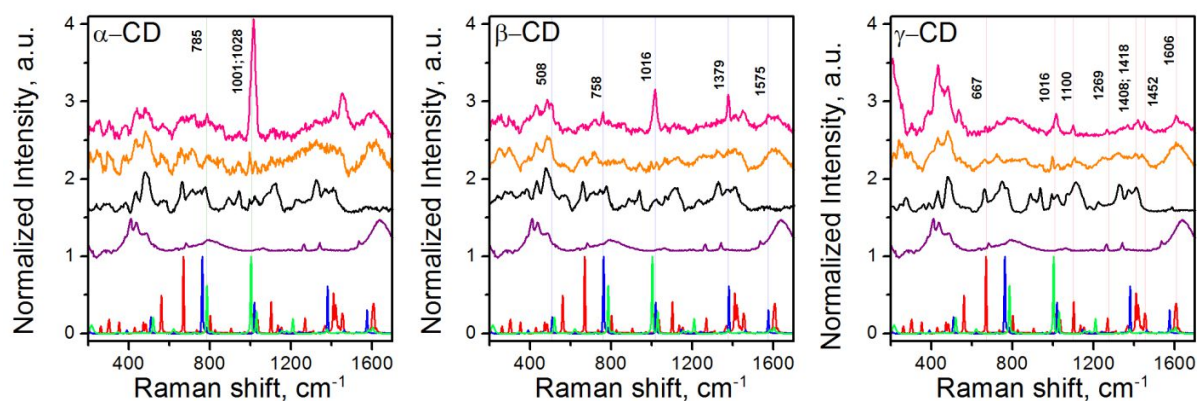


Figure 4.4 SERS based study of GNPs functionalised by three thiolated CDs and their ability in pollutants sensing. For each CD, the bottom spectrum corresponds to the superposition of the TOL, NAP and FL Raman spectra (green: TOL, blue: NAP and red: FL). The purple spectra correspond to the SERS signal of as prepared GNPs. The black spectra are the Raman signatures of the CD-SH. The orange spectra were obtained after GNPs functionalisation by thiolated CD derivatives and finally the pink spectra correspond to a signal obtained after mixing functionalised GNPs with the solution of mixed pollutants (TOL, NAP and FL).

Functionalised GNPs were then tested for the detection of TOL, NAP and FL in their mixed solution. For this purpose 1 ml of each thiolated CDs based GNPs dispersed in distilled water were mixed with $100\text{ }\mu\text{L}$ of pollutants mixture in methanol. The concentration of each targeted pollutant in the mixture was $100\text{ }\mu\text{M}$. Results of conducted SERS measurements of these solutions after 2 h incubation are presented Figure 4.4 (pink spectra). The reference spectra of TOL, NAP and FL are also given at the bottom of each graph as green, blue and red spectra, respectively.

In the graph dedicated to α -CD two new peaks can be seen. The positions of these peaks are comparable with the ones found in the spectrum of TOL: the one at 785 cm^{-1} and the doublet at 1001 cm^{-1} and 1028 cm^{-1} . It is worth to note that, CO stretching vibrational mode in methanol can be also seen at this wavenumber [18], thus, the high intensity of later band observed in a spectrum of α -CD-GNP in pollutant mixture is the most likely combined of vibrations belonging to TOL and methanol. No pre-concentration of NAP or FL was achieved by α -CD based GNP.

Other CDs based colloidal systems also demonstrated selective molecular detection. For instance, in spectrum of β -CD-GNP mixed with pollutants, four new peaks belonging to NAP were observed at 508 cm^{-1} , 758 cm^{-1} , 1379 cm^{-1} and 1575 cm^{-1} . Additional peak at 1016 cm^{-1} is comparable with the one registered in NAP Raman spectrum at 1019 cm^{-1} but could as well include signal from TOL and methanol. Remaining sensing system based on GNP decorated by γ -CDs preferably interacted with FL molecules. Peaks belonging to FL were observed at 667 cm^{-1} , 1100 cm^{-1} , 1269 cm^{-1} , 1408 cm^{-1} , 1418 cm^{-1} , 1452 cm^{-1} and 1606 cm^{-1} .

To conclude, size selective molecular detection by colloidal GNP coated with different thiolated CDs revealed similarities observed by Raman study performed on host-guest complexes formed between native CDs and same pollutant molecules. The observed SERS signal of targeted molecules is quite low for a given high concentration of pollutants in the solution. Despite that, performed study provided first proofs of both successful thioated CDs based surface functionalisation and their ability for selective sensing of the targeted molecules.

4.3.3.3 Thiolated CDs application for GNCs functionalisation

Similar functionalisation procedure was applied to graft the thiolated CDs to the GNCs surface. Briefly, SERS substrates were first washed in UV-ozone cleaner and then immersed for 12 hours in a solution of DMF/water mixture with 3 mM of thiolated CDs. After incubation nanostructures were rinsed in DMF (2 x 1 hour) and in water (2 x 1 hour). Extinction spectroscopy and SERS were used to monitor the surface functionalisation steps. Figure 4.5 summarises the results obtained by extinction spectroscopy for thiolated α -CD. After functionalisation of GNCs the LSPR is redshifted indicating that the CDs molecules are actually grafted at the surface.

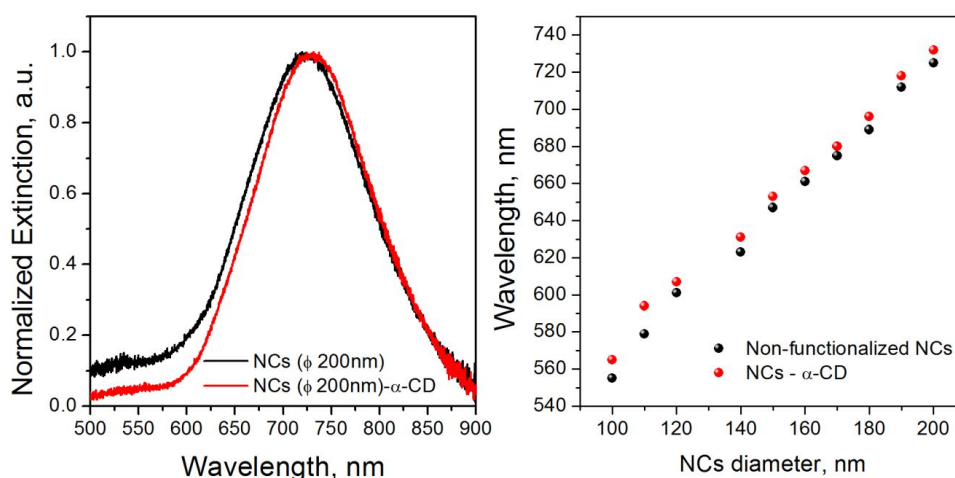


Figure 4.5 Right: Extinction spectra of the GNCs before (black spectrum) and after (red spectrum) the functionalisation by the thiolated α -CD. Left: LSPR positions for diameters GNCs from 100 up to 200 nm before (black dots) and after (red dots) the functionalisation by the thiolated α -CD.

Table 3 LSPR position redshift after surface functionalisation using thiolated α -, β - and γ -CDs, and recorded on diameter from 80 nm up to 200 nm.

n-CD-SH	n-CD-SH MM, g/mol	Shift in LSPR position, nm	
		GNPs ϕ 80nm	GNSs ϕ 100-200 nm
α -CD-SH	1068	8	5-10
β -CD-SH	1247	3	1-4
γ -CD-SH	1425	4	1-8

The left graph in Figure 4.5 shows the LSPR positions recorded on different diameter GNCs arrays from 100 nm up to 200 nm. As a consequence of the surface functionalisation the LSPR positions are red-shifted between 5 and 10 nm for all diameters. Experiments performed on the two other kinds of thiolated CDs led to similar observation (data summarised in Table 3).

Interestingly, smaller LSPR position redshifts between 1-4 nm and 1-8 nm were registered after GNCs functionalisation by β -CD-SH and γ -CD-SH, respectively. From all experimentally registered extinction results it is clearly visible that LSPR position shift does not depend on the mass of the grafted molecule. The smallest α -CD-SH led to higher LSPR red-shift. Regarding literature, α -CD was found to form multilayer. More precisely it has been demonstrated that in the bulk solution α -CD constructs oligomers with the CDs already grafted at the surface [19]. Thus the α -CD should form denser layer at the surface than the other CDs which induces a higher redshift of the LSPR.

Unfortunately, we notice major drawbacks using such SERS substrate for pollutant detection: (i) after functionalisation, the SERS signal of the grafted CDs was not observable and (ii) no spectral differences were noticed after incubating substrates in increasing concentrations of pollutants (the maximum concentrations investigated were 400 ppm for TOL, 25 ppm for NAP and 10 ppm for FL).

Only one SERS substrate functionalised with α -CD-SH gave some positive results (see Figure 4.6). Worth to note, that this sensor was contaminated by polymeric material prior surface functionalisation. As in case of all tested substrates signal of CD was not observed. However, after incubation in solutions with different concentrations of TOL (50 ppb, 50 ppm and 400 ppm, incubation time for one concentration was 2 hours) the SERS spectra exhibited new peaks at 754 cm^{-1} , 897 cm^{-1} , 1074 cm^{-1} , 1245 cm^{-1} , 1291 cm^{-1} and 1391 cm^{-1} . Intensities of mentioned peaks increased with the TOL concentration. Furthermore, the observed signal could not be directly compared with the TOL Raman reference spectrum. This observation would lead to the conclusion, that TOL molecules were pre-concentrated at the nanosensor surface not by attached α -CDs cavities but more by non-specific adsorption onto polymeric contamination.

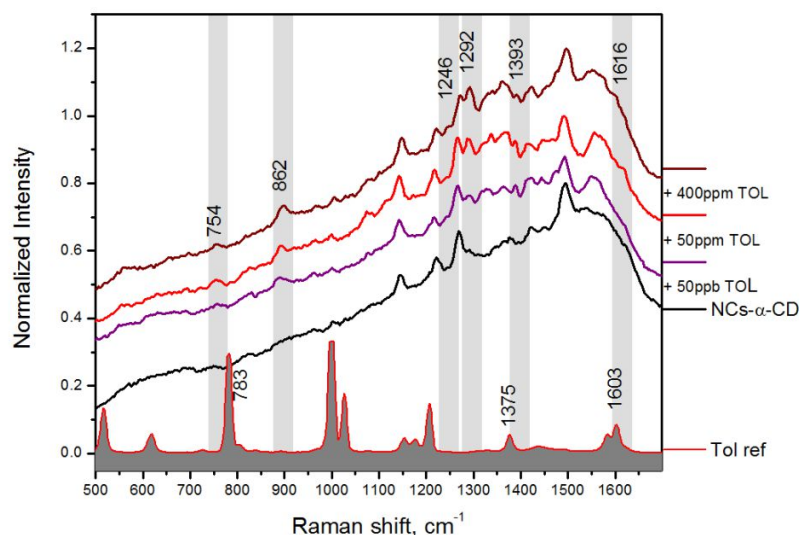


Figure 4.6 SERS spectra of thiolated α -CD functionalised GNCs (black) and of the detection of TOL for various concentrations: 50 ppb (purple spectrum), 50 ppm (red spectrum) and 400 ppm (brown spectrum) in water. SERS spectra are the average of 9 individual measurements on different diameter GNCs arrays (from 130 nm up to 200 nm). TOL Raman spectrum is given for comparison in grey.

To explain why performed SERS experiments have failed it is worth to discuss few factors. First of all, selected surface functionalisation strategy by applying multithiolated n-CDs generally not produces well packed and organized monolayers. It has been reported in literature that just 64 % of surface coverage was achieved by self assembly of per-thiolated β -CD on gold [11]. The reason of this low coverage is related to the steric effects that involves a misorientation of the CD torus axis. In order to slightly increase number of CD molecules on the surface Nelles *et al.*, proposed to include a spacer between the CD molecule and the thiol group [5]. In this case the CDs based layer organization would be tuned by the intermolecular interactions between the spacer groups. Other strategy that could improve the monolayer formation is the application of long chain monothiolated CD derivatives [4]. In latter reference gold surface coverage was increased by a factor 4 using monothiolated CD with the alkane chain spacer of 10 carbon atoms.

Per-thiolated CDs without spacer group were selected in this study with the aim to form the closest monolayer to the gold surface and thus to benefit of the strongest SERS enhancement for the targeted molecules detection. In all cases after the functionalisation the LSPR band is redshifted indicating CDs presence at the nanostructured surface; however the signals of grafted CDs or of pollutant molecules were not observed. The fact of possible insufficient monolayer formation leads to discuss the sensing limitations in such system, due to non-homogeneous electromagnetic field enhancement distribution at the surface of the nanostructures. It has been assumed that corners and sharp edges of

nanostructures evidence much larger electromagnetic field enhancement compared to smooth areas [20]. Thus, it is highly possible that thiolated CDs grafting on sharp corners is prohibited due to steric hindrance. This would explain why no targeted molecule detection was observed by multithiolated CDs based SERS substrates. On the other hand, result of TOL sensing by contaminated α -CD decorated GNCs suggested promising perspectives in application of CDs based polymers.

For the last study low cost commercially available β -CD polymer has been selected as a good candidate to overcome difficulties related with the surface coverage problem.

4.3.3.4 β -CD polymer application for GNCs decoration

Direct physical adsorption of β -CD polymer (schema of molecular structure can be seen in figure 2 in ANNEX 3) was tested by depositing a drop of a water solution of 100 μ L containing 1g.L⁻¹ of polymer on the GNCs (incubation time: 5 min). The SERS substrate was then washed with pure water and dried under flow of nitrogen. Extinction spectra were monitored on different diameters (from 130 nm up to 200 nm) of GNCs before and after surface functionalisation (Figure 4.7 left). The right graph in Figure 4.7 shows the position of LSPR for each diameter of GNCs before (black dots) and after (red dots) physical polymer adsorption. The redshifted LSPR positions between 3 and 6 nm led to the conclusion that nearly homogeneous physical adsorption of β -CD polymer was achieved.

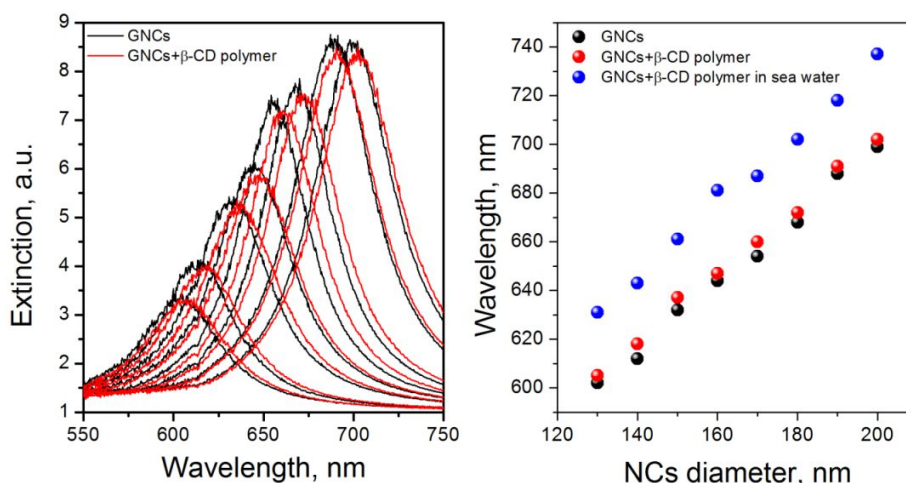


Figure 4.7 Left: Extinction spectra of various diameters of GNCs from 130 nm up to 200 nm before (black spectra) and after (red spectra) surface functionalisation by β -CD polymer. Right: LSPR position versus GNCs diameter before (black dots) and after (red dots) polymer adsorption and measured in artificial sea water (blue dots).

As in previous studies we tested this substrate for the pollutant detection. Based on previous observations, NAP, as targeted molecule was chosen to ensure the highest possibility of host-guest complex formation. It is worth noting that SERS was measured in liquid conditions during this experiment preventing from NAP molecules evaporation. First extinction measurements were

performed in liquid conditions (artificial sea water) to determine which diameter of GNCs will provide the highest SERS signal (Figure 4.7). For these measurement a microscopic slide with a cavity was used (see figure 2 in ANNEX 1).

Large change in refractive index, around GNCs due to great salinity of the artificial sea water, redshifted the LSPR position by around 30 nm. Thus, 150 nm diameter GNCs were selected to obtain the best SERS enhancement using laser at 660 nm.

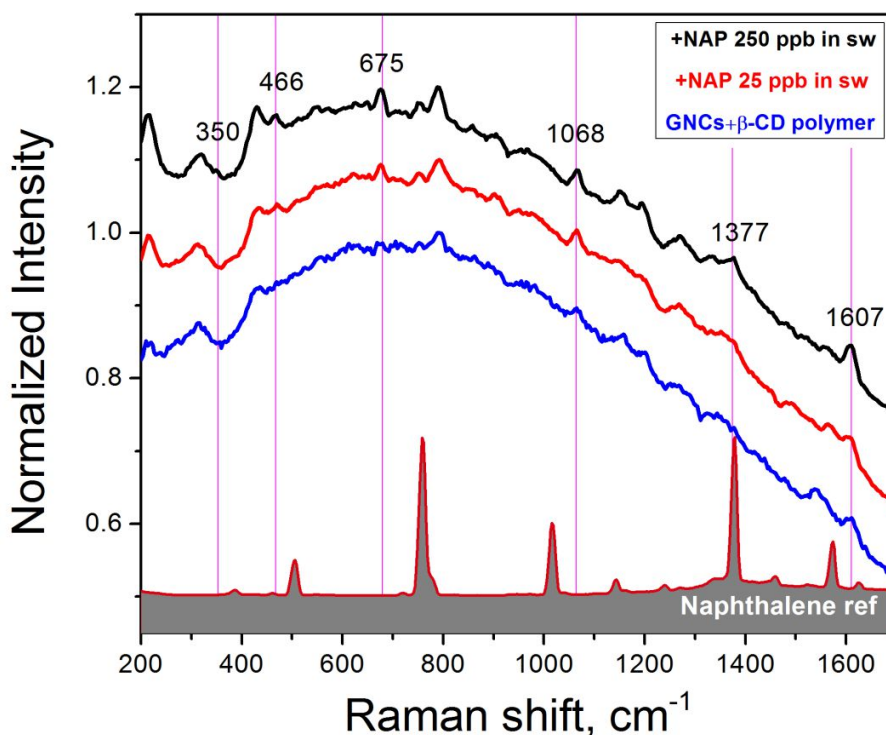


Figure 4.8 SERS spectrum of β -CD polymer adsorbed on GNCs (blue line) and of the detection of NAP at 25 ppb concentration (red line) and 250 ppb concentration (black line) in sea water. At the bottom the NAP Raman reference spectrum is given in grey. Power of laser was set at $450 \mu W$, accumulation time was 20s. Each spectrum is an average of 5 measurements. Used objective was $\times 60$ with a correction collar set to 1.1 mm (N.A. 0.7)

SERS measurements were first conducted on β -CD polymer modified GNCs in sea water (Figure 4.8 blue spectrum). Many low intensity bands were observed at 752 cm^{-1} , 792 cm^{-1} and 1607 cm^{-1} but cannot be assigned directly to the previous described β -CD vibrations. The substrate was then tested for NAP detection by immersing it in different NAP concentrations (25 ppb and 250 ppb) in sea water/methanol (9/1) mixture. 2 hours of incubation time was set for each concentration and SERS measurements were then acquired. Results are presented in Figure 4.8 as red and black spectra for 25 ppb and 250 ppb concentrations, respectively. It is noticeable, that the relative intensities of some peaks presented in β -CD polymer modified GNCs spectrum was slightly amplified after interaction with the pollutant molecules. For instance, peaks at 675 cm^{-1} , 1068 cm^{-1} and 1607 cm^{-1} show an

increased intensity. Moreover, after incubation in NAP solutions, new peaks appeared in the spectra at 350 cm^{-1} and 466 cm^{-1} as well but they are not comparable with the ones in NAP reference spectrum. However, their intensities increased with higher investigated pollutant concentration. Furthermore, the band at 1377 cm^{-1} raised after incubating substrate in 250 ppm NAP solution can be attributed to NAP in plane CC stretching.

As a conclusion, performed conceptual study based on β -CD polymer application for nano-structured surface decoration showed positive results. Considering this strategy for the design of SERS sensors dedicated to pollution monitoring, chemical attachment of polymer has to be ensured.

4.3.4 References

- 1 Boger, J., Corcoran, R. J. and Lehn, J.-M. (1978). Cyclodextrin chemistry. Selective modification of all primary hydroxyl groups of α - and β -cyclodextrins, *Helvetica Chimica Acta*, **61**, pp. 2190-2218.
- 2 Khan, A. R., Forgo, P., Stine, K. J. and D'Souza, V. T. (1998). Methods for Selective Modifications of Cyclodextrins, *Chemical Reviews*, **98**, pp. 1977-1996.
- 3 Maeda, Y. and Kitano, H. (1995). Inclusional Complexation by Cyclodextrins at the Surface of Silver As Evidenced by Surface-Enhanced Resonance Raman Spectroscopy, *The Journal of Physical Chemistry*, **99**, pp. 487-488.
- 4 Weisser, M., Nelles, G., Wohlfart, P., Wenz, G. and Mittler-Neher, S. (1996). Immobilization kinetics of cyclodextrins at gold surfaces, *The Journal of Physical Chemistry*, **100**, pp. 17893-17900.
- 5 Nelles, G., Weisser, M., Back, R., Wohlfart, P., Wenz, G. and Mittler-Neher, S. (1996). Controlled Orientation of Cyclodextrin Derivatives Immobilized on Gold Surfaces, *Journal of the American Chemical Society*, **118**, pp. 5039-5046.
- 6 Hill, W., Fallourd, V. and Klockow, D. (1999). Investigation of the adsorption of gaseous aromatic compounds at surfaces coated with heptakis(6-thio-6-deoxy)-beta-cyclodextrin by surface-enhanced Raman scattering, *Journal of Physical Chemistry B*, **103**, pp. 4707-4713.
- 7 Xie, Y., Wang, X., Han, X., Song, W., Ruan, W., Liu, J., Zhao, B. and Ozaki, Y. (2011). Selective SERS detection of each polycyclic aromatic hydrocarbon (PAH) in a mixture of five kinds of PAHs, *Journal of Raman Spectroscopy*, **42**, pp. 945-950.
- 8 Xie, Y., Wang, X., Han, X., Xue, X., Ji, W., Qi, Z., Liu, J., Zhao, B. and Ozaki, Y. (2010). Sensing of polycyclic aromatic hydrocarbons with cyclodextrin inclusion complexes on silver nanoparticles by surface-enhanced Raman scattering, *Analyst*, **135**, pp. 1389-1394.
- 9 Xu, J. Y., Wang, J., Kong, L. T., Zheng, G. C., Guo, Z. and Liu, J. H. (2011). SERS detection of explosive agent by macrocyclic compound functionalized triangular gold nanoprisms, *Journal of Raman Spectroscopy*, **42**, pp. 1728-1735.
- 10 Gadelle, A. and Defaye, J. (1991). Selective Halogenation at Primary Positions of Cyclomaltooligosaccharides and a Synthesis of Per-3,6-anhydro Cyclomaltooligosaccharides, *Angewandte Chemie International Edition in English*, **30**, pp. 78-80.
- 11 Rojas, M. T., Koeniger, R., Stoddart, J. F. and Kaifer, A. E. (1995). Supported Monolayers Containing Preformed Binding Sites. Synthesis and Interfacial Binding Properties of a Thiolated .beta.-Cyclodextrin Derivative, *Journal of the American Chemical Society*, **117**, pp. 336-343.
- 12 Grand, J., Kostcheev, S., Bijeon, J. L., de la Chapelle, M. L., Adam, P. M., Romyantseva, A., Lérondel, G. and Royer, P. (2003). Optimization of SERS-active substrates for near-field Raman spectroscopy, *Synthetic Metals*, **139**, pp. 621-624.

- 13 Bender, M. L. and Komiyama, M. (1978). Cyclodextrin Chemistry: Springer-Verlag Berlin Heidelberg.
- 14 Li, W., Lu, B., Sheng, A., Yang, F. and Wang, Z. (2010). Spectroscopic and theoretical study on inclusion complexation of beta-cyclodextrin with permethrin, *Journal of Molecular Structure*, **981**, pp. 194-203.
- 15 Egyed, O. (1990). Spectroscopic studies on beta-cyclodextrin, *Vib. Spectrosc.*, **1**, pp. 225-227.
- 16 Socrates, G. (2001). *Infrared and Raman Characteristic Group Frequencies: Tables and Charts (3ed)* (Chichester (U.K.) ed.): Wiley.
- 17 Chen, X.-m. (2011). Inclusion Complex of β -cyclodextrin with CTAB in Aqueous Solution, *Chinese Journal of Chemical Physics*, **24**, pp. 484.
- 18 Boyaci, I. H., Genis, H. E., Guven, B., Tamer, U. and Alper, N. (2012). A novel method for quantification of ethanol and methanol in distilled alcoholic beverages using Raman spectroscopy, *Journal of Raman Spectroscopy*, **43**, pp. 1171-1176.
- 19 Lee, J.-Y. and Park, S.-M. (1998). Electrochemistry of Guest Molecules in Thiolated Cyclodextrin Self-Assembled Monolayers: An Implication for Size-Selective Sensors, *The Journal of Physical Chemistry B*, **102**, pp. 9940-9945.
- 20 Haes, A. J., Zou, S., Schatz, G. C. and Van Duyne, R. P. (2004). Nanoscale Optical Biosensor: Short Range Distance Dependence of the Localized Surface Plasmon Resonance of Noble Metal Nanoparticles, *The Journal of Physical Chemistry B*, **108**, pp. 6961-6968.

4.4 Conclusion

To conclude this chapter, the good results obtained by TG analysis, Raman spectroscopy and DFT calculations provided sufficient proofs on the complex formation between organic pollutants (TOL, NAP and FL) and three forms of CDs (α , β , γ -CD) in the solid state. Moreover, the CDs specificity regarding the guest size was evaluated. These results encouraged to exploit CDs ability of pollutants pre-concentration for SERS based detection. In order to graft CDs to a gold surface thiol groups were chemically attached to CD. Raman and NMR techniques were used to characterize synthesized thiolated-CDs derivatives.

First application of thiolated-CDs to a functionalisation of colloidal nanoparticles provided similar results of size selective molecular pre-concentration as it was observed by Raman study performed on host-guest complexes formed between native CDs and same pollutant molecules. However, the experiments repeated on GNCs fabricated by EBL lithography were rather unsuccessful. Non-homogeneous surface coverage was discussed to explain this failure. In order to overcome later limitation β -CD polymer was tested for nano-structured surface decoration. The conceptual try in NAP detection at very low concentrations demonstrated encouraging results.

5 Exploitation of diazonium salts for nanosensors functionalisation for pollutant detection

5.1 Introduction

Strategies of the design of nanosensors often based on pollutants pre-concentration via non-specific physical adsorption driven by weak van der Waals or hydrophobic interactions. For this manner, different properties possessing polymeric coatings or the molecules forming Self Assembled Monolayer can be employed.

In this chapter diazonium salts applications for a SERS based nanosensor functionalisation will be investigated. Diazonium salts are the considerable alternative to the SAMs. It covalently grafts to the conductive surfaces, forming stable and robust coating layers. Moreover, under controlled conditions the thickness of latter phenyl derivatives layer can be customized in order to provide more interaction sites for an analyzed analyte. The study on diazonium salts described in this chapter will start from their chemical synthesis. In this part, Raman spectroscopy based study was performed on synthesized diazonium salts and their corresponding primary amines in order to confirm the success of diazonium salt synthesis as well as assign the characteristic vibrational signatures. Completed study led to further diazonium salts implementation on the nanostructured gold surface functionalisation. Primarily, EBL substrates were used due to its variable diameters nanocylinders with reproducible surface geometry. Four synthesized diazonium salts were employed for the surface functionalisation. The investigation of formed coating layers were then investigated by SERS. When possible, DFT modeling and XPS investigation were performed, in order to better understand the nature of the interface between surface and the organic coating. Collecting evidences of controllable surface functionalisation on nanostructures fabricated by EBL encouraged to involved commercially available SERS substrates. Reproducing the same protocol of the surface functionalisation, prepared nanosensors were then tested for pre-concentration and detection of selected targeted pollutants (naphthalene, fluoranthene and benzo[a]pyrene).

It is worth to note, that sections in this chapter are in preparation to be submitted in the international journals as the research articles. Supplementary informations for these sections can be found in ANNEX 4 - ANNEX 6.

5.2 Raman characterization of phenyl-derivatives: from primary amine to diazonium salts

Stéphanie Betelu^{1‡*}, Inga Tijunelyte^{2‡}, Leïla Boubekour-Lecaque³, Ioannis Ignatiadis¹, Anne Caroline Schnepf¹, Erwann Guenin², Nadia Bouchemal², Nordin Félij³, Emmanuel Rinnert⁴, Marc Lamy de la Chapelle².

¹BRGM, Water, Environment and Eco-technology Division, F-45060 Orléans Cedex 02, France

²University Paris 13, Sorbonne Paris Cité, CSPBAT laboratory, UMR 7244 CNRS, UFR SMBH, 74, Rue Marcel Cachin, 93017 Bobigny, France

³Univ Paris Diderot, Sorbonne Paris Cité, ITODYS, UMR 7086 CNRS, 15 rue J-A de Baïf, 75205 Paris Cedex 13, France

⁴IFREMER, Brittany center, Measurements, Detection and Sensors Laboratory, CS10070, 29280 Plouzané, France

Supplementary Information in ANNEX 4

Abbreviations

ADD: Aryl-Diazonium Derivatives

DS: Benzenediazoniumtetrafluoroborate

DS-COOH: 4-carboxybenzene diazoniumtetrafluoroborate

DS-C₁₀H₂₁: 4-decyl benzenediazoniumtetrafluoroborate

DS-(CH₂)₂NH₂: 4-(aminoethyl) benzenediazoniumtetrafluoroborate

DFT: Density Functional Theory

NBO: Natural Bond Orbital

Keywords:

Phenyl-amines, Diazonium salts, Synthesis and Characterization, RAMAN, DFT calculations.

5.2.1 Abstract

This paper reports on a preliminary study designed as a lead-in to further examinations to investigate, improve and/or control reaction pathways using the synthesized diazonium salt.

The objective is to provide, by using Raman spectroscopy, the characterization of phenyl-derivatives fate, from phenyl-amines to Aryl-Diazonium Derivatives (ADD). Four ADD have been investigated (i) benzene diazoniumtetrafluoroborate (DS), (ii) 4-decyl benzene diazoniumtetrafluoroborate (DS-C₁₀H₂₁), (iii) 4-carboxybenzene diazoniumtetrafluoroborate (DS-COOH) and (iv) 4-(aminoethyl) benzene diazoniumtetrafluoroborate (DS-(CH₂)₂NH₂). In this work, Raman investigation of the above synthesized ADD confirmed the existence of the N≡N bond stretching in the range 2285-2305 cm⁻¹. Moreover, the strong band related to the both CH in plane bending and C-N stretching modes, in the range 1073-1080 cm⁻¹, constitutes an actual signature of phenyl derivatives stemming from ADD.

Furthermore, the H-N-(ring) symmetric stretching modes, the ring-N as well as the benzene ring vibrational modes, the C-H related vibrations and the functions in para-position carried by the aromatic ring have been analyzed and discussed. The effect of the structural changes as well as conformational rearrangements from amines to ADD and the influence of the substituent located in the para-position on the Raman modes have been examined. Finally, Raman experiments supported by DFT modelling allowed us to determine the crystalline structure of DS-COOH.

Currently, the tailoring of the surface chemistry of functionalised Gold NanoStructures (GNS, electron beam nano-lithographed SERS substrates) is in progress in order to examine and strengthen the nature of the interface between the GNS and the organic coating for further development of robust SERS nanosensors for (bio)sensing.

5.2.2 Introduction

Aryl-Diazonium Derivatives (ADD) are a class of highly useful reaction intermediates or reagents. Their salts are generally obtained from the diazotization of aromatic amines in the presence of hydrogen tetrafluoroborate, hexafluorophosphate or hexafluoroantimonate as counter-ions [1].

Aryl-diazonium salts are widely used in organic chemistry as reactants in different syntheses. For instance, the process of nitrogen elimination from diazoniumcations is a fundamental stage of the Meerwein [2] and Sandmeyer [3,4] reactions. For both of these reactions, the improvement of the yield depends on the application of diazonium salts, which lose dinitrogen effectively.

Moreover, the rise in popularity of aryl-diazonium salts has resulted from their efficiency in surface functionalisation. Indeed, this methodology gives rise to covalently attached coatings bearing a wide range of functional groups onto conducting or semi conducting materials [5-14]. In addition, the grafting can be accomplished by either chemical (spontaneous grafting), electrochemical or physical methodologies [5-12,15]. Surface functionalisation using diazonium salts has thus turned up as one of the most powerful method for linking coatings [8,13,14], (bio)molecules [16,17], polymers [18-20] or nanoparticles[21]. The resulting high performance materials show improved chemical and physical properties and find widespread applications [22].

Whatever the diazonium salt application, the identification of the molecular bonds is of a great importance in order to investigate, improve and/or control reaction pathways. Among the methodologies, one of the most accurate methods is based on Raman spectroscopy for the determination of specific vibrational modes and thus for the identification of the molecular bonds and structures.

In this work, four ADD have been synthesized and investigated.

- Benzenediazoniumtetrafluoroborate (DS)
- 4-carboxybenzene diazoniumtetrafluoroborate (DS-COOH)
- 4-decyl benzenediazoniumtetrafluoroborate (DS-C₁₀H₂₁)
- 4-(aminoethyl) benzenediazoniumtetrafluoroborate (DS-(CH₂)₂NH₂).

This work provides the characterization of the fate of phenyl-derivatives: from phenyl-amine derivatives to ADD by using Raman spectroscopy. Of particular interest, the N≡N group vibrations, the H-N-(ring) symmetric stretching modes, the ring-N as well as the benzene ring vibrational modes, the C-H related vibrations and the para functions carried by the aromatic ring, are analyzed and discussed. For some bands, the effect of the structural changes as well as conformational rearrangements from the amine to the diazonium salt is examined. The influence of the substituent

located in the para position is discussed. In addition, Density Functional Theory (DFT) calculations and Natural Bond Orbital (NBO) charges have been performed for DS-COOH in order to provide a better insight on the bands assignment and to strengthen Raman spectra interpretation.

5.2.3 Experimental

5.2.3.1 Materials and reagents

Sodium nitrite (NaNO_2), Tetrafluoroboric acid (HBF_4), diethyl ether (>98%, ACS reagent), aniline, 4-docyl-aniline, 4-aminobenzoic acid, 4-(2-aminoethyl)-aniline were purchased from Sigma Aldrich.

5.2.3.2 Diazonium salt synthesis

Diazonium salts were obtained by the oxidation of the corresponding aryl-amine at 0°C by using sodium nitrite. For the four different diazonium salts, 4 mmol of the corresponding amine were mixed with 2 mL of tetrafluoroboric acid dissolved in 7 mL of milli-Q water. Then, the mixture was cooled in ice for 15 minutes. Afterwards, a solution of 300 mg of sodium nitrite dissolved in less than 1 mL of milli-Q water was added dropwise. During the reaction, the temperature was maintained at 0°C . After two hours of reaction, the mixture was filtered through $0.2\ \mu\text{m}$ cellulose ester filters (Whatman, France) and generously washed with cold diethyl ether. Only $\text{DC}_{10}\text{H}_{21}$ was rinsed with milli-Q water.

Diazonium salts purification has consisted (i) in dissolving the crude solid into small amount of deionized water and (ii) the recrystallization into diethyl ether. Recrystallization procedure lasts for 48 hours at 6°C . Recrystallized diazonium salts were filtered ($0.2\ \mu\text{m}$ of cellulose ester filters (Whatman, France), dried and stored at -20°C .

It is worth noting that the choice of the aryl-diazonium salts was motivated by the development of “long life” robust (bio)sensors since they could be used for surface functionalisation in order to provide accurate preconcentration of (bio)organic compounds for sensitive and reproducible sensing. The physical and the chemical properties of the salts related to their interaction ability are summarised as follow:

- Benzenediazoniumtetrafluoroborate (DS) is the simplest salt and has been chosen as a reference and because of the availability of the aromatic cycle for π - π stacking.
- 4-decyl benzenediazoniumtetrafluoroborate ($\text{DS-C}_{10}\text{H}_{21}$) has a long apolaralkyl chain that has a lipophilic and hydrophobic character to pre-concentrate non-polar molecules.

- 4-carboxybenzene diazoniumtetrafluoroborate (DS-COOH) and 4-(aminoethyl) benzenediazoniumtetrafluoroborate (DS-(CH₂)₂NH₂) can both be used for biomolecules coupling or for polar molecules pre-concentration.

The influence of the substituent located in the para position will be discussed and more especially in term of the nature and the force of the substituent (the mesomeric effect provided by COOH as well as the inductive effect provided by the CH₂CH₂NH₂ and the C₁₀H₂₁ substituents (Table S1)). The study of these four aryl-diazonium salts explains why the electron-donating substituent is not effective in this study.

5.2.3.3 Raman measurements

Raman measurements were recorded on pure chemicals (in powder form essentially unless otherwise stated) with a Raman microspectrometer Labram HR800 (Horiba Scientific). For both, amines and diazonium salts, a laser diode at 691 nm (Ondax) has been used to avoid any molecular resonance. For diazonium salts and the 4-aminobenzoic acid, the scattered light was collected by a 100x objective with numerical aperture (N.A.) of 0.9. For liquid compounds (aniline, 4-(2-aminoethyl)-aniline and 4-decylaniline), a water immersion objective (100x, N.A. = 1.0) was used. The spectral resolution was less than 2 cm⁻¹ and spectral calibration was performed daily via silicon sample. All the presented spectra are baseline corrected and normalized using the spectrometer software (LabSpec, Horiba Scientific). For calculations, spectra were normalized regarding the C=C stretching mode [23] observed between 1570 and 1611 cm⁻¹.

5.2.3.4 Nuclear Magnetic Resonance (NMR) measurements

Synthesized diazonium salts and their primary amines were also characterized by NMR measurements. Spectra were recorded using a Bruker Avance III 400 MHz instrument. The procedure, the NMR spectra and the ¹H chemical shifts are presented in the Supporting Information. The structure of the salts as well as indexation of protons is presented in scheme 1S. Both the amines and diazonium salts RMN spectra are presented in Figure S1.

5.2.3.5 Computational details

All calculations were carried out using the Gaussian 09 suite of programs [24] using the B3LYP exchange and correlation functional [25,26] along with the 6-311++G(d,p) basis set for all atoms. The structures were optimized without symmetry constraint (see Supporting Information). The vibrational wavenumbers and normal modes were calculated within the harmonic approximation. A scaling factor of 0.976 was chosen on the basis of previously published work [27]. For technical constraints, calculations were only performed for diazonium cation.

5.2.4 Results and discussion

Figures 1, 2, 3 and 4 compare Raman spectra obtained for A) the primary amines and B) the corresponding synthesized diazonium salts.

The wavenumber of important peaks are reported in table 1 and their assignments have been provided with the help of the literature [23,28,29]. It is worth noting that the spectrum obtained for aniline is in a good agreement with the one provided by Badawiet *al.* (2013) [23]. Most of their band assignments were used as reference for this work. In addition, some interactions can occur between two salts in crystalline state, especially for the DS-COOH because carboxyphenyl-derivatives are both H-bonding donor and acceptor. The resonance of carbonyl group causes a negative charge at the oxygen which can induce intermolecular hydrogen bonding, enhancing the formation of dimers. Thus, they preferentially self-organize as dimers in the crystalline state [30-32]. To investigate the dimer formation and to have a clear assignment of the Raman bands of the DS-COOH, DFT calculations and Natural Bond Orbital (NBO) charges have only been performed. In this case, two models were examined. The first one considers monomer units (named as CBN₂) whereas the second one considers dimers of DS-COOH (named as CBN₂ dimer). The main experimental features of DS-COOH normal Raman spectrum are properly reproduced with the model CBN₂ (Figure 5 and Table 2). The comparison between the acquired and the predicted Raman spectrum is also presented on figure 5 and the Raman band assignments of important peaks are reported on table 2. The crystalline state of DS-COOH regarding CBN₂ and CBN₂dimer models is discussed over the presentation of the different investigated modes of the phenyl-derivatives.

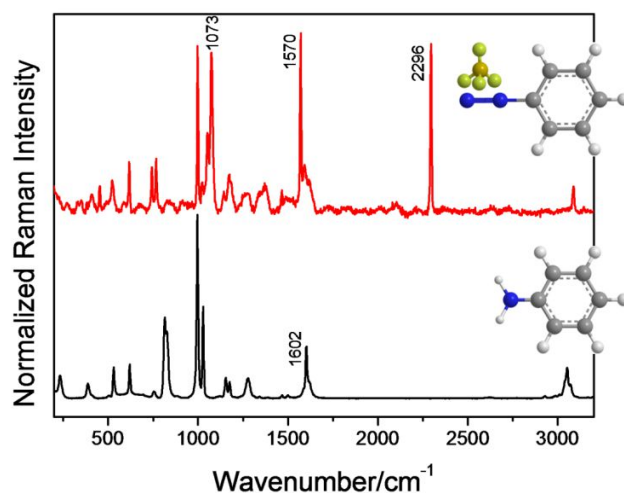


Figure 1: Raman spectra of aniline (black spectrum) and the corresponding diazonium salt: benzenediazoniumtetrafluoroborate, DS (red spectrum).

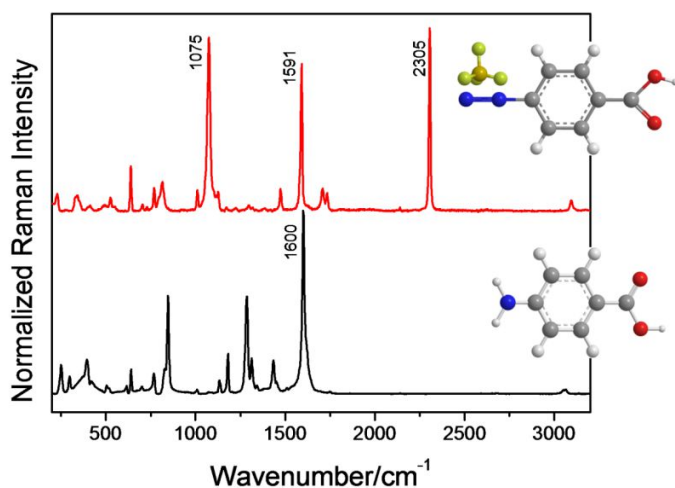


Figure 2: Raman spectra of 4-aminobenzoic acid (black spectrum) and the corresponding diazonium salt: 4-carboxybenzene diazonium tetrafluoroborate, DS-COOH (red spectrum).

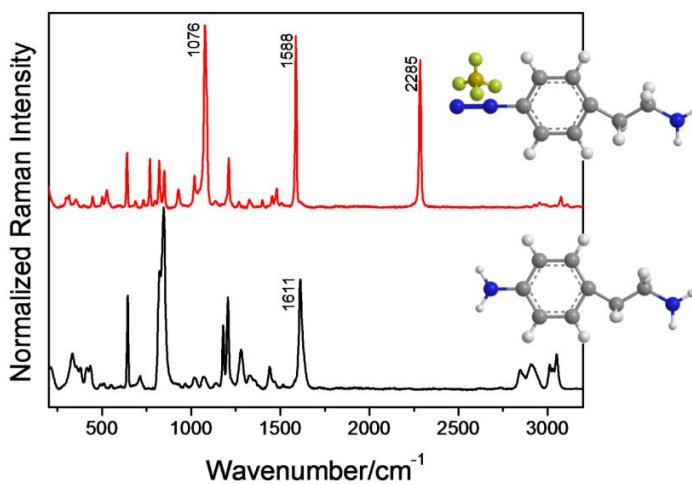


Figure 3: Raman spectra of 4-(2-Aminoethyl)aniline (black spectrum) and the corresponding diazonium salt: DS-(CH₂)₂NH₂ (red spectrum).

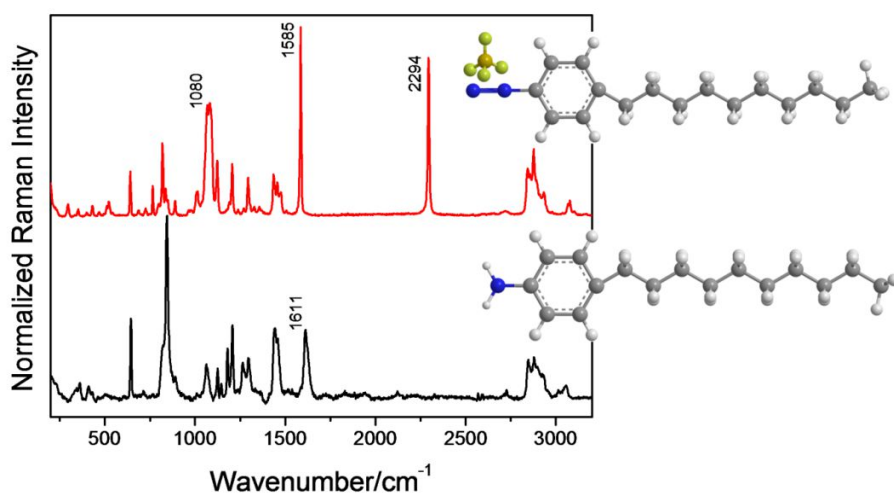


Figure 4: Raman spectra of 4-decylaniline (black spectrum) and the corresponding diazonium salt: 4-decyl benzenediazonium tetrafluoroborate, DS-C₁₀H₂₁ (red spectrum).

Table 1: Universal band assignments for Raman spectra obtained experimentally for primary amines and for the corresponding diazonium salts.

Raman wavenumber/cm ⁻¹								Assignment
Amines				DS				
Aniline	COOH	(CH ₂) ₂ NH ₂	C ₁₀ H ₂₁	DS	DS-COOH	DS-(CH ₂) ₂ NH ₂	DS-C ₁₀ H ₂₁	
386								Aromatic ring-N in plane bending
619	638	643	644	617	637	640	639	Ring deformation[23]
755				743				p CH wagging[23,28]
814	828	822	822		796	820	819	o;m CH wagging[23,28]
827	845	845	844		814	849	837	Ring breathing[23]
995 1027				997 1021				Ring deformation + ring breathing for benzene and mono-substituted derivatives [23,28] CC stretching vibration (coupled with CH in plane bending vibration) [29,38]
		1067	1062			1082	1079	C-C stretching (aliphatic chain) [28]
				1073	1075	1076	1080	CH in plane bending for p-substituted and mono-substituted benzenes [12,28]coupled with C-N stretching
1154				1142				m;p CH in plane bending [23,28]
1175	1179	1177	1179	1174	1170vw	1198vw	1190vw	m;o CH in plane bending [23,28]
1279	1286	1279	1265					ring-N str + ring breathing + o-CH in plane bending [23]
		1469	1459			1454	1456	CH ₂ scissoring[43]
1602	1600	1611	1611	1570	1591	1588	1585	C=C stretching [23]
	1748				1708 1732			C=O stretching
				2296	2305	2285	2294	N≡N stretching [23,28]
		2813-2986	2813-2986			2813-2986	2813-2986	Symmetric and anti-symmetric CH stretch of n-alkanes [28]
3053-3071	3049-3063	3014-3051	3016-3057	3087	3096	3076	3066 3077	Aromatic CH stretch of benzene derivative [23,28]

5.2.4.1 Raman characterization of the diazonium salts

N≡N group vibrations

The particularity of diazonium salts is their N₂⁺ function obtained by the oxidation of the corresponding amine. The emergence of strong peaks observed at 2296, 2305, 2285 and 2294 cm⁻¹ for DS, DS-COOH, DS-(CH₂)₂NH₂ and DS-C₁₀H₂₁ respectively (figures 1, 2, 3, and 4, Table 1) on the salts spectra compared to the aniline ones can be assigned to the N≡N bond [12,28]. In comparison

with the experimental data acquired for each compound, DFT calculations performed on DS-COOH revealed strong similarities in this spectral range (fig. 5). The calculated position for N≡N stretching mode was found at 2293 cm⁻¹ for CBN₂ and at 2304 cm⁻¹ for CBN₂dimer. This similarity between the theoretical position and the experimental one (N≡N stretching mode for DS-COOH is recorded at 2305 cm⁻¹) strengthens the fact that the best model to reproduce the vibrational features of the normal Raman spectra was a dimeric arrangement of diazonium cation via H-bonds.

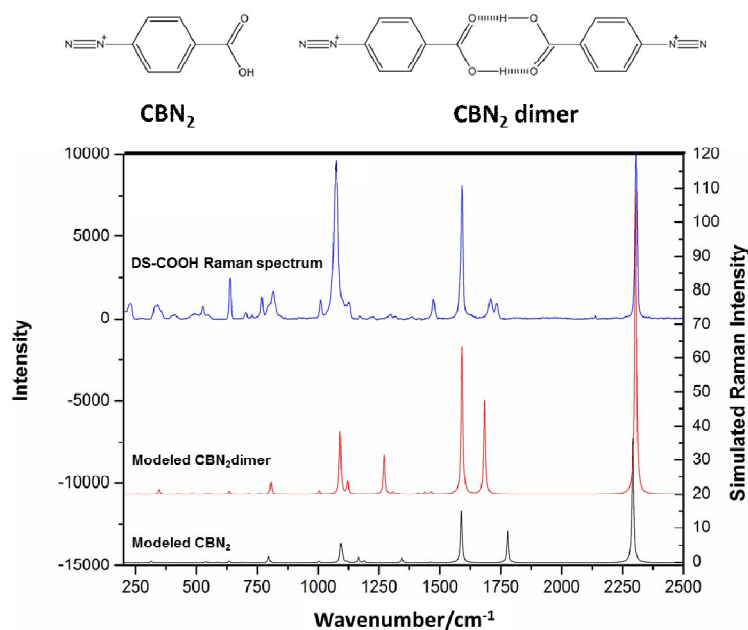


Figure 5: Comparison of the experimental Raman spectra recorded for DS-COOH and the calculated vibrational features of the salt by considering monomers (CBN₂) and a dimeric arrangement via H-bonds (CBN₂ dimer).

According to Socrates [28], the position of N≡N vibration mode is dependent on the nature of the ring substituent located in the para-position of the diazonium salt. Observed results show that the substituents have a rather low effect on the N≡N fragment following the observed wavenumber shifts (Table 1 and figure S2 in Supporting Information). Nevertheless, concerning DS-COOH, the COOH electron-withdrawing tendency was confirmed by the calculation of the C_{N≡N}NBO charges. Indeed, the C_{N≡N(DS-COOH)} NBO charges is equal to 0.012 in comparison with C_{N≡N(DS)} NBO charges which is equal to 0.003. As a consequence, a shift of +9 cm⁻¹ of the N≡N vibration mode has been found for DS-COOH in comparison with DS. The electron-withdrawing groups (i.e. COOH) induce an increase of the contribution of a structure like c1ccc(cc1)[N+]#N and hence induce a shift of the N≡N stretching vibration to higher wavenumbers [28]. Latter explanation is consistent with the experimental observation since the relative intensity of the N≡N bond for DS-COOH is increased by 23% in comparison with DS,

DS-C₁₀H₂₁ and DS-CH₂CH₂NH₂ (figure S2 and table S2 in Supporting Information). On the contrary, electron-donating groups located in para-positions induce an increase of the contribution of a structure like $\text{C}_6\text{H}_4\text{N}^+=\text{N}^-$ and hence, a decrease of the N≡N stretching vibration wavenumber. Such shifts are effectively observed on our experimental results since shifts of -11 cm⁻¹ and -2 cm⁻¹ of the N≡N vibration mode have been evaluated for DS-(CH₂)₂NH₂ and DS-C₁₀H₂₁ respectively in comparison with the one observed for DS. Between these two electron-donating groups (CH₃ and NH₂), NH₂ has higher inductive effect (NH₂ substituent constants (σ_p) = -0.66; CH₃ substituent constants (σ_p) = -0.17) [33,34]. Moreover, the inductive effect drops off rapidly with the number of σ bonds. That is why (i) the negative shift in wavenumber observed for N≡N vibration of DS-(CH₂)₂NH₂ is higher than the one observed for DS-C₁₀H₂₁ and (ii) the negative shift in wavenumber observed for N≡N vibration for DS-C₁₀H₂₁ is not significantly different from the one observed for DS.

H-N-(ring) symmetric stretching mode

In addition to the occurrence of the N≡N stretching vibration, the disappearance of the N-H symmetric stretching is observed in the high wavenumber range 3250-3400 cm⁻¹ (Fig. 6) for the primary amines. This observation indicates the successful synthesis of the diazonium salts with a high production rate (confirmed by NMR study with the disappearance of the η band on the NMR spectra, see Supporting Information).

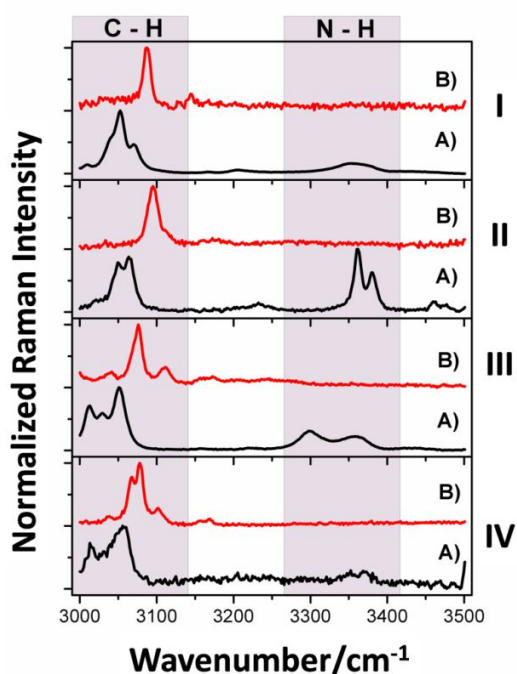


Figure 6: Comparison of aromatic C-H stretching and N-H stretching modes between the four synthesized diazonium salts (B red lines) and the corresponding primary amines (A black lines). Roman numbers from I to IV correspond to DS, DS-COOH, DS-(CH₂)₂NH₂ and DS-C₁₀H₂₁, respectively.

Ring-N vibrational modes

According to Badawi *et al.* [23] and Wojciechowski *et al.* [29], peak located at 386 cm^{-1} for aniline molecule (figure 1) corresponds to aromatic ring-N in plane bending. However, this vibrational mode is less obvious for the para-substituted amines. Possible explanation is that, aromatic ring vibration modes depend on the mass of the substituent [28]. Thus, in the range of $200\text{-}580\text{ cm}^{-1}$, lots of vibrational modes can be observed depending on the nature of the para-substituted group (figures 2, 3, 4). The same conclusion can be given for the range of $1250\text{-}1290\text{ cm}^{-1}$ (another range where a band corresponding to C-N vibration can be located). Raman bands for the amines observed between 1265 cm^{-1} and 1279 cm^{-1} (Table 1) and assigned to ring-N stretching, ring breathing, ortho-CH in plane bending [23] is no more observable in the spectra of the diazonium salts. This effect can be due to significant structural changes and conformational rearrangements. Indeed, the theoretical and experimental data provided by literature indicate that the neutral aniline in its ground electronic state (1A_1) is non-planar. The dihedral angle between the NH_2 plane and the $\text{C}_6\text{H}_5\text{N}$ plane has been determined as $37 \pm 2^\circ$ with the assumption that the C-N bond makes an angle of $1.5\text{-}2.3^\circ$ [29]. In comparison, the corresponding diazonium salt (aryl-diazonium) is a quasi-planar molecule [35], with the assumption that the C-N bond makes an angle of 0.5° [36]. The main factor responsible for this quasi-planarity is undoubtedly the strong through-bond interaction between the ring and the N_2 group, which are known to be a strong electron donor and the strongest known electron acceptor, respectively [35]. In agreement with the literature [29,35,37], this bond is lengthened such as the coplanarity is maintained. Additional explanation could be related with the electron charge density redistribution in the C-N bond. This is consistent with the observation that the diazonium group is one of the most powerful σ -electron and π -electron acceptors [37].

Benzene ring and C-H related vibrations

Comparing Raman spectra between amines and diazonium salts, several common bands related to the benzene ring vibrations can be observed.

First of all, the strong band related to the benzene ring stretching mode (Table 1) can be noticed on all Raman spectra in the range of $1585\text{-}1611\text{ cm}^{-1}$. According to Wojciechowski *et al.* [29], this band is essentially related to ortho-meta C-C stretching modes. From phenyl-amine derivatives to diazonium salts, this band is the most significant signature of the benzene ring. In comparison with the primary amines, this band is shifted to lower wavenumber for all salts. These shifts are close to 25 cm^{-1} for all salts except for the DS-COOH, maybe due to the higher weight of the N_2 group compared to the NH_2 that induces a decrease of the vibration frequency. In the case of the DS-COOH, a shift

less than 10 cm^{-1} is observed maybe due to the dimeric form of the salt that reduces the weight effect of the N_2 .

Two intensive and distinct peaks also assigned to the ring deformation and the ring breathing mode (coupled with CH in plane bending vibration) of benzene and of mono-substituted derivatives are found in the Raman spectrum of aniline at around 1000 cm^{-1} (Fig. 1 and Table 1, trigonal ring breathing vibration) and 1027 cm^{-1} (Fig. 1 and Table 1) [29,38]. For DS, these bands are slightly shifted at 997 cm^{-1} and 1021 cm^{-1} . In case of para-substituted amines and diazonium salts (disubstituted benzene derivatives) these vibrational modes are not allowed [28].

Bands assigned to ring deformation ($\text{C}=\text{C}-\text{C}$ in plane deformation) in the region of $617\text{-}644\text{ cm}^{-1}$ (Table 1) are presented for both amines and diazonium salts. In agreement with Socrates [28], bands shift to higher wavenumber for para-substituted aromatic compounds in comparison with mono-substituted compounds.

According to Badawi *et al.* (2013) [23], the vibrational mode located at 827 cm^{-1} (Table 1) for aniline can be assigned to a ring breathing mode (coupled with ring-N stretching and ring deformation). This band is widely shifted to higher wavenumbers ($844\text{-}845\text{ cm}^{-1}$) for para-substituted amines. For instance, shifts of -31 cm^{-1} and -7 cm^{-1} towards lower wavenumbers were observed for DS-COOH and DS- $\text{C}_{10}\text{H}_{21}$ respectively, comparing with their primary amines, whereas in the Raman spectrum of the DS- $(\text{CH}_2)_2\text{NH}_2$ a shift of $+4\text{ cm}^{-1}$ was found. Commonly for all substituted diazonium salts intensity of this vibrational mode is strongly decreased and it is no more observed in Raman spectrum of DS. Another vibrational mode at 814 cm^{-1} assigned o,m-CH wagging (Table 1 and figures 2, 3 and 4) was found to behave in similar manner as previously described for the ring breathing mode. The shift of these bands can essentially be due to structural changes and conformational rearrangements caused by the presence of the N_2^+ [35,37].

Concerning the ring C-H related vibrations, bands assigned to (i) p-CH wagging (coupled with ring-N wagging and o-CH wagging) at 755 and 743 cm^{-1} (table 1) and (ii) m,p-CH bending (coupled with ring deformation) at 1154 and 1142 cm^{-1} (table 1) are only observed for aniline and DS, due to mono-substitution.

The very strong band observed around 1075 cm^{-1} and related to the CH in plane bending (coupled with ring-N stretching mode) for mono- and para-substituted benzenes observed in spectra of the diazonium salts is of particular interest (Figure 1 red spectrum as well as figure 2, 3 and 4 red spectra; Table 1). The observation of this band constitutes the most astonishing phenomenon. This characteristic band can be assigned to the electron charge density redistribution within the structures

caused by the presence of N_2^+ . It constitutes the indisputable signature of the phenyl-derivatives stemming from diazonium salts.

According to the literature, aromatic C-H symmetric and anti-symmetric stretching modes occur above 3000 cm^{-1} and exhibit a multiplicity of weak to moderate bands [39]. In comparison with amines, CH stretching (table 1) is shifting towards the higher wavenumber for the diazonium salts (Fig. 6). This shift indicates a strengthening of the C-H bond maybe due to a new charge distribution on the ring after the substitution of the NH_2 by the N_2^+ [29]. Obtained result is in good agreement with ones provided by literature for aniline and its corresponding diazonium salt [29,35,37].

Functions in para- position carried by the aromatic ring

With regards to the different para functions in para- position carried by the aromatic ring (i.e. $COOH$, $(CH_2)_2NH_2$ and $C_{10}H_{21}$), some characteristic bands have been identified.

Concerning $(CH_2)_2NH_2$, $C_{10}H_{21}$ and their corresponding diazonium salts, symmetric and anti-symmetric CH_3 stretches of n-alkanes as well as symmetric CH_2 stretch of n-alkanes have been identified clearly in the range of $2813\text{-}2986\text{ cm}^{-1}$ (figures 3 and 4, table 1). In addition, C-C stretching mode in the range of $1062\text{-}1082\text{ cm}^{-1}$ (table 1) and CH_2 scissoring in the range of $1454\text{-}1469\text{ cm}^{-1}$ (table 1). Some significant changes in the peak position or intensity can be noticed, meaning that the simple modification of the molecule from the aniline form to the diazonium salt could have strong influence on the vibrational modes of the alkyl chain in para-position.

Concerning aminobenzoic acid derivatives (figure 2, Table 1), the weak bands observed in the $1700\text{-}1750\text{ cm}^{-1}$ region are characteristic features of the carboxylic group due to the C=O stretching vibration. They were respectively assigned to the symmetric and the antisymmetric stretching vibrations at 1708 and 1732 cm^{-1} . The antisymmetric stretch is usually seen at a higher wavenumber than the symmetric one [40]. With regards to DFT calculations (figure 5, Table 2), the CBN_2 model simulated spectrum predicts a single C=O stretching mode, $\nu_{sym}(C=O)_{CBN_2}$, at 1778 cm^{-1} . This result is in good agreement with the literature [28]: when the carbonyl is not interacted by hydrogen bond (the monomer case), the stretching bands appear in the range $1760\text{-}1735\text{ cm}^{-1}$. In comparison, the dimer should be characterized by two C=O stretching modes, respectively the symmetric C=O stretching mode ($\nu_{sym}(C=O)_{CBN_2\text{dimer}}$) at 1683 cm^{-1} and the antisymmetric C=O stretching mode ($\nu_{asym}(C=O)_{CBN_2\text{dimer}}$) at 1729 cm^{-1} . With regards to the Raman calculations of the C=O stretching mode in the CBN_2 model ($\nu_{sym}(C=O)_{CBN_2}$ at 1778 cm^{-1}), the theoretical shift towards the lower wavelength of the symmetric C=O stretching mode in the dimer ($\nu_{sym}(C=O)_{CBN_2\text{dimer}}$ at 1683 cm^{-1}) is due to the change in the polarizability of the CO group induced by the hydrogen bonding. One can

notice that the simulated Raman spectrum for CBN₂ dimer only exhibits this later symmetric mode ($\nu_{\text{sym}}(\text{C}=\text{O})_{\text{CBN}_2\text{dimer}}$) at 1683 cm⁻¹. This is in agreement with the fact that CBN₂ dimer features a center of symmetry imposing the mutual exclusion rule for vibrational modes. In this framework, the $\nu_{\text{sym}}(\text{C}=\text{O})_{\text{CBN}_2\text{dimer}}$ is Raman active while $\nu_{\text{asym}}(\text{C}=\text{O})_{\text{CBN}_2\text{ dimer}}$ is Raman inactive. This mutual exclusion rule explains why the simulated Raman spectrum for an isolated CBN₂dimer exhibits only the symmetric C=O stretching.

However, the same dimer considered in the crystal packing presents a lower symmetry which suspends the mutual exclusion rule; both $\nu_{\text{sym}}(\text{C}=\text{O})_{\text{CBN}_2\text{dimer}}$ and $\nu_{\text{asym}}(\text{C}=\text{O})_{\text{CBN}_2\text{ dimer}}$ becoming Raman active. This is consistent with the observation of two peaks onto the experimental Raman spectrum of DS-COOH for both the symmetric and the antisymmetric C=O stretching modes. The shift towards the higher wavenumber observed experimentally for the symmetric C=O stretching (from the theoretical $\nu_{\text{sym}}(\text{C}=\text{O})_{\text{CBN}_2\text{ dimer}}$ value calculated at 1683 cm⁻¹ to the experimentally $\nu_{\text{sym}}(\text{C}=\text{O})_{\text{DS-COOH}}$ measured value at 1708 cm⁻¹) is assumed by the presence of the BF₄⁻ into the crystalline structure of DS-COOH in agreement with the effect provided by the electronegative atoms which increase the C=O stretching vibration wavenumber [41,42]. In addition and in agreement with the results shown on table 2, the similarities between the experimental and the theoretical position of $\nu(\text{N}\equiv\text{N})$, $\nu(\text{C}=\text{C})$, ring breathing (and $\nu(\text{C}-\text{H})$ in plane, $\nu_{\text{sym}}(\text{C}-\text{N})$, $\nu_{\text{sym}}(\text{CO}-\text{H})$ as well as $\nu(\text{C}-\text{H})$ in plane) confirm the fact that the best model to reproduce the vibrational features of the normal Raman spectra is a dimeric arrangement of DS-COOH via H-bonds.

Table 2: Comparison of the experimental and calculated wavenumbers considering CBN₂ and CBN₂dimer for modeling. Assignments of the main peaks.

DS-COOH	CBN ₂		CBN ₂ dimer	
Experimental/ cm ⁻¹	Calculated/ cm ⁻¹	Assignment	Calculated/ cm ⁻¹	Assignment
2305	2293	$\nu(\text{N}\equiv\text{N})$	2304	$\nu(\text{N}\equiv\text{N})$
	1778	$\nu_{\text{sym}}(\text{C}=\text{O})$		
1708			1684	$\nu_{\text{sym}}(\text{C}=\text{O})$
1732			×	$\nu_{\text{asym}}(\text{C}=\text{O})$
1591	1588	$\nu(\text{C}=\text{C})$	1590	$\nu(\text{C}=\text{C})$
1293wvw	1344	$\delta(\text{CO}-\text{H})$	1271	$\delta_{\text{sym}}(\text{CO}-\text{H})$
	1165	$\delta(\text{C}-\text{H})$ in plane and $\delta(\text{CO}-\text{H})$		
1127 ww			1122	$\delta(\text{C}-\text{H})$ in plane
1075	1093	$\delta(\text{C}-\text{H})$ in plane, $\nu(\text{C}-\text{N})$ and $\nu(\text{C}-\text{O})$	1090	$\delta(\text{C}-\text{H})$ in plane, $\nu_{\text{sym}}(\text{C}-\text{N})$
814	797	Ring breathing	807	Ring breathing

×Calculated CBN₂ dimer features a center of symmetry imposing the mutual exclusion rule for vibrational modes. In this framework, the $\nu_{\text{sym}}(\text{C}=\text{O})$ is Raman while $\nu_{\text{asym}}(\text{C}=\text{O})$ is Raman inactive.

5.2.5 Conclusion

The first stage of this work has consisted in the complete Raman characterization of the synthesized diazonium salts in comparison with Raman spectra provided for amines. Raman investigation of synthesized diazonium salts confirmed the existence of the stretching of the $\text{N}\equiv\text{N}$ bond in the expected spectral range: $2285\text{-}2305\text{ cm}^{-1}$ (2296 , 2285 , 2305 , and 2294 cm^{-1} for DS, DS-COOH, DS-(CH_2) $_2$ NH $_2$ and DS-C $_{10}$ H $_{21}$, respectively). The disappearance of the H-N-(ring) symmetric stretching observed in the range $3299\text{-}3361\text{ cm}^{-1}$ for the primary amines is another evidence of effectiveness of the salt synthesis. Moreover, from our results, we can assess that the very strong band related to the combination of both (i) CH in plane bending for mono- and para-substituted benzenes and (ii) C-N stretching observed in the range $1073\text{-}1080\text{ cm}^{-1}$ constitutes an actual spectral signature of the phenyl-derivatives stemming from diazonium salts.

Furthermore, the whole characterization of the fate of phenyl-derivatives has also been examined and discussed by using Raman spectroscopy ($\text{N}\equiv\text{N}$ group vibrations, H-N-(ring) symmetric stretching modes, ring-N as well as benzene ring vibrational modes, C-H related vibrations and para functions carried by the aromatic ring). In this study we notably took into account both (i) the effect of the structural changes as well as conformational rearrangements from the amine to the diazonium salt and (ii) the influence of the substituent located in the para position (i.e. the nature and force of the mesomeric effect of the substituent) on the Raman modes. Raman experiments were in good agreements with the DFT modelling that has allowed us to determine the crystalline structure of the DS-COOH.

Corresponding Author

*s.betelu@brgm.fr; Tel. 0033238643268; Fax.0033238644797.

Author Contributions

All authors have given approval to the final version of the manuscript. ‡These authors contributed equally.

Acknowledgment

This work was funded by ANR ECOTECH (Production durable et technologies de l'environnement); REMANTAS project: Enhanced Raman scattering for aquatic media: a new technology for on-site analysis 2011-2014 (REMANTAS project; ANR-11-ECOT-0010).

5.2.6 References

- [1] L. Kurti, B. Czako, *Strategic Applications of Named Reactions in Organic Synthesis*, Elsevier Academic Press, Boston, 2005.
- [2] H. Meerwein, E. Büchner, K. van Emster, *J. Prakt. Chem.* 152 (1939) 237.
- [3] T. Sandmeyer, *Chem. Ber.* 17 (1884) 2650.
- [4] H.H. Hodgson, *Chem. Rev.* 40 (1947) 251.
- [5] A. Adenier, N. Barré, E. Cabet-Deliry, A. Chaussé, S. Griveau, F. Mercier, J. Pinson, C. Vautrin-UI, *Surface Science* 600 (2006) 4801.
- [6] A. Adenier, E. Cabet-Deliry, A. Chaussé, S. Griveau, F. Mercier, J. Pinson, C. Vautrin-UI, *Chemistry of materials* 17 (2005) 491.
- [7] S. Betelu, C. Vautrin-UI, A. Chaussé, *Electrochemistry Communications* 11 (2009) 383.
- [8] S. Betelu, C. Vautrin-UI, J. Ly, A. Chaussé, *Talanta* 80 (2009) 372.
- [9] M. Delamar, R. Hitmi, J. Pison, J. Savéan, *Journal of the American Chemical Society* 114 (1992) 5883.
- [10] E. Bekyarova, M.E. Itkis, P. Ramesh, C. Berger, M. Sprinkle, W.A. de Heer, R.C. Haddon, *Journal of American Chemistry Society* 131 (2009) 1336.
- [11] C.M. Combellas, F. Delamar, F. Kanoufi, J. Pinson, F.I. Podvorica, *Chemistry of Materials* 17 (2005) 3968.
- [12] L. Laurentius, S.R. Stoyanov, S. Gusarov, A. Kovalenko, R. Du, G.P. Lopinski, M.T. McDermott, *ACS Nano* 5 (2011) 4219.
- [13] J.L. Bahr, J. Yang, D.V. Kosynkin, M.J. Bronikowski, R.E. Smalley, J.M. Tour, *J. Am. Chem. Soc.* 123 (2001) 6536–6542.
- [14] P. Allongue, M. Delamar, B. Desbat, O. Fagebaume, R. Hitmi, J. Pinson, J.M. Saveant, *J. Am. Chem. Soc.* 119 (1997) 201.
- [15] M. Bouriga, M.M. Chehimi, C. Combellas, P. Decorse, F. Kanoufi, A. Deronzier, J. Pinson, *Chem. Mater.* 25 (2013) 90.
- [16] A. Kowalczyk, B. Wagner, M. Karbarz, A.M. Nowicka, *Sens. Actuators B* 208 (2015) 220.
- [17] M. Zheng, S. Griveau, C. Dupont-Gillain, M.J. Genet, C. Jolival, *Bioelectrochemistry*.
- [18] R. Ahmad, A. Mocaer, S. Gam-Derouich, A. Lamouri, H. Lecoq, P. Decorse, P. Brunet, C. Mangeney, *Polymer* 57 (2015) 12.
- [19] S. Mahouche Chergui, N. Abbas, T. Matrab, M. Turmine, E. Bon Nguyen, R. Losno, J. Pinson, M.M. Chehimi, *Carbon* 48 (2010) 2106.
- [20] M. Raicopol, C. Andronescu, R. Atasiei, A. Hanganu, A.M. Manea, I. Rau, F. Kajzar, L. Pilan, *Synthetic Metals* 206 (2015) 84.
- [21] N. German, A. Ramanavicius, A. Ramanaviciene, *Sens. Actuators B* 203 (2014) 25.
- [22] J.Z.W. Wicks, F.N. Jones, S.P. Pappas, D.A. Wicks, *Organic Coatings: Science and Technology*, Third Edition, J. Wiley & Sons, Hoboken, 2007.
- [23] H.M. Badawi, W. Förner, S. Ali, *Spectrochim Acta A Mol Biomol Spectrosc.* 112 (2013) 388.
- [24] F. R. A. Gaussian 09, M. J.; Trucks, G. W.; Schlegel, H. B.; Scuseria, G. E.; Robb, M. A.; Cheeseman, J. R.; Scalmani, G.; Barone, V.; Mennucci, B.; Petersson, G. A.; Nakatsuji, H.; Caricato, M.; Li, X.; Hratchian, H. P.; Izmaylov, A. F.; Bloino, J.; Zheng, G.; Sonnenberg, J. L.; Hada, M.; Ehara, M.; Toyota, K.; Fukuda, R.; Hasegawa, J.; Ishida, M.; Nakajima, T.; Honda, Y.; Kitao, O.; Nakai, H.; Vreven, T.; Montgomery, Jr., J. A.; Peralta, J. E.; Ogliaro, F.; Bearpark, M.; Heyd, J. J.; Brothers, E.; Kudin, K. N.; Staroverov, V. N.; Kobayashi, R.; Normand, J.; Raghavachari, K.; Rendell, A.; Burant, J. C.; Iyengar, S. S.; Tomasi, J.; Cossi, M.; Rega, N.; Millam, J. M.; Klene, M.; Knox, J. E.; Cross, J. B.; Bakken, V.; Adamo, C.; Jaramillo, J.; Gomperts, R.; Stratmann, R. E.; Yazyev, O.; Austin, A. J.; Cammi, R.; Pomelli, C.; Ochterski, J. W.; Martin, R. L.; Morokuma, K.; Zakrzewski, V. G.; Voth, G. A.; Salvador, P.; Dannenberg, J. J.; Dapprich, S.; Daniels, A. D.; Farkas, Ö.; Foresman, J. B.; Ortiz, J. V.; Cioslowski, J.; Fox, D. J. *Gaussian, Inc., Wallingford CT, 2009.*
- [25] A.D. Becke, *J. Chem. Phys.* 98 (1993) 5648.
- [26] C. Lee, W. Yang, R.G. Parr, *Phys. Rev. B* 37 (1988) 785.

- [27] S.Z. Fairchild, C.F. Bradshaw, W. Su, S.K. Guharay, *Appl. Spectrosc.* 63 (2009) 733.
- [28] G. Socrates, *Infrared and Raman Characteristic Group Frequencies: Tables and Charts* (Third Edition), J. Wiley & Sons, West Sussex, 2001.
- [29] P.M. Wojciechowski, W. Zierkiewicz, D. Michalska, P. Hobza, *J. Chem. Phys.* 118 (2003) 10900.
- [30] L. Mahe, A. Izuoka, T. Sugawara, *J. Am. Chem. Soc.* 114 (1992) 7904.
- [31] M.L. Rahman, H.C. Kwong, M.M. Yusoff, G. Hegde, M.I. Mohamed Tahir, M.Z.A. Rahman, *Acta Cryst.* E68 (2012) o2958.
- [32] Q.-D. Yu, Y.-Y. Liu, *Acta Cryst.* E65 (2009) o2326.
- [33] C. Hansch, A. Leo, R.W. Taft, *Chem. Rev.* 91 (1991) 165.
- [34] L.P. Hammett, *J. Am. Chem. Soc.* 59 (1937) 96.
- [35] H. Zollinger, *Diazo chemistry: aromatic and heteroaromatic compounds*, Volume 1, New York 1994.
- [36] M. Cygler, M. Przybylska, R.M. Eloffson, *Can. J. Chem.* 60 (1982) 2852.
- [37] M.A. Vincent, L. Radom, *J. Am. Chem. Soc.* 100 (1978) 3306.
- [38] H.M. Badawi, *Spectrochim. Acta* 109A (2013) 213.
- [39] J. Coates, in: R.A. Meyers (Ed.), *Encyclopedia of Analytical Chemistry*, J. Wiley & Sons, Chichester, 2000.
- [40] D. Lin-Vein, N.B. Colthup, W.G. Fateley, J.G. Grasselli, *The Handbook of Infrared and Raman Characteristic Frequencies of Organic Molecules*, Academic Press, San Diego, 1991.
- [41] J.R. Barcello, C. Otero, *Spectrosc. Acta* 18 (1962) 1231.
- [42] A.J. Collins, K.J. Morgan, *J. Chem. Soc.* (1963) 3437.
- [43] C.S. Venkateswaran, N.S. Pandya, *Proc. Indian Acad. Sci. Section A* 15 (1942) 396.

5.3 Diazonium salt-based SERS substrates: at the root of the development of innovative “long life” robust SERS sensors

Stéphanie Betelu^{1‡}, Inga Tijunelyte^{2‡}, Leïla Boubekeur-Lecaque^{3‡}, Ioannis Ignatiadis¹, Anne Caroline Schnepf^{4‡}, Joyce Ibrahim³, Timothée Toury³, Erwann Guenin², Nathalie Lidgi-Guigui², Nordin Félidj³, Emmanuel Rinnert⁵, Marc Lamy de la Chapelle²*

¹BRGM, Water, Environment and Eco-technology Division, F-45060 Orléans Cedex 02, France

²Université Paris13, Sorbonne Paris Cité, Laboratoire CSPBAT, CNRS, (UMR7244), 74 rue Marcel Cachin, 93017 Bobigny, France

³ Univ Paris Diderot, Sorbonne Paris Cité, ITODYS, UMR 7086 CNRS, 15 rue J-A de Baïf, 5205 Paris Cedex 13, France

⁴University of Technology of Troyes (UTT), 12, rue Marie Curie, 10000 Troyes, France

⁵IFREMER, Brest center, Interfaces and Sensors Group, BP 70, 29280 Plouzané, France

Supplementary Information in ANNEX 5

ABBREVIATIONS

DSCOOH, 4-carboxybenzene diazoniumtetrafluoroborate.

DSC₁₀H₂₁, 4-decyl benzenediazoniumtetrafluoroborate.

DS(CH₂)₂NH₂, 4-(aminoethyl) benzenediazoniumtetrafluoroborate.

DS, Benzenediazoniumtetrafluoroborate.

GNS, gold nanostructures

PAH, Poly Aromatic Hydrocarbons

KEYWORDS:

Sensors, Gold Nanostructures (GNS); Diazonium salts; Surface functionalisation; RAMAN, SERS, XPS. Electron beam nano-Lithography (EBL), XPS, DFT calculations.

5.3.1 Abstract

The development of analytical tools allowing on-site accurate and sensitive measurements is of primary importance and would be a very meaningful innovation, especially for the organic compounds sensing. Their development also denotes a serious challenge in terms of sensitivity, accuracy, repeatability and robustness. For this purpose, electron beam nano-lithographed gold nanostructures have been selected as the best analytical tool for the development of reproducible SERS sensors. In addition, surface functionalisation via diazonium salts has been considered as attractive methods to develop robust sensors. In this context, tailoring the surface chemistry of the SERS substrates has been one of the first key factors of this work.

This paper provides the vibrational characterization of four selected diazonium salts and their phenyl derivatives grafted the SERS active surfaces using Raman and SERS spectroscopy. When possible, RAMAN and SERS experiments were combined with DFT modeling. In addition, XPS on functionalised plane gold was realized in order to examine and comfort the nature of the interface between surface and the organic coating.

Results provided by SERS, XPS and DFT calculations led us to conclude that the spontaneous grafting realized on gold in case of DS-COOH is providing Au-ring-N=N-R linkage coating like structure.

5.3.2 Introduction

Thanks to (i) the improvement on electronics that led to miniaturize RAMAN spectrometer [1], (ii) the great progress of nano-scale technology of nanosensors, essentially based on colloid systems [2;3], and (iii) surface chemistry applying Self-Assembled Monolayers (SAMs), Surface Enhanced Raman Spectroscopy (SERS) has been identified as a promising tool for sensing on-site [4;5;3;6-10].

Among the investigated strategies for the development of robust devices, surface functionalisation via diazonium salt has been selected as one of the most powerful alternative to SAMs. Indeed, immobilization of aryldiazonium is a versatile method, allowing stable grafted organic layers, bearing a wide range of functional groups. The grafting can be accomplished by either chemical (spontaneous grafting) [11-14], electrochemical [15-17] or physical [18] methodologies. However, the surface functionalisation using diazonium salt is still under investigation due to the existence of several grafting pathways. Indeed, according to literature [11;13], grafting via diazonium salt involves a reductive electron transfer from the conductive or semi-conductive surface to the diazonium salt concerted with the cleavage of dinitrogen [19]. This phenomenon leads to the generation of aryl radicals, followed by the binding of these radicals to the surface via carbon-metal covalent bonds (Figure 1 A) [20]. In this case, SERS technique has been used to ascertain the existence of covalent bonds between gold surface and the coating [14]. Aryl radicals can also bind to aromatic rings already attached to the conductive surface (Figure 1 B) [20]. The thickness of the coating can vary from a monolayer (thickness ~1 nm) to 5 nm thick multilayers [21]. In addition to these two pathways, the direct reaction of the diazonium cation with surface functional groups [22] (Figure 1 C) as well as the formation of an azophenyl radical after diazonium salt reduction and its direct bond (i) to the conductive surface (Figure 1 D) [23] or (ii) to an aromatic ring already attached to the conductive surface (Figure 1 E) [24;22] have also been reported.

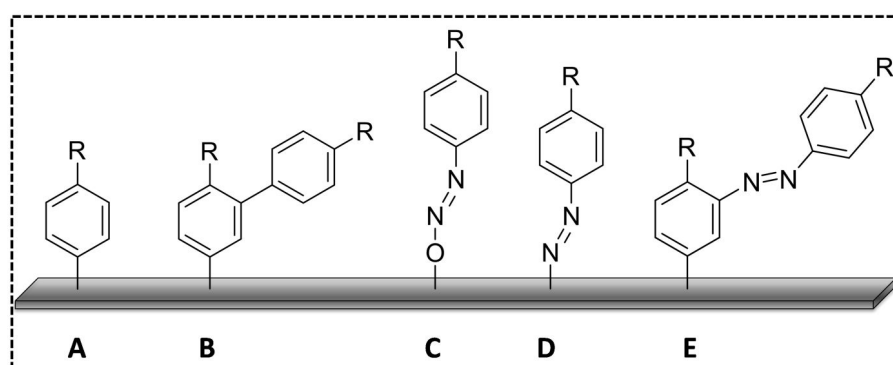


Figure 1: Different pathways for aryl derivatives grafting to conductive surfaces.

These phenomena (corresponding to Figure 1 C, D, E) were essentially evidenced by X-ray photoelectron spectroscopy (XPS) due to the presence of a peak at 400 eV in the nitrogen 1s core-

level spectral region. Belanger and co-workers were the first to claim the presence of azo groups onto carbon-based substrates functionalised by electrochemistry [22] and by spontaneous grafting [25], even for the achievement of monolayers [25]. This last observation was attributed to the coupling of the diazonium cations with carbon surfaces having phenolic-type oxygenated functionalities to form an azo bond (Figure 1 C). In 2012, Ricci *et al.* [23] have provided some evidence of the formation of an azo bond on gold substrates after the electroreduction of carboxybenzenediazonium salts, particularly by using the 4-amino (2,3,5,6-tetrafluoro)-carboxybenzenediazonium salts, which is likely to form monolayers due to hindrance to the 3- and 5-positions on phenyl ring [26]. According to the authors, the formation of the azo bond on gold was evidenced by the presence of both (i) the N 1S peak observed at 400eV by XPS and (ii) the presence of an azo stretching mode ($\nu_{\text{N=N}}$) observed at 1392 cm^{-1} by Polarization Modulation-Infrared Reflection-Adsorption Spectroscopy (PM-IRRAS) [27]. Also in 2012, Mesnage *et al.*, [28] have provided some evidence of the formation of an azo bond on gold substrates that were spontaneously functionalised by using NO_2 , Br- and CH_3S -diazonium salts. The Au-N bond was evidenced by XPS due to the presence of a peak containing gold nitrides at 398.1 eV.

Whatever the pathway of the surface functionalisation by using diazonium salts, the robustness of the grafted layer has already been demonstrated [16;29;30]. However, in order to apply diazonium salt-based sensor for molecular sensing by SERS, exhaustive surface analysis and vibrational modes identification is of primer importance. In this context, tailoring the surface chemistry of the diazonium salt-based gold nano-structures (DS-based GNS) as SERS substrates is one of the first key factors for successful applications in sensing.

This study provides the characterization of the fate of phenyl derivatives: from the diazo-phenyl derivatives to grafted layers by using SERS spectroscopies. SERS substrates were fabricated by electron beam nano-lithography (EBL) that has been identified as one of the most appropriate approach to control the geometrical parameters of the sensitive part of the optical support (size, shape and disposition of gold nanostructures) and prepare well defined and reproducible nanostructured materials [31]. Four diazonium salts were selected to be used such as to develop “long life” robust SERS sensors that could provide accurate and reproducible detection of organic compounds:

- Benzenediazoniumtetrafluoroborate (DS) as model system and in addition for pollutant pre-concentration because of the availability of the cycle for π - π stacking.
- 4-decyl benzenediazoniumtetrafluoroborate ($\text{DC}_{10}\text{H}_{21}$) featuring a long hydrophobic chain that could be helpful for the pre-concentration of apolar molecules.
- 4-carboxybenzene diazoniumtetrafluoroborate (DS-COOH) and 4-(aminoethyl) benzenediazoniumtetrafluoroborate (DS-(CH_2)₂NH₂), for both (i) the pre-concentration of polar molecules and (ii) offering reactive functionalities (NH₂, COOH) for (bio)chemical coupling.

The effective chemical grafting was examined by comparing Raman spectra obtained for each synthesized diazonium salts with the SERS spectra of phenyl derivatives grafted to GNS.

In addition, X-ray photoelectron spectroscopy (XPS) was preceded on the grafted plane gold surfaces to examine the nature of the interface between the GNRs and the organic coating. Finally, Density Functional Theory (DFT) calculations has been performed on SERS spectra of DS and DS-COOH based sensors in order to provide a better insight on the bands assignment and to support SERS spectra interpretation.

5.3.3 Methods

5.3.3.1 Materials and reagents

Sodium tetrafluoroborate (NaBF_4), diethyl ether (>98%, ACS reagent), benzenediazoniumtetrafluoroborate, 4-decyl benzenediazoniumtetrafluoroborate, 4-carboxybenzene diazoniumtetrafluoroborate, 4-(aminoethyl) benzenediazoniumtetrafluoroborate, sulfuric acid (0.1 mol L⁻¹), were purchased from Sigma Aldrich. Ethanol (96%, technisolv) was purchased from VWR; Methanol (100%, Reg.Ph.Eur) from Prolabo. Suprapur sulfuric acid (95-98%) was supplied by JT Baker. NaNO_2 “cristallisépur” was obtained from Labosi.

5.3.3.2 Diazonium salt synthesis

The synthesis of diazonium salts was done according to the reaction between aryl amines and a sodium nitrile at 0°C [32]. Briefly, $4 \cdot 10^{-3}$ mol L⁻¹ of the amine was dissolved in HBF_4 acid solution; the solution was allowed to cool for 15 min. Sodium nitrite ($4.3 \cdot 10^{-3}$ mol dissolved in milliQ water) was added dropwise to the acidic amine solution under stirring. The mixture was allowed to react for 40 min. A precipitate appears in the solution which was then filtered and rinsed with glacial ether. The salt was then dried under vacuum and kept at - 20°C.

5.3.3.3 SERS substrates

Gold was chosen as the most robust material for the elaboration of nanostructures on borosilicate glass substrates because of its resistance through time, its ruggedness and the possibility to be used in all aquatic environments. Electron Beam Lithography (EBL) and Lift-off techniques were used in order to fabricate the nanostructures of desired shape, size and arrangement [31] ensuring control of geometrical parameters for reproducible substrates. Gold nanostructures (GNS) were displayed in patterns ($50\mu\text{m} \times 50\mu\text{m}$) with arrays of GNS diameters varying from 100 nm to 200 nm. The height of GNS was set to 60 nm evaporated on 3 nm of chromium as an adhesive layer. The gratings between nanocylinders were kept constant to 200 nm (from edge to edge).

Prior any experiment fabricated GNS were cleaned using UV-Ozone (PSD-UV - Benchtop UV-Ozone Cleaner, Novascan) for 20 min. Substrates were then rinsed four times by immersion in ethanol. If necessary, a second washing cycle procedure was realized.

5.3.3.4 Surface functionalisation

Chemical grafting was used to functionalise the gold nanostructures for SERS-based surface investigation (Figure 2). For this purpose, SERS substrates were immersed in 10 mL solution of the diazonium salt (10^{-3}mol L^{-1}) dissolved in H_2SO_4 (10^{-2}mol L^{-1}) during 12 hours at 4°C under mild stirring (orbital stirring table). They were then rinsed 3 times by immersion into milliQ water 10 mL over 10 min and dried under nitrogen.

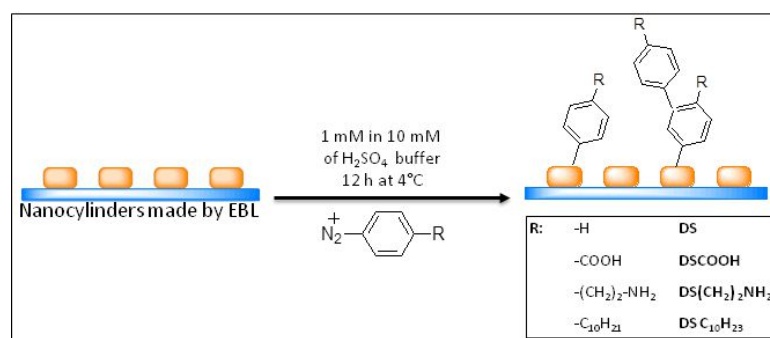


Figure 2 Graphical illustration on studied SERS active nanosensors prepared using four different diazonium salts.

5.3.3.5 Optical measurements

Raman measurements were pursued synthesized diazonium salts with the Labram HR800 system using 691 nm excitation line of Thorium-Argon (Th-Ar) laser. The scattered light was collected by an objective of 100 fold magnification (0.9 N.A.). SERS measurement were performed in back scattering geometry, with i) 660 nm Helium-Neon (He-Ne) laser (Xplora micro-spectrometer) and ii) 691 nm Th-Ar laser (spectrometer). The spectral resolutions of 3 cm^{-1} and less than 2 cm^{-1} were

obtained by using Xplora and Labram HR800 spectrometers, respectively. The laser power density as well as the accumulation time and number of repetitions were varying in order to obtain good signal to noise ratios. The extinction spectra were recorded in transmission configuration with Xplora micro-spectrometer using objective of 20 fold magnification (NA 0.4).

5.3.3.6 Computational details

All calculations were carried out using the Gaussian 09 suite of programs [33] using the B3LYP exchange and correlation functional [34] [35] along with the 6-311++G(d,p) basis set for all atoms but gold [36] [37]. The LANL2DZ basis set consisting of Effective Core Potential (ECP) and double- ζ quality functions for valence electrons was employed for Au [38]. The structures were optimized without symmetry constraint (see Supporting Information). The vibrational frequencies and normal modes were calculated within the harmonic approximation and a scaling factor of 0.976 was chosen on the basis of previously published work [39].

5.3.4 Results and discussion

5.3.4.1 Raman and SERS measurements/DFT calculations

In order to control/comfort the nature of the interface between the GNRs and the organic coating, the characterization of the diazonium salts and their formed layers on the nanostructured surface has been examined by Raman and SERS. This section details the different pathways related to (i) the benzene ring, (ii) the C-H related vibrations, and (iii) the para functions beared by the aromatic cycle (i.e. COOH, CH₂CH₂NH₂ and C₁₀H₂₁).

Figures 3, 4, 5 and 6 compare RAMAN and SERS spectra obtained for synthesized diazonium salts (red spectra) and the diazonium-based GNS (blue spectra).

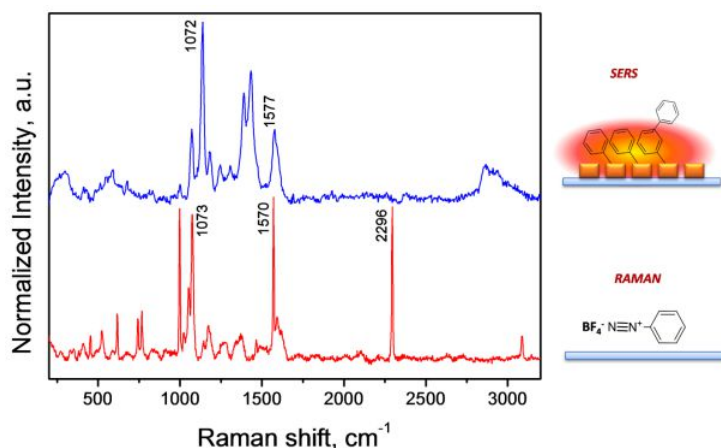


Figure 3: Raman spectra of DS (red) and SERS spectra of the DS based GNS (blue).

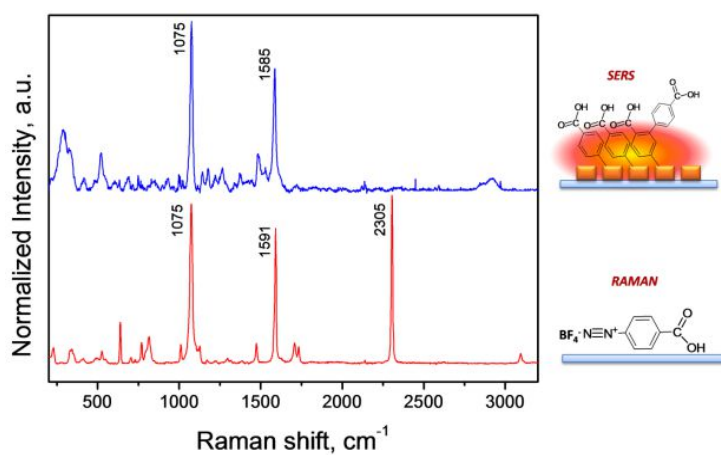


Figure 4: Raman spectra of DS-COOH (red) and SERS spectra of the DS-C₁₀H₂₁-based GNS (blue).

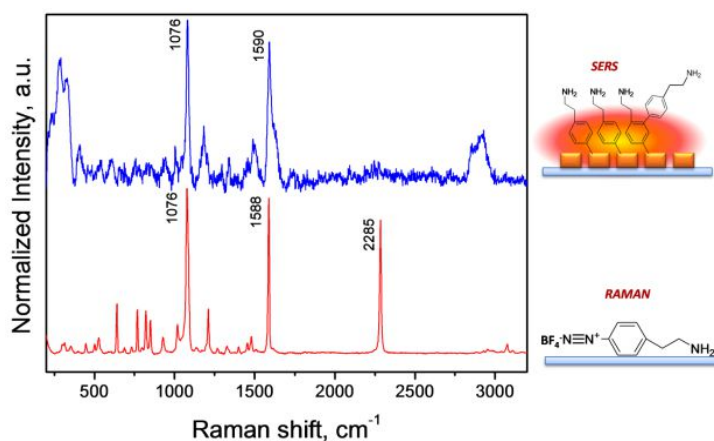


Figure 5: Raman spectra of DS-(CH₂)₂NH₂ (red) and SERS spectra of the DS-(CH₂)₂NH₂-based GNS (blue).

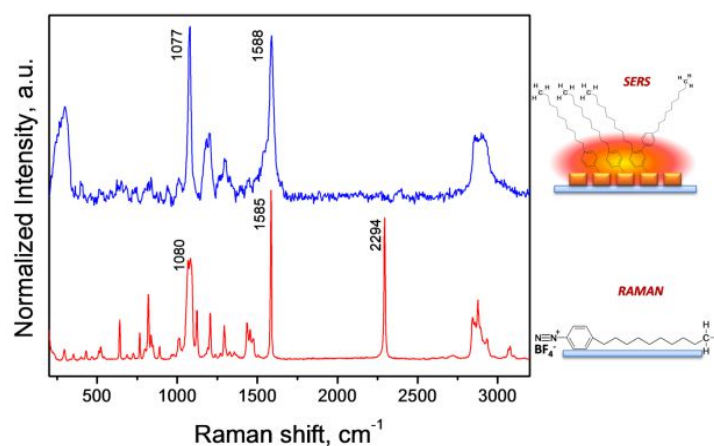


Figure 6: Raman spectra of DS-C₁₀H₂₁ (red) and SERS spectra of the DS-C₁₀H₂₁-based GNS (blue).

The frequency of important peaks are reported in table 1; assignments have been provided with the help of literature [40-42]. DFT calculations and NBO charges have only been performed for DS, DCOOH.

Table 1: Band assignments for RAMAN and SERS spectra obtained for the synthesized diazonium salts and functionalised nanostructures.

N°	DS				diazonium-based GNS				Assignment
	DS	DS-COOH	DS-(CH ₂) ₂ NH ₂	DS-C ₁₀ H ₂₁	DS	DS-COOH	DS-(CH ₂) ₂ NH ₂	DS-C ₁₀ H ₂₁	
1	2296	2305	2285	2294					N≡N stretching [40;41]
3	1570	1591	1588	1585	1577	1585	1590	1588	C=C stretching [40]
4	997 1021				999 vw				Ring deformation + ring breathing for benzene and mono-substituted derivatives[40;41]
5	617	637	640	639					Ring deformation[40]
6		814	849	837					Ring breathing[40]
7		796	820	819					o;m CH wagging [40;41]
8	743								p CH wagging [40;41]
9	1162				1138				m;p CH in plane bending [40;41]
10	1073	1075	1076	1080	1072	1075	1076	1077	CH in plane bending for p- and monosubstituted benzenes [14;41]
11	1174	1170vw	1198vw	1190vw	1182	1177vw	1183 vw	1180 vw	m;o CH in plane bending [40;41]
12	3087	3096	3076	3066 3077					Aromatic CH stretch of benzene derivative [40;41]
13			2813-2986	2813-2986			2813-2956	2815-2970	Symmetric and anti-symmetric CH stretch of n-alkanes [41]
14			1082	1079					C-C stretching (aliphatic chain) [41]
15			1454	1456			1455 vw	1449vw	CH ₂ scissoring[43]
16		1732 1708				1708			C=O stretching

5.3.4.2 Raman characterization of the diazonium salts

The particularity of diazonium salts is their N₂⁺ function obtained by the oxidation of the corresponding amine. According to Socrates [41] and Laurentius *et al.* [14], diazonium salts have a strong band in the region of 2300-2130 cm⁻¹ due to the stretching mode of the N≡N bond. Raman investigation of synthesized diazonium salts confirmed the existence of this later mode in the given area. More precisely, the emergence of strong peaks observed at 2296, 2305, 2285 and 2294 cm⁻¹ for DS, DCOOH, D(CH₂)₂NH₂ and DC₁₀H₂₁ respectively (figures 3, 4, 5 and 6, Table 1 N°1). DFT calculations performed on DS and DSCOOH compounds revealed strong similarities in this spectral

region. For instance, the $\text{N}\equiv\text{N}$ stretching mode calculated for DS was observed at 2291 cm^{-1} while experimentally observed same mode was at 2296 cm^{-1} . Comparing Raman and SERS spectra later peak is absent in SERS spectra for all diazonium salts giving the first proof of efficient chemisorption.

Further comparison of Raman spectra of diazonium salts and SERS spectra of grafted phenyl derivatives, several common bands related to the benzene ring vibrations can be observed.

First of all, the strong band related to the benzene ring stretching mode (Table 1 N°3) can be seen in both Raman and SERS spectra in the range $1585\text{-}1611\text{ cm}^{-1}$. According to Wojciechowski *et al.* (2003) [42], this band is essentially related to stretching modes of aromatic C2-C3 and C5-C6. For all investigated diazonium salts including their grafted layers, this band is the most significant signature of the benzene ring. In case of phenyl derivatives grafted to a GNS, this vibration is one of the mainly enhanced modes. This observation can be explained by the surface selection rules [44]: the vibrational modes that involve a large change of the polarizability perpendicular to the metal surface should be the most enhanced. In SERS spectra of functionalised nanostructures (figure 3, 4, 5, 6 blue spectra), this band is followed by a shoulder observed at the higher wavenumber. According to Liu *et al.* (2010) [45], it can be assigned to a charge transfer from grafted phenyl derivatives to the gold.

Retaining on C=C–C related vibrations, two intensive and distinct peaks assigned to ring deformation and ring breathing for benzene and mono-substituted derivatives are found just in the Raman spectrum of DS at around 997 cm^{-1} (Fig. 3 and Table 1, N°4: trigonal ring breathing vibration) and 1021 cm^{-1} (Fig. 3 and Table 1, N°4: CC stretching vibration coupled with CH in plane bending vibration) [42]. For DS chemisorbed onto the GNCs just were weak intensity peak can be observed at 999 cm^{-1} . On the other hand, in the case of para-substituted diazonium salts these vibrational modes are not evidenced [41].

Bands assigned to ring deformation (C=C–C in plane deformation) in the region of $617\text{-}644\text{ cm}^{-1}$ (Table 1, N°5) are presented for all diazonium salts. In agreement with Socrates [41], bands shift towards the higher wavelengths for para-substituted aromatic compounds in comparison with mono-substituted compounds. These bands are also no more found in SERS spectra of grafted phenyl derivatives. As well as the ring deformation mode observed in Raman spectra of para-substituted diazonium salts [40]. Peaks related to this vibration were observed at 814 cm^{-1} for DS-COOH and it has shifted towards higher wavenumber ($849\text{-}837\text{ cm}^{-1}$) for DS(CH)₂NH₂ and DSC₁₀H₂₁.

Of particular interest is the very strong band related to the CH in plane bending for mono- and para-substituted benzenes observed in spectra of the diazonium salts and their grafted layers (Figure 3, 4, 5, 6 Table 1, N°10). The obtainment of this characteristic band can be attributed to the electron

charge density redistribution within the structures caused by the presence of $N_2^+BF_4^-$ for diazonium salts and of metal for grafted phenyl derivatives. Concerning SERS spectra of diazonium salt-based grafted layers, registered enhancement of this later CH in plane bending mode, suggests that the chemisorbed molecules have adopted a perpendicular orientation with respect to the Au surface [46], in agreement with the previous observation done for the ring deformation mode detected at 1585cm^{-1} . This prediction is also confirmed by the presents of m,o-CH in plane bending mode at $1177\text{-}1179\text{ cm}^{-1}$ (Table 1, N°11) seen for all grafted phenyl derivatives.

Concerning different para functions carried by the aromatic cycle (i.e. COOH, $CH_2CH_2NH_2$ and $C_{10}H_{21}$), some characteristic bands have been identified. For $(CH_2)_2NH_2$, $C_{10}H_{21}$ bearing diazonium salts, symmetric and anti-symmetric CH_3 stretch of n-alkanes as well as symmetric CH_2 stretch of n-alkanes have been clearly identified in the region $2813\text{-}2986\text{ cm}^{-1}$ (table 1, N°13) (for DSCOOH, the presence of bands at this region ($2815\text{-}2956$) is due to substrate contamination by polymeric organic substances). In addition, C-C stretching mode in the region of $1079\text{-}1082\text{ cm}^{-1}$ (table 1, N°14); and CH_2 scissoring in the region $1454\text{-}1456\text{ cm}^{-1}$ (table 1, N°15) were also observed in case of compounds bearing donating group in para position. Later bands intensity is strongly diminished in spectra of $DS(CH_2)_2NH_2$ and $DSC_{10}H_{21}$ grafted on GNS. This can be explained by steric hindrance caused by means of the disordered grafted carbon chains. Concerning DSCOOH derivatives (figure 4, Table 1 N°16), the weak and very weak bands observed in the $1700\text{-}1800\text{ cm}^{-1}$ region are the characteristic features of the carboxylic group due to the C=O stretching vibration. In agreement with the calculations providing a dimeric arrangement for DCOOH via H-bonds, the Raman spectrum of DCOOH (figure 3) exhibits two C=O stretching vibrations, the symmetric and the antisymmetric stretching vibrations, respectively at 1708 and 1732 cm^{-1} . The antisymmetric stretch is usually seen at a higher wavenumber than the symmetric one [47]. Concerning the grafted nanostructure, a very weak band is observed at 1708 cm^{-1} .

5.3.4.3 Investigations of nature of the interface between the surface and the coating

The successful chemisorption of the phenyl derivative molecules onto the gold nanostructures (GNS) have been evidenced in SERS spectra (fig. 3, 4, 5, 6) by observing both: (i) the absence of the characteristic $N\equiv N$ group vibration band and (ii) the presence of the strongest characteristic bands of diazonium salts (Table 1, N°3, N°10, N°11).

The grafting of DSCOOH derivative on the gold SERS substrates was modeled by DFT. The spontaneous grafting of DSCOOH on gold surface could proceed through dediazonation leading to the carboxyphenyl-gold adduct with formation of Au-C bond (CB-Au) or through the cationic mechanism leading to azo adducts with formation of Au-N bond (CB- N_2 -Au). In addition to the

monolayer models on gold surface, the grafting of multilayers of aryl groups was also considered using biphenyl adducts on gold. (see Supporting Information Fig. S1) [48].

The confrontation of experimental SERS spectra with the simulated spectra of CB-Au and CB-N₂-Au shows that the main features are reproduced. However, the strong band predicted by DFT at 1720 cm⁻¹ and corresponding to the C=O stretching mode $\nu(\text{C}=\text{O})$, is absent in the experimental SERS spectrum. Previous SERS studies on the adsorption of benzoic acid on silver highlighted the influence of the pH on the $\nu(\text{C}=\text{O})$ band. The latter proved to be absent in the recorded normal Raman spectra for benzoic acid dissolved in solution at pH=13.

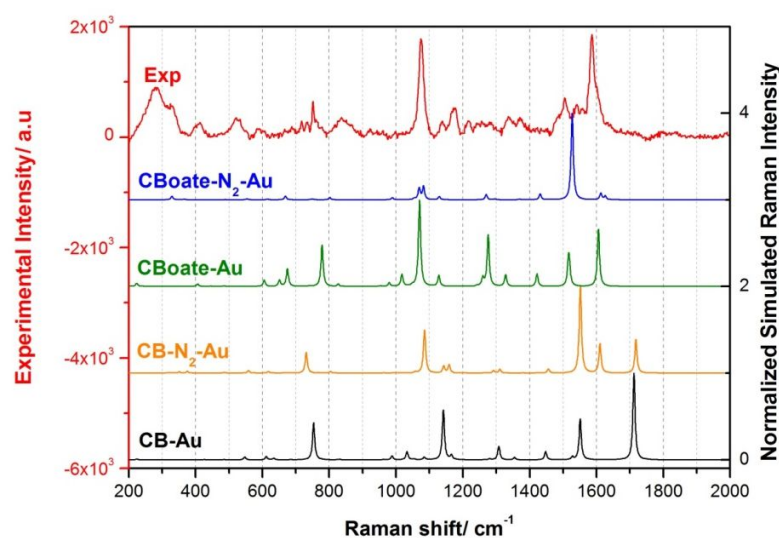


Figure 7: Comparison of the experimental SERS spectra recorded for DS-COOH with the spectra obtained by DFT modeling for different adducts.

In our case, given that after incubation of GNS arrays in DSCOOH solution, the functionalised platform was washed several times with water at neutral pH, the resulting carboxyphenyl layer is likely in the carboxylate form. Therefore, the possibly of deprotonated monolayer were modeled by DFT as CBoate-Au and CBoate-N₂-Au (see Fig. 7). As expected, the stretching mode $\nu(\text{C}=\text{O})$ is in those cases are absent. In addition, the model CBoate-Au seems to be the best model to reproduce the spectral characteristics of the experimental SERS both in terms of position and intensity.

5.3.4.4 XPS measurement

In order to confirm the hypotheses on the nature of the interface between surface and the organic coating drawn from obtained SERS and DFT calculations, the XPS measurement were performed on planar gold samples functionalised by DSCOOH via spontaneous grafting.

The C1s, N1s and Au4f high resolution XPS spectra (HR-XPS) are shown in Figure 8. The Carbon 1s region displays three components at 284.6, 286. And 288.7 eV assigned to CC/CH, C-O, and COOH

groups respectively. However, observation of an Au-C bond by XPS was impossible due to the non-significant difference in electronegativity between carbon and gold atoms ($\chi_{\text{C}} = 2.55$ and $\chi_{\text{Au}} = 2.54$ using the Pauling scale). The N 1s region revealed a component attributed to $-\text{N}=\text{N}-$ bonds found at 399.7 eV [49;22;25;28], demonstrating the multilayer linkage via azo bonds.. In agreement with [28], no Au-N bonds could be observed in the spectra corresponding to the COOH-DS-based coating.

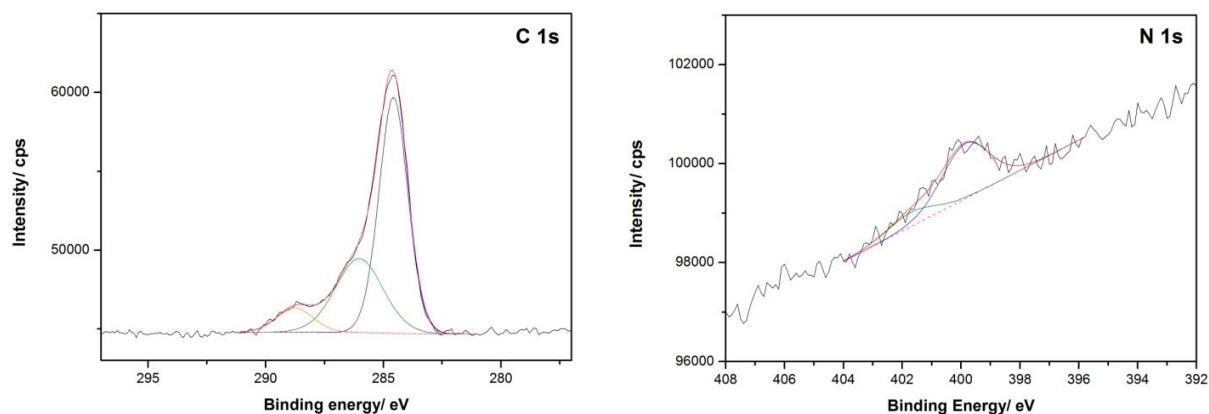


Figure 8: HR-XPS spectra of C 1s (left panel) and N 1s (right panel) regions recorded for DSCOOH adsorbed on planar gold film. The overall fitted data are reported as red line.

5.3.5 Conclusion

In this study the tailoring the surface chemistry of the developed grafted gold nanostructures as SERS substrates has been selected as the first key factor for the implementation of the sensors. For this purpose, the phenyl derivatives were characterized using Raman and SERS spectroscopies. When possible, RAMAN and SERS experiments were combined with DFT modelling. The obtainment of bands related to CH in plane bending for p-substituted and mono-substituted benzenes (observed in the range $1075\text{-}1074\text{ cm}^{-1}$) and with aromatic ring deformations found in the range of $1570\text{-}1591\text{ cm}^{-1}$ brought irrefutable evidence of the phenyl derivatives based coating formation on nanostructured substrates. Comparison of SERS spectrum for DSCOOH coating with the spectra of different adducts modelled by DFT led to the conclusion that DSCOOH grafting to a GNSs was driven by radical mechanism ensuring C-Au covalent bond. In addition, results obtained by XPS showed that no presence of Au-N bond confirming latter assumption. On the other hand, the N 1s region found component attributed to $-\text{N}=\text{N}-$ bonds suggest the multilayer formation linked via azo bonds. Thus, all results provided by SERS, DFT calculations and XPS led us to conclude that the spontaneous grafting realized on gold via DS-COOH is in good agreement with the achievement of a coating like structure E represented in Figure 1.

AUTHOR INFORMATION

Corresponding Author

*s.betelu@brgm.fr

* marc.lamydelachapelle@univ-paris13.fr

ACKNOWLEDGMENT

This work was funded by ANR ECOTECH (Production durable et technologies de l'environnement); REMANTAS project: Enhanced Raman scattering for aquatic media: a new technology for on-site analysis 2011-2014 (REMANTAS project (ANR-11-ECOT-0010)).

5.3.6 References

- 1 Young, M. A., Stuart, D. A., Lyandres, O., Glucksberg, M. R. and Van Duyne, R. P. (2004). Surface-enhanced Raman spectroscopy with a laser pointer light source and miniature spectrometer, *Canadian Journal of Chemistry*, **82**, pp. 1435–1441.
- 2 Otto, A., Mrozek, I., Grabhorn, H. and Akemann, W. (1992). Surface-enhanced Raman scattering, *Journal of Physics: Condensed Matter*, **4**, pp. 1143–1212.
- 3 Peron, O., Rinnert, E., Lehaitre, M., Crassous, P. and Compere, C. (2009). Detection of polycyclic aromatic hydrocarbon (PAH) compounds in artificial sea-water using surface-enhanced Raman scattering (SERS), *Talanta* **79**, pp. 199–204.
- 4 Allan, I. J., Vrana, B., Greenwood, R., Mills, G. A., Roig, B. and Gonzales, C. (2006). A “toolbox” for biological and chemical monitoring requirements for the European Union’s Water Framework Directive, *Talanta*, **69**, pp. 302–322.
- 5 Peron, O., Rinnert, E., Florent, C., Lehaitre, M. and Compere, C. (2010). First steps of in situ surface-enhanced Raman scattering during shipboard experiments, *Society for Applied Spectroscopy*, **64**, pp. 1086–1093.
- 6 Peron, O., Rinnert, E., Toury, T., Lamy de la Chapelle, M. and Compère, C. (2011). Quantitative SERS sensors for environmental analysis of naphthalene, *The Analyst*, **136**, pp. 1018–1022.
- 7 Prien, R. D. (2007). The future of chemical in situ sensors, *Marine Chemistry*, **107**, pp. 422–432.
- 8 Rogers, J. A., Jackman, R. J. and Whitesides, G. M. (1997). Constructing single- and multiple-helical microcoils and characterizing their performance as components of microinductors and microelectromagnets, *Journal of Microelectromechanical Systems*, **6**, pp. 184–192.
- 9 Ulman, A. (1996). Formation and Structure of Self-Assembled Monolayers, *Chemical Reviews*, **96**, pp. 1533–1554.
- 10 Zielinski, O., Busch, J. A., Cembella, A. D., Daly, K. L., Engelbrektsson, J., Hannides, A. K. and Schmidt, H. (2009). Detecting marine hazardous substances and organisms: sensors for pollutants, toxins, and pathogens, *Ocean Science Discussion*, **6**, pp. 953–1005.
- 11 Adenier, A., Cabet-Deliry, E., Chaussé, A., Griveau, S., Mercier, F., Pinson, J. and Vautrin-UI, C. (2005). Grafting of nitrophenyl groups on carbon without electrochemical induction, *Chemistry of materials*, **17**, pp. 491–501.
- 12 Bekyarova, E., Itkis, M. E., Ramesh, P., Berger, C., Sprinkle, M., de Heer, W. A. and Haddon, R. C. (2009). Chemical modification of epitaxial graphene: spontaneous grafting of aryl groups, *Journal of American Chemistry Society*, **131**, pp. 1336–1337.
- 13 Combellas, C. M., Delamar, F., Kanoufi, F., Pinson, J. and Podvorica, F. I. (2005). Spontaneous grafting of iron surfaces by reduction of aryldiazonium salts in acidic or neutral aqueous solution. Application to the protection of iron against corrosion., *Chemistry of Materials*, **17**, pp. 3968–3975.
- 14 Laurentius, L., Stoyanov, S. R., Gusarov, S., Kovalenko, A., Du, R., Lopinski, G. P. and McDermott, M. T. (2011). Diazonium-Derived Aryl Films on Gold Nanoparticles: Evidence for a Carbon–Gold Covalent Bond, *ACS Nano*, **5**, pp. 4219–4227
- 15 Betelu, S., Vautrin-UI, C. and Chaussé, A. (2009). Novel 4-carboxyphenyl-grafted screen-printed electrode for trace Cu(II) determination, *Electrochemistry Communications*, **11**, pp. 383–386.
- 16 Betelu, S., Vautrin-UI, C., Ly, J. and Chaussé, A. (2009). Screen-printed electrografted electrode for trace uranium analysis, *Talanta*, **80**, pp. 372–376.
- 17 Delamar, M., Hitmi, R., Pison, J. and Savéan, J. (1992). Covalent modification of carbon surfaces by grafting of functionalized aryl radicals produced from electrochemical reduction of diazonium salts, *Journal of the American Chemical Society*, **114**, pp. 5883–5884.
- 18 Bouriga, M., Chehimi, M. M., Combellas, C., Decorse, P., Kanoufi, F., Deronzier, A. and Pinson, J. (2013). Sensitized Photografting of Diazonium Salts by Visible Light, *Chem. Mater.*, **25**, pp. 90–97.
- 19 Andrieux, C. P. and Pinson, J. (2003). The Standard Redox Potential of the Phenyl Radical/Anion Couple, *Journal of the American Chemical Society* **125**, pp. 14801–14806.

- 20 Boukerma, K., Chehimi, M. M., Pinson, J. and Blomfield, C. (2003). X-ray Photoelectron Spectroscopy Evidence for the Covalent Bond between an Iron Surface and Aryl Groups Attached by the Electrochemical Reduction of Diazonium Salts, *Langmuir*, **19**, pp. 6333–6335.
- 21 Adenier, A., Barré, N., Cabet-Deliry, E., Chaussé, A., Griveau, S., Mercier, F., Pinson, J. and Vautrin-UI, C. (2006). Study of the spontaneous formation of organic layers on carbon and metal surfaces from diazonium salts, *Surface Science*, **600**, pp. 4801–4812.
- 22 Saby, C., Ortiz, B., Champagne, G. Y. and Bélanger, D. (1997). Electrochemical Modification of Glassy Carbon Electrode Using Aromatic Diazonium Salts. 1. Blocking Effect of 4-Nitrophenyl and 4-Carboxyphenyl Groups, *Langmuir* **13** pp. 6805–6813.
- 23 Ricci, A. M., Mendez De Leo, L. P., Williams, F. J. and Calvo, E. J. (2012). Some Evidence for the Formation of an Azo Bond during the Electroreduction of Diazonium Salts on Au Substrates, *ChemPhysChem* **13**, pp. 2119–2127.
- 24 Laforgue, A., Addou, T. and Belanger, D. (2005). *Langmuir* **21**, pp. 6855–6865.
- 25 Toupin, M. and Bélanger, D. (2008). Spontaneous Functionalization of Carbon Black by Reaction with 4-Nitrophenyldiazonium Cations, *Langmuir* **24**, pp. 1910–1917.
- 26 Combellas, C., Kanoufi, F., Pinson, J. and Podvorica, F. (2008). *J. Am. Chem. Soc.*, **130**, pp. 8576–8577.
- 27 Jung, U., Kuhn, S., Cornelissen, U., Tuzek, F., Strunskus, T., Zaporojtchenko, V., Kubitschke, J., Herges, R. and Magnussen, O. (2011). *Langmuir* **27**, pp. 5899–5908.
- 28 Mesnage, A., Lefèvre, X., Pascale, J., Deniau, G. and Palacin, S. (2012). Spontaneous Grafting of Diazonium Salts: Chemical Mechanism on Metallic Surfaces, *Langmuir*, **28**, pp. 11767–11778.
- 29 Bahr, J. L., Yang, J., Kosynkin, D. V., Bronikowski, M. J., Smalley, R. E. and Tour, J. M. (2001). Functionalization of carbon nanotubes by electrochemical reduction of aryl diazonium salts: a bucky paper electrode, *J. Am. Chem. Soc.*, **123**, pp. 6536–6542.
- 30 Allongue, P., Delamar, M., Desbat, B., Fagebaume, O., Hitmi, R., Pinson, J. and Saveant, J. M. (1997). Covalent Modification of Carbon Surfaces by Aryl Radicals Generated from the Electrochemical Reduction of Diazonium Salts, *Journal of American Chemistry Society*, **119**, pp. 201–207.
- 31 Grand, J., Kostcheev, S., Bijeon, J. L., Lamy de la Chapelle, M., Adam, P. M., Rumyantseva A., Léron del, G. and Royer, P. (2003). Synthetic Metals, *Optimization of SERS-active substrates for near-field Raman spectroscopy*, **139**, pp. 621–624.
- 32 Griveau, S., Mercier, D., Vautrin-UI, C. and Chaussé, A. (2007). Electrochemical grafting by reduction of 4-aminoethylbenzenediazonium salt: Application to the immobilization of (bio)molecules, *Electrochemical Communication*, **9**, pp. 2768–2773.
- 33 Frisch, M. J., Trucks, G. W., Schlegel, H. B., Scuseria, G. E., Robb, M. A., Cheeseman, J. R., Scalmani, G., Barone, V., Mennucci, B., Petersson, G. A., Nakatsuji, H., Caricato, M., Li, X., Hratchian, H. P., Izmaylov, A. F., Bloino, J., Zheng, G., Sonnenberg, J. L., Hada, M., Ehara, M., Toyota, K., Fukuda, R., Hasegawa, J., Ishida, M., Nakajima, T., Honda, Y., Kitao, O., Nakai, H., Vreven, T., Montgomery Jr., J. A., Peralta, J. E., Ogliaro, F., Bearpark, M. J., Heyd, J., Brothers, E. N., Kudin, K. N., Staroverov, V. N., Kobayashi, R., Normand, J., Raghavachari, K., Rendell, A. P., Burant, J. C., Iyengar, S. S., Tomasi, J., Cossi, M., Rega, N., Millam, N. J., Klene, M., Knox, J. E., Cross, J. B., Bakken, V., Adamo, C., Jaramillo, J., Gomperts, R., Stratmann, R. E., Yazyev, O., Austin, A. J., Cammi, R., Pomelli, C., Ochterski, J. W., Martin, R. L., Morokuma, K., Zakrzewski, V. G., Voth, G. A., Salvador, P., Dannenberg, J. J., Dapprich, S., Daniels, A. D., Farkas, Ö., Foresman, J. B., Ortiz, J. V., Cioslowski, J. and Fox, D. J. (2009). Gaussian 09: Gaussian, Inc., Wallingford, CT.
- 34 Becke, A. D. (1993). Density-functional thermochemistry. III. The role of exact exchange, *The Journal of Chemical Physics*, **98**, pp. 5648–5652.
- 35 Lee, C., Yang, W. and Parr, R. G. (1988). Development of the Colle-Salvetti correlation-energy formula into a functional of the electron density, *Physical Review B*, **37**, pp. 785–789.
- 36 Clark, T., Chandrasekhar, J., Spitznagel, G. W. and Schleyer, P. V. R. (1983). Efficient diffuse function-augmented basis sets for anion calculations. III. The 3-21+G basis set for first-row elements, Li–F, *Journal of Computational Chemistry*, **4**, pp. 294–301.

- 37 Francl, M. M., Pietro, W. J., Hehre, W. J., Binkley, J. S., Gordon, M. S., DeFrees, D. J. and Pople, J. A. (1982). Self-consistent molecular orbital methods. XXIII. A polarization-type basis set for second-row elements, *The Journal of Chemical Physics*, **77**, pp. 3654-3665.
- 38 Hay, P. J. and Wadt, W. R. (1985). Ab initio effective core potentials for molecular calculations. Potentials for the transition metal atoms Sc to Hg, *The Journal of Chemical Physics*, **82**, pp. 270-283.
- 39 Fairchild, S. Z., Bradshaw, C. F., Su, W. and Guharay, S. K. (2009). Predicting Raman spectra using density functional theory, *Appl Spectrosc*, **63**, pp. 733-741.
- 40 Badawi, H. M., Förner, W. and Ali, S. (2013). A comparative study of the infrared and Raman spectra of aniline and o-, m-, p-phenylenediamine isomers, *Spectrochim Acta A Mol Biomol Spectrosc.* , **112**, pp. 388-396.
- 41 Socrates, G. (2001). *Infrared and Raman Characteristic Group Frequencies: Tables and Charts (3ed)* (Chichester (U.K.) ed.): Wiley.
- 42 Wojciechowski, P. M., Zierkiewicz, W. and Michalskaa, D. (2003). Electronic structures, vibrational spectra, and revised assignment of aniline and its radical cation: Theoretical study, *Journal of Chemical Physics*, **118**, pp. 10900-10911.
- 43 Venkateswaran, C. S. and Pandya, N. S. (1942). The Raman spectra of organic compounds: Diethyl disulphide, *Proc. Indian Acad. Sci.*, **Section A 15**, pp. 396–400.
- 44 Hallmark, V. and Champion, A. (1986). Selection rules for surface Raman spectroscopy: experimental results *J. Chem. Phys.*, **84**, pp. 2933–2941.
- 45 Liu, L. and Guo, Q. X. (2002). The Driving Forces in the Inclusion Complexation of Cyclodextrins, *Journal of Inclusion Phenomena and Macrocyclic Chemistry* **42**, pp. 1-14.
- 46 Baia, M., Baia, L., Kiefer, W. and Popp, J. (2004). Surface-enhanced Raman scattering and density functional theoretical study of anthranil adsorbed on colloidal silver particles, *J. Phys. Chem. B*, **108**, pp. 17491–17496.
- 47 Kambhampati, P., Child, C. M., Foster, M. C. and Champion, A. (1998). On the chemical mechanism of surface enhanced Raman scattering: Experiment and theory, *The Journal of Chemical Physics*, **108**, pp. 5013-5026.
- 48 Ahmad, R., Boubekeur-Lecaque, L., Nguyen, M., Lau-Truong, S., Lamouri, A., Decorse, P., Galtayries, A., Pinson, J., Felidj, N. and Mangeney, C. (2014). Tailoring the Surface Chemistry of Gold Nanorods through Au–C/Ag–C Covalent Bonds Using Aryl Diazonium Salts, *The Journal of Physical Chemistry C*, **118**, pp. 19098-19105.
- 49 Doppelt, P., Pinson, J., Podvorica, F., Verneyre, S. and Hallais, G. (2007). Surface modification of conducting substrates. Existence of azo bonds in the structure of organic layers obtained from diazonium salts. , *Chem. Mater.* , **19**, pp. 4570–4575.

5.4 Diazonium salt-based SERS active sensor: towards detection and quantitation of the aromatic hydrocarbons in water samples

Inga Tijunelyte^{1‡}, Stéphanie Betelu^{2‡}, Jonathan Moreau⁴, Ioannis Ignatiadis², Catherine Berho², Nathalie Lidgi-Guigui¹, Erwann Guénin¹, Catalina David³, Sébastien Vergnole³, Emmanuel Rinnert⁴, Marc Lamy de la Chapelle¹

¹CSPBAT laboratory, UMR 7244, UFR SMBH, University of Paris 13, 74, Rue Marcel Cachin, 93017 Bobigny, France

²BRGM, F-45060 OrléansCedex 02, France

³HORIBA Jobin Yvon SAS, 16-18 rue du Canal, 91165 Longjumeau Cedex, France

⁴IFREMER, Brittany center, Detection, Sensors and Measurements Laboratory, CS10070, 29280 Plouzané, France

Supplementary Information in ANNEX 6

KEYWORDS:

Polynuclear aromatic hydrocarbon (PAH); Surface Enhanced Raman Scattering (SERS); Nanosensor; Diazonium salt; Surface functionalisation; Detection.

5.4.1 Abstract

New type of nanosensor for SERS based environmental pollutants detection is presented. This work was essentially conducted on Polycyclic Aromatic Hydrocarbons (PAHs): naphthalene (NAP), fluorethene (FL) and benzo[a]pyrene (BaP). Commercially available SERS substrates based on gold nanostructures (GNS) were chemically functionalised using diazonium salts. SERS analyses have then been conducted with DS-based GNS and DC₁₀H₂₁-based GNS in order (i) to investigate the capability of nanosensor to pre-concentrate and sense the organic pollutants alone and in mixture and (ii) to compare the influence of the group borne by the grafted GNS and (iii) to select the most appropriate coating for PAHs sensing. Targeted molecules were measured in water/methanol (9/1 v/v) samples. Investigation of solutions containing different concentrations in the range of nmol.L⁻¹ to µmol.L⁻¹ led to establish the calibration curves and to determine the performances of the sensors. DC₁₀H₂₁-based GNS was selected as the most efficient. The calculated LOD and LOQ were respectively (i) 0.091 ppm (0.45 µmol/L) and 0.277 ppm (1.4 µmol/L) for FL, (ii) 0.045 ppm (0.18 µmol/L) and 0.138 ppm (0.5 µmol/L) for BaP and (iii) 0.045 ppm (0.18 µmol/L) and 0.138 ppm (0.5 µmol/L) for NAP. The examination of the correlation between the calculated LOD values and the Kow factor of investigated PAHs suggested the suitability of developed nanosensor for the pre-concentration of highly non-polar PAH compounds. Moreover, since targeted molecules pre-concentration was essentially based on weak forces (hydrophobic and π-π stacking interactions), surface regeneration step was optimized.

5.4.2 Introduction

Within the scopes of the latest European Water Framework Directives (2000/60/EC, 2006/118/EC and 2006/11/EC), the development of analytical tools allowing on-site accurate and sensitive detection of pollutants in the environmental waters is of primary importance concern. While extensive efforts have been devoted to develop highly sensitive, reproducible, accurate and robust analytical sensors for on-site or *in situ* monitoring of trace elements (i.e. qualitative and quantitative analysis) [1-8], considerable attention has to be provided for organic contaminants.

Among the strategies investigated to achieve this need, novel extraction techniques have been widely reported. Solid phase microextraction (SPME) [9-12] or stir bar sorptive extraction (SBSE) [13] combined with gas chromatography (GC) [14-16], high performance liquid chromatography (HPLC) [17;16], mass spectrometry (MS) [18], Raman spectroscopy [11] or capillary electrophoresis (CE) led to accurate results down to pg.L^{-1} for chlorinated solvents [17], BTEXs [11], and polycyclic aromatic hydrocarbons (PAHs) [10;16]. Despite high sensitivity, suggested procedures using these passive sensors do not overcome the limitations for on-site monitoring: co-injection of solvents [19;20] and handling desorption procedure under high temperature or pressure [21].

New alternative methodologies, with similar performances have thus been investigated for this purpose. Due to the sensitivity up to ng.L^{-1} , a considerable interest has been devoted on piezoelectric chemical sensors (quartz crystal microbalance, QCM) [22-32]. It has been demonstrated that QCM is a relevant tool to investigate the pre-concentration of organic contaminants using coated polymers or calixarenes. [23;33;24-30;32]. However, QCM based sensors application for simultaneous detection of organic compounds in natural samples has not been reported; probably due to their lack in molecular recognition.

In comparison, latter issues related to the molecular identification in complex environmental conditions can be defeated by exploiting Surface Enhanced Raman Spectroscopy (SERS). SERS is a powerful technique providing the enhancement of Raman signal by both electromagnetic and chemical effects. The first comes from the interaction between the incident light and the metallic nanostructures inducing a local enhancement of the electromagnetic field through the excitation of localized surface plasmon [34-36]. As a consequence the Raman signal of any molecule located at the close vicinity of the nanostructure surface can be enhanced up to 10^8 folds [37-39]. The second effect contributing in Raman signal enhancement up to 10^2 folds is due to electronic interaction between the molecules and the metallic nanostructure (i.e. charge transfer between surface and chemisorbed molecules) [40]. Based on nanostructured metallic surface, SERS nanosensors are able to detect very

low concentration of analyte thus, to reach high sensitivity and low limit of detection down to the individual molecule [41] [42] [43].

Thanks to (i) the improvement on electronics that led to miniaturize Raman spectrometer [12], (ii) the progresses of nano-scale technology of nanosensors, essentially based on colloid systems [44;45], and (iii) the surface chemistry (i.e. Self-Assembled Monolayers (SAMs)), SERS has already been identified as a promising tool for on-site monitoring of organic contaminants at the ng.L^{-1} level [46;47;45;48-52]. However, despite great improvements made to produce colloidal nanostructures with controlled size and shape [44;45], such SERS nanosensors encounter a major drawback related with a poor SERS signal reproducibility due to uncontrollable aggregation of metal colloids. Concerning SAM's, they are recognized as excellent systems for sensing applications since they offer well-defined organization and densely-packed structures [53]. However, limitations with regard to the stability of the covalent bond and hence the stability of the resultant SAM's have been demonstrated [54;55]. Nevertheless, all of these works suggest particularly interesting standpoints for the development of new type "long life" robust SERS sensors that could provide accurate and reproducible detection of organic compounds.

In order to overcome the lack of reproducibility and taking advantage of increasing number of SERS substrates available commercially, we have selected substrates based on gold nanorods from Wavelet, devoted for highly reproducible very sensitive measurements. For surface functionalisation, diazonium salts have been selected as a powerful innovative alternative to SAMs. In the literature immobilization of aryldiazonium is defined as a versatile method, allowing stable grafted organic layers [56-62]. Thanks to both: sensor robustness ensured by chemically grafted aryldiazonium based layers and tunable surface properties provided by wide variety of available diazonium salts, functionalised SERS sensor has been herein studied for the detection and the quantitation of three PAHs: naphthalene (NAP), fluoranthene (FL) and benzo[a]pyrene (BaP). Among the 130 PAHs released into the environment, these three ones belong to the priority substances under the Water Framework Directives (2000/60/EC) and the United States Environment Protection Agency. These selected pollutants were investigated in this study in order to demonstrate the proof of concept of the new designed SERS based nanosensor capability in molecular sensing. Compounds were analyzed alone and in mixture. Investigations of the targeted molecules were realized with different concentrations prepared in water/methanol (9/1 v/v) solutions. Calibration curves and detection limits were established for each compound. Moreover, since the pre-concentration of targeted molecules at the nanosensor surface was essentially based on weak molecular forces, we showed that developed nanosensor can be successfully regenerated and reused.

5.4.3 Experimental

5.4.3.1 Reagents and material

Diethyl ether ($\geq 98\%$), Tetrafluoroboric acid (49.5-50.5%), Sodium Nitrite ($\geq 97\%$), Aniline ($\geq 99.5\%$), 4-dodecylanilin (97%), Naphthalene (99%), Fluoranthene (98%) and Benzo[a]pyrene ($\geq 96\%$ HPLC) were purchased from Sigma Aldrich and used without further purification. Ethanol (96%) and methanol (100%) were purchased from VWR; Sulfuric acid (95-98%) was supplied by JT Baker. Milli-Q water (resistivity of $18.2 \text{ M}\Omega\cdot\text{cm}^{-1}$) was used for all experiments.

5.4.3.2 Diazonium salt chemical synthesis

Benzene-diazonium-tetrafluoroborate (DS) and 4-dodecyl benzene-diazonium-tetrafluoroborate (DS- $\text{C}_{10}\text{H}_{21}$), were proceeded regarding the reaction between aryl amines and a sodium nitrile at 0°C [63]. Briefly, primary amine ($4 \cdot 10^{-3} \text{ mol}\cdot\text{L}^{-1}$) was dissolved in tetrafluoroboric acid (HBF_4) solution and the mixture was then allowed to cool for 15 min. Pre-cooled aqueous sodium nitrite ($4.3 \cdot 10^{-3} \text{ mol}\cdot\text{L}^{-1}$) solution was dropwise added to the acidic amine mixture under stirring. The mixture was then allowed to react for 40 min. Presented precipitates appeared during reaction were filtered through $0.2 \mu\text{m}$ cellulose ester filters (Whatman, France) and generously washed: DS with cold diethyl ether and $\text{DC}_{10}\text{H}_{21}$ rinsed using with milli-Q water. Diazonium salts purification has consisted in dissolving the retentive into small amount of milli-Q water and re-crystallization into diethyl ether. Re-crystallization procedure took 48 hours at 6°C . Afterwards, prepared salts were dried under vacuum and preserved at -20°C .

Synthesized diazonium salts (DS and DS- $\text{C}_{10}\text{H}_{21}$) were characterized by Nuclear Magnetic Resonance (NMR). Spectra were recorded using BrukerAvance III 400 MHz instrument in d-DMSO solvent. TMS was used as an internal standard.

DS: ^1H NMR (400 MHz, DMSO-d): d (ppm) 7.96-8.00 (t, $J = 7.9 \text{ Hz}$, 2H); 8.24-8.28 (t, $J = 7.6 \text{ Hz}$, 1H); 8.66-8.68 (d, $J = 8.3 \text{ Hz}$, 2H). DS- $\text{C}_{10}\text{H}_{21}$: ^1H NMR (400 MHz, DMSO-d): d (ppm) 0.84-0.87 (t, $J=6.4 \text{ Hz}$, 3H); 1.25 (s, 14H); 1.61 (s, 2H); 2.81-2.85 (t, $J=7.6 \text{ Hz}$, 2H); 7.81-7.83 (d, $J = 8.4 \text{ Hz}$, 2H); 8.55-8.57 (d, $J = 8.4 \text{ Hz}$, 2H).

5.4.3.3 SERS substrate

Commercially available gold nanorod arrays (WAVELET) (later in the text referred as gold nanostructures, GNSs) were purchased by ST Japan company and were used in this study as SERS active substrates.

5.4.3.4 Chemical grafting

Chemical (spontaneous) grafting of diazonium salt was performed in order to functionalise the GNSs. SERS substrates were first immersed in 30 mL solution containing diazonium salt (10^{-3} mol.L $^{-1}$) dissolved in H $_2$ SO $_4$ (10^{-3} mol.L $^{-1}$). Substrates were left to incubate during 12 hours at +4°C. They were then rinsed 3 times under mild stirring by immersion into (i) milli-Q water and (ii) pure methanol, over 10 min for each immersion. Afterwards, functionalised substrates were dried under mild nitrogen flux.

5.4.3.5 Targeted molecule solutions

Naphtalene (NAP), Fluoranthene (FL) and Benzo[a]pyrene (BaP) were used as model molecules to test the diazonium salts-based SERS sensor capability of molecular sensing. Due to solubility issues stock solutions were prepared by dissolving the targeted pollutants in pure methanol (MeOH). Stock solutions of NAP, FL and BaP were prepared at different concentrations as follows: 1000 mg.L $^{-1}$ for NAP (1mg of NAP in 1 mL of MeOH), 200 mg.L $^{-1}$ for FL (2mg of FL in 10 mL of MeOH) and 10 mg.L $^{-1}$ for BaP (1mg of BaP in 100 mL of MeOH), and stored at -20°C. Stock solutions were daily diluted into Milli-Q water (10% of pollutant stock solution in 90% of water) in order to obtain mother solutions which then were stored at +4°C and used for further dilutions.

5.4.3.6 Nanosensor surface regeneration

The pre-concentration of targeted pollutants by designed SERS nanosensors was driven by the weak forces such as hydrophobic interactions or π - π stacking. In order to regenerate the surface different solvents were tested including ethanol, methanol, acetonitrile. Among all, surface washing with methanol was found to be the most efficient. Thus after performing the detection of different selected pollutants SERS nanosensors were rinsed with methanol for 30 min.

5.4.3.7 Raman and SERS measurements

Raman and SERS measurements were performed using prototype of portable micro-Raman spectrometer (HORIBA Scientific) designed for on-site applications. The instrumental set-up was equipped with a 691 nm laser diode (Ondax) and a 60x fold magnification objective (0.7 N.A.) with a collar for glass correction (Olympus). Spectral range was recorded from 414 up to 2100 cm $^{-1}$ with a spectral resolution around 2 cm $^{-1}$. For SERS experiments power of laser was set at 4 mW in order to avoid molecular degradation induced by thermal effects. Accumulation time for SERS measurements was 20s with 3 accumulations to reach higher signal/noise ratio. Spectral calibration was daily performed on a crystalline silicon sample (peak position at 520 cm $^{-1}$).

5.4.3.8 Chemometrics

In order to remove the Raman and SERS spectral background in a similar way for all of the spectra while keeping the analytical signal intact an algorithm was programmed in MatLab 7.0.1 based on Eilers work [64]. The background correction was possible by minimizing the following S function:

$$S = \sum_{(i)} \kappa_i (y_i - z_i)^2 + \lambda \sum_{(i)} (\Delta^2 z_i)^2 \quad (1)$$

with y the signal intensity for each i wavenumber, z the baseline, λ the smoothing parameter and p the asymmetric one as $\kappa_i = p$ if $y_i > z_i$ and $\kappa_i = 1 - p$ otherwise. The last term was defined as follows:

$$\Delta^2 z_i = (z_i - z_{i-1}) - (z_{i-1} - z_{i-2}) \quad (2)$$

The two parameters needed for the calculations, p and λ , were set to values 10^3 and 10^{-3} , respectively. Exceptionally, for the DS-C₁₀H₂₁ based system during the detection of BaP, λ value was set one order of magnitude higher in order to remove fluorescence induced by impurities.

5.4.4 Results and discussion

5.4.4.1 Diazonium salt based surface functionalisation

Surface functionalisation by aryldiazonium is a convenient method leading to robust grafted organic coating. The grafting can be accomplished by either chemical (spontaneous grafting) [59-62], electrochemical [56-58] or photochemical methods [65;66]. The spontaneous grafting strategy was used in this study to functionalise SERS active substrates. The substrates were immersed into diazomium salt (DS and DS-C₁₀H₂₁) solutions and incubated at +4 °C for 12 hours. The temperature control during the functionalisation step is important in order to power the covalent grafting and by the same time to reduce rate of spontaneous polymerization [67]. Functionalised substrates were then investigated by SERS. The spectra can be seen in figure 1A for DS-GNSs and figure 1 B for DS-C₁₀H₂₁-GNSs (black spectra). Spectra are presented in real intensities with removed background using the algorithm detailed in experimental section (figure S1 in supplementary information illustrates the background removal process). Recorded spectra shows number of features in the spectral ranges where vibrations related to the aromatic ring can be found (see figure S2 in the supplementary information for direct comparison between the grafted phenyl derivatives SERS spectra and the Raman spectra of the diazonium salts). The peak at 1075 cm⁻¹ and 1079 cm⁻¹ for DS and DS-C₁₀H₂₁, respectively, assigned to combined C-H in plane bending and C-N stretching modes [68] constitutes the irrefutable signature of the coating. Thus, these later peaks were used as an internal reference. Moreover, this selection was also supported by the observation that these peaks do not overlap with the targeted pollutants Raman signature.

5.4.4.2 PAHs detection using diazonium salt based nanosensors

Diazonium salt coated SERS substrates were then engaged for the sensing of the targeted molecules. Three PAHs were selected for this study due to their different solubility related to their polarity properties defined by the octanol-water partition coefficient, K_{ow} . The K_{ow} of each compound are summarized in table 1. In comparison, FL polarity is intermediate between the one of NAP and BaP. It was thus targeted as the optimal compound for primer investigation to determine the influence of the surface coating by DS and DS- $C_{10}H_{21}$ for the pre-concentration and the detection of PAHs.

Table 1. Physical properties of selected targeted pollutants [69].

PAHs	Structure	Solubility in water ($mg.L^{-1}$)	K_{ow}
Naphthalene (NAP)		32	2300
Fluoranthene (FL)		0.26 at 25 °C	340000
Benzo[a]pyrene (BAP)		0.0038 at 25 °C	10^6

Selection of substrate, detection of fluoranthene (FL)

The functionalised SERS substrates were incubated in FL solution of 5 ppm for 30 min. SERS was then measured in 6 different randomly selected areas on the substrates. Averaged spectra for FL detection are shown in figure 1 (red spectra) whereas the blue spectra are the Raman reference of solid state FL for comparison. All spectra are presented with removed backgrounds.

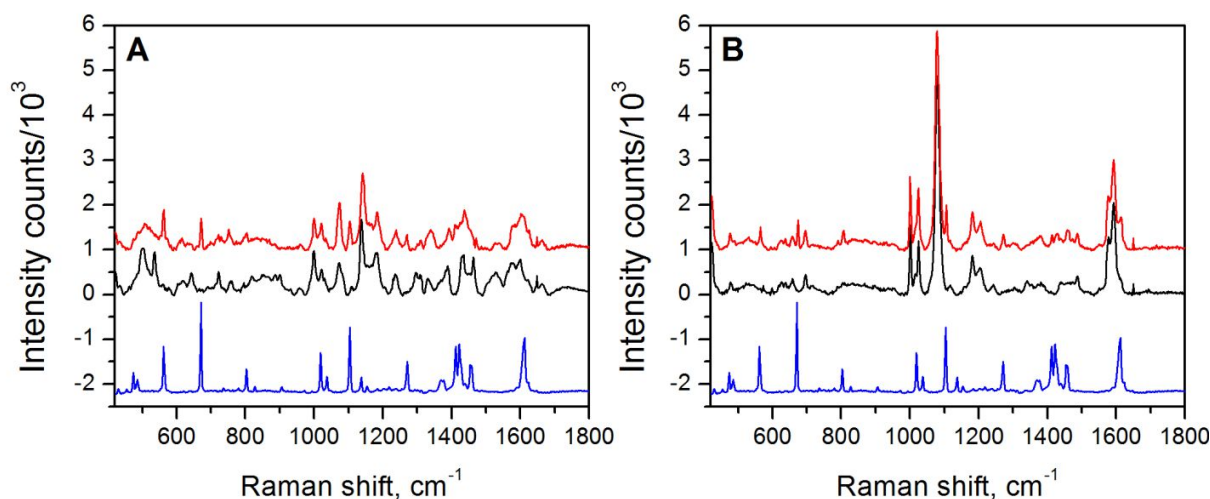


Figure 1: FL detection at 5 ppm concentration using GNSs functionalised with (A) DS and (B) $DS-C_{10}H_{21}$. The black and red spectra correspond to the SERS signal before and after incubation in the FL solution, respectively. Blue spectra in both graphs correspond to FL Raman reference. Red and blue spectra in the graphs are shifted vertically for a better observation.

The presence of several peaks assigned to FL (summarized in table 2) indicated the successful pre-concentration and the detection of FL by both sensors.

Table 2: Positions in cm^{-1} of the main PAHs bands observed in SERS spectra (see references [70;71] for assignments)

Fluoranthene (FL)	Benzo[a]pyrene (BaP)	Naphthalene (NAP)
562	615	511
672	1215	762
803	1239	1021
1018	1345	1382
1104	1385	1577
1270	1623	
1612		

Interaction between FL and the coating layer did not induce important shifts in the position of FL peaks. On the contrary, the relative intensity has been slightly modified. For instance, vibrational modes around 1400 cm^{-1} in Raman spectrum of FL were found to be very weakly enhanced in SERS spectrum measured on $\text{DC}_{10}\text{H}_{21}$ -coated GNS. On the DS-coated GNS these peaks are strongly overlapped by the signal of grafted layer.

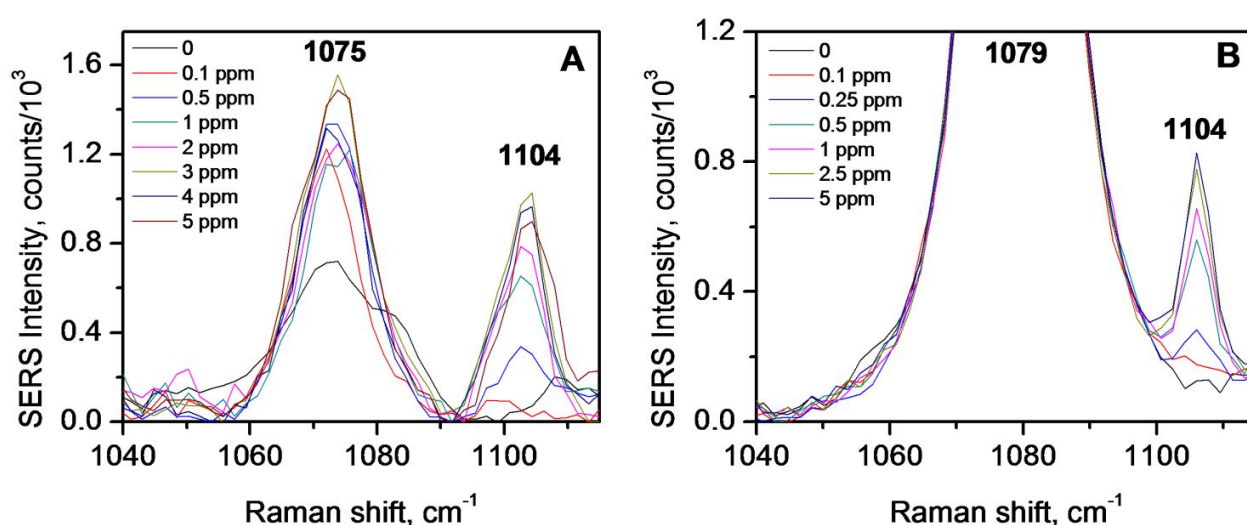


Figure 2: FL detection at the concentration range between 0.1 ppm up to 5 ppm on GNSs functionalised with (A) DS and (B) $\text{DC}_{10}\text{H}_{21}$.

The strong FL peak observed at around 1104 cm^{-1} assigned to C-C in-plane stretching mode was used to establish the calibration curves in order to compare analytical performances of both nanosensors. The substrates were fixed to the fluidic cell and FL solutions with increasing concentrations from 0.1 ppm up to 5 ppm ($0.5 \mu\text{mol/L}$ - $25 \mu\text{mol/L}$) were injected at a flow rate of $3 \mu\text{L}\cdot\text{min}^{-1}$ for half an hour for each solution. Between each concentration SERS was measured in 6 different places on the surface. Averaged spectra are shown on figure 2, focusing on the peak at 1104 cm^{-1} . For the calibration curves (figure 3), this peak was normalized with regard to the peak at 1075 cm^{-1} or at

1079 cm^{-1} , characteristic of DS or $\text{DC}_{10}\text{H}_{21}$, respectively (CH in plane bending for p-substituted and mono-substituted benzenes and C-N stretching) and plotted as a function of the concentration.

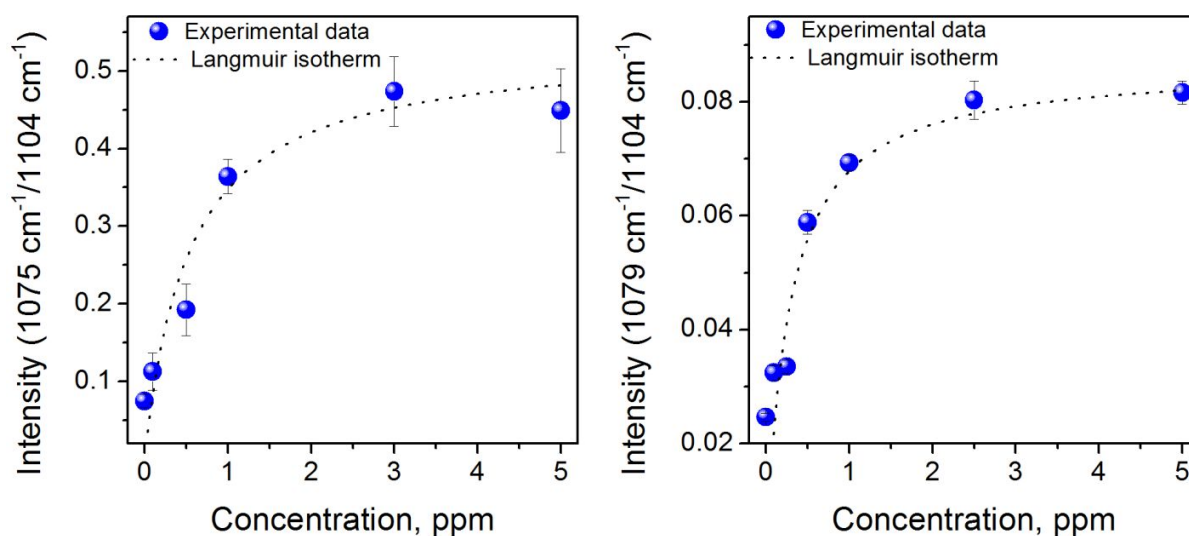


Figure 3: Calibration curves of FL detection on GNSs functionalised with (A) DS and (B) $\text{DC}_{10}\text{H}_{21}$.

Both calibration curves were fitted using the Langmuir adsorption isotherm expressed as follows:

$$I = \frac{I_{max}Kc}{1 + Kc} \quad (9)$$

where I is the normalized SERS intensity, K the adsorption constant and c the concentration of analyte.

One can notice that above 3 ppm the equilibrium is reached for both sensors. The calibration curves were found to be linear in the range of 0.1-1 ppm for DS coating layer and 0.1-0.5 ppm for $\text{DC}_{10}\text{H}_{21}$ coating layer. Thus, the fitted curve slopes were used for the calculation of the limits of detection (LOD) and the limits of quantitation (LOQ). LOD is defined as the lowest concentration of analyte in the sample that can be detected [72]. For each sensor LODs were calculated using the formula: $\text{LOD}=3.3\sigma$, where σ is the standard deviation of blank response. LODs of FL were found to be 0.200 ppm (0.99 $\mu\text{mol/L}$) and 0.091 ppm (0.45 $\mu\text{mol/L}$) for DS-based and $\text{DC}_{10}\text{H}_{21}$ -based nanosensors, respectively. LOQ is the lowest concentration of an analyte that can be determined with acceptable precision and accuracy. LOQs were calculated using the same formula that was used for the calculation of LOD with an increased confidence level to 10, $\text{LOQ}=10\sigma$. In this case, the calculated LOQs values were 0.609 ppm (3 $\mu\text{mol/L}$) and 0.277 ppm (1.4 $\mu\text{mol/L}$) for DS-based and $\text{DC}_{10}\text{H}_{21}$ -based nanosensors, respectively. Obtained results indicate twice better LOD and LOQ for the quantitation of FL by using the $\text{DC}_{10}\text{H}_{21}$ as functionalisation layer. This can be explained by two effects. The first one is related with the homogeneity of the coating. As it was mentioned before, surface functionalisation using diazonium salts is driven by two parallel mechanisms: grafting and

random polymerization [67]. SERS obtained on DC₁₀H₂₁-based nanosensors showed very reproducible signal all over the surface, while DS-based substrate gave the variations in the peaks distribution and in the intensity (Figure S3, in supplementary information), leading to higher standard deviation values. The conclusion that can be made is that both diazonium salts efficiently graft to the surface, but rate of polymerization is higher in the case of DS; probably because the open sites provided by the aromatic ring (absence of any substitution) leading to a lack of steric hindrance. Second effect which might explain the results is the polar properties of the coatings. The log K_{ow} provided for the primary amines (0.90 for aniline and 7.55 for 4-dodecylanilin [73]) suggests that DS-C₁₀H₂₁ based coating could be much more nonpolar, hence more suitable for nonpolar compounds pre-concentration. Due to a better sensitivity, DC₁₀H₂₁-based nanosensor was chosen for further detection of the other targeted analytes (NAP and BAP).

Detection of benzo[a]pyrene (BaP)

The calibration curve for BaP was performed on DS-C₁₀H₂₁-based GNS in the same manner as for FL. In comparison with FL, the investigated concentrations of BaP were in the range of 0.1 ppm-0.75 ppm (0.4 μmol/L-3 μmol/L) because of the low solubility of BaP (see table 1). 3 μmol/L was used as the highest concentration to be investigated because over this value BaP was not soluble into water/methanol (9/1 v/v) solution. The spectra presented in figure 4 A is an average spectra for each concentration obtained after half of hour of pre-concentration. The successful pre-concentration and detection was confirmed by emerged BaP peaks summarized in table 2. Most of the peaks positions were found identical to the ones in BaP Raman reference spectrum (see figure S4 in supplementary information). However, BaP peak at 1236 cm⁻¹ corresponding to ring stretching and C-H stretching modes was found shifted 3 cm⁻¹ towards higher wavenumber upon adsorption on the nanosensor surface, while the one observed at 1348 cm⁻¹ assigned to ring stretching shifted 3 cm⁻¹ to the lower wavenumber.

In order to establish the calibration curve, the intensity of the peak at 1239 cm⁻¹ belonging to BaP was normalized regarding the characteristic band of the coating at 1079 cm⁻¹. Obtained data points are presented in the figure graph B.

The calibration plot was found to be linear over the range 0.1-0.5 ppm (0.4-2 μmol/L) while the saturation of the surface was not reached in this case. The limiting factor was the solubility of BaP in water/methanol (9/1 v/v). The calculated LOD and LOQ were 0.045 ppm (0.18 μmol/L) and 0.138 ppm (0.5 μmol/L), respectively.

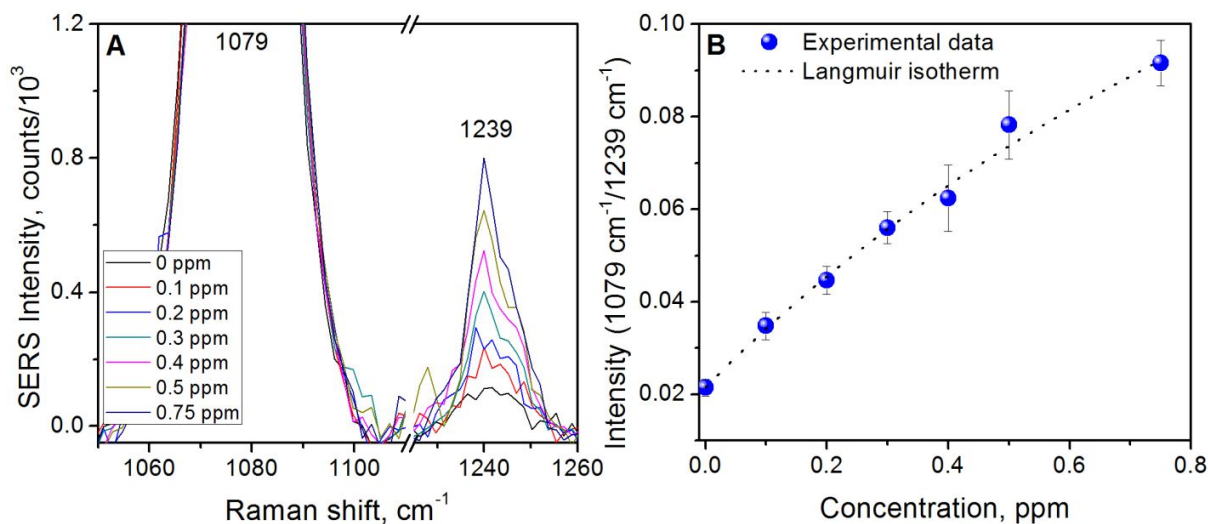


Figure 4: Graph A presents the BaP detection at the concentration range on DS-C₁₀H₂₁- based GNSs; graph B demonstrates the obtained calibration curve of BaP on DC₁₀H₂₁-based GNS.

Detection of naphthalene (NAP)

For the study of NAP pre-concentration and detection, SERS measurements were carried out as previously in milli-Q-MeOH (9/1 v/v) media containing different concentrations of NAP from 1 ppm up to 50 ppm (7.8 μmol/L-390 μmol/L). NAP peaks observed in the SERS spectra showed in figure 5 are summarized in table 2. Peak at 1382 cm⁻¹, assigned to C=C stretching mode has been chosen to establish the calibration curve shown in Figure 5 B because it is the only peak that do not overlap with the vibrational signature of the coating.

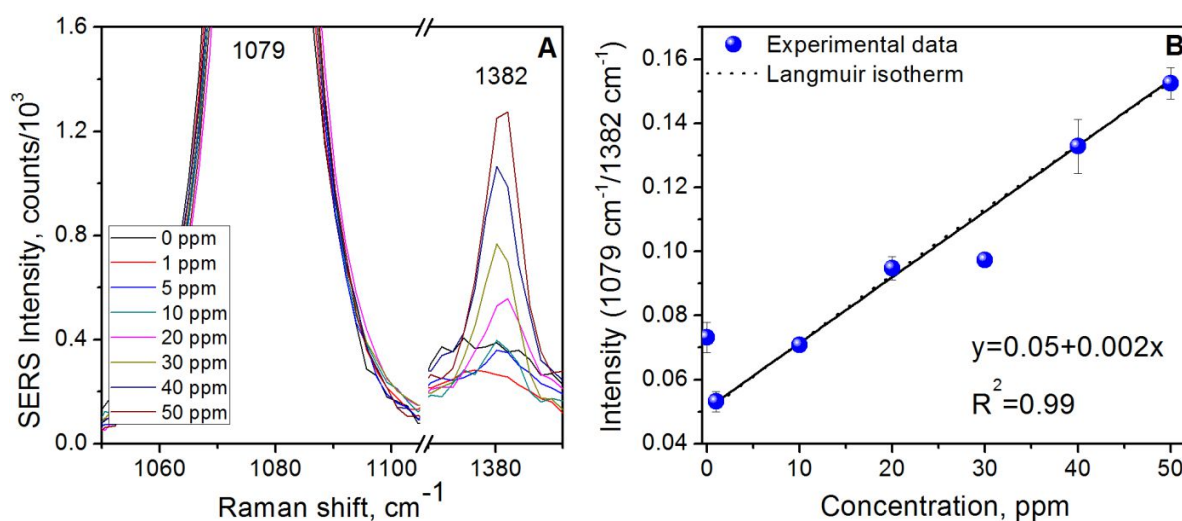


Figure 5: Graph A presents the NAP detection at the concentration range on DS-C₁₀H₂₁- based GNSs; graph B demonstrates the obtained calibration curve of NAP on DS-C₁₀H₂₁-based GNS.

The calibration curve was found to be linear over the investigated range. The LOD and LOQ were calculated to be 15 ppm (0.12 mmol/L) and 47 ppm (0.36 mmol/L), respectively. In the figure 5 A, it is clearly visible that the signal around 1380 cm^{-1} has decreased after incubation in the first NAP solution of 1 ppm concentration. Due to latter change in the signal of the coating, decrease in SERS intensity can be observed for the first concentration of NAP (figure 5 B). Thus, in this case, the actual LOD for NAP could be much lower than the one calculated using 3.3 sigma criterion if the interaction between the analyte and the coating would be taken into account. Analysis in the mixture of analytes

The experiment using the mixture of the three investigated pollutants was performed in order to further assess the feasibility of the designed nanosensor for PAHs sensing in water samples and to additionally demonstrate the obtained SERS spectra suitability for intentional on-site screening purposes. For this experiment, mixed solution of FL (5 ppm), NAP (5 ppm) and BaP (0.75 ppm) was prepared in pure water/methanol (9/1 v/v) media. Of all, the concentration of BaP was notably lower due to solubility issue discussed previously. The substrate was exposed to the prepared mixture for a half an hour before starting the SERS measurements. The averaged SERS spectra obtained before and after substrate exposure to the pollutants solution are showed in figure 6 as red and black spectrum respectively. At the selected concentrations FL and BaP were detected and well identified. NAP on another hand, showed very low intensity single peak at 762 cm^{-1} whereas peaks in other spectral regions were overlapped by either signal of the coating (i.e. at 1022 cm^{-1}) or other analytes (i.e. the peak used for establishing a calibration curve for NAP at 1382 cm^{-1} was found combined with the signal of BaP)

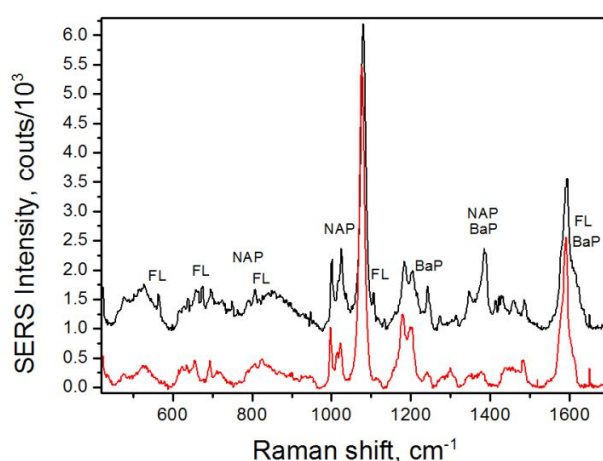


Figure 6: SERS based pollutants detection in their mixed media presented in black spectrum. Red spectrum shows the SERS signal of DSC₁₀H₂₁-based GNSs for comparison. Demonstrated spectra are averaged from six individual measurements followed up the baseline removal. Black spectrum in the graph is lifted by 1.10^3 counts for a better observation.

5.4.4.4 Feasibility of the developed nanosensor for PHAs sensing

Obtained results of conducted investigations on targeted pollutants in their individual solution and in the mixture provide important information on both: the DS-C₁₀H₂₁-based nanosensor feasibility for PAHs sensing and the selectivity versus FL, BaP and NAP. First of all, the LOD for investigated PAHs compounds were found to vary by two orders of magnitude. The correlation of the observed LOD values versus the log Kow factor of investigated analytes is presented in figure 7 (black spheres). These results suggest that developed nanosensor containing the hydrophobic coating is more suitable for the pre-concentration of highly nonpolar PAH compounds.

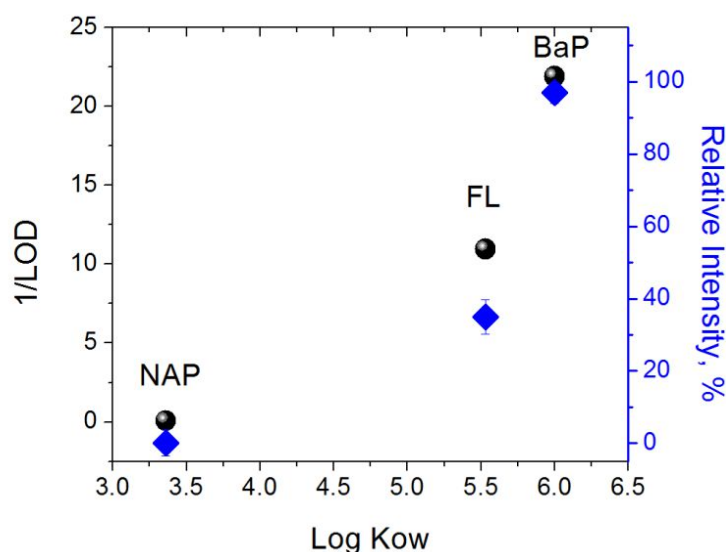


Figure 7: Correlation of the calculated LOD values (black spheres) and the observed related SERS intensities of the analytes in their mixed media (blue rombs) plotted as a function of the Kow factor of investigated PAHs.

The later assessment was confirmed by the results obtained from the pollutants detection in mixed media. Blue spheres in the figure 7 demonstrate the relative SERS intensity of the observed pollutants peaks which was calculated as follows:

$$Relative\ Intensity\ (\%) = 100\% * \frac{I'_{Peak\ of\ Analyte}}{I'_{Peak\ of\ Coating}} * \frac{I_{Peak\ of\ Coating}}{I_{Peak\ of\ Analyte}} \quad (10)$$

where I' is the intensity of the selected peaks measured during the experiment in pollutants mixture and I is the intensity of the peaks obtained during pollutants detection in their individual solutions. The peaks for this calculation were kept the same as the ones followed for the establishment of a calibration curves (the peak of coating at 1079 cm⁻¹ and the peaks at 1104 cm⁻¹, 1239cm⁻¹ and 1382cm⁻¹ for FL, BaP and NAP, respectively). Using this formula, first, the relative intensity of the

signal belonging to the pollutants obtained in mixed media was found. In the second step, it was compared with the value given by the calibration curve and then expressed in percentage. Starting from FL established calibration curve indicates that at 5 ppm concentration the adsorption equilibrium was reached with a maximum relative intensity of 0.086 ± 0.003 . At the same concentration investigated FL in mixed media showed a relative intensity of 0.031 ± 0.001 leading to 35 % of surface saturation. In the case of BaP, at a concentration of 0.75 ppm the relative intensity of the peak at 1239cm^{-1} demonstrated in the calibration curve and the one obtained in the mixture was found to be almost identical. Calculated value of 97 % shows that the adsorption of BaP onto the nanosensor surface is not restricted by the presence of competitive analytes. The calculation of NAP signal contribution in the SERS spectra registered in the mixture was more challenging. Due to the low intensity of single NAP peak non-overlapped it was not possible to quantify it using the same formula. The approximate contribution of NAP was calculated indirectly. Since NAP and BaP both have peaks around 1382cm^{-1} by subtracting SERS spectra of BaP detection at 0.75 ppm concentration from the one measured in the mixture relative intensity of NAP was found to be 0.14 %.

Calculated relative intensities of the analytes peaks in the SERS spectra obtained investigating the pollutants detection in their mixed media confirmed that, developed DS- $\text{C}_{10}\text{H}_{21}$ -based nanosensor serves to pre-concentrate and detect highly hydrophobic molecules where, the strength of an interaction between the coating and the analyte is decreasing along with its K_{ow} value. Moreover, designed SERS nanosensor allowed the sensitivity for a detection of BaP comparable with the one obtained by the application of colloidal nanoparticles [74;75].

5.4.5 Conclusion

With the presented study we have demonstrated a new approach for the design of SERS nanosensor for the reversible non-polar pollutants pre-concentration and detection. Employed benzene-diazonium-tetrafluoroborate (DS) and its analog bearing hydrophobic alkane chain 4-dodecyl benzene-diazonium-tetrafluoroborate (DS- $\text{C}_{10}\text{H}_{21}$) were tested for substrate surface functionalisation and subsequent pre-concentration of targeted molecules. Due to the lower rate of spontaneous polymerization, DS- $\text{C}_{10}\text{H}_{21}$ -based GNSs were found to be highly reproducible. Using this nanosensor we have demonstrated the detection of NAP, FL and BaP at 15 ppm, 0.45 ppm and 0.045 ppm, respectively. The LODs of the detected molecules were found in correlation with their physicochemical properties. Thus, demonstrated DS- $\text{C}_{10}\text{H}_{21}$ -based GNSs selectivity towards highly nonpolar molecules such as BaP suggests that varying the nature of aryldiazonium salts applied to the surface functionalisation the nanosensor for specific kind of pollutants can be optimized.

The level of BaP detection obtained in this study is comparable with the ones documented in the literature by using colloidal nanoparticles. Given that the major drawback of colloidal nanoparticles application for pollutants monitoring is the signal reproducibility, our proposed nanosensor due to demonstrated sensitivity, reproducibility and reusability has a great potential to be applied for *in-situ* measurements. Work is in progress in order to increase the performances of the developed sensor for the detection of PAHs in natural water samples.

5.4.6 References

- 1 Bessbousse, H., Nandhakumar, I., Decker, M., Barsbay, M., Cuscito, O., Lairez, D., Clochard, M. C. and Wade, T. L. (2011). Functionalized nanoporous track-etched β -PVDF membrane electrodes for lead(II) determination by square wave anodic stripping voltammetry, *Analytical Methods*, **3**, pp. 1351-1359.
- 2 Betelu, S., Parat, C., Petrucciani, N., Castetbon, A., Authier, L. and Potin-Gautier, M. (2007). Semicontinuous Monitoring of Cadmium and Lead with a Screen-Printed Sensor Modified by a Membrane, *Electroanalysis*, **19**, pp. 399-402.
- 3 Buffle, J. and Tercier-Waeber, M. L. (2005). Trends in Analytical Chemistry, *Voltammetric environmental trace-metal analysis and speciation: from laboratory to in situ measurements*, **24**, pp. 172-191.
- 4 Finch, M. S., Hydesa, D. J., Clayson, C. H., Weiglb, B., Dakinc, J. and Gwilliam, P. (1998). A low power ultra violet spectrophotometer for measurement of nitrate in seawater: introduction, calibration and initial sea trials, *Analytica Chimica Acta*, **377**, pp. 167-177.
- 5 Mikkelsen, Ø., Skogvold, S. M. and Schröder, K. H. (2005). Continuous heavy metal monitoring system for application in river and seawater, *Electroanalysis*, **17**, pp. 431-439.
- 6 Parat, C., Betelu, S., Authier, L. and Potin-Gautier, M. (2006). Determination of labile trace metals with screen-printed electrode modified by a crown-ether based membrane, *Analytica Chimica Acta*, **573**, pp. 573-574.
- 7 Tercier, M. L., Buffle, J., Zirino, A. and de Vitre, R. R. (1990). In situ voltammetric measurement of trace elements in lakes and oceans, *Analytica Chimica Acta*, **237**, pp. 429-457.
- 8 Zirino, A., Lieberman, S. H. and Clavell, C. (1978). Measurement of Cu and Zn in San Diego Bay by automated anodic stripping voltammetry, *Environmental Sciences & Technology*, **12**, pp. 73-79.
- 9 Heglund, D. L. and Tillota, D. C. (1996). Determination of Volatile Organic Compounds in Water by Solid Phase Microextraction and Infrared Spectroscopy, *American Chemical Society*, **30**, pp. 1212-1219.
- 10 Potter, D. W. and Pawliszyn, J. (1994). Rapid determination of polyaromatic hydrocarbons and polychlorinated biphenyls in water using solid-phase, *Environmental Science Technology*, **28**, pp. 298-305.
- 11 Wittkamp, B. L. and Tillota, D. C. (1995). Determination of BTEX Compounds in Water by Solid-Phase Microextraction and Raman Spectroscopy, *Analytical Chemistry*, **67**, pp. 600-605.
- 12 Young, M. A., Stuart, D. A., Lyandres, O., Glucksberg, M. R. and Van Duyne, R. P. (2004). Surface-enhanced Raman spectroscopy with a laser pointer light source and miniature spectrometer, *Canadian Journal of Chemistry*, **82**, pp. 1435-1441.
- 13 Demeestere, K., Dewulf, J., De Witte, B. and Van Langenhove, H. (2007). Review: Sample preparation for the analysis of volatile organic compounds in air and water matrices, *Journal of Chromatography A*, **1153**, pp. 130-144.

- 14 Arthur, C. L., Killiam, L. M., Motlagh, S., Lim, M., Potter, D. W. and Pawliszyn, J. (1992). Analysis of substituted benzene compounds in groundwater using solid-phase microextraction, *Environmental Sciences & Technology*, **26**, pp. 979-983.
- 15 Buchholz, K. D. and Pawliszyn, J. (1993). Determination of phenols by solid-phase microextraction and gas chromatographic analysis. , *Environmental Sciences & Technology*, **27**, pp. 2844-2848.
- 16 Zhang, Z. and Pawliszyn, J. (1995). Quantitative Extraction Using an Internally Cooled Solid Phase Microextraction Device, *Analytica Chemistry*, **67** pp. 34-43.
- 17 Arthur, C. L. and Pawliszyn, J. (1990). Solid phase microextraction with thermal desorption using fused silica optical fibers, *Analytical chemistry*, **62**, pp. 2145–2148.
- 18 Qiaoa, M., Qia, W., Liua, H. and Qua, J. (2013). Simultaneous determination of typical substituted and parent polycyclic aromatic hydrocarbons in water and solid matrix by gas chromatography–mass spectrometry, *Journal of Chromatography A*, **1291** pp. 129-136.
- 19 Eisert, R. and Levsen, K. (1995). Determination of Pesticides in Aqueous Samples by Solid-Phase Microextraction In-Line Coupled to Gas Chromatography-Mass Spectrometry, *Journal of The American Society for Mass Spectrometry*, **6**, pp. 1119-1130.
- 20 Roy, G., Vuillemin, R. and Guyomarch, J. (2005). On-site determination of polynuclear aromatic hydrocarbons in seawater by stir bar sorptive extraction (SBSE) and thermal desorption GC–MS, *Talanta*, **66**, pp. 540-546.
- 21 Huang, X., Qiu, N., Yuan, D. and Huang, B. (2009). A novel stir bar sorptive extraction coating based on monolithic material for apolar, polar organic compounds and heavy metal ions, *Talanta*, **78**, pp. 101-106.
- 22 Brunink, J. A. J., Di Natale, C., Bungaro, F., Davide, F. A. M., D'Amico, A., Paolesse, R., Boschi, T., Faccio, M. and Ferri, G. (1995). The application of metalloporphyrins as coating material for quartz microbalance-based chemical sensors, *Analytica Chimica Acta*, **325**, pp. 53-64.
- 23 Cygan, M. T., Collins, G. E., Dunbar, T. D., Allara, D. L., Gibbs, C. G. and Gutsche, C. D. (1999). Calixarene monolayers as quartz crystal microbalance sensing elements in aqueous solution, *Analytica Chemistry*, **71**, pp. 142-148.
- 24 Harbeck, M., Erbahar, D. D., Gürol, I., Musluoglu, E., Ahsen, V. and Öztürk, Z. Z. (2010). Phthalocyanines as sensitive coatings for QCM sensors operating in liquids for the detection of organic compounds, *Sensors and Actuators B*, **150**, pp. 346-354.
- 25 Lieberzeit, P., Halikias, K., Afzal, A. and Dickert, F. (2008). Polymers imprinted with PAH mixtures-comparing fluorescence and QCM sensors, *Analytical Bioanalytical Chemistry*, **392**, pp. 1405-1410.
- 26 Lucklum, R., Rösler, S., Hartmann, J. and Hauptmann, P. (1996). On-line detection of organic pollutants in water by thickness shear mode resonators, *Sensors and Actuators B*, **35-36**, pp. 103-111.
- 27 Menon, A., Zhou, R. and Josse, F. (1998). Coated-quartz crystal resonator (QCR) sensors for on-line detection of organic contaminants in water, *IEEE Transactions on Ultrasonics and Ferroelectric and Frequency Control* **45**, pp. 1416-1426.
- 28 Patel, R., Zhou, R., Zinszer, K. and Josse, F. (2000). Real-time detection of organic compounds in liquid environments using polymer-coated thickness shear mode quartz resonator, *Analytica Chemistry*, **72**, pp. 4888-4898.
- 29 Pejcic, B., Barton, C., Croke, E., Eadington, P., Jee, E. and Ross, A. (2009). Hydrocarbon sensing. Part 1: Some important aspects about sensitivity of a polymer-coated quartz crystal microbalance in the aqueous phase, *Sensors and Actuators B: Chemical*, **135**, pp. 436-443.
- 30 Rösler, S., Lucklum, R., Borngräber, R., Hartmann, J. and Hauptmann, P. (1998). Sensor system for the detection of organic pollutants in water by thickness shear mode resonators, *Sensors and Actuators B*, **48**, pp. 415-424.
- 31 Schierbaum, K. D., Weimar, U. and Göpel, W. (1992). Comparison of ceramic, thick-film and thin-film chemical sensors based upon SnO₂, *Institute of Physical and Theoretical Chemistry*, **7**, pp. 709-716.

- 32 Zhou, R., Haimbodi, M., Everhart, D. and Josse, F. (1996). Polymer-coated QCR sensors for the detection of organic solvents in water, *Sensors and Actuators B*, **35**, pp. 176-182.
- 33 Dickert, F. L., Lieberzeit, P., Miarecka, S. G., Mann, K. J., Hayden, O. and Palfinger, C. (2004). Synthetic receptors for chemical sensors-subnano- and micrometre patterning by imprinting techniques, *Biosensors and Bioelectronics*, **20** pp. 1040-1044.
- 34 Schatz, G. C. and Van Duyne, R. P. (2002) *Handbook of Vibrational Spectroscopy*, chapter "Electromagnetic Mechanism of Surface Enhanced Raman Spectroscopy," (Wiley) pp. 759.
- 35 Wokaun, A. (1984). Surface-Enhanced Electromagnetic Processes, *Solid State Physics*, **38**, pp. 223-294.
- 36 Guillot, N. and de la Chapelle, M. L. (2012). The electromagnetic effect in surface enhanced Raman scattering: Enhancement optimization using precisely controlled nanostructures, *Journal of Quantitative Spectroscopy and Radiative Transfer*, **113**, pp. 2321-2333.
- 37 Albrecht, M. G. and Creighton, J. A. (1977). Intense Raman spectra of pyridine at a silver electrode, *Journal of the American Chemical Society* **99**, pp. 5215-5217.
- 38 Fleischmann, M., Hendra, P. J. and McQuillan, A. J. (1974). Raman spectra of pyridine adsorbed at a silver electrode, *Chemical Physics Letters*, **26**, pp. 163-166.
- 39 Jeanmaire, D. L. and Van Duyne, R. P. (1977). Surface raman spectroelectrochemistry: Part I. Heterocyclic, aromatic, and aliphatic amines adsorbed on the anodized silver electrode, *Journal of Electroanalytical Chemistry and Interfacial Electrochemistry*, **84**, pp. 1-20.
- 40 Kambhampati, P., Child, C. M., Foster, M. C. and Campion, A. (1998). On the chemical mechanism of surface enhanced Raman scattering: Experiment and theory, *The Journal of Chemical Physics*, **108**, pp. 5013-5026.
- 41 Guillot, N. and Lamy de la Chapelle, M. (2012). Lithographed nanostructures as nanosensors, *Journal of Nanophotonics*, **6**, pp. 064506-064501-064506-064528.
- 42 Kneipp, K., Wang, Y., Kneipp, H., Perelman, L. T., Itzkan, I., Dasari, R. R. and Feld, M. S. (1997). Single Molecule Detection Using Surface-Enhanced Raman Scattering (SERS) *Physical Review Letters*, **78**, pp. 1667-1670.
- 43 Nie, S. and Emory, S. R. (1997). Probing Single Molecules and Single Nanoparticles by Surface-Enhanced Raman Scattering, *Science*, **275**, pp. 1102-1106.
- 44 Otto, A., Mrozek, I., Grabhorn, H. and Akemann, W. (1992). Surface-enhanced Raman scattering, *Journal of Physics: Condensed Matter*, **4**, pp. 1143-1212.
- 45 Peron, O., Rinnert, E., Lehaitre, M., Crassous, P. and Compere, C. (2009). Detection of polycyclic aromatic hydrocarbon (PAH) compounds in artificial sea-water using surface-enhanced Raman scattering (SERS), *Talanta* **79**, pp. 199-204.
- 46 Allan, I. J., Vrana, B., Greenwood, R., Mills, G. A., Roig, B. and Gonzales, C. (2006). A "toolbox" for biological and chemical monitoring requirements for the European Union's Water Framework Directive, *Talanta*, **69**, pp. 302-322.
- 47 Peron, O., Rinnert, E., Florent, C., Lehaitre, M. and Compere, C. (2010). First steps of in situ surface-enhanced Raman scattering during shipboard experiments, *Society for Applied Spectroscopy*, **64**, pp. 1086-1093.
- 48 Peron, O., Rinnert, E., Toury, T., Lamy de la Chapelle, M. and Compère, C. (2011). Quantitative SERS sensors for environmental analysis of naphthalene, *The Analyst*, **136**, pp. 1018-1022.
- 49 Prien, R. D. (2007). The future of chemical in situ sensors, *Marine Chemistry*, **107**, pp. 422-432.
- 50 Rogers, J. A., Jackman, R. J. and Whitesides, G. M. (1997). Constructing single- and multiple-helical microcoils and characterizing their performance as components of microinductors and microelectromagnets, *Journal of Microelectromechanical Systems*, **6**, pp. 184-192.
- 51 Ulman, A. (1996). Formation and Structure of Self-Assembled Monolayers, *Chemical Reviews*, **96**, pp. 1533-1554.
- 52 Zielinski, O., Busch, J. A., Cembella, A. D., Daly, K. L., Engelbrektsson, J., Hannides, A. K. and Schmidt, H. (2009). Detecting marine hazardous substances and organisms: sensors for pollutants, toxins, and pathogens, *Ocean Science Discussion*, **6**, pp. 953-1005.
- 53 Chow, E., Hibbert, D. B. and Gooding, J. J. (2005). *Analyst*, **130**, pp. 831-837.

- 54 Delamarche, E., Michel, B., Kang, H. and Gerber, C. (1994). Thermal Stability of Self-Assembled Monolayers, *Langmuir*, **10**, pp. 4103-4108.
- 55 Horn, A. B., Russell, D. A., Shorthouse, L. J. and Simpson, T. R. E. (1996). Ageing of alkanethiol self-assembled monolayers, *Journal of the Chemical Society*, **92**, pp. 4759-4762.
- 56 Betelu, S., Vautrin-UI, C. and Chaussé, A. (2009). Novel 4-carboxyphenyl-grafted screen-printed electrode for trace Cu(II) determination, *Electrochemistry Communications*, **11**, pp. 383-386.
- 57 Betelu, S., Vautrin-UI, C., Ly, J. and Chaussé, A. (2009). Screen-printed electrografted electrode for trace uranium analysis, *Talanta*, **80**, pp. 372-376.
- 58 Delamar, M., Hitmi, R., Pison, J. and Savéan, J. (1992). Covalent modification of carbon surfaces by grafting of functionalized aryl radicals produced from electrochemical reduction of diazonium salts, *Journal of the American Chemical Society*, **114**, pp. 5883-5884.
- 59 Adenier, A., Cabet-Deliry, E., Chaussé, A., Griveau, S., Mercier, F., Pinson, J. and Vautrin-UI, C. (2005). Grafting of nitrophenyl groups on carbon without electrochemical induction, *Chemistry of materials*, **17**, pp. 491-501.
- 60 Bekyarova, E., Itkis, M. E., Ramesh, P., Berger, C., Sprinkle, M., de Heer, W. A. and Haddon, R. C. (2009). Chemical modification of epitaxial graphene: spontaneous grafting of aryl groups, *Journal of American Chemistry Society*, **131**, pp. 1336-1337.
- 61 Combellas, C. M., Delamar, F., Kanoufi, F., Pinson, J. and Podvorica, F. I. (2005). Spontaneous grafting of iron surfaces by reduction of aryldiazonium salts in acidic or neutral aqueous solution. Application to the protection of iron against corrosion., *Chemistry of Materials*, **17**, pp. 3968-3975.
- 62 Laurentius, L., Stoyanov, S. R., Gusarov, S., Kovalenko, A., Du, R., Lopinski, G. P. and McDermott, M. T. (2011). Diazonium-Derived Aryl Films on Gold Nanoparticles: Evidence for a Carbon-Gold Covalent Bond, *ACS Nano*, **5**, pp. 4219-4227
- 63 Griveau, S., Mercier, D., Vautrin-UI, C. and Chaussé, A. (2007). Electrochemical grafting by reduction of 4-aminoethylbenzenediazonium salt: Application to the immobilization of (bio)molecules, *Electrochemical Communication*, **9**, pp. 2768-2773.
- 64 Eilers, P. H. C. (2003). A Perfect Smoother, *Analytical Chemistry*, **75**, pp. 3631-3636.
- 65 Busson, M., Berisha, A., Combellas, C., Kanoufi, F. and Pinson, J. (2011). Photochemical grafting of diazonium salts on metals, *Chemical Communications*, **47**, pp. 12631-12633.
- 66 Bouriga, M., Chehimi, M. M., Combellas, C., Decorse, P., Kanoufi, F., Deronzier, A. and Pinson, J. (2013). Sensitized Photografting of Diazonium Salts by Visible Light, *Chemistry of materials*, **25**, pp. 90-97.
- 67 Abiman, P., Wildgoose, G. G. and Compton, R. G. (2008). Investigating the mechanism for the covalent chemical modification of multiwalled carbon nanotubes using aryl diazonium salts, *Int. J. Electrochem. Sci*, **3**, pp. 104-117.
- 68 Ahmad, R., Boubekour-Lecaque, L., Nguyen, M., Lau-Truong, S., Lamouri, A., Decorse, P., Galtayries, A., Pinson, J., Felidj, N. and Mangeney, C. (2014). Tailoring the Surface Chemistry of Gold Nanorods through Au-C/Ag-C Covalent Bonds Using Aryl Diazonium Salts, *The Journal of Physical Chemistry C*, **118**, pp. 19098-19105.
- 69 Manoli, E. and Samara, C. (1999). Polycyclic aromatic hydrocarbons in natural waters: sources, occurrence and analysis, *TrAC Trends in Analytical Chemistry*, **18**, pp. 417-428.
- 70 Qu, L.-L., Li, Y.-T., Li, D.-W., Xue, J.-Q., Fossey, J. S. and Long, Y.-T. (2013). Humic acids-based one-step fabrication of SERS substrates for detection of polycyclic aromatic hydrocarbons, *Analyst*, **138**, pp. 1523-1528.
- 71 Tjunelyte, I., Dupont, N., Milosevic, I., Barbey, C., Rinnert, E., Lidgi-Guigui, N., Guenin, E. and de la Chapelle, M. (2015). Investigation of aromatic hydrocarbon inclusion into cyclodextrins by Raman spectroscopy and thermal analysis, *Environ Sci Pollut Res*, pp. 1-13.
- 72 IUPAC. Compendium of Chemical Terminology, n. e. t. G. B. C. b. A. D. M. a. A. W. B. S. P., Oxford (1997). XML on-line corrected version: <http://goldbook.iupac.org> (2006-) created by M. Nic, J. Jirat, B. Kosata; updates compiled by A. Jenkins. ISBN 0-9678550-9-8.

- 73 Wayne Schultz, T., Lin, D. T. and Michelle Arnold, L. (1991). QSAR in Environmental Toxicology QSARs for monosubstituted anilines eliciting the polar narcosis mechanism of action, *Science of The Total Environment*, **109**, pp. 569-580.
- 74 Na, W., Hai-Feng, Y., Xuan, Z., Rui, Z., Yao, W., Guan-Feng, H. and Zong-Rang, Z. (2009). Synthesis of anti-aggregation silver nanoparticles based on inositol hexakisphosphoric micelles for a stable surface enhanced Raman scattering substrate, *Nanotechnology*, **20**, pp. 315603.
- 75 Fu, S., Guo, X., Wang, H., Yang, T., Wen, Y. and Yang, H. (2015). Functionalized Au nanoparticles for label-free Raman determination of ppb level benzopyrene in edible oil, *Sensors and Actuators B: Chemical*, **212**, pp. 200-206.

5.5 Conclusion

In this study, new type of nanosensor for SERS based environmental pollutants detection has been presented. In the first stage of this work the complete Raman characterization of the synthesized diazonium salts in comparison with Raman spectra provided for amines has been provided. Raman investigation of synthesized diazonium salts confirmed the successful chemical diazonium salts synthesis as well as allowed of identification of vibrational signatures for each obtained aryl diazo compound. Further in this study, synthesized diazonium salts were applied for a SERS active surface functionalisation in order to design a new type of SERS based nanosensors. During this study characteristic vibrations of phenyl derivatives grafted to the surface have been identified and assigned with the help of DFT modeling. Due to its geometry and the fewer number of consisting atoms DSCOOH was found as a good rough model to discuss the structure of its grafted layers. Thus, comparison of SERS spectrum for of latter DSCOOH based coating with the spectra of different adducts modelled by DFT led to the conclusion that grafting is driven by a radical mechanism ensuring C-Au covalent bond. In addition, results obtained by XPS showed the existence of the component attributed to $-N=N-$ bonds suggesting the multilayer formation linked via azo bonds.

In the last part of this study commercially available SERS substrates decorated by diazonium salts based coating were conceptually tested for they performance in PAH detection. Pre-concentration and detection of three pollutants: naphthalene, fluoranthene and benzo[a]pyrene were performed in their in water/methanol (9/1 v/v) samples. This investigation of pollutants solutions containing different concentrations (from nmol.l^{-1} to $\mu\text{mol.l}^{-1}$) led to establish the calibration curves and to determine the detection limits. Moreover, since targeted molecules pre-concentration by these kind of coating layers is essentially based on weak forces (hydrophobic and π - π stacking interactions), surface regeneration step was successfully applied. Latter study confirmed that, diazonium salts can be effectively applied as a tool to create nanosensors that are sensitive, reproducible and reusable.

6 Nanoplasmonics exploitation for selective nanosurface functionalisation

6.1 Introduction

Among surface modification strategies, “click chemistry” gained increasing attention for its numerous benefits: high efficiency, simple realization, rapidity, chemoselectivity, feasibility in water media and enhanced yields. UV light or temperature-mediated thiol-ene or thiol-yne reactions involve the addition of the thiol to an alkene or alkyne, respectively. Latter reactions have already been reported to permit great diversity of functionalisation on several surfaces and allow multiple functionalisation by conjugating other “click chemistry” methodologies. If well controlled “click chemistry” approach could serve for multifunctional surfaces preparation for selective pre-concentration of different targeted molecules in complex environment, using one nanosensor.

This chapter will be devoted to prove the concept of local molecular immobilization at the nanoscale by performing thiol-ene “click” reaction *in situ* on plasmonic nanostructures irradiated by visible light. The study presented in this chapter is prepared to be submitted in RSC Nanoscale as research article. The supplementary information to support latter investigation can be found in ANNEX 7.

6.2 Nanoplasmonics tuned “click chemistry”

Inga Tijunelyte¹, Erwann Guenin¹, Nathalie Lidgi-Guigui¹, Florent Colas², Joyce Ibrahim³,
TimothéeToury³, Marc Lamy de la Chapelle^{1*}

¹*Université Paris13, Sorbonne Paris Cité, Laboratoire CSPBAT, CNRS, (UMR7244), 74 rue Marcel Cachin,
93017 Bobigny, France*

²*IFREMER, Centre de Brest, Interfaces and Sensors and Group, BP 70, 29280 Plouzané, France*

³*Université de Technologie de Troyes, Laboratoire de Nanotechnologie et d'Instrumentation Optique, Institut
Charles Delaunay, FRE 2848, 12 rue Marie Curie, 10004 Troyes, France*

Keywords: Thiol-ene click chemistry, SERS, nanoplasmonics

*Corresponding author: marc.lamydelachapelle@univ-paris13.fr

6.2.1 Abstract

Nanoplasmonics is a growing field of optical condensed matter science dedicated to optical phenomena at the nanoscale level in metal systems¹. Extensive research on noble metallic nanoparticles (NPs) has arisen within the last two decades due to their ability to keep the optical energy concentrated in the vicinity of NPs, in particular, the ability to create optical near-field enhancement followed by heat generation. We have exploited these properties in order to induce a localised “click” reaction in the vicinity of gold nanostructures under unfavourable experimental conditions. We demonstrate that this reaction can be controlled by the plasmonic properties of the nanostructures and we propose two physical mechanisms to interpret the observed plasmonic tuning of the “click” chemistry.

6.2.2 Introduction

Nanoplasmonic effects are governed by coherent oscillations of the free electron gas of metal nanoparticles (NPs) at the incident electric field frequency. The excitation of these modes, called localized surface plasmons (LSP)^{2,3}, can be further enhanced if the frequency of the incoming light matches the LSP resonance (LSPR) frequency⁴. The unique optical properties of the metal NPs induced by LSP excitation are of great interest in the fields of physics^{5,6} and biology^{7,8}. It may also be exploited in chemistry⁹. This latter field can significantly benefit from the application of nanoplasmonics as an efficient source of electrons, light and heat. The control of chemical reactions at the metallic surfaces is a crucial parameter for many applications. For instance, a two-photon photopolymerization of a thin photo-resist layer SU8 has been achieved locally inside the nanogaps between lithographic gold nanostructures due to the near-field enhancement induced by LSP excitation¹⁰. Galloway et al. have also demonstrated light assisted protein immobilization in the nanogap between two gold nanoantennae within a nanometric accuracy¹¹. In their study, the authors exploited the cleavage of disulfide bridges in the proteins resulting in their subsequent attachment to the gold nanoantennae in the regions of the highest near-field enhancement. Another important parameter to control the speed and yield of chemical reactions is the temperature generated by LSP. Thermoplasmonics is a recent field of research, which has proved to be highly applicable for many chemical approaches. Cao *et al.* have used the local heat generated by metallic NP through laser illumination to control the position and growth direction of a single semiconductor nanowire¹².

In this paper, we demonstrate that the plasmonic properties of metallic NPs can be exploited to induce “click” chemistry reactions. Introduced less than two decades ago, this set of reactions is described as simple, widely scoped, modular, generating high yields, and producing only harmless

byproducts that can be isolated by non-chromatographic methods¹³. In particular, a copper-catalysed azide/alkyne click reaction has received considerable attention in organic and polymer chemistry¹⁴ but also in nanosurface chemistry¹⁵. Another reaction: thiol-ene coupling, fulfills the click chemistry concept as well. This reaction known for over 100 years¹⁶ and recently rediscovered¹³, consists in grafting thiol-bearing molecules to a carbon double bond. The applications of this reaction have had significant impact in polymer synthesis and material science^{17,18}, and has attracted growing interest in surface functionalisation and modifications^{19,20}. Generally, this reaction is performed through UV light or thermal activation, with the presence of a radical initiator.

In this contribution, we demonstrate that the thiol-ene coupling can be simply initiated in the visible range using nanoplasmonic effects. The kinetics of this reaction was monitored *in situ* by Surface Enhanced Raman Scattering (SERS). By investigating the reaction rates on different diameters of gold nanocylinders (NCs) made by electron-beam lithography (EBL) we claim that this reaction can be tuned by controlling the NCs plasmonic properties.

6.2.3 Results and discussion

Thiol-ene “click” reaction involves the addition of a thiol to an alkene group via a free-radical mechanism²¹ (Figure 1).

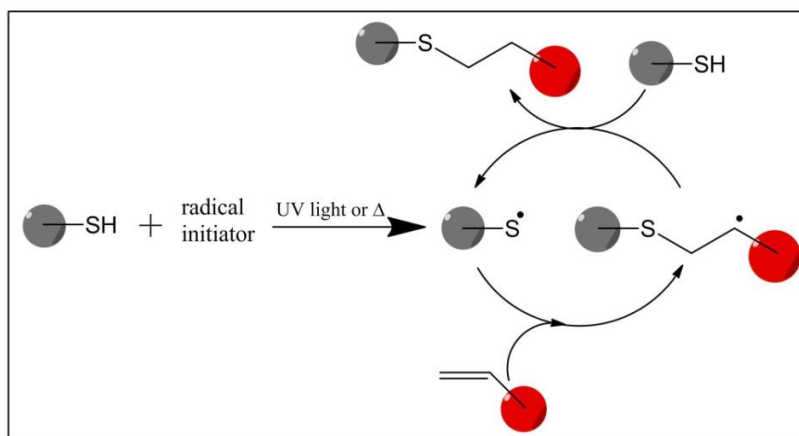


Figure 1: Schematic illustration of the free-radical thiol-ene coupling mechanism.

Briefly, in the initiation step the thiol group is converted to a thiyl radical thanks to the interaction with a photo or thermal radical initiator exposed to UV light^{22,23} or to a specific temperature²⁴, respectively. This thiyl radical can then react with the C=C bond to form a carbon centred radical. From this step the initiation is turned to a propagation step resulting in the formation of a thio ether as a reaction product and a new thiyl radical subsequently involved in the reaction chain.

In our case, the click reaction was performed using 2,2'-Azobis(2-methylpropionamidine) dihydrochloride (AAPH) as radical initiator, allyl mercaptan as double bond substrate and thiophenol as reactant. The AAPH is known to be decomposed into cationic radicals under UV light (365 nm) or temperature above 60 °C (See supplementary information). The reaction was initiated at the surface of the gold NCs (figure 2a) in aqueous environment and using a 660 nm laser beam (figure 2b). The allyl mercaptan was grafted onto the NCs surface through the S-Au bond whereas the AAPH and the thiophenol were free in solution (figure 2c).

Since EBL allows the fine control of the size and shape of the nanostructures at the nanometer scale, the substrates benefit from the reproducibility of both: LSPR position and SERS signal^{25,26}. Arrays of NCs (figure 2d) with different diameters: 110, 140 and 200 nm were fabricated to investigate whether the thiol-ene click reaction can occur due to plasmonic effects.

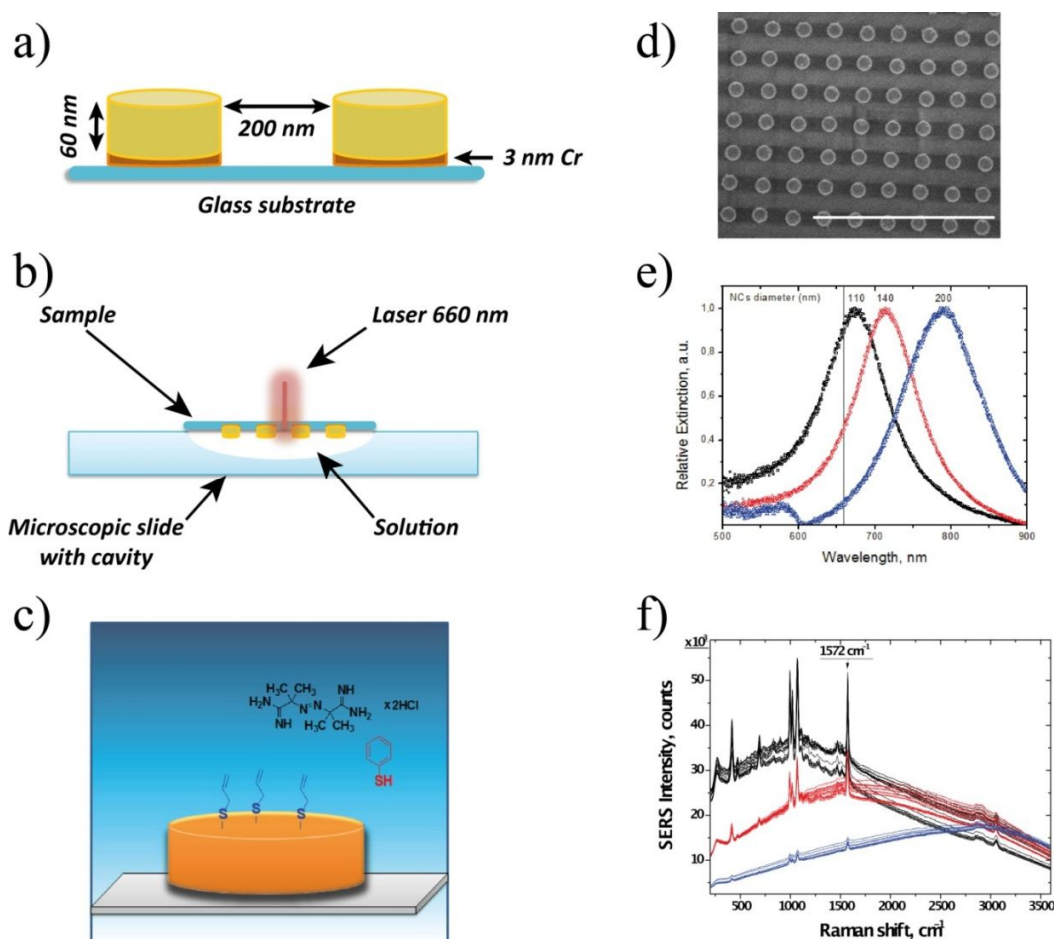


Figure 2: a) Schema of the nanocylinders (NCs) used in the experiments. b) Schema of the experimental configuration. c) Schema of the thiol-ene reaction configuration. d) Scanning electron microscopy image of an array of NCs with a diameter of 200 nm. e) Extinction spectroscopy measurements on 110 nm (black curve), 140 nm (red curve) and 200 nm (blue curve) NCs arrays. The grey line indicates the laser wavelength used for thiol-ene reaction initiation and SERS investigation. f) SERS spectra of grafted thiophenol onto gold NCs of 110 nm (black spectra), 140 nm (red spectra) and 200 nm (blue spectra) diameter.

As shown by the extinction spectra of the NCs in aqueous environment (figure 2e), the 110 nm diameter NCs were found to have a LSPR position close to 660 nm (excitation laser wavelength) whereas 140 nm NCs had a LSPR position red-shifted compared to 660 nm. For the 200 nm NCs, the excitation wavelength was nearly out of resonance, resulting in a largely less intense electromagnetic near-field. The reaction kinetics were evaluated for the three diameters in order to observe changes in reaction performances depending on the mismatch between the LSPR position and the laser wavelength.

In situ thiol-ene click reaction

To initiate the reaction, the solution of AAPH and thiophenol was deposited on a microscopic slide with a cavity and the substrate with NCs decorated with grafted allyl mercaptan was then placed above the slide with the NCs inside the solution. Local reaction at the microscale level was implemented using the excitation laser focused with a 60x objective (N.A. 0.70) through the NCs substrate. The reaction kinetics were then monitored by SERS in real time using the same laser wavelength. SERS spectra were first recorded on the 110 nm NCs: one spectrum each minute for a total duration of 30 min. The process was then reproduced on the NCs of 140 nm and finally on the NCs of 200 nm (figure 2f).

The peaks observed in the SERS spectra correspond to the thiophenol vibrations. Due to method limitations (including placing the substrate in liquid and laser focusing procedures) the NCs were exposed to the solution for about 4 min before the first SERS measurement was made. For this reason the SERS signal of thiophenol was not strictly equal to zero on the first SERS spectrum indicating a spontaneous thiophenol interaction with non-blocked gold areas. To follow the reaction kinetics, the intensity of the peak at 1572 cm^{-1} assigned to an aromatic C=C vibration was plotted versus reaction time (figure 3a) for all NCs diameters. The observed SERS intensity of the thiophenol increases and reaches a plateau, when the gold surface is saturated. Reaction times of less than 10 min were observed for the 110 nm and the 140 nm diameters whereas for the 200 nm, saturation was not achieved even after 40 min of reaction. 10 min is very fast for this thiol-ene reaction since it has been estimated to be of several hours in normal conditions (*i.e.* without NCs and with UV excitation)²⁷. To determine precisely the reaction time, the experimental data were fitted with a first order Langmuir isotherm assuming that during the reaction a single layer of thiophenol was formed:

$$\theta = \theta_{\text{sat}} \left[1 - \exp\left(-\frac{t}{\tau}\right) \right] \quad (11)$$

where θ is the surface coverage, θ_{sat} is the coverage saturation, t is the time and τ is the reaction time constant.

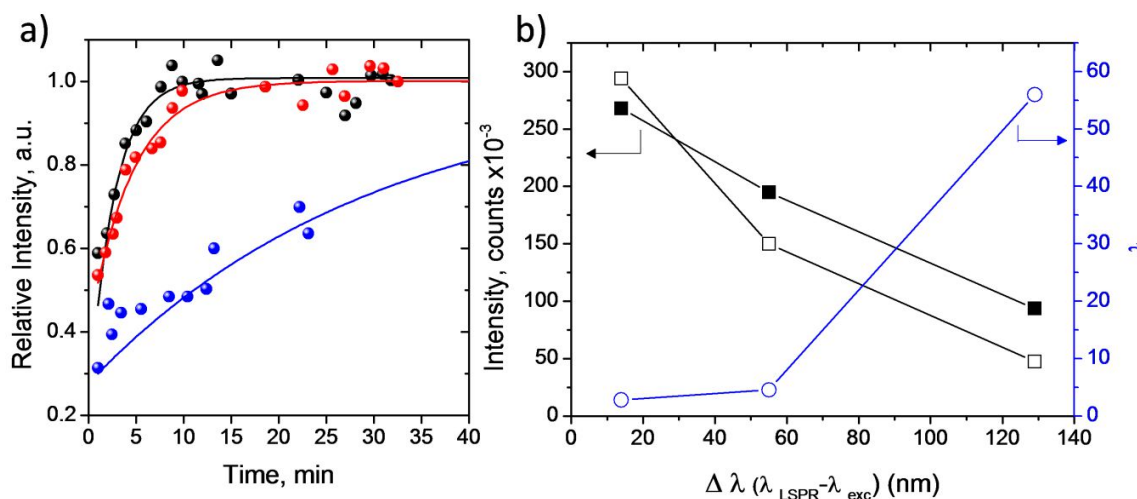


Figure 3: a) Relative SERS intensities of the integrated peak at 1572 cm^{-1} versus reaction time for the 110 nm (black dot), 140 nm (red dot) and 200 nm (blue dot) NCs. Solid lines correspond to the fitting of the experimental points using the equation (1) (110 nm: black line, 140 nm: red line and 200 nm: blue line). b) Absolute SERS intensity at saturation and reaction time plotted versus the mismatch between the LSPR position of NCs and the laser excitation wavelength. Hollow dot: reaction time for the 110 nm, 140 nm and 200 nm NCs. Hollow square: absolute SERS intensities of the thiophenol measured on the 110 nm, 140 nm and 200 nm NCs for the thiol-ene reaction after surface saturation. Plain square: absolute SERS intensities of the thiophenol measured on the 110 nm, 140 nm and 200 nm NCs for the experiment C3 and after surface saturation.

Figure 3b shows the reaction time constant, τ , that corresponds to the time required to reach 63% of SERS signal saturation versus the shift between the LSPR position of NCs and the laser excitation wavelength, $\Delta\lambda = \lambda_{\text{LSPR}} - \lambda_{\text{exc}}$. It is clearly visible, that the reaction time is strongly dependent on the LSPR position. A twenty times faster reaction was observed on highly resonant 110 nm NCs compared to 200 nm NCs. Unexpectedly, 140 nm NCs with a 54 nm difference between the LSPR position and the excitation wavelength reveals a slightly lower reaction efficiency compared to the one measured on 110 nm NCs.

In order to demonstrate that our experiments actually correspond to the thiol-ene “click” chemistry, the experimental conditions were modified to perform negative controls, since the grafting of thiophenol on the NCs can be attributed to two other mechanisms: spontaneous grafting or competitive replacement. On one hand, it is known that short molecules with the thiol group - like allyl mercaptan - form non-homogeneous self-assembled monolayers (SAM) due to the lack of intermolecular interactions²⁸. This leaves non-blocked active gold sites for spontaneous thiophenol grafting. On the other hand, competitive molecular displacement could occur directly on the gold surface, inducing the replacement of allyl mercaptan by thiophenol²⁹. Thus, the SERS signal measured in the thiol-ene experiments could then also include contributions from these two

thiophenol-gold interactions. For this concern, three negative controls (experiments C1 to C3) were designed to analyze the thiophenol grafting rate *via* side reactions (figure 4). The first negative control (experiment C1) was designed to duplicate the thiol-ene reaction without a radical initiator. The second negative control (experiment C2) was dedicated to observe the competitive thiophenol adsorption by replacing molecules grafted onto the gold surface. Herein, mercaptoethanol was used instead of allyl mercaptan to avoid any reaction between thiophenol and the allyl group. The last negative control was devoted to the monitoring of the spontaneous adsorption of thiophenol on non-functionalised NCs (experiment C3). All these experiments were performed in the same manner as previously described for the thiol-ene reaction. The reaction kinetics of the three negative controls recorded on the 110 nm NCs are shown in figure 4 and are compared to the kinetics of the thiol-ene reaction.

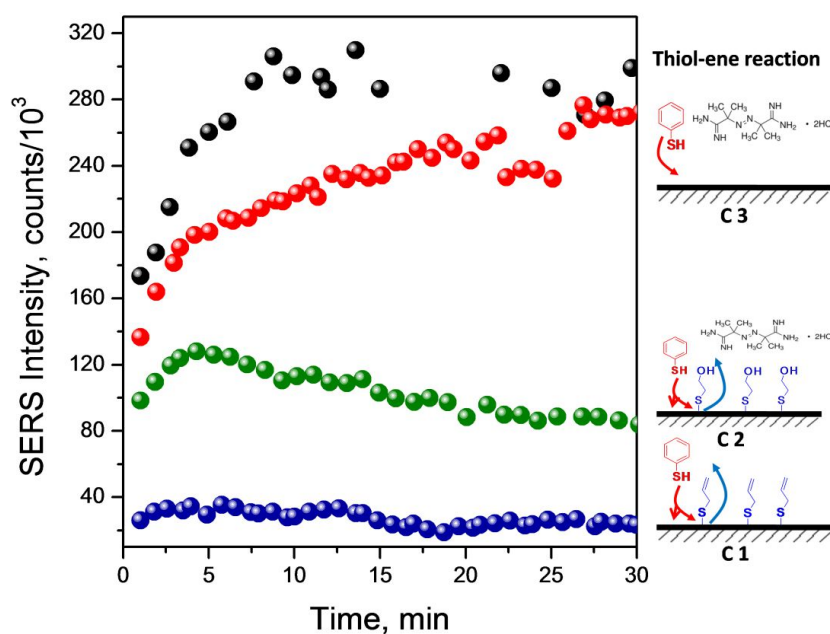


Figure 4: SERS intensities of the integrated peak at 1572 cm^{-1} for the thiol-ene reaction and for all three negative controls recorded on 110 nm NCs (black dot: thiol-ene reaction, blue dots: C1 negative control, green dots: C2 negative control, red dots: C3 negative control). The schemas of the different reactions are given on the right of each curve.

The SERS signal for the experiments C1 and C2 are nearly constant with time. This suggests that in the latter experimental conditions, thiophenol was interacting spontaneously by replacing the short thiols previously deposited on the surface. Since this mechanism is a competitive one, equilibrium was reached very rapidly (less than a few minutes) resulting in a constant SERS signal. However, the measured signal is significantly lower than the one recorded during the thiolene reaction, meaning that the high level of the thiophenol signal observed with the thiolene reaction cannot be explained by

a simple competitive mechanism. In fact, the non-zero SERS signal observed prior to the thiol-ene reaction start (figure 3a and figure 4 black circles) might be assigned to the competitive replacement mechanism. The fast increase in the SERS signal was then induced by the initiated thiol-ene reaction. Furthermore, the comparison of the thiol-ene reaction signal to the one achieved during experiment C1 suggests that AAPH is essential to initiate the thiol-ene reaction.

The SERS signal recorded in experiment C3 is relevant to the kinetics of thiophenol SAM formation. Two main observations can be made from the comparison between the experiment C3 and the thiol-ene reaction. Firstly, thiol-ene kinetics is faster than the spontaneous grafting of thiophenol suggesting the strong contribution of the “click” chemistry process. Secondly, the signal at saturation in experiment C3 is comparable to the one observed in the thiol-ene reaction. This means that the same NCs coverage has been achieved using either the thiol-ene or the simple thiol reaction.

By comparing the different reaction kinetics associated with each negative control experiment (C1 to C3), it is evident that thiophenol grafting onto NCs under conditions demonstrated in figure 3 is favored by the thiol-ene “click” reaction acting as a dominant mechanism.

The contribution of plasmon to the thiol-ene reaction can then be elaborated. To provide evidence, we compared the SERS intensities obtained after surface saturation for the thiol-ene reaction and for experiment C3 on the three NCs diameters (figure 3b). During experiment C3, the grafting of thiophenol should not be dependent on the plasmonic properties of the NCs since the thiol reaction with gold is not thermally or optically activated. The SERS signal ratio between NCs diameters observed in this experiment is thus only due to the effect of the LSPR position compared to the excitation wavelength³⁰ and does not reflect the modification in the coverage rate of the thiophenol on the NCs with different diameters. As expected for experiment C3, the ratio between SERS signal on 110 nm NCs is 2.5 larger than the one measured on the 200 nm due to plasmonic effects on the SERS signal. In the case of the thiol-ene reaction, this ratio is much higher, close to 6. Such a large ratio can only be explained by the higher efficiency of the thiol-ene reaction in thiophenol grafting. Thus, when the LSPR is shifted relative to the excitation wavelength, the thiol-ene reaction is less efficient whereas it is enhanced when the LSPR is close to the excitation wavelength. This is clear evidence that radical reaction is induced and can be tuned by the plasmonic properties of the NCs.

Plasmonic mechanisms

Thanks to NMR experiments (see supplementary information), we have demonstrated that the thiol-ene reaction monitored herein on the plasmonic substrates cannot be initiated at 660 nm wavelength

without the plasmonic substrates. In a conventional thiol-ene experiment either a UV or a thermal activation is necessary to initiate the reaction, even if this latter effect seems to be less efficient (see supplementary information). Thus, we propose two processes related to the plasmonic properties of the NCs to interpret our results.

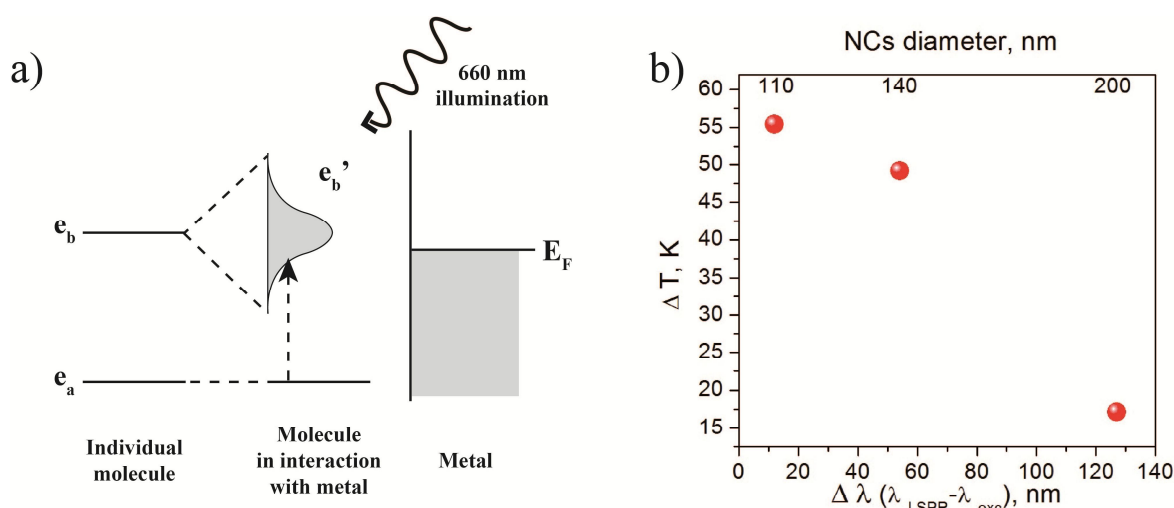


Figure 5: a) Schema of the photonic mechanism. On the left, the electronic configuration of an individual molecule with two levels (e_a and e_b) is represented. On the right, the same molecule is shown but in interaction with a metallic surface. The upper electronic level of the molecule is then broadened (e_b' in the middle schema) due to the interaction with the metallic electronic states (right schema with E_F the Fermi level). The dotted arrow in the middle schema represents the excitation of the molecule through the 660 nm illumination. b) Temperature increases plotted versus the mismatch between LSPR position of NCs and the laser excitation wavelength on the 110 nm, 140 nm and 200 nm NCs. The temperature increases were calculated using Discrete Dipole Approximation method.

The first one, which we call the photonic process, is related to the optical excitation of the radical initiator. It is known that when a molecule is in the close vicinity of a metallic surface its electronic levels are broadened as illustrated in figure 5a^{31,32}. Electronic transitions can then occur at wavelengths outside the UV range whereas they are forbidden for the same molecules in solution and without metal. Through this process, the radical can be formed under initiation with a 660 nm wavelength. As the electromagnetic near-field is enhanced when the LSPR is close to the excitation wavelength, the formation of the radical should be favored as well. As a consequence, the reaction rate is highly improved on resonant NCs.

The second contributing mechanism is related to a thermal process. Discrete Dipole Approximation (DDA) calculations were performed to determine the near-field at the vicinity of the NCs surface (see supplementary information) and the increase in temperature around the NCs was then derived (figure

5b)³³. Though an increase in temperature was obtained for all diameters it was found to be strongly dependent on the LSPR shift relative to the excitation wavelength. Nearly the same increase in temperature was calculated for 110 nm and 140 nm NCs, close to 50-55°C, whereas it was close to 15°C for 200 nm NCs. The attained temperatures were then high enough to induce the formation of the radical (70-75°C for the 110 and 140 nm NCs and 35°C for the 200 nm NCs). The LSPR dependency on the kinetics (figure 3b) can be explained by such LSPR dependency on the temperature. Comparing plots in figures 3b and 5b, one can notice that the slope of the temperature curve is opposite to the one of the reaction time constant, τ . More precisely, the temperature increase induced around the 110 and 140 nm NCs accelerates the speed of the thiol-ene coupling reaction, while a lower temperature increase found in the 200 nm NCs results in a rather slow reaction rate.

We assume that both processes, thermal and photonic, are taking place since they are directly related to the plasmonic properties of the NCs. Both processes contribute simultaneously to the enhancement of the thiol-ene reaction efficiency.

To confirm this conclusion and to further improve thiol-ene reaction localisation, we set up one last experiment. To do this we performed an experiment contrary to the one carried out previously (Figure 2c). In this case, the thiol groups (butanedithiol) were grafted onto the 110 nm NCs surface whereas the molecules consisting in alkene function (pentenoyl-nitroaniline) and AAPH were dispersed in solution (figure 6a). As demonstrated in figure 6c, the reaction measured on three different points was working by means of a few minutes (τ measured from 2.1 to 7.9 minutes). Similar behaviour was observed for all recorded spots and the reaction was reproducible from one point to another. These results confirm that in this configuration the radical formed on the thiol group is only present at the focal point. In previous experiments (allyl mercaptan grafted on the surface), the radicals were formed on the thiophenol in the solution and then the initiation of the thiol-ene reaction outside the laser spot could not be excluded. In the present experiment, the thiol-ene reaction could only occur locally inside the laser spot where the thiol groups were grafted. Accordingly, the reaction was limited to the laser spot and thus was highly localised. This paves the way to a quick and easy method to localise surface functionalisation via the “click” process at the nanometer scale through plasmonic effects.

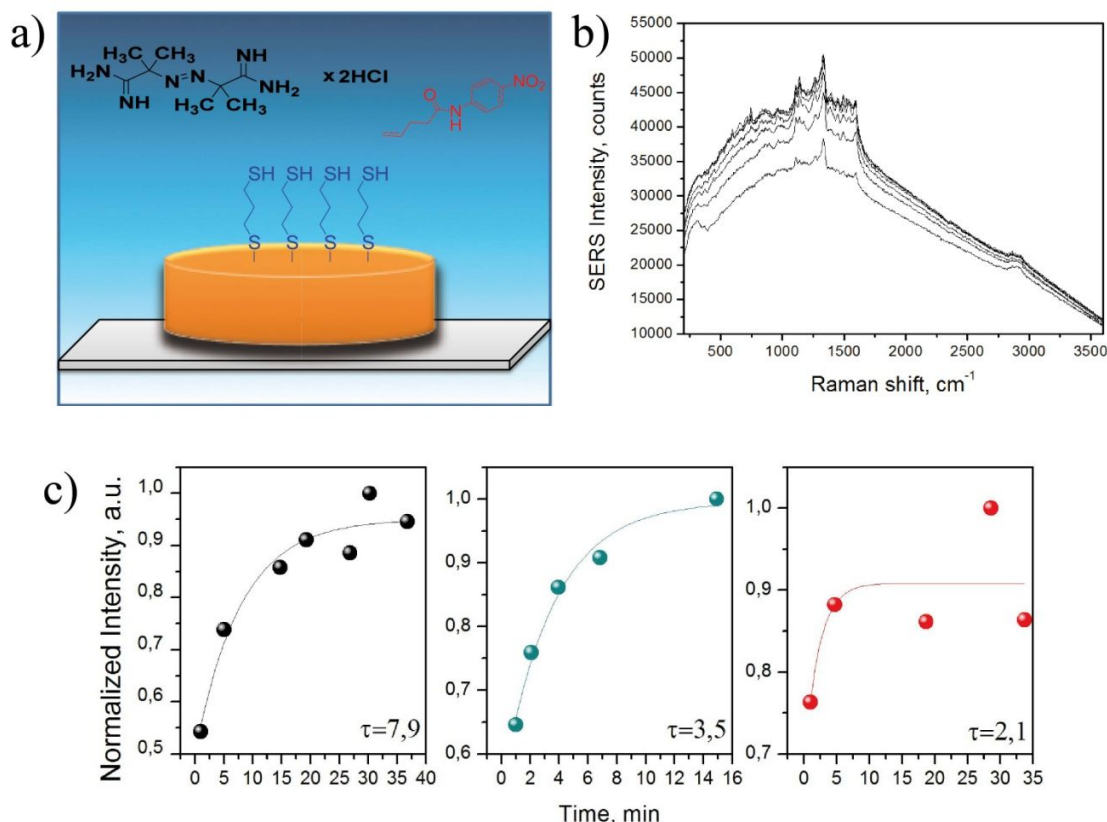


Figure 6: a) Schema of the thiol-ene reaction configuration. b) SERS spectra of grafted pentenoyl-nitroaniline to 110 nm NCs. c) Relative SERS intensities of the integrated peak at 1332 cm^{-1} versus reaction time for three different points on the SERS substrate. The solid lines correspond to the fitting of the experimental points using the equation (1). The reaction time constant, τ , in minutes is given in insert for each point.

6.2.4 Conclusion

We have demonstrated that the thiol-ene reaction can be induced at the surface of gold NCs even if the experimental conditions are not favourable, through the exploitation of the plasmonic properties of the nanostructures. These experiments demonstrate that the thiol-ene reaction can be performed in a few minutes and that by tuning the LSPR position we are able to control the kinetics of the reaction as well as the reaction localisation. This effect interpreted as the combination of both photonic and thermal effects can be used to enhance and control chemical reactions at the nanoscale level.

6.2.5 Methods

6.2.5.1 Materials

2,2'-azobis(2-methylpropionamide) dihydrochloride (AAPH, 97%), 2-mercaptoethanol (BME, 99%), ethanol (99.8%), 4-pentenoyl chloride (98%), 4-nitroaniline (99%), 1,4-butanedithiol (97%) and thiophenol (thiophenol, 99%) were purchased from Sigma-Aldrich (France) and allyl mercaptane

(2-propene-1-thiol, 70%) was obtained from Acros Organic (France). All reagents were used without further purification. Deionized water with resistance of 18.2 M Ω .cm was used in all described experiments as the reaction medium.

6.2.5.2 SERS active substrates

Gold nano-cylinder (NCs) arrays on glass produced by electron beam lithography and lift-off techniques^{34,35} were used for this study. The substrates were designed to contain the variable diameters of NCs: 110 nm, 140 nm and 200 nm. The height of the cylinders was set at 60 nm evaporated on 3 nm of chromium for better gold adhesion on glass. The gap between two NCs was kept constant at 200 nm to avoid any effect of near-field coupling.

6.2.5.3 General procedure for chemical reactions on gold surface

Prior to each experiment, gold NCs were cleaned as follows: substrates were immersed in ethanol for 10 min, dried using nitrogen and treated by ozone under intense 185 nm and 254 nm ultraviolet light (PSD Standard UV-Ozone Cleaner, Novascan), ensuring the removal of organic contaminants. Substrates were then once again immersed in ethanol for 10 min, dried and investigated by Extinction and Surface Enhanced Raman Spectroscopies in aqueous conditions using the microscopic side with the mould (Carl Roth).

6.2.5.4 Thiophenol grafting by thiol-ene click chemistry

The substrate was incubated in allyl mercaptan solution of 0.08 M in ethanol for 12 hours ensuring self-assembled monolayer (SAM) like coating formation to block the gold surface. As-prepared gold NCs based substrate was then ready to be introduced to a reaction mixture containing thiophenol (0.25 mM) and AAPH (0.25 mM) dissolved in deionized water. The sample was placed on a microscopic slide where the mould was filled with 100 μ L of reaction mixture. The thiol-ene click reaction was then monitored by SERS.

6.2.5.5 Experiment C1: Thiophenol interaction with allyl mercaptan functionalised gold NCs

The substrate was functionalised with allyl mercaptan and then placed on a microscopic slide containing 100 μ L of aqueous thiophenol solution (0.25 mM). Contrary to the experiment above, the radical initiator was not included here. Thiophenol interaction with double bonds decorated surface was then monitored by SERS.

6.2.5.6 Experiment C2: thiophenol interaction with mercaptoethanol functionalised gold NCs

The substrate was incubated in mercaptoethanol solution of 0.1 M in ethanol for 12 hours to block the free gold surface. The functionalised substrate was then orientated onto a microscopic slide with a

mould filled with 100 μL of the aqueous solution containing thiophenol (0.25 mM) and AAPH (0.25 mM). Thiophenol interaction with mercaptoethanol was then monitored by SERS.

6.2.5.7 Experiment C3: thiophenol interaction with non-functionalised gold NCs

The cleaned substrate with gold NCs arrays was directly placed on a microscopic slide with the mould filled with 100 μL of solution containing thiophenol (0.25 mM) and AAPH (0.25 mM) in deionized water. Thiophenol interaction with non-functionalised gold surface was then monitored by SERS.

6.2.5.8 Pentenoyl-nitroaniline interaction with butanedithiol functionalised gold NCs

The substrate was first functionalised using butanedithiol (10 mM in ethanol) by incubating it in solution for 12 h. The substrate was then washed with ethanol and placed on a microscopic slide containing 100 μL of aqueous solution with dissolved pentenoyl-nitroaniline (0.2 mM) and AAPH (0.2 mM). Pentenoyl-nitroaniline was chemically synthesized from 4-pentenoyl chloride and 4-nitroaniline, using a nucleophilic addition reaction. As in the experiments above, molecular grafting by thiol-ene reaction was then monitored by SERS.

6.2.5.9 Raman spectroscopy measurements

SERS and extinction measurements were recorded using Xplora ONE (Horiba scientific) spectrometer. For SERS, a laser of 660 nm excitation wavelength with the power of 0.45 mW was focused on the sample with x60 objective (N.A. 0,70). Integration time for signal collection was set at 15s. Each spectrum was the average of two repetitive measurements. Applied grating of 600 grooves/mm ensured a spectral resolution of 3 cm^{-1} .

6.2.5.10 Nuclear Magnetic Resonance (NMR) measurements

Nuclear Magnetic Resonance (NMR) measurements were performed in deuterium oxide using Bruker Avance III 400 MHz instrument.

Acknowledgements

The authors want to acknowledge the REMANTAS ANR project (ANR-11-ECOT-0010) for financial support.

Author contributions

I. Tijunelyte performed the experiments. I. Tijunelyte, E. Guenin, N. Lidgi-Guigui and M. Lamy de la Chapelle conceived and designed the experiments and analysed the experimental results. M. Lamy de la Chapelle proposed the plasmonic mechanisms. F. Colas performed the DDA calculations. J. Ibrahim and T. Toury designed and produced the plasmonic substrates.

Competing financial interests

The authors state that they have no competing financial interests.

6.2.6 References

- 1 Stockman, M. I. Nanoplasmonics: past, present, and glimpse into future. *Optics express* **19**, 22029-22106 (2011).
- 2 Bohm, D. & Pines, D. A Collective Description of Electron Interactions. I. Magnetic Interactions. *Physical Review* **82**, 625-634 (1951).
- 3 Ritchie, R. H. Plasma Losses by Fast Electrons in Thin Films. *Physical Review* **106**, 874-881 (1957).
- 4 Petryayeva, E. & Krull, U. J. Localized surface plasmon resonance: Nanostructures, bioassays and biosensing—A review. *Analytica Chimica Acta* **706**, 8-24 (2011).
- 5 Pelton, M., Aizpurua, J. & Bryant, G. Metal-nanoparticle plasmonics. *Laser & Photonics Reviews* **2**, 136-159 (2008).
- 6 Volpe, G., Noack, M., Acimović, S. S., Reinhardt, C. & Quidant, R. Near-Field Mapping of Plasmonic Antennas by Multiphoton Absorption in Poly(methyl methacrylate). *Nano Lett.* **12**, 4864-4868 (2012).
- 7 Urban, A. S., Pfeiffer, T., Fedoruk, M., Lutich, A. A. & Feldmann, J. Single-Step Injection of Gold Nanoparticles through Phospholipid Membranes. *ACS Nano* **5**, 3585-3590 (2011).
- 8 Raphael, M. P. *et al.* A New Methodology for Quantitative LSPR Biosensing and Imaging. *Analytical Chemistry* **84**, 1367-1373 (2011).
- 9 Baffou, G. & Quidant, R. Nanoplasmonics for chemistry. *Chemical Society Reviews* **43**, 3898-3907 (2014).
- 10 Ueno, K. *et al.* Nanoparticle Plasmon-Assisted Two-Photon Polymerization Induced by Incoherent Excitation Source. *Journal of the American Chemical Society* **130**, 6928-6929 (2008).
- 11 Galloway, C. M. *et al.* Plasmon-Assisted Delivery of Single Nano-Objects in an Optical Hot Spot. *Nano Lett.* **13**, 4299-4304 (2013).
- 12 Cao, L., Barsic, D. N., Guichard, A. R. & Brongersma, M. L. Plasmon-Assisted Local Temperature Control to Pattern Individual Semiconductor Nanowires and Carbon Nanotubes. *Nano Lett.* **7**, 3523-3527 (2007).
- 13 Kolb, H. C., Finn, M. G. & Sharpless, K. B. Click Chemistry: Diverse Chemical Function from a Few Good Reactions. *Angewandte Chemie International Edition* **40**, 2004-2021 (2001).
- 14 Meldal, M. & Tornøe, C. W. Cu-Catalyzed Azide-Alkyne Cycloaddition. *Chemical Reviews* **108**, 2952-3015 (2008).
- 15 Li, N. & Binder, W. H. Click-chemistry for nanoparticle-modification. *J. Mater. Chem.* **21**, 16717-16734 (2011).
- 16 Posner, T. Beiträge zur Kenntniss der ungesättigten Verbindungen. II. Ueber die Addition von Mercaptanen an ungesättigte Kohlenwasserstoffe. *Berichte der deutschen chemischen Gesellschaft* **38**, 646-657 (1905).
- 17 Lowe, A. B. Thiol-ene "click" reactions and recent applications in polymer and materials synthesis. *Polymer Chemistry* **1**, 17-36 (2010).
- 18 Lowe, A. B. Thiol-ene "click" reactions and recent applications in polymer and materials synthesis: a first update. *Polymer Chemistry* **5**, 4820-4870 (2014).
- 19 Han, X., Wu, C. & Sun, S. Photochemical reactions of thiol-terminated self-assembled monolayers (SAMs) for micropatterning of gold nanoparticles and controlled surface functionality. *Applied Surface Science* **258**, 5153-5156 (2012).
- 20 Lallana, E., Sousa-Herves, A., Fernandez-Trillo, F., Riguera, R. & Fernandez-Megia, E. Click Chemistry for Drug Delivery Nanosystems. *Pharmaceutical Research* **29**, 1-34 (2012).
- 21 Griesbaum, K. Problems and Possibilities of the Free-Radical Addition of Thiols to Unsaturated Compounds. *Angewandte Chemie International Edition in English* **9**, 273-287 (1970).
- 22 Khire, V. S., Kloxin, A. M., Couch, C. L., Anseth, K. S. & Bowman, C. N. Synthesis, characterization and cleavage of linear polymers attached to silica nanoparticles formed using thiol-acrylate conjugate addition reactions. *Journal of Polymer Science Part A: Polymer Chemistry* **46** (2008).

- 23 Jonkheijm, P. *et al.* Photochemical Surface Patterning by the Thiol-Ene Reaction. *Angewandte Chemie International Edition* **47**, 4421-4424 (2008).
- 24 Dupin, D., Schmid, A., Balmer, J. A. & Armes, S. P. Efficient Synthesis of Poly(2-vinylpyridine)-Silica Colloidal Nanocomposite Particles Using a Cationic Azo Initiator. *Langmuir* **23** (2007).
- 25 Guillot, N. & Lamy de la Chapelle, M. Lithographed nanostructures as nanosensors. *Journal of Nanophotonics* **6**, 064506-1-28 (2012).
- 26 Anker, J. N. *et al.* Biosensing with plasmonic nanosensors. *Nat Mater* **7**, 442-453 (2008).
- 27 Northrop, B. H. & Coffey, R. N. Thiol-Ene Click Chemistry: Computational and Kinetic Analysis of the Influence of Alkene Functionality. *Journal of the American Chemical Society* **134**, 13804-13817 (2012).
- 28 Chi, Zhang, J. & Ulstrup, J. Surface Microscopic Structure and Electrochemical Rectification of a Branched Alkanethiol Self-Assembled Monolayer. *The Journal of Physical Chemistry B* **110**, 1102-1106 (2006).
- 29 Kakiuchi, T. *et al.* Phase Separation of Alkanethiol Self-Assembled Monolayers during the Replacement of Adsorbed Thiolates on Au(111) with Thiols in Solution. *Langmuir* **16**, 7238-7244 (2000).
- 30 Guillot, N. & de la Chapelle, M. L. The electromagnetic effect in surface enhanced Raman scattering: Enhancement optimization using precisely controlled nanostructures. *Journal of Quantitative Spectroscopy and Radiative Transfer* **113**, 2321-2333 (2012).
- 31 Furtak, T. E. & Reyes, J. A critical analysis of theoretical models for the giant Raman effect from adsorbed molecules. *Surface Science* **93**, 351-382 (1980).
- 32 Gersten, J. I., Birke, R. L. & Lombardi, J. R. Theory of Enhance I Light Scattering from Molecules Adsorbed at the Metal-Solution Interface. *Physical Review Letters* **43**, 147-150 (1979).
- 33 Baffou, G. *et al.* Photoinduced Heating of Nanoparticle Arrays. *ACS Nano* **7**, 6478-6488 (2013).
- 34 Grand, J. *et al.* Optimization of SERS-active substrates for near-field Raman spectroscopy. *Synthetic Metals* **139**, 621-624 (2003).
- 35 Grand, J. *et al.* Role of localized surface plasmons in surface-enhanced Raman scattering of shape-controlled metallic particles in regular arrays. *Physical Review B* **72**, 033407 (2005).

6.3 Conclusion

In this chapter we have demonstrated the successful attempt in local molecular immobilization by implementation of thiol-ene “click” reaction on highly plasmonic nanostructures. Comparing with the results obtained from the negative controls we have shown that the reaction rate can be triggered by controlling the position of the LSP resonance compared to the excitation wavelength used to initiate the reaction.

These results open new path in highly selective, very rapid, facile and localised surface functionalisation. This concept can be then exploited widely for the design of multi-functional nanosensors.

GENERAL CONCLUSION AND PERSPECTIVES

Within the scopes of this thesis, different approaches of SERS nanosensor surface functionalization were tested in order to design a (bio)-receptor layer capable in organic pollutants pre-concentration. During this study, we have considered three strategies, which were as follows: (i) to design of highly selective nanosensor functionalised by anti-body against BaP, (ii) to test the size selective nanosensors based on CDs and (iii) to examine DS derivative based nanosensor for the pre-concentration and the detection of highly nonpolar aromatic compounds.

For the study related with the anti-body based SERS nanosensors, primarily, the concept of antibody immobilisation *via* carbodiimide coupling was tested by using model proteins such as anti-BSA and anti-RNASE. Herein, the results obtained by SPR and LSPR showed the successful surface functionalisation as well as the analytes (BSA and RNASE, respectively) detection. However, conducted SERS investigation did not confirm the specific interaction between anti-body and antigen. In fact, while SERS signal of immobilized antibodies was not achieved, the spectra of detected antigens were rather strong, indicating that observed antigens are non-specifically adsorbed on the surface. The main drawback of this kind of anti-body based SERS nanosensor is the great size of attached biomolecules. With this regard, the approach has been improved by performing enzymatic anti-bodies digestion. Resulted F(ab)₂ fragments were then used for direct substrate functionalisation. SERS spectra of physically adsorbed F(ab)₂ were successfully recorded. Moreover, the SERS signal of protein was found to be very reproducible. Conducted experiments on the BaP detection at 500 ppb concentration on latter nanosensor and two negative controls, confirmed that the sensor with adsorbed F(ab)₂ fragments improves the detection of the analyte. Obtained results are very encouraging to continue on this strategy.

Further improvements in this system could be related with the disulfide bonds reduction of the F(ab)₂, resulting in two Fab fragments. The application of the latter ones to the surface functionalisation would ensure covalently bounded protein with analyte binding site orientated very closely to the surface. Similar result could be achieved using thiol-ene reaction, where radical initiator would break the disulfide bonds, and the resulted thiyl radicals would attach to the sensor surface pre-decorated by molecules bearing alkene groups.

Secondly, in this study, the applications of cyclodextrins (CDs) for the pre-concentration of pollutants were investigated. Initially, the host-guest complexes formation between pollutants (TOL, NAP and FL) and CDs has been examined by Raman spectroscopy and TG analysis. As expected, certain selective activity of the CDs was found against different analytes regarding their size. More precisely, we observed that: α -CD forms host-guest complexes with TOL, while β -CD is more interacting with NAP and γ -CD preferably encapsulates FL.

In order to apply CDs for surface functionalisation, chemical synthesis of thiolated CDs was successfully performed. The primary OH groups replacement by SH groups was confirmed by NMR and Raman spectroscopy. First attempt to test the thiolated-CDs based functionalisation was performed on colloidal GNPs. The presence of grafted thiolated CDs was confirmed by monitoring changes in GNPs extinction spectra before and after functionalisation, as well as by SERS. The molecular pre-concentration in regards to the selectivity achieved by these nanosensors was found to be similar to the one observed in the study of host-guest complexes formed in solid state. However, the further attempt to reproduce these experiments using GNCs made by EBL as SERS active substrate has failed. Insufficient surface coverage was discussed as a possible reason of the non observation of the receptor layer based on thiolated CDs and of the targeted pollutants.

Few strategies could be considered regarding the surface functionalisation by CDs. Having thiolated derivatives, it is possible to graft them onto the surface by thiol-ene or thiol-yne processes. Alkyne-azide cycloaddition reaction could also be an interesting solution if instead of SH groups CDs would be produced bearing N_3 groups. Moreover, in the literature the synthesis of CDs coupled with diazonium salt has been demonstrated. The reactivity of N_2 group presented on diazonium salts towards metals is sufficient to ensure homogeneous surface coverage. Moreover, sufficient surface coating can be achieved using CD-polymers as well. As it was demonstrated in this study, nanosensor with physically adsorbed CD-polymer led to the NAP detection at 250 ppb concentration. The drawback of this system was the stability of the coating (observed the loss in the polymer coating when sensor was introduced into sea water).

One can notice that for both $F(ab)_2$ fragments based and thiolated CDs based surface functionalisation, the exploitation of thiol-ene “click” reaction could be meaningful. Local molecular immobilisation thanks to the thermal or photonic effects created in the near field of plasmonic nanoparticles could be well applied to graft latter molecules on the sensor surface. Well controlled nanoplasmonics mediated “click” process could be applied for selective molecular immobilisation on limited surface area, opening the way to the design of multi-functional nanosensors with the capability of (multi)-selective molecular pre-concentrations.

The last strategy exploited in this thesis was related with diazonium salts (DSs) application for the design of nanosensors pre-concentrating pollutants *via* non-specific physical adsorption driven by weak Van der Waals or hydrophobic interactions. Before exploiting DSs for the surface functionalisation, detailed Raman spectroscopy based study was conducted on synthesized DSs in order to (i) confirm the successful chemical DSs synthesis and (ii) identify the vibrational signatures of each obtained aryl diazo compounds. In the same manner study was continued after performing DSs based surface functionalisation. First surface functionalisation approach was tested on GNCs made by EBL. Performing SERS based investigation we have assigned characteristic vibrations of phenyl derivatives grafted to the surface. With the help of DFT modeling and XPS experiments on flat gold surface we have discussed the mechanism of DS-COOH grafting to the surface. Established protocol of DS based surface functionalisation resulted in very reproducible coatings between nanosensors; DS and DS-C₁₀H₂₁ were considered as good candidates to pre-concentrate nonpolar pollutants. In this case commercially available SERS substrates were functionalised by both DSs and were tested for PAH detection. Due to the lower rate of spontaneous polymerization, -based GNSs were found to be highly reproducible. This nanosensor led to the detection of NAP, FL and BaP with the limits of detection (LODs) of 15 ppm, 0.45 ppm and 0.045 ppm, respectively. It is worth to note that latter detections were achieved using the prototype Raman micro-spectrometer designed by Horiba Scientific in the frameworks of REMANTAS project.

Latter results showed that the DS-C₁₀H₂₁ based nanosensor performance is depending on the physicochemical properties of the coating as well as of analytes. This observation suggests that by applying different DSs the resulting nanosensor can be customized regarding the polarity of the targeted molecules. Hence, the application of DSs to the design of SERS based nanosensors is very promising. As a matter of fact, the achieved LODs could be significantly improved by well fitting the physicochemical properties of coating layer in regards to the selected analytes. The lower molecular detection could be reached by optimizing some other parameters. For instance, as it was discussed, DSs tend to polymerize creating non-homogeneous multi-layers. During this study we did not consider the thickness of obtained coating layer, but as it was shown in the chapter of anti-bodies exploitation, the distance of analyte to the surface is critical for efficient detection. Thus, the protocol of the DS based surface functionalisation should be improved.

All described surface functionalisation strategies were first exploited on the GNCs produced by EBL due to their reproducibility. However, these substrates did not lead to successful molecular detection. For this reason, the experiments were reproduced and detection of analytes were observed using the colloidal nanoparticles (in solution or deposited on a substrate) or commercial SERS substrates. This leads to the conclusion that SERS substrates are an essential component of SERS nanosensors and

have to be seriously considered and carefully selected. The good balance between the reproducibility and the sensitivity of the substrate has to be found.

Other general observation is related with the measuring conditions. Investigated molecules have a different volatilities and it is necessary to perform experiments in liquid conditions. During this study we used two systems: (i) a microscopic slide with the mould or (ii) a liquid cell. The first system was found highly non-beneficial for many reasons, mostly because of the great risk to contaminate sample at any step. Liquid cell, on the other hand, is a comfortable tool to use and is very important working with this kind of molecules. Also it is essential for *in-situ* applications.

ANNEX 1: Experimental SERS set-ups

In this section, the instrumental set-ups used in this study will be described. The SERS nanosensor design required the determination of the optical properties of the gold nanostructures. Such measurements were done using extinction spectroscopy. Raman and SER spectroscopy were used for the nanosensors characterization and its performance in molecular detection.

These measurements were conducted using a Xplora (Horiba Scientifics) and a Labram HR800 (Horiba Scientifics) micro-spectrometers. The configurations for LSPR and Raman/SERS measurements are illustrated in Figure 1. For acquiring extinction spectra, white light is transmitted through the sample. A fraction of the photons are absorbed and scattered by the sample while the transmitted light is collected by the objective. The grating is then separating the light in shorter frequency range in order to measure intensity of the light regarding its wavelength with a charge-coupled device (CCD).

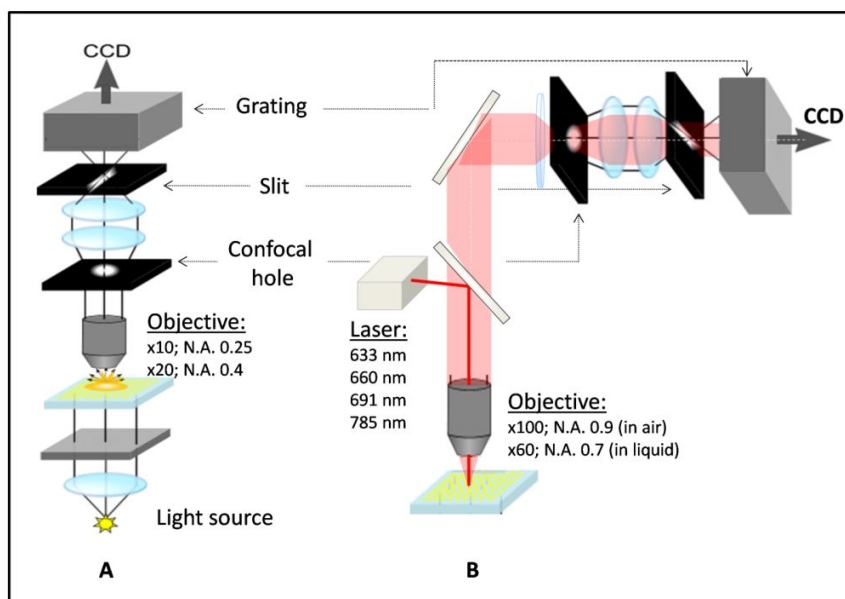


Figure 1: Schematic illustration of LSPR (A) and Raman/SERS (B) experimental configurations.

Raman and SERS measurements were performed in backscattering configuration. In this way, excitation monochromatic laser light is focused on the sample through a high numerical-aperture objective whereas the Raman signal is collected through the same objective. The collected scattered light is then passing through an edge filter to remove the Rayleigh-scattered light. Finally the light is analysed with a spectrometer and recorded by a CCD camera.

The lasers used during this study are 633 nm, 660 nm, 691 m and 785 nm. The selection of laser was determined in regards to the applied SERS active substrates. In order to achieve maximum signal enhancement laser wavelength was selected to match the wavelength of LSPR position. In SERS, laser was focused with x100 fold magnification objective (N.A. 0.9) for a measurement in the air, and with x60 fold magnification objective (N.A. 0.7) for a measurements in liquid conditions. The latter objective is equipped with a correction collar to focus the laser at the nanostructures surface through a glass slide (see Figure 2 illustrating sample orientation for measurements in liquid conditions).

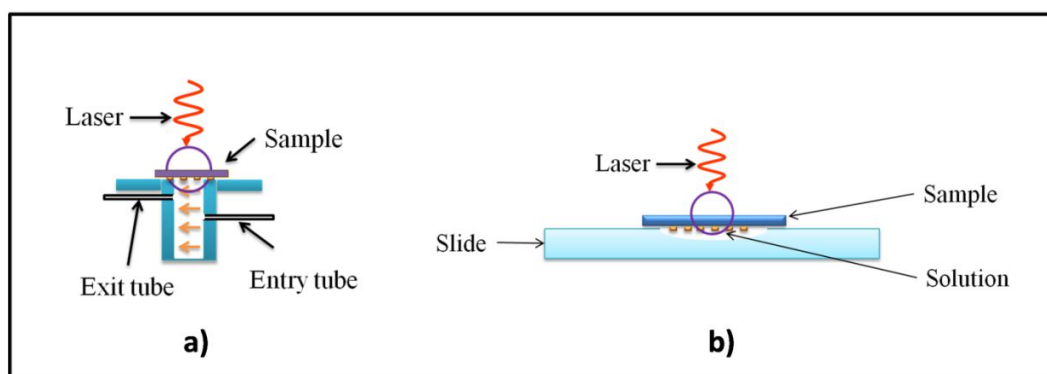


Figure 2 Schematic illustration of a) the liquid cell and b) microscopic slide with a cavity used to ensure liquid conditions.

Liquid conditions for SERS experiments were ensured using home-designed liquid cell or commercially available microscopic slide with a mould. In the first case the measurements can be made in dynamically exchanging environment thanks to peristaltic pump attached to a liquid cell. In the second configuration the cavity presented on microscopic slide is filled with the constant amount of liquid. In both cases SERS substrates are placed on the top with the nanostructures orientated in the liquid. Therefore the laser for SERS measurements was focused through the glass.

In the course of the project a Raman set-up was developed by Horiba Scientifics (figure 3). This portable micro-Raman spectrometer was designed for on-site applications. It is equipped with a micro-fluidic cell (figure 3 A) whereas liquid is circulated by a peristaltic pump. In this configuration the laser with excitation wavelength of 691 nm is focused from the bottom though the glass with a x60 fold magnification objective (0.7 N.A.). The optical table is placed under the protective shield (figure 3 B). Assembled spectrometer is integrated in the portable box (figure 3 C)

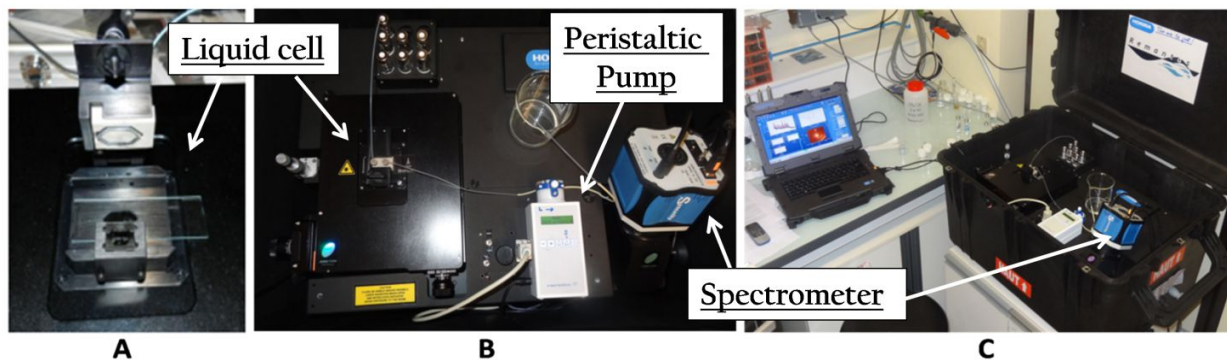


Figure 3: Photography of the portable Raman instrumental set-up developed by HORIBA Scientifics. Picture A shows the micro-fluidic cell and picture B the up stage with the sample holder, liquid cell and peristaltic pump. The integrated Raman set-up in its box can be seen in picture C.

ANNEX 2: ELECTRONIC SUPPLEMENTARY MATERIAL for Investigation of aromatic hydrocarbons inclusion into cyclodextrins by Raman spectroscopy and thermal analysis

Inga Tijunelyte^a, Nathalie Dupont^a, Irena Milosevic^a, Carole Barbey^a Emmanuel Rinnert^b Nathalie
Lidgi-Guigui^a, Erwann Guenin^a, Marc Lamy de la Chapelle^a

Table 6 Calculated frequencies and intensities for the most important normal modes of TOL (among 39 normal modes in Cs representation), experimental data for TOL alone and TOL engaged in complexes with α , β and γ CD

N°	Sym.	Calcul.	R.I.	Assigm.	TOL	R.I.	α CD:TO L	β CD: TOL	γ CD: TOL
1	A'	518	4,30	δ (CC stretch.)	516	1,54	520	519	518
2	A'	783	4,00	δ (ring breath.)	781	5,21	787	779	780
3	A'	999	4,19	δ	999	5,20	997	998	998
4	A'	1031	1,55	δ	1026	1,29	1027	1026	1026
5	A'	1157	0,44	δ (CH sciss.)	1152	0,43	-	-	-
6	A'	1179	0,53	δ (CH sciss.)	1175	0,38	-	-	-
7	A'	1203	1,09	δ (CC stretch.)	1206	1,52	-	1204	1204
8	A'	1594	0,38	δ	1582	0,62	1580	1581	1582
9	A'	1616	1	δ	1603	1,00	1603	1603	1603
10	A'	2933	1,92	δ (CH sym. stretch. CH ₃)	2921	3,62	-	-	
11	A'	3060	2,39	δ (CH sym. stretch. ring)	3058	5,53	3056	3051	3053

γ out plane of the molecule; δ in plane of the molecule

Table 7 Calculated frequencies and intensities for the most important normal modes of NAP (among 48 normal modes in D2h representation), experimental data for NAP alone and NAP engaged in complexes with α,β and γ CD

N ^o	Sym	Calcul.	R.I.	Assigm.	NAP	R.I.	α -CD:NA P	R.I.	β -CD:NA P	R.I.	γ -CD:NA P	R.I.
1	B3g Ag	509 (2 bands)	1,25;2,3 2	δ	508	0,42	509	2,07	510	1,19	510	1,50
2	Ag	758	2,33	δ (CC stretch.)	761	1,73	763	2,39	758	1,65	759	1,40
3	B2g	771	0,10	γ	781	0,17	773	0,07	773	0,16	769	0,32
4	Ag	1025	1,00	δ (CC stretch.)	1019	1,00	1025	1,00	1024	1,00	1025	1,00
5	Ag	1370	2,45	δ (CC stretch.)	1379	0,88	1381	2,09	1376	2,83	1376	2,80
6	Ag	1582	0,34	δ	1575	0,52	1578	0,79	1576	0,37	1577	0,29
7	B3g	1637	0,08	δ	1627	0,05	1630	0,16	1629	0,14	1629	0,14
8				γ (CH Sym. stretch.)	-	-	3044	0,17	3045	0,20	3039	0,16
9	Ag	3060	0,99	δ (CH Sym. stretch.)	3050	0,72	3057	0,62	3055	0,47	3055	0,55

γ out plane of the molecule; δ in plane of the molecule

Table 8 Calculated frequencies and intensities for the 72 normal modes of FL, experimental data for FL alone and FL in complex. Vibrational modes which are most impacted (demonstrated important shift or strongly vary in relative intensity) by complex formation are marked in bold

N°	Sym.	Calcul.	R.I. (reg.1101)	Assigm.	FL	R.I. (reg.1101)	Complex	R.I. (reg.1102)
1	B1	101	0.04	γ				
2	A2	119	0.28	γ				
3	B1	163	0.02	γ (Rings A)				
4	B2	204	0.28	δ	204	0.11	202	0.09
5	A2	251	---	γ (Rings A)	261	0.31	268	0.29
6	B1	293	0.66	γ	300	0.70	296	0.32
7	A1	349	0.45	δ	352	0.50	350	0.39
8	B1	428	0.03	γ (Ring B)				
9	A2	429	0.15	γ	428	0.26	---	---
10	B1	458	---	γ (Rings A)	452	0.10	437	0.05
11	B2	468	0.46	δ	471	0.39	469	0.27
12	A1	484	0.16	δ (Rings A)	484	0.40	479	0.77
13	B2	559	0.02	δ				
14	A1	560	0.58	δ (Rings A)	560	1.41	559	0.62
15	A2	564	0.01	γ				
16	B2	615	---	δ				
17	B1	619	---	γ A				
18	A2	638	0.01	γ				
19	A1	672	0.45	δ (Ring B)	669	2.73	669	0.65
20	A2	736	0.01	γ (Rings A)	734	0.11		
21	B1	742	0.01	γ (Ring B)				
22	B2	762	0.01	δ				
23	B1	775	0.01	γ (Rings A)	778	0.20		
24	A2	781	---	γ				
25	A1	801	0.20	δ (Rings A)	801	0.58	802	0.24
26	B1	824	0.01	γ (Rings A)	825	0.12	824	0.02

27	A2	867	0.01	γ (Ring B)				
28	A1	889	0.03	δ				
29	A2	897	---	γ (Rings A)				
30	B1	905	0.02	γ (Rings A)	904	0.17		
31	B1	929	---	γ (Ring B)				
32	A2	957	---	γ (Rings A)				
33	B1	966	0.01	γ (Rings A)				
34	A2	967	---	γ (Ring B)				
35	B2	970	0.01	δ	970	0.01		
36	B2	1018	0.01	δ (Rings A)				
37	A1	1023	0.34	δ (Ring B)	1018	1.25	1016	0.35
38	A1	1041	0.12	δ (Rings A)	1036	0.42	1033	0.10
39	B2	1084	---	δ (Ring B)				
40	A1	1101	1.00	δ	1101	1.00	1102	1.00
41	B2	1139	0.07	δ	1134	0.32	1135	0.11
42	A1	1159	0.03	δ (Ring B)	1153	0.27	1155	0.05
43	B2	1161	0.01	δ				
44	A1	1184	0.10	δ (Rings A)	1182	0.08	1182	0.03
45	B2	1210	0.13	δ	1215	0.12		
46	B2	1229	---	δ (Rings A)	1236	0.10		
47	A1	1267	0.79	δ (Rings A)	1269	0.70	1267	0.70
48	B2	1291	0.02	δ (Ring B)	1299	0.12		
49	A1	1314	0.02	δ	1309	0.14		
50	B2	1369	0.06	δ (Rings A)	1361	0.18		
51	A1	1375	0.18	δ	1372	0.40	1372	0.40
52	A1	1414	0.48	δ	1409	1.71	1410	0.67
53	A1	1425	0.31	δ (Rings A)	1423	1.20	1424	1.07
54	B2	1443	0.02	δ	1436	0.32		
55	A1	1457	0.40	δ	1455	0.90	1453	0.85
56	B2	1477	---	δ				
57	B2	1493	0.01	δ				
58	A1	1584	0.03	δ (Ring B)	1587	0.21	1590	0.16

59	A1	1609	0.24	δ CC str.+ CCC Scis. + CCH Scis. (Rings A)	1601	0.67	1604	0.25
60	A1	1611	0.95	δ CC str.+ CCC.+ CCH Scis. (Rings A)	1608	1.72	1610	1.14
61	B2	1614	0.23	δ CC str. (Ring B)	1620	0.12	1621	0.26
62	B2	1626	0.01	δ CC str. (Rings A)				
63	B2	3034	0.03	δ CH str.				
64	B2	3034	0.02	δ CH str	3022	0.17	3037	0.05
65	A1	3034	---	δ CH str. (Rings A)				
66	A1	3040	0.02	δ CH str. (Ring B)	3034	0.09	3051	0.24
67	B2	3044	0.02	δ CH str. (Rings A)				
68	A1	3045	0.08	δ CH str. (Rings A)	3048	0.83	3059	0.05
69	B2	3050	0.05	δ CH str. (Ring B)				
70	B2	3056	0.02	δ CH str. (Rings A)				
71	A1	3057	0.16	δ CH str. (Rings A)				
72	A1	3061	0.15	δ CH str. (Ring B)	3062	0.20	3068	0.04

γ out plane of the molecule; δ in plane of the molecule

ANNEX 3: Chemical shift obtained by NMR of CD and CD-SH

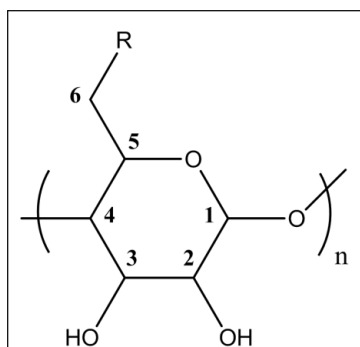


Figure 5.6.1 Chemical structure of modified CDs; α -CD: $n = 6$; β -CD: $n = 7$; γ -CD: $n = 8$. $R = I$ for Per-6-iodo-cyclodextrin or $R = SH$ for Per-6-thio-cyclodextrin.

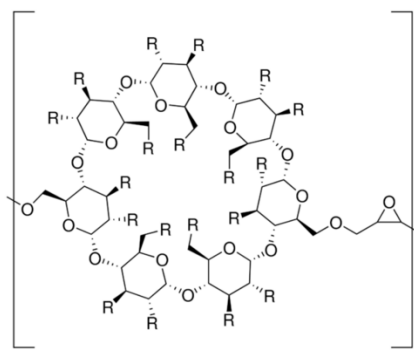


Figure 5.6.2 Chemical structure of β -CD-polymer

Per-6-iodo- α -cyclodextrin: ^1H NMR (CD_3SOCD_3) δ (ppm) 5.80 (d, $J = 6.6$ Hz, 6H, 2-OH), 5.64 (s, 6H, 3-OH), 4.94 (d, $J = 2.7$ Hz, 6H, H-1), 3.88-3.66 (m, 12H, H-6b, H-5), 3.66-3.42 (m, 12H, H-3, H-6a), 3.42-3.21 (m, 18H, H-2, H-4).

Per-6-iodo- β -cyclodextrin: ^1H NMR (CD_3SOCD_3) δ (ppm) 6.06 (d, $J = 6.4$ Hz, 7H, 2-OH), 5.95 (s, 7H, 3-OH), 4.99 (d, $J = 3$ Hz, 7H, H-1), 3.8 (d, $J = 9.4$ Hz, 7H, H-6b), 3.69-3.54 (m, 14H, H-3, H-5), 3.49-3.23 (m, 21H, H-2, H-4, H-6a).

Per-6-iodo- γ -cyclodextrin: ^1H NMR (CD_3SOCD_3) δ (ppm) 5.98 (m, 16H, OH-2, OH-3), 5.03 (d, $J = 2.7$ Hz, 6H, H-1), 3.82 (d, $J = 9.3$ Hz, 8H, H-6b), 3.74-3.50 (m, 16H, H-3, H-5), 3.50-3.18 (m, 24H, H-2, H-4, H-6a).

Per-6-thio- α -cyclodextrin: ^1H NMR (CD_3SOCD_3) δ (ppm) 5.70 (d, $J = 7$ Hz, 6H, 2-OH), 5.55 (d, $J = 2.2$ Hz, 6H, 3-OH), 4.91 (d, $J = 2.9$ Hz, 6H, H-1), 3.85-3.65 (m, 12H, H-3, H-5), 3.46-3.24 (m, 12H, H-2, H-4), 3.18-3.06 (m, 6H, H6-b), 2.85-2.69 (m, 6H, H6-a), 2.17 (t, $J = 8.3$ Hz, 6H, SH).

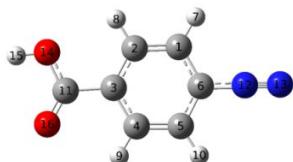
Per-6-thio- β -cyclodextrin: ^1H NMR (CD_3SOCD_3) δ (ppm) 5.93 (d, $J = 6.7$ Hz, 7H, 2-OH), 5.82 (s, 7H, 3-OH), 4.93 (d, $J = 3.2$ Hz, 7H, H-1), 3.64 (dt, $J = 18.5, 8.7$ Hz, 14H, H-3, H-5), 3.43-3.27 (m, 14H, H-2, H-4), 3.25-3.13 (m, 7H, H6-b), 2.82-2.68 (m, 7H, H6-a), 2.13 (t, $J = 8.3$ Hz, 7H, SH).

Per-6-thio- γ -cyclodextrin: ^1H NMR (CD_3SOCD_3) δ (ppm) 5.96 (m, 16H, 2-OH, 3-OH), 4.96 (s, 8H, H-1), 3.83-3.49 (m, 16H, H-3, H-5), 3.47-3.24 (m, 16H, H-2, H-4), 3.22-3.06 (m, 8H, H6-b), 2.82-2.62 (m, 8H, H6-a), 2.19 (t, $J = 7.8$ Hz, 8H, SH).

ANNEX 4: Electronic supplementary information on Raman characterization of phenyl derivatives: from primary amine to diazonium salts

Stéphanie Betelu^{1*}, Inga Tijunelyte², Leïla Boubekeur-Lecaque³, Ioannis Ignatiadis¹, Anne Carolinne Schnepf¹, Erwann Guenin², Nadia Bouchemal², Nordin Félij³, Emmanuel Rinnert⁴, Marc Lamy de la Chapelle².

X- Optimized geometry and three lower frequencies CBN₂



Tag	Symbol	X	Y	Z
1	C	-0.0199110	0.1510500	0.0241040
2	C	0.0246340	0.1947420	1.4071920
3	C	1.2513620	0.0755640	2.0760730
4	C	2.4516120	-0.0891910	1.3694950
5	C	2.4479750	-0.1378770	-0.0118820
6	C	1.2011610	-0.0153730	-0.6516510
7	H	-0.9521520	0.2407600	-0.5193060
8	H	-0.8885360	0.3212990	1.9734250
9	H	3.3779500	-0.1773050	1.9240590
10	H	3.3597850	-0.2645210	-0.5818690
11	C	1.3433630	0.1189900	3.5827330
12	N	1.1746230	-0.0617820	-2.0322260
13	N	1.1551660	-0.0985930	-3.1378250
14	O	0.1412520	0.2791970	4.1514310
15	H	0.2474350	0.3007070	5.1166320
16	O	2.3860850	0.0194400	4.1699100

	1	2	3							
Frequencies --	58.7134	78.5478	142.7250							
Red. masses --	7.1456	8.4031	9.8093							
Frcconsts --	0.0145	0.0305	0.1177							
IR Inten --	1.5044	0.0218	1.1777							
RamanActiv --	0.2817	1.2395	3.7563							
Depolar (P) --	0.7500	0.7500	0.7500							
Depolar (U) --	0.8571	0.8571	0.8571							
Atom	AN	X	Y	Z	X	Y	Z	X	Y	Z
1	6	-0.02	-0.19	0.01	0.03	0.24	-0.01	-0.20	0.02	0.01
2	6	-0.02	-0.17	0.01	0.03	0.25	-0.01	-0.18	0.02	0.02
3	6	0.00	0.01	0.00	0.02	0.18	-0.01	-0.16	0.02	0.00
4	6	0.02	0.19	-0.01	0.03	0.23	-0.01	-0.18	0.02	-0.02
5	6	0.02	0.21	-0.01	0.02	0.21	-0.01	-0.20	0.02	-0.01
6	6	0.00	0.01	0.00	0.02	0.16	-0.01	-0.21	0.02	0.00
7	1	-0.04	-0.35	0.01	0.03	0.23	-0.01	-0.21	0.02	0.03
8	1	-0.03	-0.29	0.01	0.03	0.27	-0.01	-0.17	0.02	0.04
9	1	0.04	0.31	-0.01	0.02	0.22	-0.01	-0.17	0.02	-0.04
10	1	0.04	0.37	-0.01	0.02	0.19	-0.01	-0.21	0.02	-0.02
11	6	0.00	-0.03	0.00	-0.01	-0.09	0.00	0.05	0.00	-0.01
12	7	0.00	-0.01	0.00	-0.01	-0.12	0.00	0.02	0.00	0.00
13	7	0.00	-0.02	0.00	-0.05	-0.44	0.02	0.57	-0.06	-0.01
14	8	0.04	0.37	-0.01	-0.03	-0.23	0.01	0.16	-0.01	0.22
15	1	0.04	0.32	-0.01	-0.05	-0.43	0.02	0.34	-0.03	0.20
16	8	-0.05	-0.40	0.01	-0.02	-0.21	0.01	0.16	-0.03	-0.21

CBN₂dimer

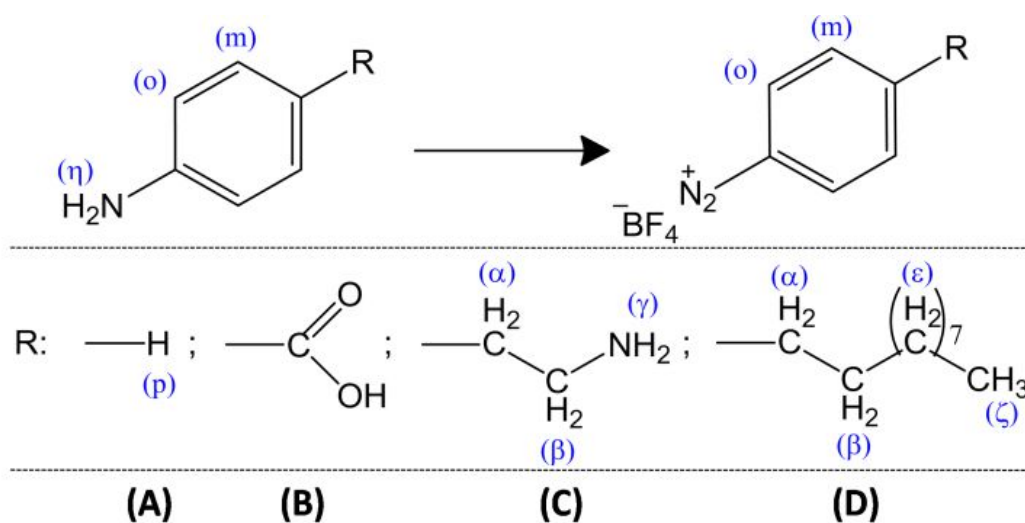


Tag	Symbol	X	Y	Z
1	C	-0.0335970	0.0065090	0.2775450
2	C	-0.0416790	-0.0333280	1.6628870
3	C	1.1663890	-0.0323510	2.3744160
4	C	2.4003440	-0.0046680	1.7101860
5	C	2.4487540	0.0225400	0.3269690
6	C	1.2200910	0.0207730	-0.3538170
7	H	-0.9515780	-0.0065840	-0.2967550
8	H	-0.9831080	-0.0550670	2.1956720
9	H	3.3148570	-0.0046900	2.2897160
10	H	3.3885110	0.0443030	-0.2104420
11	C	1.1769970	-0.0612010	3.8815360
12	N	1.2469070	0.0479690	-1.7406210
13	N	1.2690810	0.0696430	-2.8453580
14	O	-0.0242280	-0.0863310	4.4116280
15	H	0.0290220	-0.1043120	5.4063820
16	O	2.2269060	-0.0599950	4.5047580
17	C	2.5118260	-0.1871160	11.3345900
18	C	2.5199250	-0.1603210	9.9492470
19	C	1.3118600	-0.1608850	9.2377100
20	C	0.0778930	-0.1881310	9.9019370
21	C	0.0294660	-0.2153150	11.2851540
22	C	1.2581270	-0.2139660	11.9659440
23	H	3.4298040	-0.1873630	11.9088950
24	H	3.4613630	-0.1389190	9.4164680
25	H	-0.8366170	-0.1877890	9.3224040
26	H	-0.9103000	-0.2367460	11.8225620
27	C	1.3012710	-0.1319930	7.7305850
28	N	1.2312890	-0.2411280	13.3527510
29	N	1.2091320	-0.2627740	14.4574880
30	O	2.5025000	-0.1069520	7.2004920
31	H	2.4492560	-0.0889290	6.2057370
32	O	0.2513730	-0.1332010	7.1073450

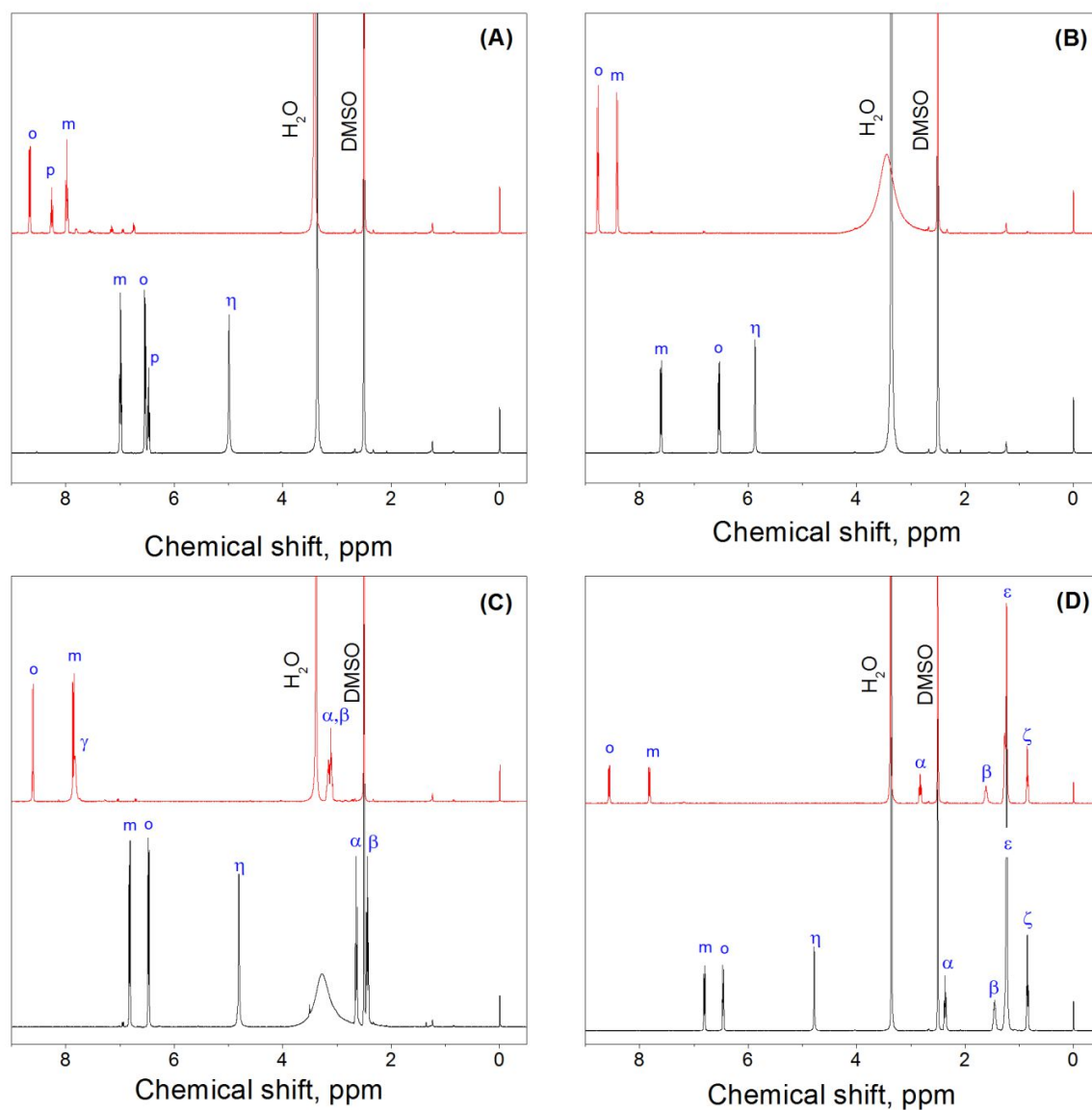
	1	2	3						
Frequencies --	15.5021	31.1718	38.0136						
Red. masses --	11.1250	3.8081	9.2208						
Frcconsts --	0.0016	0.0022	0.0079						
IR Inten --	5.8957	0.0637	5.3874						
RamanActiv --	0.0000	0.0000	0.0000						
Depolar (P) --	0.7497	0.7203	0.7500						
Depolar (U) --	0.8570	0.8374	0.8571						
Atom AN	X	Y	Z	X	Y	Z	X	Y	Z
1 6	0.00	0.08	0.00	0.00	0.18	0.01	0.06	0.02	-0.09
2 6	0.00	-0.04	0.00	0.00	0.17	0.01	-0.04	0.01	-0.09
3 6	0.00	-0.09	0.00	0.00	0.00	0.00	-0.09	0.00	0.00
4 6	0.00	-0.04	0.00	0.00	-0.17	-0.01	-0.04	-0.01	0.09
5 6	0.00	0.08	0.00	0.00	-0.18	-0.01	0.06	-0.01	0.09
6 6	0.00	0.13	0.00	0.00	0.00	0.00	0.11	0.00	0.00
7 1	0.00	0.12	0.00	-0.01	0.31	0.01	0.10	0.03	-0.15
8 1	0.00	-0.08	0.00	0.00	0.30	0.01	-0.08	0.03	-0.15
9 1	0.00	-0.09	0.00	0.01	-0.30	-0.01	-0.08	-0.03	0.15
10 1	0.00	0.12	0.00	0.00	-0.31	-0.01	0.10	-0.03	0.16
11 6	0.00	-0.20	0.00	0.01	0.00	0.00	-0.17	0.00	0.00
12 7	0.00	0.26	0.00	-0.01	0.00	0.00	0.22	0.00	0.00
13 7	0.00	0.36	0.01	-0.01	0.00	0.00	0.32	0.00	0.01
14 8	0.00	-0.23	0.00	0.01	0.05	0.00	-0.19	0.00	-0.04
15 1	0.00	-0.27	-0.01	0.01	0.02	0.00	-0.22	0.00	-0.04
16 8	0.00	-0.24	0.00	0.01	-0.04	0.00	-0.19	-0.01	0.03
17 6	0.00	0.08	0.00	0.00	0.18	0.01	0.06	0.02	-0.09
18 6	0.00	-0.04	0.00	0.00	0.17	0.01	-0.04	0.01	-0.09
19 6	0.00	-0.09	0.00	0.00	0.00	0.00	-0.09	0.00	0.00
20 6	0.00	-0.04	0.00	0.00	-0.17	-0.01	-0.04	-0.01	0.09
21 6	0.00	0.07	0.00	0.00	-0.18	-0.01	0.06	-0.01	0.09
22 6	0.00	0.13	0.00	0.00	0.00	0.00	0.11	0.00	0.00
23 1	0.00	0.12	0.00	-0.01	0.31	0.01	0.10	0.03	-0.15
24 1	0.00	-0.08	0.00	0.00	0.30	0.01	-0.08	0.02	-0.15
25 1	0.00	-0.09	0.00	0.01	-0.30	-0.01	-0.08	-0.03	0.15
26 1	0.00	0.12	0.00	0.00	-0.31	-0.01	0.10	-0.03	0.16
27 6	0.00	-0.20	0.00	0.01	0.00	0.00	-0.17	0.00	0.00
28 7	0.00	0.26	0.00	-0.01	0.00	0.00	0.22	0.00	0.00
29 7	0.00	0.36	0.01	-0.01	0.00	0.00	0.32	0.00	0.01
30 8	0.00	-0.23	0.00	0.01	0.05	0.00	-0.19	0.00	-0.04
31 1	0.00	-0.27	-0.01	0.01	0.02	0.00	-0.22	0.00	-0.04
32 8	0.00	-0.24	0.00	0.01	-0.04	0.00	-0.19	-0.01	0.03

NMR Characterization

Synthesized diazonium salts and their primary amines were characterized by Nuclear Magnetic Resonance (NMR). Spectra were recorded using a Bruker Avance III 400 MHz instrument. ^1H chemical shifts are presented in ppm (part per million) values relative to TMS referenced to the internal residual in d-DMSO solvent. Data are reported as follows: s = singlet, d = doublet, t = triplet, m = multiplet and coupling constants are given in Hz. The structures of the amines and salts as well as indexation of protons are presented in scheme S1. Both the amines and diazonium salts RMN spectra are presented in Figure S1.



Scheme S1: Structures of amine and diazonium salt with the indexation of protons.



FigureS1: Chemical shift comparison between primary amines (black spectra) and their diazonium salts (red spectra) for aniline (A), 4-aminobenzoic acid (B), 4-(2-aminoethyl)aniline (C) and 4-decylniline (D).

Aniline:

^1H NMR (400 MHz, DMSO- d^6): δ (ppm) 4.99 (s, 2H, H- η); 6.47 (t, J = 7.3 Hz, H, H-p); 6.54 (d, J = 7.7 Hz, 2H, H-o); 7.00 (dd, J = 7.3 and 7.7 Hz, 2H, H-m).

Benzenediazonium salt:

^1H NMR (400 MHz, DMSO- d^6): δ (ppm) 7.98 (dd, J = 7.6 and 8.3 Hz, 2H, H-m); 8.26 (t, J = 7.6 Hz, H, H-p); 8.67 (d, J = 8.3 Hz, 2H, H-o).

4-aminobenzoic acid:

^1H NMR (400 MHz, DMSO- d^6): δ (ppm) 5.87 (s, 2H, H- η); 6.54 (d, J = 8.4 Hz, 2H, H-o); 7.61 (d, J = 8.4 Hz, 2H, H-m).

4-carboxybenzene diazonium salt (DS-COOH):

^1H NMR (400 MHz, DMSO- d^6): δ (ppm) 8.41 (d, J = 8.4 Hz, 2H, H-m); 8.77 (d, J = 8.4 Hz, 2H, H-o).

4-(2-aminoethyl)aniline:

^1H NMR (400 MHz, DMSO- d^6): δ (ppm) 2.44 (t, J = 7.2 Hz, 2H, H- β); 2.64 (t, J = 7.2 Hz, 2H, H- α); 4.81 (s, 2H, H- η); 6.48 (d, J = 8.0 Hz, 2H, H-o); 6.82 (d, J = 8.0 Hz, 2H, H-m).

4-(2-aminoethyl)benzenediazonium salt (DS $\text{CH}_2\text{CH}_2\text{NH}_2$):

^1H NMR (400 MHz, DMSO- d^6): δ (ppm) 3.08-3.17 (m, 4H, H- α,β); 7.83 (s, 2H, H- γ); 7.86 (d, J = 8.7 Hz, 2H, H-m); 8.61 (d, J = 8.7 Hz, 2H, H-o).

4-Decylanilin:

^1H NMR (400 MHz, DMSO- d^6): δ (ppm) 0.85 (t, J = 6.4 Hz, 3H, H- ζ); 1.23 (s, 14H, H- ϵ); 1.45-1.47 (m, 2H, H- β); 2.37 (t, J = 7.6 Hz, 2H, H- α); 4.78 (s, 2H, H- η); 6.46 (d, J = 7.9 Hz, 2H, H-o); 6.81 (d, J = 7.9 Hz, 2H, H-m).

4-Decylanilinbenzenediazonium salt (DS-C10):

^1H NMR (400 MHz, DMSO- d^6): δ (ppm) 0.85 (t, J = 6.4 Hz, 3H, H- ζ); 1.25 (s, 14H, H- ϵ); 1.60-1.62 (m, 2H, H- β); 2.83 (t, J = 7.6 Hz, 2H, H- α); 7.82 (d, J = 8.4 Hz, 2H, H-m); 8.56 (d, J = 8.4 Hz, 2H, H-o).

Absence of protons from NH_2 group indicates total amine conversion to diazonium salt. The impurities represent 8 %, 1.5 %, 3 % and 4 % of the diazonium salts for DS, DS-COOH, DS- $(\text{CH}_2)_2\text{NH}_2$ and DS- $\text{C}_{10}\text{H}_{23}$, respectively.

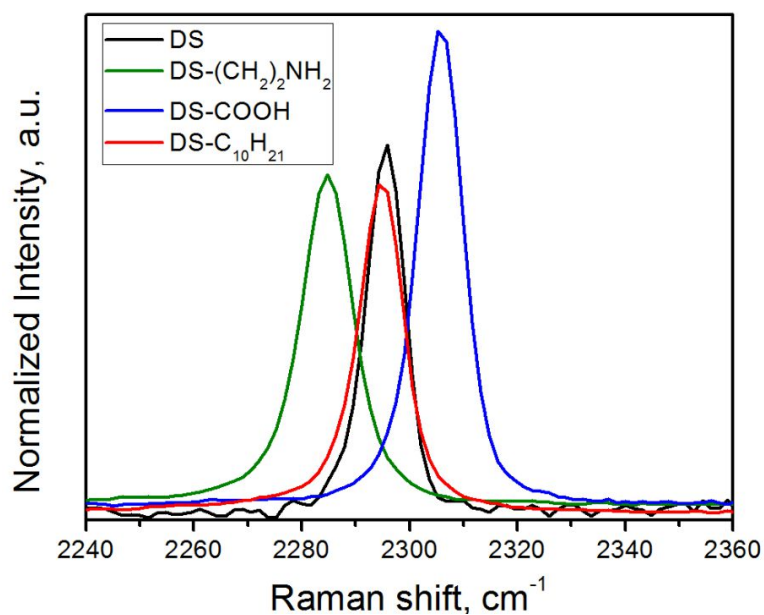


Figure S2: Raman relative intensity of $\nu(\text{N}=\text{N})$ normalized versus $\nu(\text{C}=\text{C})$ for DS, DS-COOH, DS- $\text{CH}_2\text{CH}_2\text{NH}_2$ and DS- $\text{C}_{10}\text{H}_{21}$.

Table S1: Substituent constants (σ_p) [33,34].

Group	σ_p
NH_2	-0.66
CH_3	-0.17
COOH	1.14

Table S2: Calculated relative intensity of $\nu(\text{N}=\text{N})$ normalized versus $\nu(\text{C}=\text{C})$ for DS, DS-COOH, DS- $\text{CH}_2\text{CH}_2\text{NH}_2$ and DS- $\text{C}_{10}\text{H}_{21}$ and calculated percentages of the normalized intensity versus results obtained for DS.

Diazoniumsalt	$I_{\nu(\text{N}=\text{N})} / I_{\nu(\text{C}=\text{C})}$	% versus DS
DS	0.93	100
DS-COOH	1.14	123
DS- $\text{CH}_2\text{CH}_2\text{NH}_2$	0.93	100
DS- $\text{C}_{10}\text{H}_{21}$	0.93	100

ANNEX 5: Supporting Information for Diazonium salt-based SERS substrates: at the root of the development of innovative “long life” robust SERS sensors

Stéphanie Betelu^{1*‡}, Inga Tijunelyte^{2‡}, Leïla Boubekour-Lecaque^{3‡}, Ioannis Ignatiadis¹, Anne Caroline Schnepf^{1‡}, Joyce Ibrahim³, Timothée Toury³, Erwann Guenin², Nathalie Lidgi-Guigui², Nordin Félidj³, Emmanuel Rinnert⁵, Marc Lamy de la Chapelle²

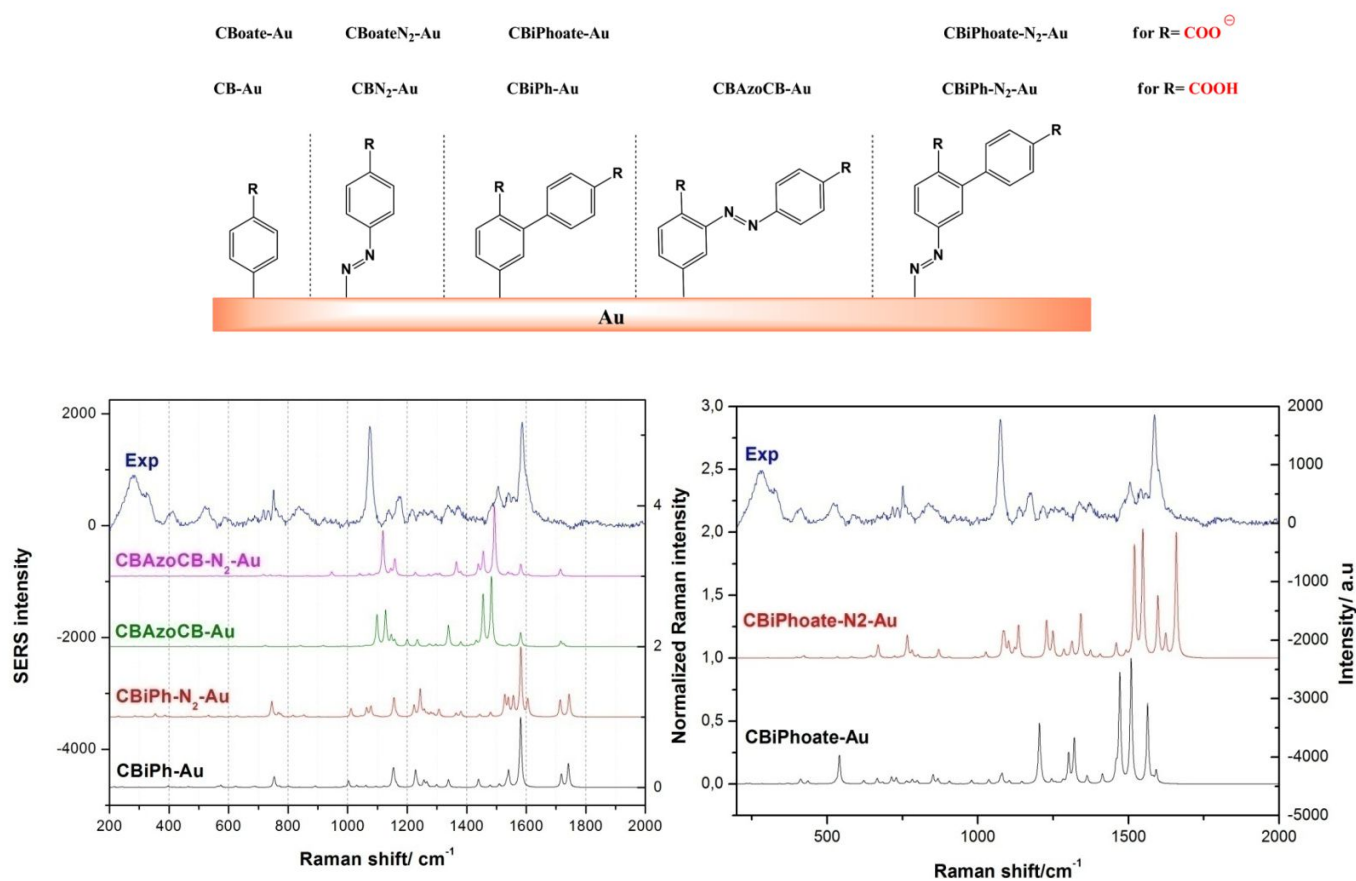


Figure S1: Additional DSCOOH adducts envisaged for DFT modeling

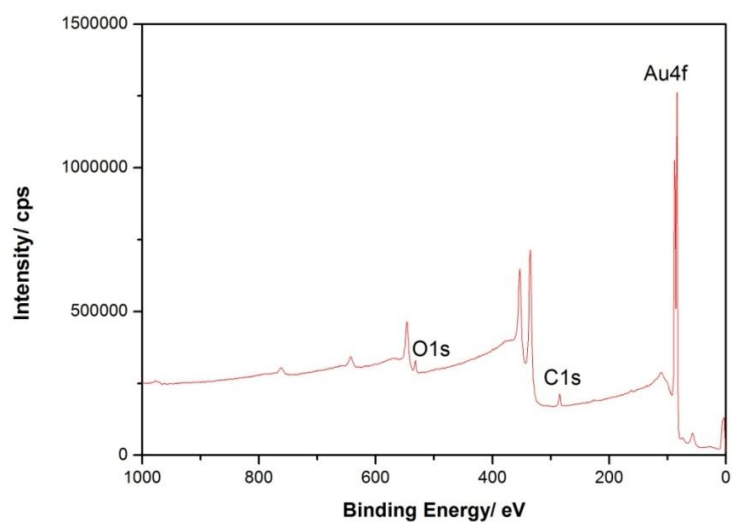


Figure S2: General XPS spectra for DSCO OH adsorbed on planar gold film.

ANNEX 6: Supplementary Information for Diazonium salt-based SERS active sensor: towards detection and quantitation of the aromatic hydrocarbons in water samples

Inga Tijunelyte^{1‡}, Stéphanie Betelu^{2‡}, Jonathan Moreau⁴, Ioannis Ignatiadis², Catherine Berho², Nathalie Lidgi-Guigui¹, Erwann Guénin¹, Catalina David³, Sébastien Vergnole³, Emmanuel Rinnert⁴, Marc Lamy de la Chapelle¹

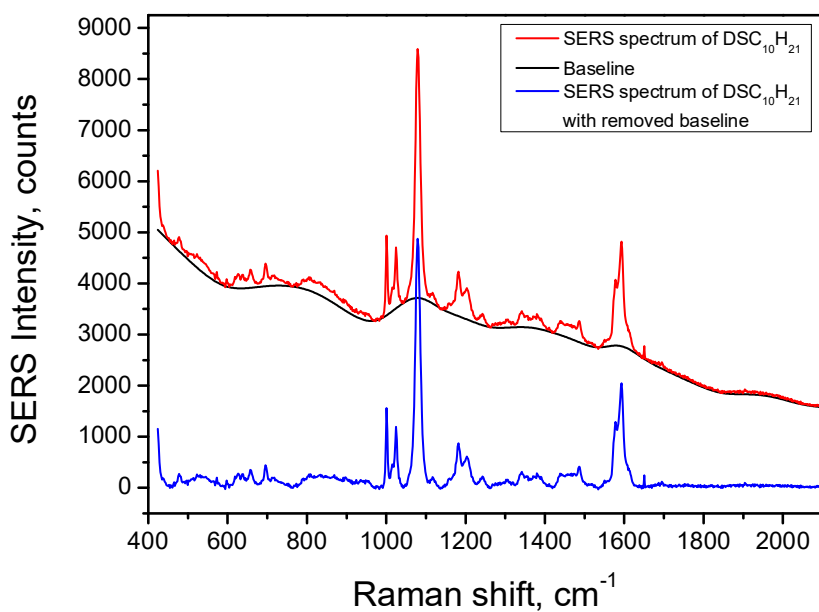
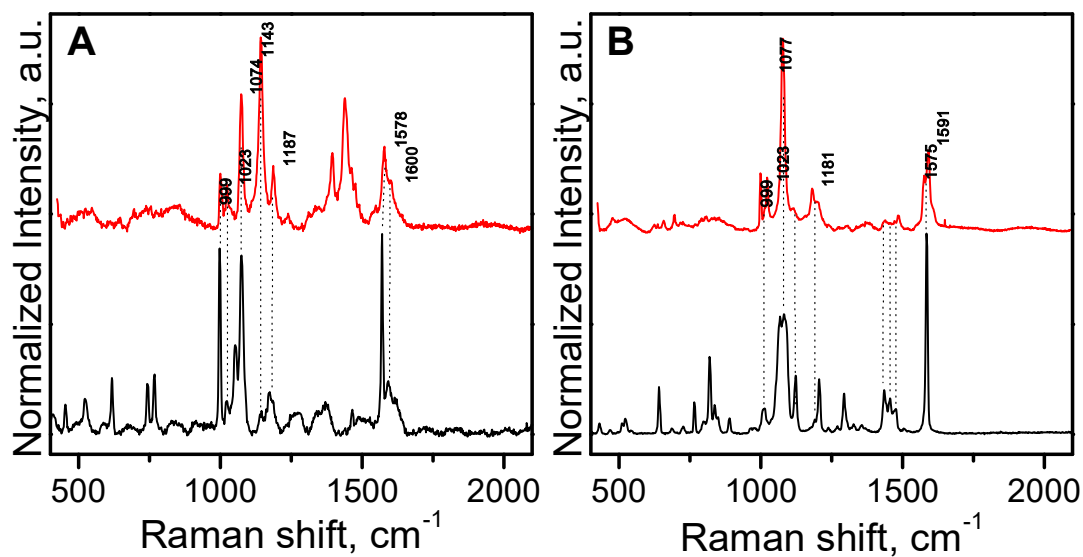


Figure S1: Example of the baseline correction procedure used in this study.



Figure

S2: Comparison of Raman signatures (back spectra) of selected diazonium salts with SERS spectra (red plots) of their grafted layers. Graph A corresponds to DS and DS-based GNs and graph B is dedicated for DSC₁₀H₂₁ and its grafted layer.

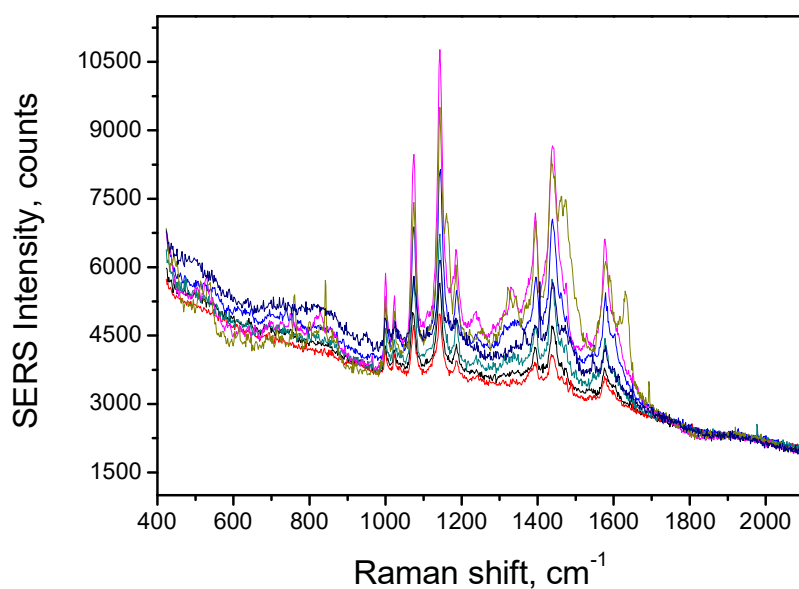


Figure S3: SERS spectra obtained on DS-based substrate.

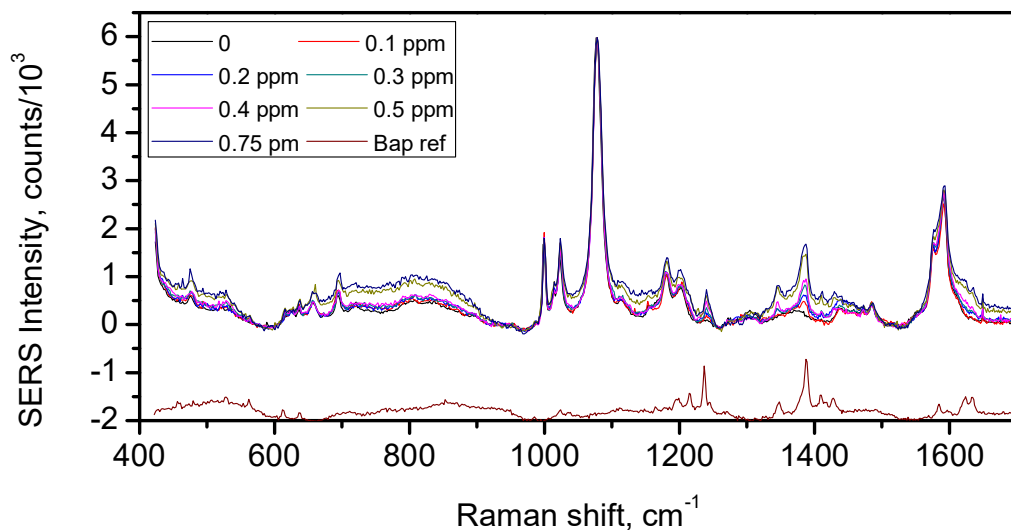


Figure S4: BaP detection with DSC₁₀H₂₁ based nanosensor. Representation of complete spectral range.

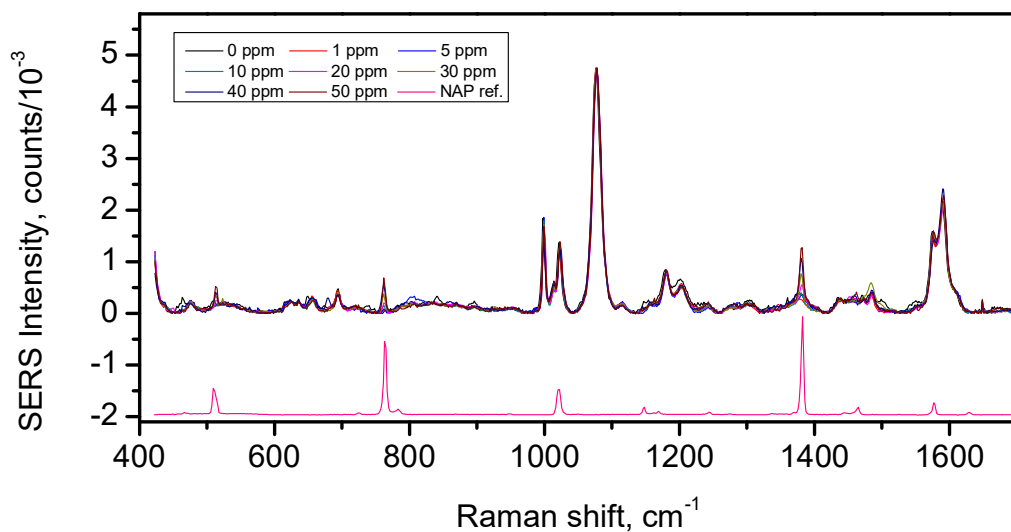


Figure S5: NAP detection by DSC₁₀H₂₁ based nanosensor. Representation of complete spectral range.

ANNEX 7: Supplementary Information for Nanoplasmonics tuned “click chemistry”

Inga Tijunelyte¹, Erwann Guenin¹, Nathalie Lidgi-Guigui¹, Florent Colas², Joyce Ibrahim³, TimothéeTourey³, Marc Lamy de la Chapelle¹

Investigation on thiol-ene reaction initiation conditions

In the article described results demonstrate successful thiol-ene reaction initiation thanks to physical effects provided by highly resonant NCs. For this reaction 2,2'-Azobis(2-methylpropionamide) dihydrochloride (AAPH) was used as a radical initiator.

In order to test this radical initiator performance in bulk conditions we have performed the thiol-ene reaction under several experimental conditions. The aqueous reaction mixture was first prepared by dissolving one equivalent of both: thiophenol (3.5 μL , 7 mmol.L^{-1}) and pentenoic acid (3.5 μg , 7 mmol.L^{-1}). This acid has been used to mimic the allyl mercaptan since the latter one has a thiol group that could directly react with the double bond of another allyl mercaptan molecule. In such conditions, it will not be able to determine the actual efficiency of the thiol-ene reaction between the thiophenol and the mercaptan. Thus we have used the pentenoic acid that have no thiol group but still have a double bond for thiol-ene reaction. Since this acid and the allyl mercaptan have similar structure, we assume that the reaction rate is also similar for both molecules. The mixture was investigated by Nuclear Magnetic Resonance (NMR) in deuterium oxide (D_2O) using Bruker Avance III 400 MHz instrument prior to the initiation of thiol-ene reaction. The figure S1 shows the ^1H NMR spectrum of the region of interest. Multiple peaks presented in ^1H NMR spectrum at 4.81-5.07 (m, 2H) and 5.78-5.9 (m, H) are assigned to the vinyl protons whereas the group of peaks at 7.11-7.34 (m, 5H) belongs to the aromatic protons.

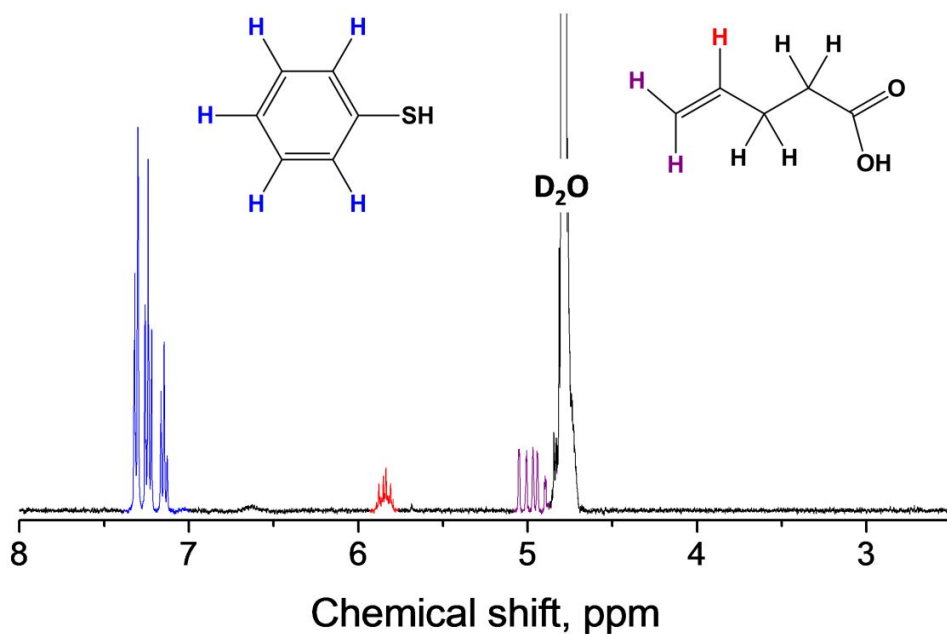


Figure S1 Nuclear Magnetic Resonance (NMR) spectrum of thiophenol and pentenoic acid mixture

After introducing the AAPH ($9.5 \text{ mg}, 7 \text{ mmol.L}^{-1}$) in solution, four different initiation conditions were performed (Figure S2.):

- 1) illumination of the solution with 660 nm laser light with a power of 0.45 mW (these conditions correspond to the exact ones used with the NCs)
- 2) illumination of the solution with 660 nm laser light with a power of 4.5 mW
- 3) heating of the solution at $60 \text{ }^{\circ}\text{C}$
- 4) illumination of the solution with UV excitation wavelength of 365 nm

For all experiments, the exposure time (illumination or heating) was set to 30 min. The thiol-ene reaction in bulk was monitored by ^1H NMR thanks to the observation of multiple peaks at 7.48 ppm and 2.71 ppm (a and b labels on the figure S2, respectively). The first peaks correspond to a shift of protons from the aromatic ring whereas the peaks at 2.71 ppm are assigned to the protons of the carbon bound to sulfur¹. No spectral changes were observed on the NMR spectra after irradiating the mixture using identical parameters as the ones described in article (laser of 660 nm with the power of 0.45 mW) and even after increasing the laser power by one order of magnitude (power of 4.5 mW). The reaction starts at very low level after incubating solution at 60°C (observation of peaks with very low intensity at 2.71 and 7.48 ppm). This observation is not surprising. In the literature, the use of AAPH for radical reaction demands heating to 60°C for 24h². The highest reaction efficiency was

observed by irradiating sample under UV light since after 30 minutes of illumination intense bands are observable.

These results indicate clearly that the thiol-ene reaction cannot be initiated using the 660 nm excitation wavelength even if the laser power density is high without any plasmonic structures. Moreover, the reaction is slow using the increase of the temperature or the UV light. It means that the plasmonic effect enhance the chemical process and accelerate the thiol-ene reaction at the nanostructure surface.

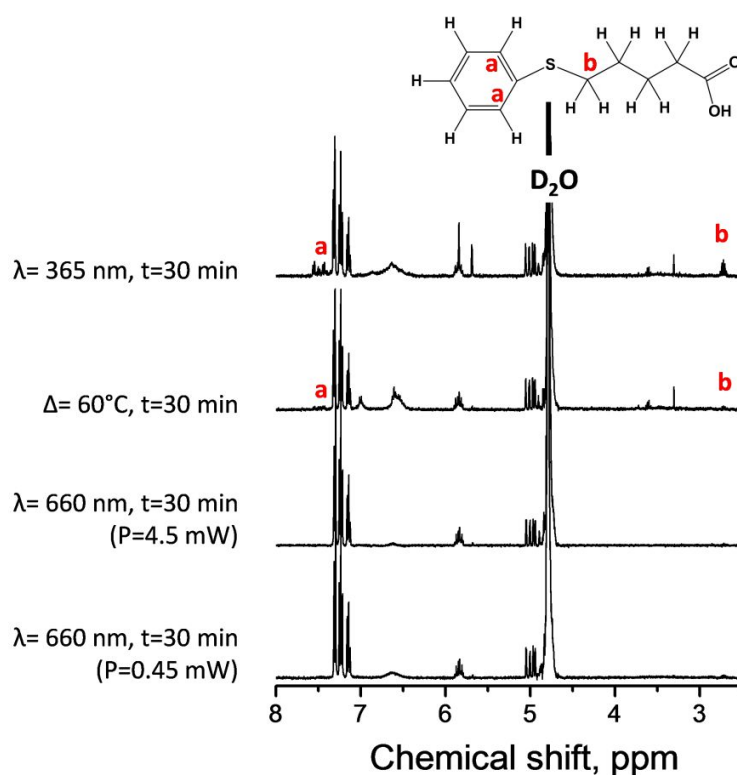


Figure S2 Nuclear Magnetic Resonance (NMR) spectra recorder after exposing mixture for thiol-ene reaction to a various initiation conditions.

SERS spectra recorded for the different experiments

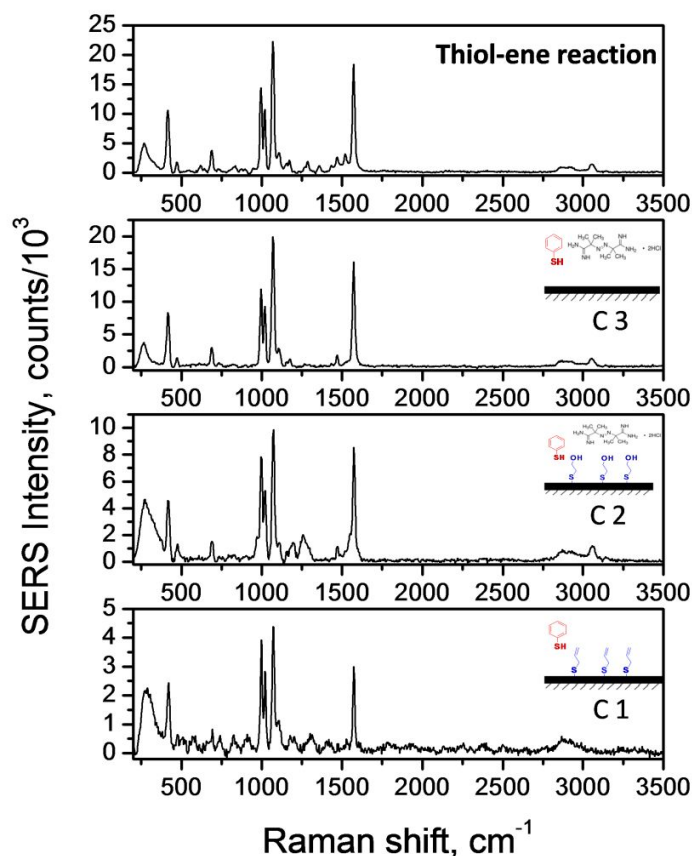


Figure S3 SERS spectra of thiophenol grafted to gold NCs *via* competitive replacement (experiments C1 and C2), spontaneous adsorption (experiment C3) or thiol-ene chemistry.

The comparison of the SERS spectra obtained after thiophenol grafting by thiol-ene reaction or by spontaneous or competitive interactions is presented on Figure S3. Except the first negative control (C1) all other SERS substrates were initially pre-functionalised by either allyl mercaptan or mercaptoethanol. After the thiophenol immobilization, all SERS spectra exhibit very similar spectral features that can be assigned to the main fingerprints of thiophenol. This means that the grafting of the thiophenol did not change its structure or its orientation on the gold surface. Moreover, the contribution of the allyl mercaptan or mercaptoethanol is actually limited to the SERS spectra which are dominated by the thiophenol contribution.

Temperature calculation

When light is absorbed by a nanoparticle (NP), part of the incoming energy is turned into heat, leading to an increase of the NP temperature (ΔT_0) and as a consequence inducing a local heat of the surrounding media. ΔT_0 is directly related to the absorption cross-section (σ_{abs}) as³:

$$\Delta T_0 = \frac{\sigma_{\text{abs}} I_{\text{inc}}}{4\pi R_{\text{eq}} \beta \kappa_{\text{surr}}} \quad \text{Eq. 1}$$

with I_{inc} the irradiance of the incoming beam in the plane of the NP, R_{eff} the effective radius of the NP (defined as the radius of a sphere of a volume equals to that of the NP), β a constant depending on the aspect ratio of the NC and κ_{surr} the thermal capacity of the surrounding medium. In our case, κ_{surr} is considered as the mean of the thermal capacity of water and glass ($\kappa_{\text{surr}} \approx 1 \text{ Wm}^{-1} \text{ K}^{-1}$).

In the case of an assembly of NPs, the heating transfer from one NP to the others contributes to the temperature increase. Considering a Gaussian beam of waist (w_0) shining an array of NPs, the collective temperature increase is proportional to the absorption cross-section of the individual NP and a geometrical parameter as⁴:

$$\Delta T_{\text{coll}} = \frac{\sigma_{\text{abs}} I_{\text{inc}}}{\kappa_{\text{surr}}} \sqrt{\frac{\ln 2}{4\pi}} \frac{1}{w_0 A} \left(1 - \frac{4\sqrt{A \ln 2}}{\pi w_0} \right) \quad \text{Eq. 2}$$

where A is the area of the lattice. In the case of a square lattice of side length D , $A=D^2$.

The absorption cross-sections of the NC assembly in a square lattice arrangement were calculated by Discrete Dipole Approximation (DDA) using DDSCAT 7.3⁵. Their diameters varied from 100 to 200 nm while their height was kept constant to 50 nm. The interparticle distance was 200 nm. A chromium adhesion layer of 2 nm thickness was added underneath each NC. The relative permittivity of gold was taken from⁶ and that of the chromium from Sopra database. The interdipole distance was set to 2 nm as a balance between mesh resolution and memory requirements. The calculations were performed with the HPC facilities of Pôle de Calcul Intensif pour la Mer⁷.

The surrounding medium was modeled by an effective medium with relative permittivity ϵ_{eff} ⁸⁻¹⁰ equal to the mean of that of the glass substrate and that of water (Eq. 1).

$$\epsilon_{\text{eff}} = \epsilon_{\text{glass}} + \epsilon_{\text{water}}$$

Eq. 1

The absorption cross-sections calculated by DDA are shown on figure S4. The position of the absorption band is red-shifted as the diameter of the NC increases. Unless for the two smallest diameters the value of the maximum is almost constant over the range of diameter considered. The best match between the laser wavelength of 660 nm and the resonance of NCs is reached for diameters of about 120-130 nm.

The temperature increases ($\Delta T = \Delta T_0 + \Delta T_{\text{coll}}$) were calculated from equations 1 and 2 for the different diameters when the NCs are illuminated by a Gaussian beam at a wavelength of 660 nm with a waist equal to the diffraction limit of the beam (1 μm) and with a power of 0.45 mW. The illumination conditions reproduce the experimental ones in order to determine the exact temperature reached above the NCs during the different chemical reaction (thiol-ene reaction and experiments from C1 to C3). The ΔT are plotted on figure S5. For small diameter NCs, the temperature increase rises with the diameter to reach 60 K with 120 nm NCs. ΔT then decreases with the diameter as the mismatch between the resonance and laser line gets larger.

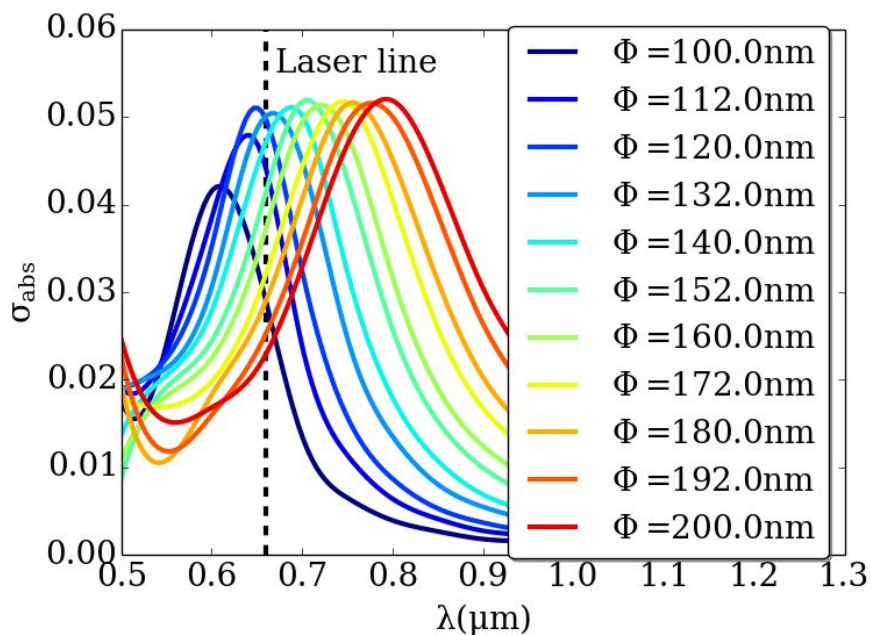


Figure S4: Absorption cross section calculated by DDA for the NC with diameter from 100 up to 200 nm. The dotted vertical line corresponds to the laser wavelength.

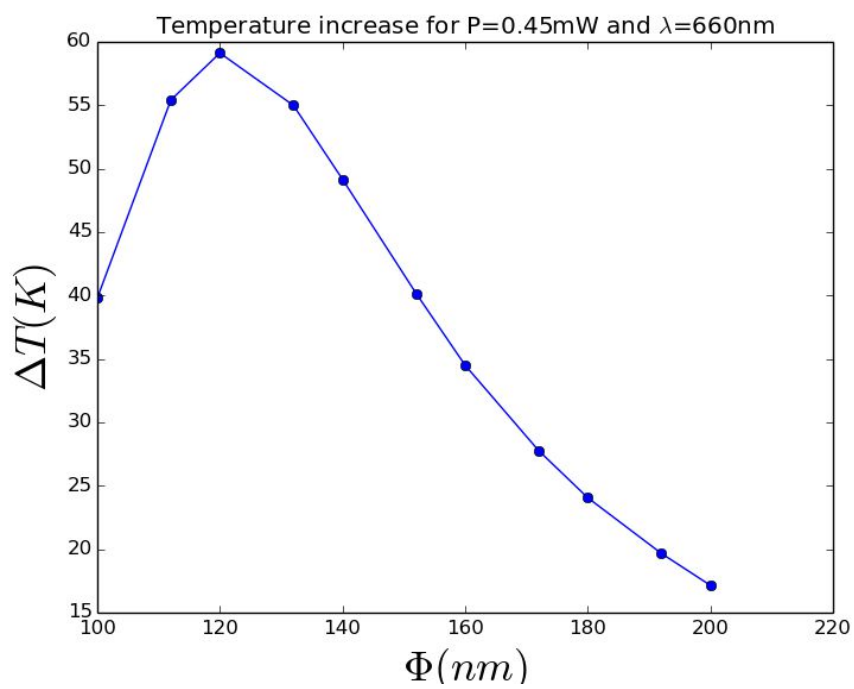


Figure S5: Temperature increase calculated around the NCs versus the NC diameter for an excitation wavelength of 660 nm and a power of 0.45 mW.

References:

- 1 Derboven, P. *et al.* Kinetic Modeling of Radical Thiol–Ene Chemistry for Macromolecular Design: Importance of Side Reactions and Diffusional Limitations. *Macromolecules* **46**, 1732-1742 (2013).
- 2 Dupin, D., Schmid, A., Balmer, J. A. & Armes, S. P. Efficient Synthesis of Poly(2-vinylpyridine)–Silica Colloidal Nanocomposite Particles Using a Cationic Azo Initiator. *Langmuir* **23**, 11812-11818 (2007).
- 3 Baffou, G., Quidant, R. & García de Abajo, F. J. Nanoscale Control of Optical Heating in Complex Plasmonic Systems. *ACS Nano* **4**, 709-716 (2010).
- 4 Baffou, G. *et al.* Photoinduced Heating of Nanoparticle Arrays. *ACS Nano* **7**, 6478-6488 (2013).
- 5 Draine, B. T. & Flatau, P. J. Discrete-Dipole Approximation For Scattering Calculations. *J. Opt. Soc. Am. A* **11**, 1491-1499 (1994).
- 6 Johnson, P. B. & Christy, R. W. Optical Constants of the Noble Metals. *Physical Review B* **6**, 4370-4379 (1972).
- 7 <http://www.ifremer.fr/pcim>.
- 8 Pelton, M., Aizpurua, J. & Bryant, G. Metal-nanoparticle plasmonics. *Laser & Photonics Reviews* **2**, 136-159 (2008).
- 9 Barchiesi, D., Kessentini, S., Guillot, N., de la Chapelle, M. L. & Grosjes, T. Localized surface plasmon resonance in arrays of nano-gold cylinders: inverse problem and propagation of uncertainties. *Optics express* **21**, 2245-2262 (2013).
- 10 Barchiesi, D. Numerical retrieval of thin aluminium layer properties from SPR experimental data. *Optics express* **20**, 9064-9078 (2012).

Abstract

Environmental water pollution by organic compounds is in continuous worldwide concern. Low molecular mass aromatic molecules consisting in benzene rings have received considerable attention due to a documented significant toxicity and carcinogenicity. Within the objectives of the European Water Framework Directives (2000/60/EC, 2006/118/EC and 2006/11/EC) aiming in water quality improvement, the development of analytical tools allowing *in-situ* accurate and sensitive detection is of primary importance and would be a meaningful innovation. With this regard, the main scope of this study was to design sensitive, reproducible, specific and reusable nanosensor for the detection of organic pollutants in environmental waters using Surface Enhanced Raman Spectroscopy (SERS).

During this study the main attention was paid to the selection of suitable receptors and strategies for SERS

nanosensor surface functionalisation in order to pre-concentrate targeted pollutants. The application of antibodies and antigen binding fragments ($F(ab)_2$) for surface decoration was found to be promising approach for highly selective nanosensor design. Another strategy exploited during this study was related with an application of cyclodextrins (CDs). Using Raman and SERS spectroscopies the size selective encapsulation of analytes was demonstrated. Finally, taking advantage of molecular identification in the complex environments offered by SERS technique, nanosensors providing non-specific molecular pre-concentration was considered. For this purpose several diazonium salts (DSs) were studied and applied to the surface functionalisation to create highly hydrophobic coating layer. The performance of such nanosensor was evaluated by detection of aromatic pollutants.

Keywords: Nanosensor; Gold Nanostructures; Diazonium salt; Cyclodextrin; Anti-body; Polycyclic Aromatic Hydrocarbons (PAHs); Surface functionalisation; RAMAN, SERS, LSPR.

Résumé

La pollution des eaux environnementales par des composés organiques est un problème mondial majeur; les molécules aromatiques de faibles masses molaires sont particulièrement concernées, leur toxicité et cancérogénicité étant avérée et bien documentée. La Directive-Cadre Européenne sur l'Eau (2000/60/EC, 2006/118/EC et 2006/11/EC) donne pour objectif d'améliorer la qualité des eaux ; dans ce contexte, le développement d'un outil analytique robuste, permettant de détecter et de quantifier précisément *in-situ* la présence de polluants constituerait une avancée majeure. L'objectif principal de cette étude est donc l'élaboration de nanocapteurs sensibles, robustes et réutilisables, permettant la détection de polluants organiques dans les eaux environnementales par Spectroscopie Raman Exaltée de Surface (SERS).

Afin d'élaborer des nanocapteurs sensibles capables de pré-concentrer les polluants visés, une attention particulière a

été portée à la sélection des substrats et aux stratégies de fonctionnalisation de surface. Tout d'abord, le greffage d'antigènes et de fragments d'antigènes ($F(ab)_2$) en surface de nanocapteurs a montré des résultats prometteurs pour l'élaboration de systèmes très sélectifs. Une seconde approche basée sur l'utilisation de cavités, les cyclodextrines (CDs), a été développée. La spectroscopie Raman et SERS a permis de démontrer la pré-concentration sélective des polluants grâce à leur taille. Enfin, la spectroscopie SERS permettant une identification moléculaire en milieu complexe, une approche permettant une pré-concentration non spécifique des polluants a été considérée. Pour cela, différents sels de diazoniums (DSs) ont été synthétisés et greffés à la surface des nanocapteurs afin de créer une couche hydrophobe permettant la pré-concentration et la détection de composés apolaires. La performance de ces nanocapteurs a été démontrée avec la détection de plusieurs polluants aromatiques.

Mots clés: Nanocapteur; Nanostructures Or; Sel de Diazonium; Cyclodextrine, Anti-corps; Hydrocarbures aromatiques polycycliques (HAP); Fonctionnalisation de Surface; Raman, SERS, LSPR.